Driving out of equilibrium superconductivity with a STM

Thomas Jalabert

THÈSE

Pour obtenir le grade de

DOCTEUR DE L'UNIVERSITE GRENOBLE ALPES

Spécialité : Physique de la matière condensée et du rayonnement

Arrêté ministériel : 25 mai 2016

Présentée par

Thomas JALABERT

Thèse dirigée par **Claude CHAPELIER**, Chercheur, CEA Grenoble,
et codirigée par **Florence LEVY-BERTRAND,** Chargée de recherches, CNRS

préparée au sein du **Laboratoire de Transport Electronique Quantique et Supraconductivité, de l'Institut de Recherche Interdisciplinaire de Grenoble – CEA Grenoble**
dans **l'École Doctorale de Physique**

Modulation de la supraconductivité hors équilibre avec un STM

Driving out of equilibrium superconductivity with a STM

Thèse soutenue publiquement le **15 décembre 2020**,
devant le jury composé de :

Madame Anne ANTHORE
MAITRESSE DE CONFERENCES, Université de Paris, Rapporteuse
Monsieur Tristan CREN
DIRECTEUR DE RECHERCHE, CNRS Délégation Paris-Centre, Rapporteur
Monsieur Teun KLAPWIJK
PROFESSEUR, Delft University of Technology - Pays-Bas, Examinateur
Madame Julia MEYER
PROFESSEURE DES UNIVERSITES, Université Grenoble Alpes, Présidente
Monsieur Clemens WINKELMANN
MAITRE DE CONFERENCES, Grenoble INP, Examinateur

Remerciements

First of all, I would like to thank all the members of the jury, Anne Anthore, Tristan Cren, Teun Klapwijk, Julia Meyer and Clemens Winkelmann for their interest in my work. Their careful reading of the manuscript and their questioning led to very interesting discussions, making the defense a nice time for scientific exchange.

Puisque la thèse est une épreuve de fond jonchée d'obstacles façon 3000m steeple, je voudrais remercier tous ceux qui m'ont aidé d'une manière ou d'une autre à les surmonter et permis d'achever ce travail. Une liste exhaustive serait difficile à établir, mais je pense à tous ceux qui ont rendu cette période aussi agréable et enrichissante que possible.

Je souhaite évidemment remercier chaleureusement mes deux encadrants Florence et Claude pour leur aide, leur soutien et leur disponibilité pendant ces trois années. Claude, travailler avec toi aura été une chance, notamment grâce à ta bienveillance et ton enthousiasme à toute épreuve. Tu es un passionné et je pense que tu fais partie de la définition du chercheur en physique. Florence, tes encouragements, ta réactivité pendant la rédaction et ton regard de non STM-iste m'auront été très précieux.

Je remercie Loïc, mon prédécesseur au labo STM, pour m'avoir formé en cryogénie, réparation des STM et même croissance de graphène sur SiC. Tu as été un très bon prof et un modèle de rigueur et d'organisation. C'est maitenant (déjà !) mon tour de céder ma place à Florie et de lui souhaiter le meilleur.

Vincent, si nous ne travaillions pas sur la même thématique nous partagions la même technique expérimentale, le STM, et t'avoir souvent cotoyé aura été un grand plaisir, que ce soit pour des discussions scientifiques ou personnelles. J'admirerai toujours ton calme et ta positivité. Tu auras aussi été un bon référent pour l'enseignement, une partie de ton métier que tu prends très à coeur, il est important de le souligner.

Je suis heureux d'avoir rencontré des collègues que je peux désormais compter parmi mes amis, et qui auront contribué à rendre l'atmosphère au travail particulièrement agréable, ce qui est très important pour les thésards et post-docs se succédant au labo.

Je remercie le groupe ayant marqué les premières années de ma thèse : je pense à Florian B., le (semi) professionnel du Python mais aussi de l'escalade dans le 7a, Romain A., l'encyclopédie sur pattes, mon co-bureau Anthony le mélomane ainsi qu'à Estelle et Florian V., nos partenaires de soirée grimpe et squat chez Florian B. Le bon vieux temps me manque déjà. Je pense également à la relève : Tom, Cécile, Florie, Estelle V., Nicolas,... Les bivouacs les soirs de canicule et barbecues dans les massifs environnants resteront de bons souvenirs. Sans oublier Simon (et Victor, Loïc M., Alex(s) et JG) et toutes les belles sorties de ski, vélo et alpinisme que nous avons partagées entre deux transferts nocturnes d'hélium.

J'aurais aimé passer plus de temps avec les nouveaux Nathan, Boris, Vivien et Marion que je commençais déjà à apprécier, mais la pandémie en aura décidé autrement.

Je remercie également Romain A., Manuel, Julia, Sarath et Benjamin pour les échanges informels qui sont très importants dans un processus de maturation scientifique. Je suis d'ailleurs prêt à croire Romain, que si tu n'avais pas eu ton propre sujet de thèse tu aurais pu être un de mes encadrants !

Je suis reconnaissant à Jean-Luc et Fred G., sans qui je n'aurais été qu'un expérimentateur privé d'échantillons. Je n'oublierai pas la gentillesse et la disponibilité de Fred, ni les passages de Jean-Luc dans mon bureau à l'heure du départ pour faire quelques blagues.

Je n'oublie pas d'avoir une pensée pour les permanents du labo: François (chef de labo m'ayant fait découvrir l'existence du LATEQs), Xavier, Romain M., Louis, Silvano, Marc, Christophe, Max, Pierre, Fred P., Iulian, Marielle et Etienne.

Je remercie Arnaud et Boris pour m'avoir supporté dans les nombreux échecs que j'ai dû affronter et Claire pour tout le reste.

Pour finir je voudrais remercier mes parents pour m'avoir encouragé à faire des études et supporté dans mes choix.

Contents

Introduction

Electrons in metals consist in a many body system of particles interacting through Coulomb repulsion. Landau showed [2] that this can be described by an independent electron gas, the Fermi liquid, whose excitations are independent fermionic particles, the *quasiparticles*. The physical properties of the material are then well explained since the many body aspect of the problem disappears except for the interaction between quasiparticles. Indeed, while delocalized wave functions account well for the electron states of the Fermi liquid, quasiparticles undergo a diffusion-like motion, interacting with lattice vibrations (phonons), defects, sample boundaries and other quasiparticles over various material dependent lengthscales.

In the presence of an attractive interaction between electrons, the BCS theory [8] explains the emergence of a superconducting state characterized by a condensate of paired electrons, the *Cooper pairs*. Nevertheless, there are always thermal excitations called equilibrium quasiparticles in a superconductor at a finite temperature. In the presence of an additional perturbation, their concentration can be further increased by out of equilibrium quasiparticles.

Two types of non-equilibrium superconductivity [111] referred to as charge and energy imbalance can be realized depending on the nature of the quasiparticles, which continuously changes from hole-like (far below the Fermi level) to electron-like (far above the Fermi level). The type of imbalance is related to the kind of perturbation, and determines the relaxation mechanisms at stake (see Chapter 8). Moreover, in some peculiar situations, a perturbation which feeds energy into the system can result in a counter intuitive enhancement of superconductivity (see Chapter 3).

Therefore, understanding the out of equilibrium quasiparticles dynamics in superconductors is of fundamental interest. It is also important in various applications. Notably, given the small value of their energy gap, superconductors were first considered as good candidates for photon detection in the far-infrared range. Here, photo-excitation with light whose frequency is sufficient to break a Cooper pair creates excess quasiparticles, which dynamics governs the efficiency and sensibility of the detector [90]. In addition, the presence of excess out of equilibrium quasiparticles which origin is not well understood [28] reduces the performances of superconducting circuits with dimensions comparable to the corresponding relaxation lengthscales. This for instance limits the cooling power of micro refrigerators based on normal metal-insulator-superconductor junctions [42] and the coherence of superconducting qubits [76, 91].

This is why substantial efforts have been made to reduce the quasiparticle density, using for example normal metal islands [92] or magnetic vortices [82] to trap out of equilibrium quasiparticles. The microscopic trapping mechanism is however not yet sufficiently understood to account for experimental observations [99]. On another hand, the spatially inhomogeneous density of states intrinsically present in disordered superconductors could explain the anomalous electrodynamics responses measured in such materials [41, 16] in terms of quasiparticle trapping. However, all these investigations have been performed by transport experiments, which only probe macroscopic volumes rendering the explanation in terms of inhomogeneity difficult.

Surprisingly, the effect of quasiparticle injection on the critical current of superconducting nanowires has been very rarely investigated [115]. This is however interesting since few is known and this may be related to the operation of existing devices, among which super-

conducting nanowires single photon detectors (SNSPDs) [90] and superconducting field effect transistors (SuFETs) [27, 85].

In order to experimentally probe the microscopic mechanisms of quasiparticle dynamics, tunnel junctions have been employed to inject out of equilibrium quasiparticles. Nonetheless, lithographed tunnel junctions lack spatial resolution and do not allow to vary the bias voltage and the tunneling current independently, which is a major drawback to whom wants to control the rate and the energy range of injected quasiparticles. In order to overcome these two limitations the novelty of this PhD work is to use a Scanning Tunneling Microscope (STM) working at very low temperature (50 mK) as a quasiparticle injector. Thus, both the tip position and the tunneling set-point are controlled. The resulting modifications of the superconducting properties are probed by measuring the critical current of thin superconducting nanowires. Special care must be paid to surface quality in order to be compatible with the STM technique. Therefore, we chose to study niobium layers capped with gold to prevent surface oxidation. The deposit is performed on already nanostructured substrates to avoid resin residuals. Finally, in addition to provide a quasiparticle injector, the STM allows to perform spatially resolved spectroscopy, with in this PhD work, a supercurrent flow or an external magnetic field. Because of the supercurrent flowing in the nanowire during the experiment, it is interesting to specify that the out of equilibrium state resulting from quasiparticle injection with the STM tip results in an energy imbalance. This corresponds to the situation encountered in many applications, including absorption of electromagnetic radiations. Besides, the spatial resolution of the STM allows to probe inhomogeneous superconducting systems on the nanometer scale, such as type II superconductors in the vortex state and disordered superconductors. Combined with transport measurements, this allows to correlate local features with macroscopic transport properties.

This PhD manuscripts is organized as follows. The first chapter begins with the description of the experimental techniques employed during this PhD work. The principles, implementation and limitations of tunneling microscopy and spectroscopy are introduced. Then, we present the new technique consisting in measuring the critical current of superconducting nanowires under injection of quasiparticles with a STM, that we called Scanning Critical Current Microscopy (SCCM). Chapter 2 presents the theories of superconductivity required to interpret our results. BCS theory deals with equilibrium properties of superconductors, while Usadel theory allows to predict out of equilibrium properties, including the weakening of superconductivity due to inverse proximity effect, supercurrent flow and out of equilibrium distribution functions. The numerical computations performed during this PhD are based on this theoretical framework. Chapter 3 reviews the existing literature experiments related to this PhD work. In particular, focus is made on the properties of superconductors driven out of equilibrium by a supercurrent flow and by quasiparticle injection. The ability to tune independently the bias voltage, tunneling current and position of the tunnel junction with a STM appears as a major improvement. The focus of Chapter 4 is the equilibrium properties of the samples studied in this PhD. We investigate the influence of the nanowires width and thickness, and of the proximity effect due to the gold capping layer on the different lengthscales and superconducting properties characterizing the samples. Chapter 5 deals with the effect of a supercurrent flow on the properties of our nanowires, namely their critical current and local density of states in the presence of a supercurrent. Chapter 6 describes the influence of quasiparticle injection on the critical current and critical temperature of our superconducting nanowires. Experimental observations evidence that a quasi equilibrium is reached in a broad range of experimental conditions. This motivates the development of a heat diffusion model allowing to probe the quasiparticle dynamics. Chapter 7 is dedicated to the study of magnetic vortices in our superconducting nanowires.

Their motion is probed by scanning tunneling microscopy. The vortices also allow to investigate the role of spatial inhomogeneities on quasiparticle dynamics. Chapter 8 is the continuation of the study presented in Chapter 6 when the energy of the injected quasiparticles is close to the gap energy. The superconducting device is in this case no longer in a quasi equilibrium state described by an electronic temperature and a Fermi distribution. This allows us to extract further information about quasiparticle relaxation far from equilibrium.

Chapter 1

Experimental techniques

Contents

The first Scanning Tunneling Microscope (STM) was developed in 1981 by Binnig and Rohrer [11]. It was worth to them the Nobel Prize in Physics five years later since it was a huge breakthrough giving access to the local properties of surfaces down to atomic resolution. Indeed, by *scanning* a very sharp and tiny probe (the tip) on the surface, a physical property at each point of a grid can be measured. This usually allows to image the sample surface roughness or to measure the local electronic density of states as it is respectively presented in Section 1 and Section 2 of the present chapter. The novelty of this PhD work is to use the STM tip as an electron injector to modify a physical property of the sample, namely the superconducting critical current of a nanowire. Section 3 presents this new technique called Scanning Critical Current Microscopy, which combines transport measurements and Scanning Tunneling Microscopy at low temperature. Finally, Section 4 gives details on the fabrication of the superconducting nanowires measured during the PhD.

1.1 Low temperature scanning tunneling microscopy

This section is dedicated to instrumentation and cryogenics. It explains how atomic resolution can be reached at sub Kelvin temperature giving technical details about the home made microscope and its main elements (piezoelectric motors, electronics, cryogenic apparatus).

1.1.1 Working principle

A STM relies on the quantum tunneling of electrons between two **conductive** electrodes (the tip and the sample) through an **insulating** barrier (vacuum). When the distance between the

tip and the sample is small enough, the wave functions of their electrons spatially overlap, so that a **bias voltage** triggers transfer of electrons from one electrode to the other through the barrier by tunnel effect, resulting in a **tunneling current**.

The main feature of the tunnel effect is that the transfer probability and therefore the tunneling current I_t depends exponentially on the distance d between the tip and the sample:

$$I_t \propto e^{-2\kappa d}, \qquad \kappa = \sqrt{\frac{2m\phi}{\hbar^2}} \tag{1.1}$$

with ϕ the work function of the electrodes (which is assumed to be the same for the sake of simplicity), m the electron mass and $\hbar$ the reduced Planck's constant. Typically, $\phi \sim 5$ eV leading to $\kappa \sim 1$ Å^{-1}. This explains why very small spatial variations of the tip lead to detectable changes of the tunneling current I_t. Fig. 1.1b schematizes the spatial resolution of a STM which is sensitive to the electronic density of the atoms: the tip height is adjusted thanks to a feedback loop in order to maintain a constant tunneling current while the sample surface is scanned.

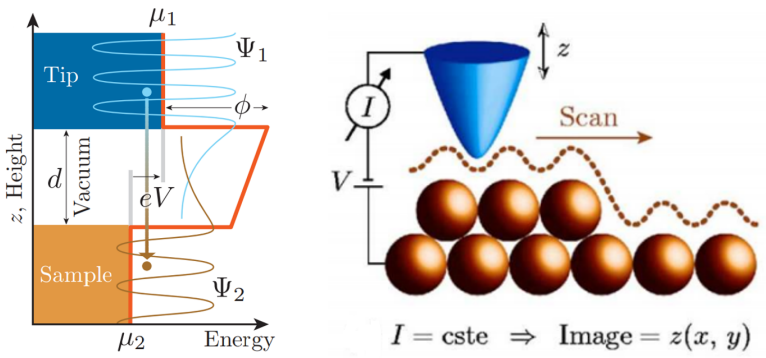

Figure 1.1: Principle of a STM: (a) Energy diagram showing the overlap between the vanishing wave functions Ψ_1 and Ψ_2 of the tip and the sample leading to electron tunneling through a barrier of width d. (b) Schematics of the constant current operating mode: the tip height keeping a constant tunneling current gives an image of the surface of the sample. Taken from [37].

Because of the above reasons, Scanning Tunneling Microscopy is only compatible with conducting samples and relies on the ability to control displacements down to the Angström scale and measure accurately small currents. That is why special attention is paid to avoid oxidation and pollution during sample and tip fabrication, the latest being hold by a piezoelectric tube allowing very small displacements in three dimensions by applying a DC voltage on its electrodes.

1.1.2 The microscope

Fig. 1.2 is a picture of the home made STM, with the main elements pointed out: the scanner tube which holds the tip is glued on an Al_2O_3 (sapphire) disk, and the sample is fixed on a sapphire prism.

Scanner tube

The STM tip is mechanically cut from a 0.5 mm diameter wire made of an alloy of platinum and iridium ($Pt_{0.9}/Ir_{0.1}$). The advantage of this alloy is that it is corrosion proof, as platinum,

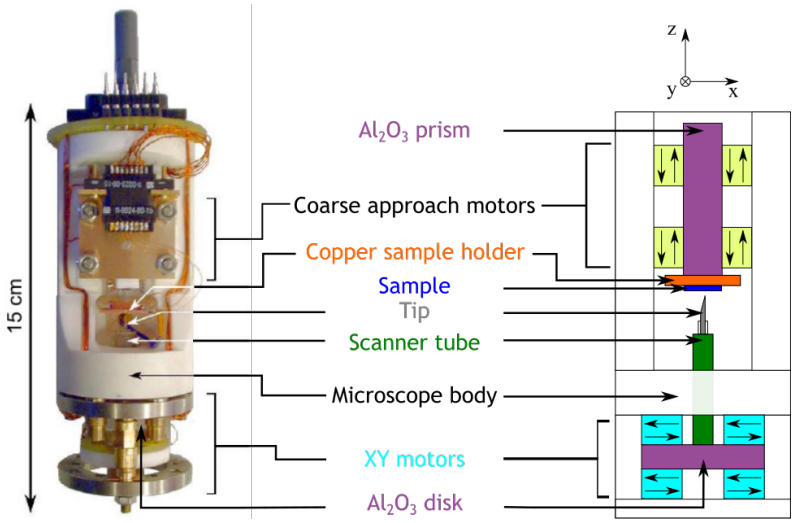

Figure 1.2: Photograph and colored schematics of the microscope with the essential components pointed out. The moving Al_2O_3 supports are in purple and the fixed microscope body in white.

prevents oxide formation, and is also stiff, shifting mechanical resonance frequencies to higher values outside the bandwidth we are interested in. The tip is glued with silver paste or embedded in the scanner tube.

The tube is made of a piezoelectric material, $PbTi_{1-x}Zr_xO_3$ (with x close to 0.5). Its inner and outer parts are covered with metal, see Fig. 1.3a. The outer part is divided in four electrically isolated parts, forming four capacitors ($\approx$ 4 nF) with the inner electrode. When a voltage is applied between two facing electrodes (X^+ and X^- or Y^+ and Y^-), the tube bends laterally over a distance $\Delta_{x,y}$. The stretching Δ_z of the tube is driven by the voltage of the inner (Z) electrode, such as:

$$\Delta_{x,y} = \frac{1.8 V_{x,y} d_{31} L^2}{\psi t} \qquad \Delta_z = \frac{d_{31} V_z L}{t} \tag{1.2}$$

where $V_{x,y}$ is the voltage between two facing electrodes, V_z is the inner electrode voltage, d_{31} a piezoelectric coefficient, L the tube length, ψ its diameter and t its wall thickness.

The tube allows to control the tip to sample distance and to scan the (xy) plane with high accuracy. Indeed, a 150 V applied voltage on the inner electrode stretches it by about 240 nm at 4 K. Nevertheless, thermal contractions during a cooling from 300 K to 4 K produce displacements of the order of tens to a hundred of microns. Therefore, coarse approach motors are required to move the sample with respect to the tip.

Z motors

During the cooling of a sample, and also at the very beginning of an experiment when one needs to bring the sample to within a few hundred microns of the tip to less than the maximum tube stretching length (to reach the tunneling regime), the prism holding the sample has to be moved with respect to the tip. This is done thanks to piezoelectric shear motors (or legs) schematized on Fig. 1.3b. These are made of a stack of polarized piezoelectric plates with copper foils as contacting electrodes in between and a polished Al_2O_3 plate on top to minimize friction with sapphire. The piezoelectric plates shear when a voltage is applied, causing lateral bending of the leg. There are two ways to take advantage of this effect: the Pan mode (developed by S. H. Pan *et al.* [83]) and the inertial mode.

- In Pan mode, each step movement of the prism is decomposed in several stages as shown

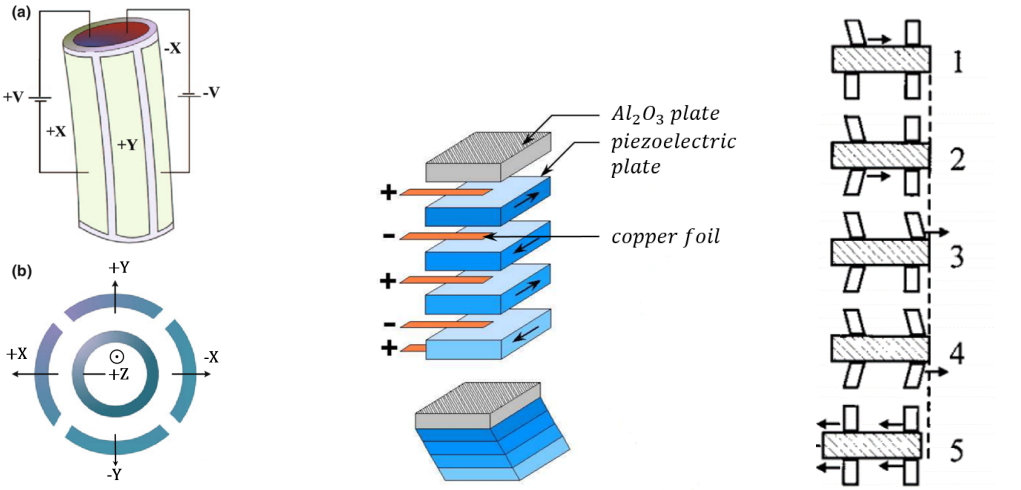

(a) Tube **(b)** Leg **(c)** Pan mode step

Figure 1.3: Schematics of the piezoelectric components of the STM.

on Fig. 1.3c. The piezoelectric legs are deformed one by one from equilibrium to bending position while the others are at rest (stage 1 to 4). The bending leg slides while the others maintain the prism at rest. Then, the prism is moved when the legs are simultaneously deformed to initial position (stage 5).

- In inertial mode, all the legs are abruptly deformed at the same time, so that they slide on the prism which stays at rest, from stage 1 to 4 on Fig. 1.3c. The deformation is still simultaneous but slower, dragging along the prism.

During approach and cooling processes, special attention must be paid to prevent a crash between the tip and the sample, which could seriously damage both the apex and metallic properties of the tip, resulting in poorly resolved images and bad quality junction for spectroscopy (see Section 1.2).

The inertial approach procedure is the following: the regulation is turned on and since no tunneling current is measured, the tube is progressively stretched out. If a tunnel current is detected in the tube range, the procedure is achieved, otherwise the tube is retracted and the coarse approach motors make a few steps forward before the tube is stretched out again, and so on. For the Pan mode approach, the tube stays stretched out to save time, the controlled displacement speed (step 5 of Fig. 1.3c) allowing the feedback loop to prevent a crash of the tip. The feedback loop settings that determine the response time when the tunnel regime is reached and the stretching speed when no current is measured must be chosen carefully.

To prevent a crash during the cooling, a straightforward strategy is to withdraw sufficiently the sample from the tip and make an approach after the cooling. Since the efficiency of the motors at low temperature is not guaranteed, the sample is maintained the closest possible from the tip thanks to the control mode. In this operation mode, the tube is fully extended and the tip to sample distance is slightly larger than the tunneling range, so that the tunneling current is zero. When thermal contractions due to the cooling bring the tip closer to the sample, a tunnel current is detected, then the tube is retracted, the coarse approach motors make a few steps back and the tube is stretched out again.

XY table

The efficiency of the piezoelectric actuators is lowered at low temperatures. Even if the breakdown voltage is a bit higher under vacuum and at low temperature, allowing to apply higher

voltages, the scanning area of the tube goes from 30 μm $\times$ 30 μm at room temperature to 3 μm $\times$ 3 μm at low temperatures. Furthermore, the thermal contractions of the microscope during the cooling randomly move laterally the tip over tens of microns relatively to the sample. Then, a system to move the scan window of the tube on the surface of the sample is required, especially if we want to find a specific area - a nanowire, for instance. The XY table is used for that purpose and has a set-up similar to the Z motors as shown on Fig. 1.2, the XY motors being in fact a stack of two motors tilted by 90 degrees allowing movement in x and y directions.

Sample holder and microscope body

The sample holder is a copper plate screwed on the copper mount glued on the sapphire prism. The latter is firmly hold between the piezoelectric stacks by a strong spring press-plate to ensure sufficient pressure between the motors and the supports and allow for high mechanical stability. The copper mount ensures good thermalization, and holds a thermometer and a heating resistor.

The microscope body is made of macor, a glass-ceramic material. It is rigid and with comparable thermal contractions as the piezoelectric ceramics glued on it preventing them to lift off at low temperature.

Electronics

A control electronics, Nanonis Scanning Probe Microscopy Control System, made by SPECS^{TM}, ensures the high voltage signals generation for the piezoelectric tube and motors, and provides the feedback loop for the regulation of the tunneling current.

The tunneling current amplifier has a large gain and a bandwidth of a few kHz. It will be further described in Section 1.3. The gain is given by the resistor value and in our case is 10^8 V/A, which allows to deal with current from approximately 10 pA to 10 nA. The bandwidth is limited to a few kHz in order to regulate the tunneling current during the scan while rejecting the high frequency noise.

Labview, a software manufactured by National Instruments^{TM}, is used to drive and coordinate the different instruments (Nanonis electronics, voltage sources, voltage and current amplifiers, lock-ins).

1.1.3 Cryogenics

On top of allowing the study of superconductors, low temperatures increase the energetic resolution of spectroscopy (see Section 1.2) and prevent thermal drift between the tip and the sample. The STM is cooled down in an inverted dilution fridge, called Sionludi. By contrast with usual dilution systems which are plunged in a liquid ^{4}He bath, the Sionludi is made of five successive cryogenic stages (100 K, 10 K, 4 K, 1 K and 0.05 K). The coldest stage remains fixed and is easily accessible as it is situated on the top of the cryostat, hence the name: Sionludi. Each stage consists in a plate on which a thermal copper shield is screwed. The stages are assembled like Russian dolls. This configuration aims to reduce thermal radiations. Each stage is supported by epoxy glass tubes to be thermally decoupled from the others. One can see on Fig. 1.4a the 5 stages and the 50 mK shield on top. Situated below the cryostat, a liquid ^{4}He dewar allows to make ^{4}He flow from the 4 K to the 100 K stage. A mixture of ^{4}He and ^{3}He can circulate in a separate closed loop circuit.

A stainless steel cover encloses hermetically the cryostat which is vacuumed before starting the cooling process. The circulation of liquid ^{4}He is next enabled, leading to cryopumping on the cold parts of the 4 K stage. The cooling from 300 K to 4 K of the upper stages is ensured by the fast circulation of the ^{3}He/^{4}He mixture thermalized by the ^{4}He vapors and inside a 4 K

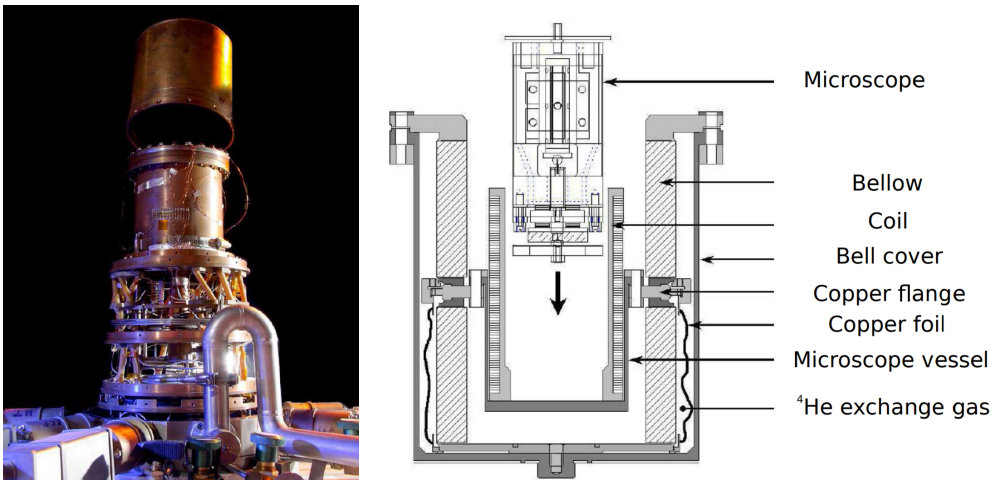

(a) Picture of the Sionludi. **(b)** Schematics of the 50 mK stage.

Figure 1.4: Home built cryogenic apparatus.

pot. Then, a first injection impedance on the ^{3}He/^{4}He circuit allows to trigger a Joule-Thomson relaxation and therefore to condense the mixture down to 1.5 K. The dilution regime and the 50 mK base temperature are eventually reached thanks to a second injection impedance.

The whole cooling process including the pumping last at least two days. Since the efficiency of the piezoelectric motors decreases with the temperature and the steps of the motors generates a non negligible amount of heat, the object of interest (e.g. the nanowire) is located on the sample surface with the STM at 4 K before starting the ^{3}He/^{4}He mixture condensation process. A clog in the mixture circuit (leading to a decrease of the flow and thus of the cooling power) stopped an experiment at the beginning of the PhD. The installation of an hydrogen trap solved the problem and no other clog happened again.

The STM is enclosed in a coil to generate perpendicular magnetic fields up to $\sim$ 50 mT. The whole Sionludi setup lies on an air-cushioned table, and the coil is hanged on a bellow in the 50 mK stage, ensuring mechanical damping as shown on Fig. 1.4b. One bar of ^{4}He exchange gas trapped between the bellow and the bell allows fast thermalization of the STM down to 300 mK, but because of the bad thermal conductance of the stainless bellow, copper foils between the bell and the flange holding the STM are required to reach 50 mK.

1.2 Scanning tunneling spectroscopy

Scanning Tunneling Spectroscopy (STS) is a powerful tool to probe the local Density Of States (DOS) of a sample with the STM spatial resolution. For superconductors, one can directly access the spectral gap of the quasiparticles. As mentioned before, the quality of the tunnel junction is at stake to obtain good images and spectroscopy measurements, because the measured data depends on the tip density of states, which is fortunately constant for a metal.

1.2.1 Tunneling current

The most common way to theoretically describe the electron tunneling between two conducting electrodes is to consider the tunneling probability as a perturbation of the eigenstates of both electrodes. These states $|l\rangle$ and $|r\rangle$ of energies $\epsilon_{l/r}$ are respectively labeled by indices l and r referring to left and right electrode. When a bias voltage V_b is applied to the junction, the two energy distributions are shifted by a factor eV_b, with e the electron charge. The transition probability per unit time $\Gamma_{l\to r}$ for an electron in l to tunnel in r is then given by Fermi's golden

rule:

$$\Gamma_{l\to r} = \frac{2\pi}{\hbar} |\langle l|H_T|r\rangle|^2 \delta(\epsilon_l - \epsilon_r - eV_b) \tag{1.3}$$

where:

- H_T is the tunneling Hamiltonian treated as a perturbation, so that $|\langle l|H_T|r\rangle|^2$ is the transmission coefficient due to the coupling between left and right electrode electronic states. This term represents the wavefunctions overlap and reflects the exponential decay of the tunneling current with the distance between the electrodes (see Eq. 1.1). In a typical experimental situation, it is reasonable to neglect the variations of the transmission coefficient with respect to electron energy and momentum when the bias voltage V_b is small compared to the Fermi energy E_F.
- we consider elastic tunneling, where the electron transfer is only allowed between states of same energy. Otherwise, one must replace the δ function by the probability $P(E)$ to exchange an energy E with the environment, for example by absorbing or emitting a photon (for experimental evidence of such a process, see [88]).

The total tunneling rate $\Gamma_{L\to R}$ is obtained summing over all the states of both electrodes, taking into account their filling factors given by Fermi-Dirac distributions $f_{l/r}(\epsilon)$:

$$\Gamma_{L\to R} = \sum_{l,r} \Gamma_{l\to r}(1 - f_r(\epsilon_r))\ f_l(\epsilon_l) \tag{1.4}$$

The net current is then $e(\Gamma_{L\to R} - \Gamma_{R\to L})$. Transforming the sum into an integral and replacing $|\langle l H_T r\rangle|^2$ by its mean (constant) value $|t|^2$ one finds:

$$I_t(V_b) = \frac{4\pi^2}{eR_Q}|t|^2 \int_{-\infty}^{\infty} dE\ N_l(E)\ N_r(E - eV_b)\ [f_l(E) - f_r(E - eV_b)] \tag{1.5}$$

where $R_Q = h/e^2$ is the quantum of resistance and $N_{l/r}(E)$ the density of states in left and right electrodes.

Consequence for a metallic STM tip. In a metal, the DOS varies on the Fermi energy scale. Since the energies explored with the bias voltage are small compared to Fermi energy, the DOS of the STM tip will be considered constant. Therefore, I_t only depends on four parameters: the tip to sample distance d (through $|t|^2$), the bias voltage V_b, the sample DOS $N_s(E)$ and the temperature T (through the Fermi-Dirac distribution). The temperature T is particularly important when we deal with spectroscopy (see next paragraph).

Neglecting the effect of temperature ($eV_b \gg k_BT$ with k_B the Boltzmann constant), the Fermi-Dirac distributions become step functions and we get:

$$I_t(V_b) \propto |t|^2 \int_0^{eV_b} dE\ N_s(E) \tag{1.6}$$

In a STM experiment, the **tunneling setpoint** is consequently given by both the bias voltage V_b and the target tunneling current I_t. The energy window that contributes to tunneling is given by eV_b. $|t|^2$ governs the barrier transparency. Therefore, lowering V_b must be balanced by reducing d in order to maintain a constant I_t. Similarly, one can reach a higher I_t at constant V_b by lowering d.

Now differentiating I_t with respect to V_b at constant d yields to:

$$G(V_b) = \frac{dI_t}{dV_b}(V_b) \propto N_s(eV_b) \tag{1.7}$$

This quantity, called **differential conductance** is the basis of STS. Indeed, at low temperature it is proportional to the sample DOS at an energy directly tuned by V_b. Experimentally, the differentiation is done by synchronous detection: a given setpoint (I_t,V_b) is chosen and sets the tip height. The feedback loop is then frozen to keep it constant, while a small AC modulation δV_b is added to a continuous V_b ramp and the resulting in phase variation δI_t of I_t is detected by a lock-in amplifier. The measured data during the DC V_b sweep is called spectrum.

1.2.2 Differential conductance and energy resolution

Considering that the DOS of the tip is energy independent and that the $|t|^2$ coefficient is constant, one can identify the left electrode with the sample and the right one to the tip and derive Eq. 1.5 with respect to V_b:

$$G = \frac{dI_t}{dV_b} \propto \int_{-\infty}^{\infty} dE\ N_s(E)\ f_t'(E - eV_b) \tag{1.8}$$

with $f'(E) = \frac{-1}{4k_BT}\cosh^{-2}\left(\frac{E}{2k_BT}\right)$. This equation shows that the differential conductance is actually the convolution of the sample DOS with a peaked function which depends on the thermal distribution of the tip. The smaller T, the closer the differential conductance is to the DOS of the sample. We thus define the energetic resolution by the full width at half maximum of $f'(E)$ which is $2\ln(3+2\sqrt{2})k_BT \simeq 3.5k_BT \approx 15\ \mu$eV at 50 mK.

Case of a superconducting sample. In an electron gas at sufficiently low temperatures and in the presence of an attractive potential, electrons near the Fermi surface tend to form Cooper pairs, no matter how weak is the attractive potential. In conventional superconductors, this attraction is attributed to an electron-lattice interaction mediated by virtual phonons, which can in some materials overcome Coulomb repulsion. In the frame of the Bardeen Cooper Schrieffer (BCS) mean field theory, superconductivity and its effects are explained by the condensation of Cooper pairs due to an attractive potential. Consequently, the quasiparticle (single particle excitation) spectrum is modified near the Fermi energy where a band gap opens (excitations are forbidden under a given energy called gap). The spectrum is given by $E_k = \sqrt{\epsilon_k^2 + \Delta^2}$ where ϵ_k is the kinetic energy of an electron in the state k, E_k is the quasiparticle excitation energy and Δ is the BCS superconducting gap [8]. Equalizing the density of states per unit of momentum in the normal and superconducting state leads to $N_s(E)dE = N_n(\epsilon)d\epsilon$. As the density of states in the normal state varies little in the energy range of Δ (of the order of the meV) in the vicinity of E_F, it will be replaced by its value at the Fermi level N_0. One obtains the density of states $N_s(E)$ of unpaired electrons in the superconducting state:

$$N_s(E) = N_0\frac{d\epsilon}{dE} = \begin{cases} N_0\frac{|E|}{\sqrt{E^2-\Delta^2}} & \text{if } |E| > \Delta \\ 0 & \text{if } |E| < \Delta \end{cases} \tag{1.9}$$

One often adds an imaginary part called Dynes parameter to the energy: $E \to E + i\Gamma$. This has the effect of smearing the BCS gap edge singularity and adding states in the subgap region, and can be physically attributed to finite quasiparticle lifetime. Indeed, since the BCS ground state relies on a coherent superposition of paired quasiparticles, their finite lifetime results in a weakening of superconductivity and more single electron states are available. Even if this finite lifetime can have many origins, such as recombination into Cooper pairs as it was first introduced by Dynes [32], the microscopic origin of this effective pair breaking term is still controversial. Nevertheless, Pekola et al. [88] showed later that the subgap current measured in a tunnel junction between a normal metal and a superconductor can be due to photon assisted tunneling. Furthermore, they demonstrated theoretically that under some conditions

on the junction, the measured DOS leads exactly to the Dynes formula with Γ depending on the temperature and impedance of the electromagnetic environment.

Consequences on energetic resolution. Tunneling spectroscopy allows to use well known spectra, as for example BCS superconducting DOS, to extract the effective temperature of the tip electron gas T_{eff} from Eq. 1.8. An effective temperature of the tip higher than the temperature measured by the thermometer accounts for the smearing of the spectra and the associated (probable) reduced energy resolution (see top panel of Fig. 1.5). Different factors decrease the resolution of our setup and may be responsible for this high effective temperature:

- The electrons of the tip may be poorly thermalized for two reasons: first, cooling of electrons occurs through a coupling with phonons which is less and less efficient at low temperature. Then, unfiltered electromagnetic radiations from environment can heat up the tip, whose end is also a nanoscale object which may not be well coupled to the bulk. That is why special care mut be taken to filtering (see Section 1.3).

- Likewise, voltage fluctuations or noise across the tunneling junction can also reduce the energetic resolution and artificially reproduce the effect of a hot tip (see Fig. 1.5). Indeed, the measured differential conductance $G_{eff}(V_b)$ differs from the sample differential conductance at V_b because of the noise characterized by a probability density $P(V)$ for the voltage to be shifted by V:

$$G_{eff}(V_b) = \int_{-\infty}^{\infty} dV \; P(V - V_b) \frac{dI_t}{dV_b}(V) \tag{1.10}$$

  An improvement in the setup to lower such a noise was to set the voltage bias across the junction thanks to a twin twisted coaxial cable to balance parasitic voltage and to add low-pass RC filters at 50 mK. (see Section 1.3). Similarly, the modulation δV_b must be taken small enough compared to the energetic resolution.

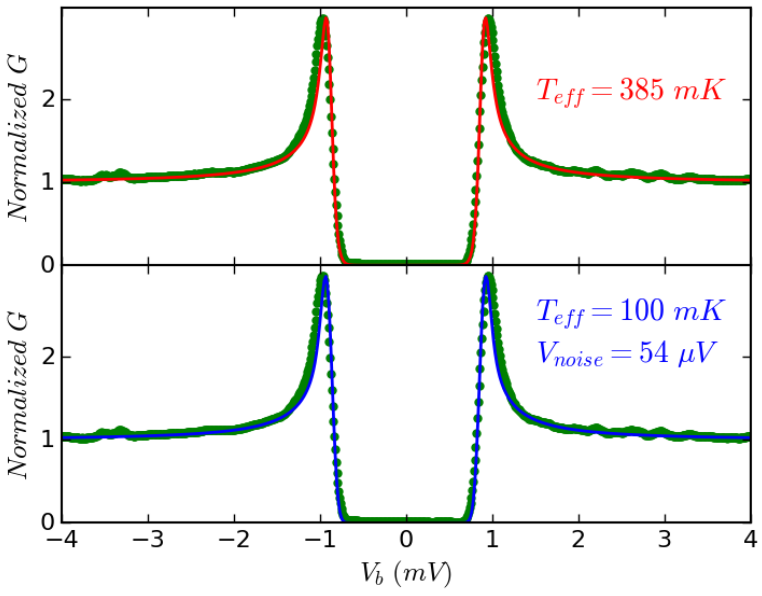

Figure 1.5: Dots: normalized differential conductance measured at 100 mK on $Nb_{15nm}\backslash Au_{5nm}$ with $\delta V_b = 20\ \mu$V. *Top panel:* BCS fit with $T_{eff} = 385$ mK. *Bottom panel:* BCS fit with $T_{eff} = 100$ mK convoluted with a gaussian voltage noise of standard deviation $V_{noise} = 54\ \mu$V. Both fits leads to the same gap $\Delta = 885\ \mu$eV and negligible Dynes parameter.

- Finally, in non perfectly BCS-like superconductors, T_{eff} plays the role of a fitting parameter as well as the Dynes parameter Γ. Indeed, in the thin Nb\Au samples studied in this PhD work, both the small thickness (smaller than the superconducting coherence length) and the inverse proximity effect can make the DOS deviate from BCS theory.

The cause of the difference between T_{eff} and the thermometer is probably a mix of the three above reasons. Indeed, previous measurements in the same fridge on boron doped diamond [96] and graphene grown on rhenium [112], revealed a BCS like dependency of the superconducting gap as a function of temperature with $T_{eff} \approx 250 - 300$ mK. This large effective temperature can be due to both poor electron thermalization and voltage noise but not to deviation from the BCS theory. But in our Nb\Au samples, hotter effective temperatures were extracted from thinner samples with larger gold to niobium ratio in Section 4.5, suggesting that the increase of T_{eff} is here mainly due to deviations from BCS theory. Nevertheless, whatever the values of T_{eff}, Γ and V_{noise} used to perform a fit, the superconducting gap Δ, which is in most cases the quantity of interest, remains unchanged. T_{eff} and V_{noise} fitting parameters being equivalent, **we will only use T_{eff}, Γ and Δ in the following.**

1.2.3 Imaging vortices

The spectrum measurement previously described is performed with a motionless tip to maintain the tunnel barrier width constant and probes the Local Density Of States (LDOS) under the tip. In a common measurement protocol called Current Imaging Tunneling Spectroscopy (CITS), the tip scans the sample surface at a given setpoint to record the topography and stops at each point of a grid to acquire a spectrum, giving access to the spatial evolution of the LDOS.

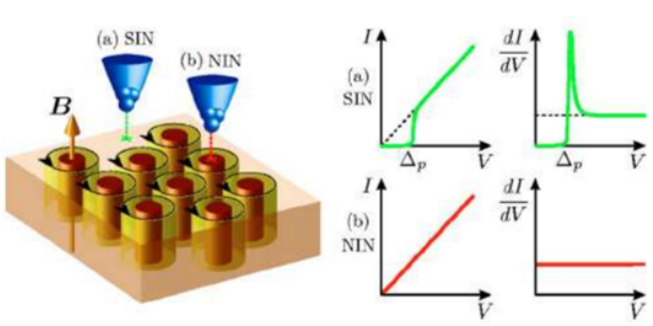

(a) Schematics of a vortex lattice probed by a STM tip and associated spectra: when the tip is between the vortices (area a), the tip probes a superconducting LDOS, whereas in a vortex core (area b), the LDOS is flat. From [37].

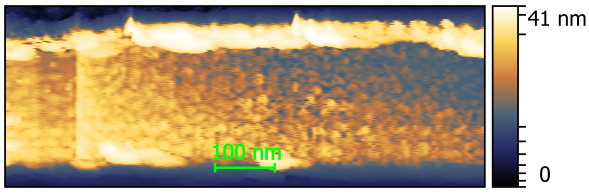

(b) Topography.

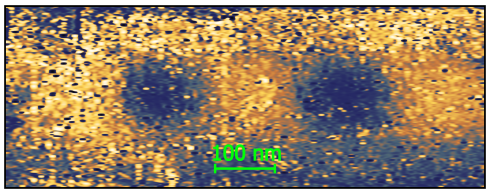

(c) Differential conductance.

Figure 1.6: STM vortex imaging: (a) CITS mode. (b) and (c) Nb\Au 300 nm wide nanowire topographic and differential conductance images recorded simultaneously in scanning mode: when the tunneling bias setpoint is set such as $eV_b \approx \Delta$ with a small AC modulation δV_b, the tip height is regulated in order to keep the mean value of I_t at the chosen current setpoint and gives the topography of the sample, while a synchronous detection measures the AC variations of I_t. The vortex cores (dark) have a lower LDOS at this energy due to the absence of coherence peaks than the superconducting (bright) regions.

This technique can for instance be used to observe vortices: indeed, in a magnetic field and for type II superconductors, magnetic vortices each carrying one superconducting flux quantum $\phi_0 = \frac{h}{2e}$ penetrate the sample [1]. The vortex core is a normal area around which a supercurrent flows in order to screen the magnetic field outside the core. In the dirty limit ($\xi_0 \ll l$ where ξ_0 is the superconducting coherence length and l the electron mean free path), the LDOS in the core is flat as in a normal metal by contrast with the superconducting regions which exhibit a gap (see Fig. 1.6a). However, a CITS is time consuming and the map of the LDOS at a well chosen energy is sufficient to distinguish between a normal and a superconducting DOS. To save some acquisition time and since it is impossible to get a tunneling current (and therefore to scan)

in a superconductor when $eV_b < \Delta$, one can set the bias voltage close to the superconducting coherence peak ($eV_b \approx \Delta$) while recording the differential conductance to obtain an image of the height of the coherence peak revealing the presence of vortices as on Fig. 1.6c.

1.3 Scanning critical current microscopy

A challenge in this PhD was to **perform simultaneously transport and STM measurements at low temperature on a single mesoscopic device**, with highly resolved tunneling setpoint. Fig. 1.7 schematizes the setup.

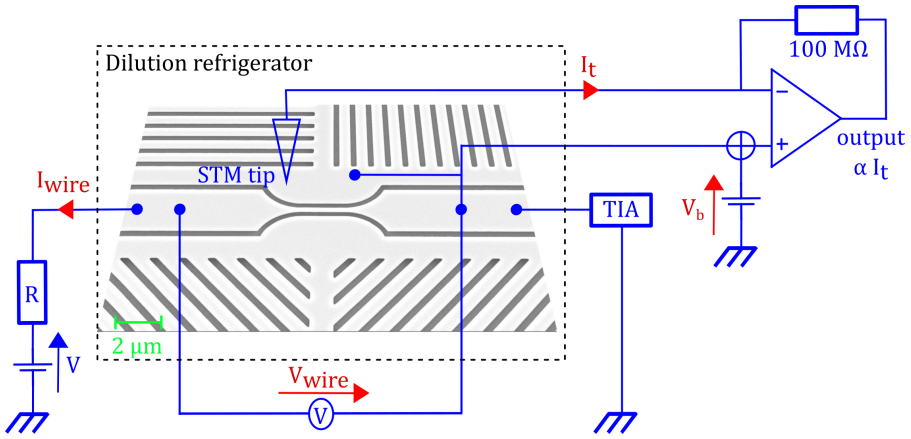

Figure 1.7: Scanning Critical Current Microscopy set-up.

Nanowire. It consists in a few micrometers long and a few hundred of nanometers wide wire between two larger leads where four electrical contacts are made. The nanowire fits in the low temperature STM scanning area. The superconducting to normal transition driven by the current occurs in the region of interest constituted by the weakest section area. The expansions between the pads and the nanowire are smooth widening to prevent any current crowding effect due to sharp corners. The nanowire is at the center of a target of lines allowing to locate it by STM.

Transport measurements. An optically driven voltage source and a resistor are used to generate the current I_{wire} which is measured by a Trans-Impedance Amplifier (TIA). The voltage across the wire V_{wire} is measured with a voltage amplifier. This allows to acquire the DC current-voltage characteristics of the wire. By replacing the voltage source by the oscillating output of a lock-in while recording both I_{wire} and V_{wire} with two lock-ins sharing the same clock, one can also measure the resistance of the wire.

The lock-ins are two 7230 DSP Lock-in Amplifiers from Ametek^{TM}and the TIA is a variable gain and low noise current amplifier from Femto^{TM}(model DLPCA-200). The voltage source delivering 0 to 5 V and the voltage amplifier with gain 10, 100 or 1000 are both home made.

Tunnel current. The tunneling junction is voltage biased by the current amplifier itself thanks to two wires connected one to the tip and the other to the sample [69]. This way, the tip is polarized to the electrical potential of the sample to which is added the bias voltage V_b. Thus, whatever the value of I_{wire} - which because of the contact resistances shifts the wire potential - the voltage across the junction is always V_b. A voltage proportional to the tunneling current I_t is given to the electronics feedback loop. Thanks to this home made amplifier in this

configuration, a controlled tunneling setpoint can be set to inject electrons from the tip to the nanowire while performing any kind of transport measurement.

Cabling. All transport and voltage supply cables are six strands stainless steel cables insulated by a teflon sheath inside a stainless steel shielding braid. The tunnel current cable and the sample potential probing cable are made of a twisted coaxial pair with a brass core. The braids are thermalized at all the dilution stages, and the strands and coaxial cores connect directly the 300 K connectors to the kapton relays (polyimide foils) of the 50 mK stage. Both stainless steel and brass are chosen to compromise low electrical impedance and high thermal resistance. Besides, since the twisted pair is used to measure very low currents, it is sensitive to tribological noise (the frictional vibrations of the braid induces charge fluctuations in the dielectric used to insulate the core and therefore current fluctuations). That is why a conductive varnish covers the dielectric and evacuates parasitic charges, making the cable a "low noise" one. Finally, using a twin twisted coaxial cable allows to accurately set "in situ" the bias voltage by balancing potential fluctuations due to thermoelectric effects or electromagnetic noise.

The wires connecting the 50 mK stage to the microscope require peculiar attention. Indeed, they must ensure good thermalization at low temperature while not transmitting mechanical vibrations, and therefore be metallic, thin and flexible. They are then made of 0.15 mm diameter copper wires except the tunnel current wire which was subject to experimentation. A coaxial cable better screens 50 Hz electrical noise but turned out to cause low frequency mechanical vibrations. It was finally replaced by a twisted pair of copper wires.

Power supply. Tunnel current amplifier, voltage source and amplifier power supply were provided by 3 different batteries to get rid of the 50 Hz noise. It resulted in a significant increase of the measured critical current. For the same reason, the voltage source was optically driven.

Filters. In order to achieve good energetic resolution (see Section 1.2) and to avoid to trigger unintentionally the superconducting to normal transition we are interested in, one must ensure good thermalization of the microscope (more specifically of the tip and the sample) and filter the external noise. To this purpose several kinds of noises have to be filtered:

- The radiations of the hot parts of the experiment to the cold ones. As explained above, the Russian dolls configuration of the cryostat limits black body radiations from the above stages, and it becomes negligible at low temperature since Stephan's law predicts an exchanged power varying as $P \propto T^4$. However, electromagnetic radiations are also transmitted through the wires. At low temperatures, the power transferred to an electron bath by this process is $P \propto T_e^2 - T_{em}^2$ [100], where $T_{em} = h\nu/k_B$ is the temperature of the electromagnetic environment. All the wires are thus thermalized at all the dilution stages. Nevertheless, in order not to heat up the 50 mK stage, low pass filters of cutoff frequency $k_B \times 50$ mK$/h \approx 1$ GHz should be added in the future.

- The high frequency noise from the environment (e.g. radio waves). Low pass filters of cutoff frequency ~ 1 MHz are added directly on the 300 K connectors to this end.

- The low frequency noise generated by the electronics and couplings to electromagnetic fields. In order to filtrate this noise as close as possible to the sample, home made low pass filters were installed on the 50 mK stage for each transport measurement wire (see Fig. 1.8). The cutoff frequency depends on the sample resistance R_s and was adjusted in order to allow transport and spectroscopy measurements at frequencies below 500 Hz.

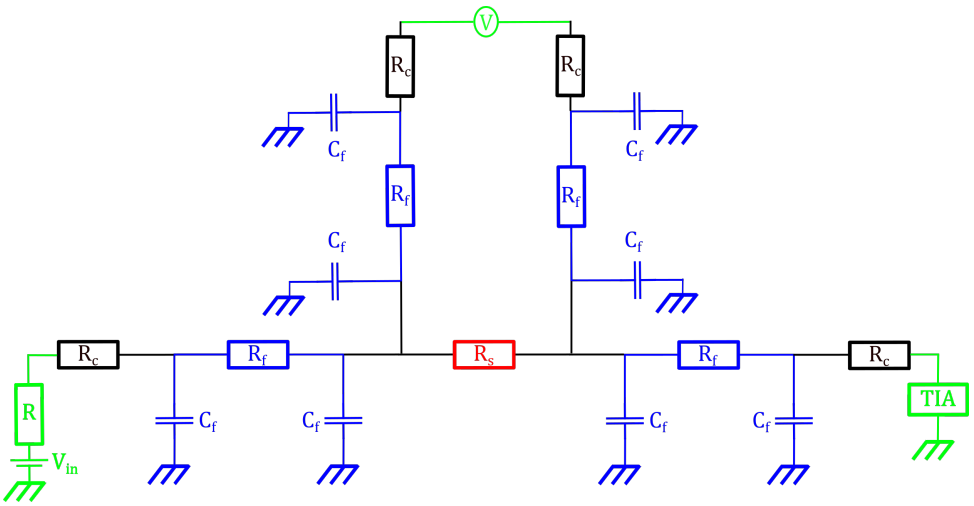

Figure 1.8: Transport measurement setup. $R_c \approx 115\ \Omega$ is the contact resistance due to the cables connecting the instruments at room temperature (in green) and the filters on the 50 mK stage (in blue). $R_f = 510\ \Omega$, $C_f = 22$ nF and R_s is the sample resistance which ranges from 0 (superconducting state) to 10-100 kΩ depending on the sample.

1.4 Sample fabrication

Scanning Tunneling Microscopy, especially when it is not carried out under Ultra High Vacuum (UHV) conditions, is very sensitive to both tip and sample surface quality. That is why on the one hand corrosion proof PtIr tips are used to preserve their flat metallic density of states. On the other hand any oxidation or pollution of the sample must be avoided, so that any lithography and etching after the deposit of the material under interest is prohibited to preserve the surface from resist residual. Thus, **the nanowire edges are patterned on the substrate before the material deposition.**

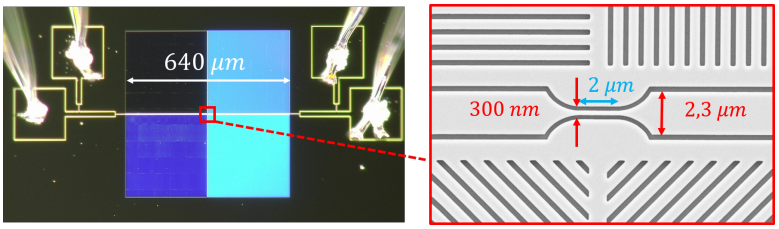

(a) Optical and SEM top views.

(b) Schematics of the side view.

Figure 1.9: Typical sample (Bilayer of Nb caped with Au).

The pattern (see Fig. 1.9a) is beforehand designed all over the sample by etching the Si/SiO_2 substrate (green and red on Fig. 1.9b). It consists in deep furrows forming on the one hand a target of lines of about 200 nm wide and 300 μm long separated by 600 nm, and on the other hand the nanowire edges. Then the superconductor under interest is deposited all over the surface. On the figure Nb (in blue) and then Au (in yellow) have been evaporated, the latter to prevent natural oxidation of Nb when the sample is exposed to ambient air. The furrows avoid electrical short between the nanowire and the rest of the sample. Finally, four electrical contacts are made and the sample is immediately put in the STM.

Lithography and etching. The substrate is made of Silicon Over Insulator (SOI), with 250 nm of Si over 3 μm of SiO_2. A 360 nm layer of resist (ZEP520A) is deposited by spin coating at 4000 rpm. Then, the pattern is designed by e-beam lithography in a JEOL6300FS.

Firstly, Reactive Ion Etching (RIE) is carried out, resulting in an efficient anisotropic etching of the Si. It is a chemical and physical etching: the surface is bombarded for about 3 mn under low pressure (6.3 mTorr) by a plasma made of Ar (75 sccm), SF_6 (10 sccm) and CH_2F_2 (24 sccm) which will also chemically react with the substrate. A power of 450 W is applied on the coil and a power of 16 W is applied on the pattern of the Inductively Coupled Plasma (ICP) etcher (Plasmalab100 from Oxford). Then the resist is removed by O_2 plasma cleaning before chemical etch of the sample with HF vapor. HF almost does not react with Si and, above all, this etching is isotropic, creating an undercut on the sidewall. About 220 nm of SiO_2 is removed in 20 mn, thanks to a gaseous mixture of 300 sccm of HF, 1200 sccm of N_2 and 338 μL/mn of alcohol under 75 Torrs.

Evaporation. the material under interest is evaporated over the already etched substrate. For most of them, it consists in niobium caped with gold evaporated by electron gun in a MEB550 from Plassys evaporator. Some amorphous indium oxide (InO) samples were also prepared by e-gun evaporation of indium in controlled O_2 environment.

Micro bonding. A 20 μm diameter Al:Si wire is used to make electrical contact between the sample pads and the sample holder by ultrasonic welding. Since this kind of soldering is difficult to perform on InO, and that the resulting bond often turned out to be poor at low temperature or to lift off during the cooling, larger contact pads were used in order to glue the wire with some epoxy.

Chapter 2

Ingredients of theory on superconductivity

Contents

2.1 Thermal equilibrium: BCS theory

The BCS theory proposed in 1957 by Bardeen, Cooper and Schrieffer is the first microscopic theory of superconductivity since its discovery in 1911 by H. Kamerlingh-Onnes. It implies several important quantitative predictions confirmed by experiments, so its authors received the Nobel Prize in Physics in 1972. Among them is the explanation for the isotope effect: the critical temperature T_c of a superconductor was found in 1950 [78] to depend on the mass M of ions forming the crystal lattice as $T_c \propto M^{-1/2}$. Such a dependence could occur if lattice vibrations were at stake, and this helped to find a mechanism for electron pairing since up to 1957 none was believed to overcome Coulomb repulsion. Indeed, a phonon mediated interaction between electrons occurs to be attractive in a narrow layer near the Fermi boundary.

Thus, the main point of BCS theory was that the attractive electron-electron interaction and the screening of Coulomb repulsion in a Fermi gas gives rise to Cooper pairs (two electrons of opposite spins and momenta), whose coherent superposition forms a macroscopic ground state. Although, the microscopic details of the attractive electron-electron interaction do not play a role in BCS theory, the implications include:

- The existence of a band gap in the single electron excitation spectrum under a given critical temperature T_c. Both the spectrum (Eq. 1.9) and the temperature dependence of this gap can be accessed and therefore confirmed experimentally in many superconductors (see Fig. 2.1: the experimental density of states as a function of energy and the temperature dependence of the gap follow the BCS prediction).

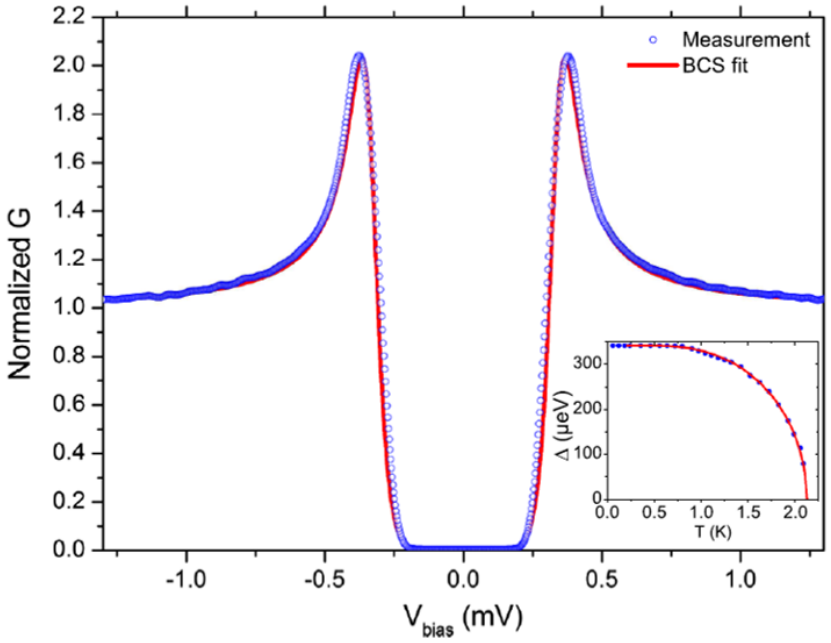

Figure 2.1: Superconducting gap of a BCS superconductor. Normalized differential conductance measured by tunneling spectroscopy on graphene grown on rhenium at 50 mK. Inset: temperature dependence of the superconducting gap. Blue dots: experimental measurements. Red line: BCS prediction. From [112].

- The ratio between the superconducting gap at zero temperature $\Delta(T=0)$ and T_c takes an universal value: $\Delta(T=0) = 1.764\ k_B T_c$. This relationship is approximately verified in most of the known superconductors in 1957.

- A relation between the superconducting critical temperature and the pairing potential:

$$k_B T_c = 1.13\ \hbar\omega_D e^{-1/(N_0 V_{eff})} \tag{2.1}$$

  where N_0 is the density of states at Fermi level, V_{eff} the (attractive) electron pairing potential and ω_D the Debye frequency. Since $\omega_D \propto M^{-1/2}$, this explains the isotope effect.

- An explanation for the Meissner effect, the perfect diamagnetism displayed by superconductors. Indeed, by contrast with the phenomenological London equations developed in 1935, BCS theory justifies microscopically the expulsion of the magnetic field from superconductors over the London penetration depth $\lambda_L = \sqrt{\frac{m}{\mu_0 n_s e^2}}$ where μ_0 is the magnetic constant and n_s the density of superconducting electrons.

- The existence of a characteristic length scale for the variations of the superconducting density n_s: the coherence length ξ. One must distinguish the clean case where ξ is also equal to the quantity $\xi_0 = \frac{\hbar v_F}{\pi\Delta}$ where v_F is the Fermi velocity, from the dirty (diffusive) limit ($l \ll \xi_0$ with l the electron mean free path) where $\xi = \sqrt{\hbar D/\Delta}$ with D the electron diffusion constant. Indeed, the superconducting state is a coherent superposition of paired electron states with energies $\pm E$ compared to Fermi level with $E \sim \Delta$ (because the electron-electron interaction turns out to be attractive for states with opposite momenta in an energy $\sim \Delta$ around Fermi level). Therefore, a dephasing $\exp(-2Eit/\hbar)$ between the wavefunctions of these states occurs as the pair propagates. Coherence is then lost after a time $t \approx \hbar/E$, i.e. after having traveled a length $v_F t$ in straight line or $\sqrt{Dt}$ by diffusion.

The superconductors verifying these implications are commonly called conventional (or BCS-like) superconductors.

Now, one must stress out that BCS theory deals with thermal equilibrium properties of superconductors, and has therefore limits. Indeed, let's remind that a fundamental characteristic of the superconducting state is that a supercurrent (a current with no resistance) can flow, leading to specific depairing mechanisms. Besides, when the superconductor is driven out of equilibrium - by local injection of electrons above Fermi level for instance - one must consider inhomogeneous systems requiring a reformulation of the theory. Thus, a new formalism relevant for out of equilibrium and inhomogeneous systems is presented below.

2.2 Out of equilibrium: Usadel theory

The Green functions allow to describe complex systems starting from a simpler one: in our case, the many body electronic system that is a superconductor will be described by a free electron system on which all the interactions will be added. Besides, in the Keldysh formalism, out of equilibrium systems are described from the equilibrium Green functions. Applied to superconductivity, this leads to Gorkov equations. Further simplifications were brought by Eilenberger and later Usadel, which roughly consist in a first order expansion of the free energy (whose validity is not at stake since the expansion parameter is Δ/E_F and therefore negligible for typical superconductors) and assuming diffusive motion for the electrons. The long and complicated derivation[1] is not presented in this thesis, but the equilibrium Usadel equations and some related physical properties are introduced.

2.2.1 Usadel equations

By contrast with BCS theory which assumes no scattering, Usadel formalism is only valid in the diffusive limit (mean free path l shorter than the superconducting coherence length ξ), which is a good approximation in many cases and especially in thin films where electrons scatter from the boundaries. Microscopically, electron states are no longer described by their wave vectors (which appear in the BCS pairing potential) but through an energy variable ϵ more relevant for a diffusive motion. Besides, Usadel equations are parameterized for practical purpose with **a pairing angle θ which is a function of the position and the energy. θ is complex and ranges in magnitude from 0 to $\pi/2$ where $\theta = 0$ corresponds to the normal state.** At equilibrium (when the distribution function of electrons is Fermi-Dirac) the equations write [10, 104, 38]:

$$\begin{gathered}\frac{\hbar D}{2}\nabla^2\theta + \left(i\epsilon - \left(\frac{\hbar}{2\tau_{sf}} + \frac{\hbar}{2D}V_s^2\right)\cos\theta\right)\sin\theta + \Delta e^{-i\phi}\cos\theta = 0 \\ \nabla(V_s\sin^2\theta) = 0\end{gathered} \tag{2.2}$$

where D is the diffusion constant, τ_{sf} is the spin flip time, ϕ is the superconducting phase, $\overrightarrow{V_s}$ is the superfluid velocity:

$$\overrightarrow{V_s} = D\left(\overrightarrow{\nabla}\phi - \frac{2e}{\hbar}\overrightarrow{A}\right) \tag{2.3}$$

and Δ is the superconducting order parameter:

$$\Delta = N_0 V_{eff}\int_0^{\hbar\omega_D} d\epsilon\ \tanh\left(\frac{\epsilon}{2k_BT}\right)\Im[\sin\theta]e^{i\phi} \tag{2.4}$$

[1] Available in [18].

with $\overrightarrow{A}$ the vector potential, N_0 the density of states at Fermi level, V_{eff} and ω_D respectively the pairing potential and the Debye frequency as defined in BCS theory, and T the temperature. The notations $\Im$ and $\Re$ stand for the imaginary and real components, respectively.

As it will be discussed later, the superfluid velocity is affected by both supercurrent and magnetic field while the superconducting order parameter is reinforced by the pairing strength. Thus, pairing tends to make $\theta = \pi/2$ while an excitation energy term $i\epsilon$ and a term describing pair breaking through spin flip scattering, current and magnetic field tend to make $\theta = 0$ (normal state). Finally, a Dynes-like parameter can be added to the energy to account for inelastic scattering: $\epsilon \rightarrow \epsilon + i\Gamma_{in}$.

All physical quantities can be computed from the function θ which is obtained by solving the self consistent set of equations Eq. 2.2, 2.3 and 2.4.

Single electron density of states

The quasiparticle density of states in the superconducting state N_s is related to the pairing angle through:

$$N_s = N_0 \Re[\cos\theta] \tag{2.5}$$

Let's stress out that when some depairing processes are at stake, the order parameter Δ can be very different from the gap observed in the Density Of States (DOS) by tunneling spectroscopy. If so, the spectral gap (roughly the energy range over which there are no available states for quasiparticles) can be zero while the material is still in the superconducting state (see Fig. 2.2), for instance under a strong supercurrent flow. In the following, **the BCS superconducting gap at zero temperature (which is equal to the order parameter in the absence of depairing) is noted $\boldsymbol{\Delta_0}$.**

Current density

For a bulk superconductor, the superconducting phase is real and determined by the boundary conditions (i.e. the reservoirs connecting both ends of the superconducting wire in the one dimensional case). At thermal equilibrium, the supercurrent density writes [10, 104]:

$$\overrightarrow{J_s} = \frac{\sigma_N}{eD}\int_0^\infty d\epsilon \ \tanh\left(\frac{\epsilon}{2k_BT}\right)\Im\left[\sin^2\theta\overrightarrow{V_s}\right] \tag{2.6}$$

with σ_N the normal state conductivity.

Without any external magnetic field, one can set $\overrightarrow{A} = \overrightarrow{0}$ and hence $\overrightarrow{V_s} = D\overrightarrow{\nabla}\phi$ so if a phase difference between the reservoirs is applied, one can notice from Eq. 2.6 that a supercurrent flows.

Meissner effect

By contrast, when no phase difference is induced, under an external magnetic field, $\overrightarrow{V_s} = \frac{-2eD}{\hbar}\overrightarrow{A}$ and one obtains London equation:

$$\overrightarrow{J_s} = -\frac{2\sigma_N}{\hbar}U_s\overrightarrow{A} \tag{2.7}$$

with:

$$U_s = \int_0^\infty d\epsilon \ \tanh\left(\frac{\epsilon}{2k_BT}\right)\Im[\sin^2\theta] \tag{2.8}$$

Using Maxwell-Ampere law ($\overrightarrow{\nabla}\times\overrightarrow{B} = \mu_0\overrightarrow{J}$ where $\overrightarrow{B} = \overrightarrow{\nabla}\times\overrightarrow{A}$), Coulomb gauge ($\nabla\overrightarrow{A} = 0$) and the fact that for a BCS superconductor at low temperature ($k_BT \ll \Delta_0$) $U_s = \frac{\pi\Delta_0}{2}$ (see

Appendix B), one obtains:

$$\nabla^2 \overrightarrow{A} = \frac{1}{\lambda_L^2} \overrightarrow{A} \tag{2.9}$$

with $\lambda_L = \sqrt{\frac{\hbar}{\pi \mu_0 \sigma_N \Delta_0}}$ the London penetration depth. The magnetic field penetrates the superconductor only over a length scale λ_L, where a supercurrent flows and create an induced magnetic field which screens the external field in the bulk.

Out of equilibrium case

In the general case, Usadel equations are more complicated and not presented here. However, the filling factor $h = 1 - 2f$ where f is the distribution function can be decomposed as the sum of an odd h_{od} and an even h_{ev} functions of the energy. Qualitatively speaking, deviations of h_{od} from its thermal equilibrium value $h_{od}^{eq}(\epsilon) = \tanh(\epsilon/(2k_BT))$ are related to an effective temperature change whereas deviations of h_{ev} from its equilibrium value $h_{ev}^{eq}(\epsilon) = 0$ are related to an effective chemical potential shift.

The order parameter writes (see Appendix C and [4]):

$$\Delta = \frac{N_0 V_{eff}}{4i} \int_{-\hbar\omega_D}^{\hbar\omega_D} d\epsilon [h_{od}(\sin\theta\ e^{i\phi} - \sin\theta^*\ e^{i\phi^*}) - h_{ev}(\sin\theta\ e^{i\phi} + \sin\theta^*\ e^{i\phi^*})] \tag{2.10}$$

At thermal equilibrium and for a bulk superconductor (for which ϕ is real) one recovers Eq. 2.4.

Similarly, for an arbitrary distribution function the current density writes (see Appendix C and [4]):

$$\begin{aligned}
\overrightarrow{J} &= \overrightarrow{J_s} + \overrightarrow{J_N} + \overrightarrow{J_{imb}} \\
\overrightarrow{J_s} &= \frac{\sigma_N}{2De} \int_{-\infty}^{\infty} d\epsilon\ h_{od}\ \Im\left[\sin^2\theta\ \overrightarrow{V_s}\right] \\
\overrightarrow{J_N} &= \frac{\sigma_N}{4e} \int_{-\infty}^{\infty} d\epsilon\ \overrightarrow{\nabla} h_{ev} \left(1 + |\cos\theta|^2 + |\sin\theta|^2 \cosh(2\phi_2)\right) \\
\overrightarrow{J_{imb}} &= \frac{\sigma_N}{4e} \int_{-\infty}^{\infty} d\epsilon\ \overrightarrow{\nabla} h_{od} |\sin\theta|^2 \sinh(2\phi_2)
\end{aligned} \tag{2.11}$$

with $\phi = \phi_1 + i\phi_2$. $\overrightarrow{J_S}$ corresponds to the supercurrent, whereas $\overrightarrow{J_N}$ and $\overrightarrow{J_{imb}}$ are dissipative quasiparticle currents, the latter being associated with an imbalance between quasiparticle excitations of type electrons and holes. At thermal equilibrium when the phase is real $\overrightarrow{J_N} = \overrightarrow{J_{imb}} = \overrightarrow{0}$ and one recovers Eq. 2.6.

For out of thermal equilibrium superconductors, both order parameter Δ and current density $\overrightarrow{J}$ depend on the distribution function $f(\epsilon)$ and not simply on the temperature T.

2.2.2 Depairing induced by a supercurrent

Let's remind that the superfluid velocity can be affected by both supercurrent (through the induced phase gradient $\overrightarrow{\nabla}\phi$, see Eq. 2.6) and magnetic field (through the induced vector potential $\overrightarrow{A}$). We will now perform reasonable assumption corresponding to our experimental conditions: we consider a superconducting wire whose width and thickness are small compared to London penetration depth λ_L, carrying in thermal equilibrium a supercurrent without external magnetic field and connected at both ends to superconducting reservoirs with energy-independent

real phases. Under these conditions, $\overrightarrow{V_s} = D\overrightarrow{\nabla}\phi$ and for simplicity we will assume an uniform phase gradient along the wire. In the following we will also neglect the spin flip rate $1/\tau_{sf}$[2] and define the depairing energy γ:

$$\gamma = \frac{\hbar}{2D} V_s^2 \tag{2.12}$$

Thus, Eq. 2.2 simplifies to:

$$\begin{gathered} \epsilon + i\gamma\cos\theta = i\Delta\frac{\cos\theta}{\sin\theta} \\ \nabla\theta = 0 \end{gathered} \tag{2.13}$$

And Eq. 2.4 gives:

$$\Delta = N_0 V_{eff} \int_0^{\hbar\omega_D} d\epsilon \ \tanh\left(\frac{\epsilon}{2k_B T}\right) \Im[\sin\theta] \tag{2.14}$$

where we have set the origin of phases such as $\phi = 0$ where the equations are solved.

NB: Without supercurrent nor magnetic field, $\gamma = 0$ and one recovers the BCS results (for more details see Appendix B), as for instance the density of states from Eq. 2.13:

$$\begin{gathered} \tan(\theta) = \frac{i\Delta}{\epsilon} \\ \Rightarrow N_s(\epsilon) = N_0 \ \Re(\cos(\theta)) = \begin{cases} N_0 \frac{|\epsilon|}{\sqrt{\epsilon^2 - \Delta^2}} & \text{if } |\epsilon| > \Delta \\ 0 & \text{if } |\epsilon| < \Delta \end{cases} \end{gathered} \tag{2.15}$$

The BCS relation between gap and pairing $\Delta = 2\hbar\omega_D \ e^{-1/N_0 V_{eff}}$ and the universal ratio $\Delta_0 = 1.764 \ k_B T_c$ stem from Eq. 2.14.

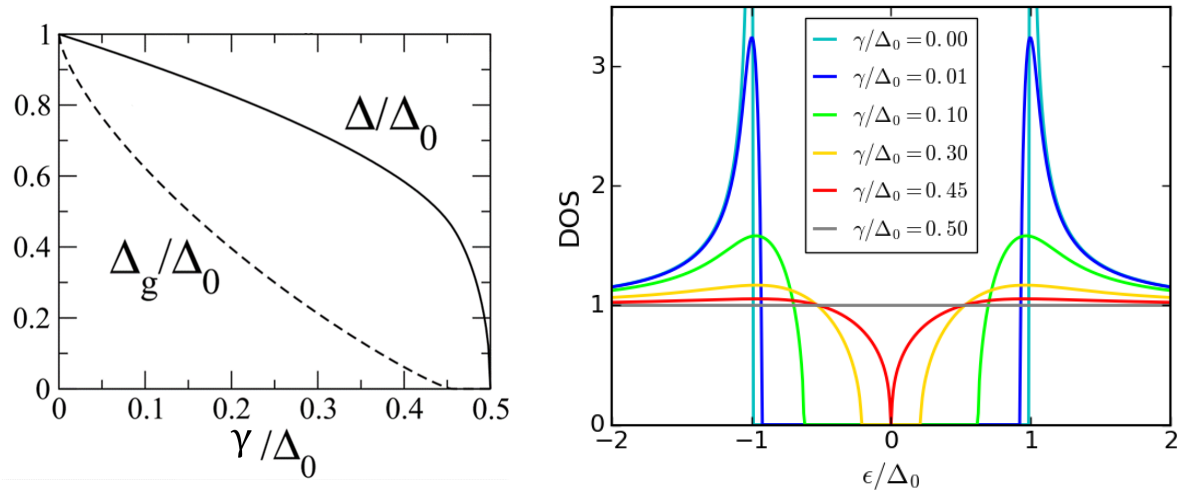

(a) **(b)**

Figure 2.2: Solution of Usadel equation with an homogeneous depairing energy at $T = 0$. (a) Order parameter (solid line) and spectral gap (dashed line) in units of the gap in the absence of pair breaking Δ_0 as a function of depairing energy γ normalized to Δ_0. From [24]. (b) Density of states as a function of reduced energy for different values of the depairing energy γ. Note that the spectral gap disappears completely for $\gamma/\Delta_0 > 0.45$, while gapless superconductivity survives up to $\gamma = 0.5\Delta_0$.

[2]The spin flip term is negligible compared to the depairing energy in the cases of interest.

Eq. 2.13 and Eq. 2.14 relate self consistently Δ to θ. One can therefore perform a numerical resolution and obtain the $\theta(\epsilon)$ and Δ for any value of γ and T. For instance, in the low temperature limit ($k_BT \ll \Delta_0$), the $\Delta(\gamma)$ curve obtained in [24] is plotted on Fig. 2.2a. The $\theta(\epsilon)$ function leads among other things to the density of states (Fig. 2.2b). Finally, **the spectral gap Δ_G is defined to be the energy over which the density of states vanishes.** It writes [103, 24]:

$$\Delta_G(T,\gamma) = \Delta(T,\gamma)\left[1 - \left(\frac{\gamma}{\Delta(T,\gamma)}\right)^{2/3}\right]^{3/2} \tag{2.16}$$

As shown on Fig. 2.2, there is a range of depairing energies ($0.45 < \gamma < 0.5$) over which the superconductor is gapless. Above $\gamma = 0.5$, the order parameter vanishes and superconductivity is suppressed.

Depairing energy due to the supercurrent

Neglecting the energy dependence of the superconducting phase ϕ Eq. 2.6 writes as follows:

$$\overrightarrow{J_s} = \frac{\sigma_N}{eD}\overrightarrow{V_s}U_s \tag{2.17}$$

Under the assumption of homogeneous current density the supercurrent writes $I_s = J_sS$ with S the wire section. Using Einstein relation $\sigma_N = N_0e^2D$, one obtains the relation between the depairing energy γ and the supercurrent I_s:

$$\frac{I_s}{I_\gamma} = \sqrt{\frac{\gamma}{\Delta_0}}\frac{U_s}{\Delta_0} \tag{2.18a}$$

$$I_\gamma = \sqrt{2}S\Delta_0^{3/2}\sqrt{\frac{N_0\sigma_N}{\hbar}} \tag{2.18b}$$

The maximum value of the function $I_s(\gamma)$ corresponds to the depairing critical current I_{dp}. For $T = 0$ (plotted on Fig. 2.3), this leads to $I^0_{dp} = 0.53I_\gamma$ and to the theoretical zero temperature critical current density:

$$J^0_{dp} = 0.75\Delta_0^{3/2}\sqrt{\frac{N_0\sigma_N}{\hbar}} \tag{2.19}$$

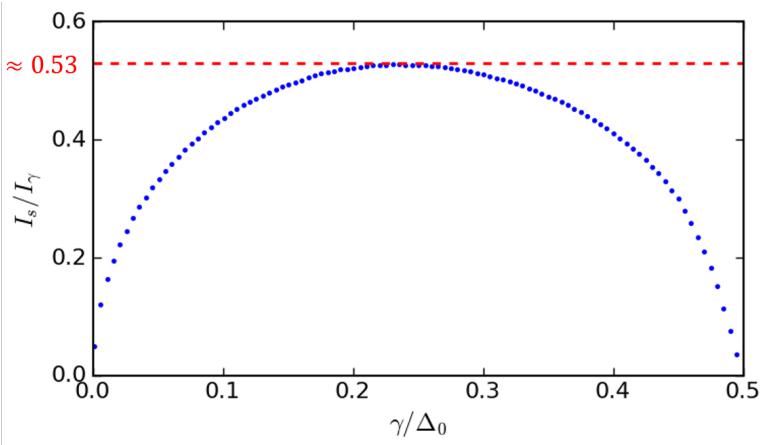

Figure 2.3: Supercurrent versus depairing energy at $T = 0$.

The numerical computation of $I_{dp}(T)$ based on Green functions (Eilenberger equations) has first been implemented by Kupryanov and Lukichev (KL) [66] for arbitrary l/ξ_0 ratios. Small

differences are predicted for different mean free paths, but the numerical computation of $I_{dp}(T)$ implemented here is based on Usadel equations and therefore corresponds to the very short mean free path limit of KL result. It leads among other things to the zero temperature depairing current density widely used in the literature $J_{dp}^0 = 0.75\Delta_0^{3/2}\sqrt{N_0\sigma_N/\hbar}$ and to the Ginzburg Landau result near the critical temperature $J_{dp,GL}(T) \propto (1 - T/T_c)^{3/2}$. The approximations can be summarized as follows:

- The superconductor is a wire in the dirty limit ($l \ll \xi$). Its transverse dimensions are small compared to London length and the superconducting phase is real at both ends.
- A supercurrent is carried at thermal equilibrium without any external magnetic field.
- The concentration of magnetic impurities is small ($\tau_{sf} \to \infty$) and the inelastic scattering is negligible ($\Gamma_{in} = 0$).

The last approximation will be questioned in the following, and some inelastic scattering will be considered in the Usadel equation:

$$\epsilon + i\Gamma_{in} + i\gamma\cos\theta = i\Delta\frac{\cos\theta}{\sin\theta} \tag{2.20}$$

which will modify the density of states (see Section 4.5). The numerical computation of $I_{dp}(T, \Gamma_{in})$ will be confronted to experimental data in Section 5.1. Finally, as evidenced by Eq. 2.20 the supercurrent (through γ) will also alter the DOS (see Section 5.2).

Depairing energy due to the magnetic field induced by the supercurrent

In the previous paragraph, we have neglected the magnetic field induced by the supercurrent. However, the supercurrent flowing in the wire creates a magnetic field, which also causes some depairing through the induced vector potential. The associated depairing energy is equal to $\gamma_A = \frac{2De^2}{\hbar}|\overrightarrow{A}|^2$.

With an homogeneous current density in a parallelogram geometry with a thickness t and a width w (see Fig. 2.4), and assuming the wire to be infinitely long and thin, the vector potential in the wire can be taken as[3]:

$$\overrightarrow{A} = -\frac{\mu_0 I_s y^2}{2wt}\overrightarrow{u_x} \tag{2.21}$$

Since w is small compared to λ_L (the length scale for variation of $\overrightarrow{A}$), only an average effect of the vector potential is seen, so averaging $|\overrightarrow{A}|^2$ over the cross section of the wire one gets:

$$\gamma_A = \frac{De^2\mu_0^2 I_s^2}{160\hbar}\left(\frac{w}{t}\right)^2 \tag{2.22}$$

For wires wider than London length, γ_A, θ and $\overrightarrow{J}$ are not homogeneous, and the depairing energy is maximum on the side of the wire.

The ratio between the depairing energy due to an homogeneous supercurrent γ_I (Eq. 2.18) and the one due to the induced magnetic field is (writing that $U_s = \frac{\pi}{2}\Delta_0$ and $\lambda_L = \sqrt{\frac{\hbar}{\mu_0\pi\sigma_N\Delta_0}}$):

$$\frac{\gamma_A}{\gamma_I} = \frac{1}{320}\left(\frac{w}{\lambda_L}\right)^4 \tag{2.23}$$

[3]Since the wire is invariant by translation along z axis and $t \ll w$ $\overrightarrow{A} = \overrightarrow{A}(y)$. The current distribution is antisymmetric with respect to any plane orthogonal to x and $\overrightarrow{A}$ is a polar vector so $\overrightarrow{A} = A(y)\overrightarrow{u_x}$. The symmetry of the current distribution with respect to $(\overrightarrow{u_x}, \overrightarrow{u_z})$ leads to $A(y) = A(-y)$. Using again Maxwell-Ampere law and Coulomb gauge one obtains $\nabla^2\overrightarrow{A} = -\mu_0\overrightarrow{J}$ and choosing $A(\pm\infty) = 0$ one gets the present equation.

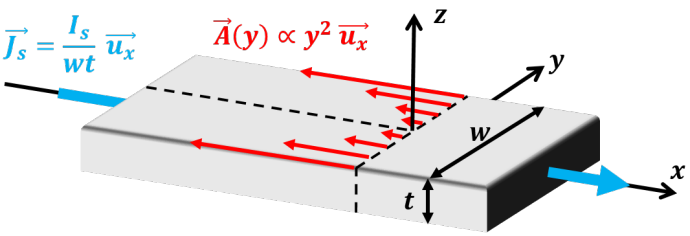

Figure 2.4: Scheme of a wire carrying an homogeneous supercurrent and associated vector potential.

So that $\gamma_A/\gamma_I \ll 1$ under the assumption of $w \ll \lambda_L$. Note that in a cylindrical geometry of diameter $w \ll \lambda_L$, one end up to the same conclusion (see Appendix A). Therefore, **the depairing energy due to the magnetic field induced by the supercurrent can be neglected**.

2.2.3 Superconducting proximity effect

In the following we consider a normal layer of thickness t_N in contact with a superconducting layer of thickness t_S and critical temperature T_c^S. We will investigate the superconducting properties of the bilayer in the limit where both thicknesses are small compared to the coherence length ξ ($t_N, t_S \ll \xi$).

The Cooper limit

The case of perfect interface between the layers (zero interlayer interface resistance) and $t_N, t_S \ll \xi$ is known as the *Cooper limit*. BCS theory relates the critical temperature to the pairing potential and the density of states at Fermi level through Eq. 2.1. For the bare superconductor it writes:

$$k_B T_c^S = 1.13\hbar\omega_D e^{-\frac{1}{N_S V_S}} \tag{2.24}$$

For a NS bilayer, the effective pairing term $[NV]_{NS}$ is an averaged value with respect to the number of states in the normal and superconducting layer [25]:

$$[NV]_{NS} = \frac{V_S N_S^2 t_S + V_N N_N^2 t_N}{N_N t_N + N_S t_S} \tag{2.25}$$

where for i=N,S, V_i is the pairing potential, N_i is the density of states at Fermi level and t_i is the thickness. For simplicity, the pairing potential V_N of the normal metal will be set to zero. Then, the critical temperature T_c of the bilayer is given by:

$$T_c = T_c^S \ \exp\left(-\frac{N_N t_N}{N_S t_S}\frac{1}{N_S V_S}\right) \tag{2.26}$$

The opposite case of infinite interface resistance corresponds to a critical temperature of the superconductor unaffected by the presence of the normal layer. Thus, the two extreme limits of interface resistance between normal and superconducting layers give upper and lower bounds for the critical temperature of the bilayers.

General theory within Usadel framework: the Fominov model

We will now release the assumption of perfect interface resistance and consider the Usadel equations in the two layers. We note the pairing angles in the normal and superconducting

layer θ_N and θ_S. The layers are thin enough ($t_N, t_S \ll \xi$) to be considered as uniform, allowing to set the order parameter Δ equal to a constant in the superconducting layer (its phase is then chosen to be zero) and $\Delta = 0$ in the normal one, although $\theta_N \neq 0$ due to the proximity effect.

The Usadel equations of Eq. 2.2 take respectively in the normal and superconducting layer the form:

$$\begin{aligned} \frac{\hbar D_S}{2}\nabla^2\theta_S + i\epsilon\sin\theta_S + \Delta\cos\theta_S = 0 \\ \frac{\hbar D_N}{2}\nabla^2\theta_N + i\epsilon\sin\theta_N = 0 \end{aligned} \tag{2.27}$$

As it can be physically intuited, the strength of the proximity depends on the transparency of the SN interface, which is controlled by the conductance per unit area at the interface g_{int} such as: $g_{int} = 2\mathcal{T}N_{ch}G_q$ where $\mathcal{T}$ is the interface transmission probability, $N_{ch} = (\lambda_F/2)^{-2}$ with λ_F the Fermi wavelength is the number of channels per unit area and $G_q = e^2/h$ is the quantum of conductance. This conductance rules the boundary condition at the interface, allowing to solve the Usadel equation for θ_S (the detailed resolution is not presented here, but is available in [38]). θ_S and θ_N are nearly spatially constant, and T_c is the critical temperature of the superconducting layer.

Critical temperature. Using the self consistent order parameter equation Eq. 2.4 and the fact that near critical temperature $|\theta| \ll 1$, the authors of [38] finally obtain:

$$\ln\left(\frac{T_c^S}{T_c}\right) = \frac{\tau_N}{\tau_S+\tau_N}\left[\Psi\left(\frac{1}{2}+\frac{\hbar}{2\pi k_B T_c}\frac{\tau_S+\tau_N}{\tau_S\tau_N}\right) - \Psi\left(\frac{1}{2}\right) - \ln\sqrt{1+\left(\frac{\tau_S+\tau_N}{\tau_S\tau_N\omega_D}\right)^2}\right] \tag{2.28}$$

where T_c^S is the critical temperature of the superconducting material (the one having a non vanishing pairing potential N_0V_{eff}), $\tau_N = \frac{2\sigma_N t_N}{D_N g_{int}}$ and $\tau_S = \frac{2\sigma_S t_S}{D_S g_{int}}$ are the the residency times in N and S layer, ω_D is the Debye frequency and Ψ is the digamma function.

Density of states. In the limit of small interface resistance, corresponding to $\frac{\tau_S\tau_N\Delta}{\tau_S+\tau_N} \ll \hbar$, the DOS in the normal and superconducting layers are the same and one obtains the BCS-like result:

$$\cos\theta_N = \cos\theta_s = \frac{\epsilon}{\sqrt{\epsilon^2-\Delta_g^2}} \tag{2.29}$$

where $\Delta_g = \frac{\tau_S\Delta}{\tau_S+\tau_N}$ is the minigap[4]. This result arises from the fact than when the average residency time is small compared to the time scale $\hbar/\Delta$, the quasiparticle states of energy smaller than Δ are delocalised over both layers and therefore all feel the pairing interaction. Interestingly, the relation $\Delta_g = 1.76k_BT_c$ is still fulfilled.

By contrast, in the limit of an opaque interface, the DOS in the S and N layers approaches respectively the BCS and normal metal results.

[4]According to the literature, one can make the distinction between minigap and spectral gap. The term minigap is often employed in the context of proximity effect and refers to the energy window over which no quasiparticle state exists. The term spectral gap is employed when some depairing processes are at stake, and refers to the gap feature observed in the DOS, no matter whether the DOS is strictly vanishing or not. In both cases, the main point is that this quantity differs from the order parameter. In this PhD, the spectral gap always designates the gap measured by STS (being sometimes different from the order parameter), since the energy resolution of the STM junction does not allow to make the distinction between minigap and spectral gap in many experimental situations.

Thus, **the measurement of the density of states by STS on the surface of the normal layer allows to distinguish between the limits of transparent and opaque interfaces.**

Coherence length. In the limit of small interface resistance, the coherence length is the lengthscale over which the pairing angles from Eq. 2.27 vary, which according to [38] is a generalization of the BCS result:

$$\xi = \sqrt{\frac{\hbar \langle D \rangle}{E_g}} \tag{2.30}$$

with $\langle D \rangle = \frac{\tau_S D_S + \tau_N D_N}{\tau_S + \tau_N}$ the averaged electron diffusion constant. In particular, the Ginzburg Landau [111] result for the upper critical field B_{c2} is still valid with this expression for ξ:

$$B_{c2} = \frac{\phi_0}{2\pi\xi^2} \tag{2.31}$$

with $\phi_0 = \frac{h}{2e}$ the superconducting flux quantum.

NB: Near T_c, Ginzburg and Landau obtained the following result:

$$\xi(T \to T_c) \approx 0.855\sqrt{\xi_0 l}\sqrt{\frac{T_c}{T_c - T}} \tag{2.32}$$

with $\xi_0 = \frac{\hbar v_F}{\pi \Delta_0}$. According to Eq. 2.30, the coherence length writes $\xi = \sqrt{\hbar D/\Delta} = \sqrt{\frac{\pi}{3}}\sqrt{\xi_0 l}$ for $T \ll T_c$. Although differing from a (small) numerical factor from the zero temperature coherence length, **the quantity $\boldsymbol{\xi_{GL} = 0.855\sqrt{\xi_0 l}}$** is easily accessible by measuring the upper critical field near the critical temperature and **will be called Ginzburg Landau coherence length in the following.**

Chapter 3

Experimental context of out of equilibrium superconductivity

Contents

From the theoretical point of view, out of equilibrium superconductivity is interesting because the theory of equilibrium superconductivity is well established. In particular, this allows to test theoretical models for quantum many body systems driven far from equilibrium. Besides, phenomenon such as the enhancement of superconductivity are paradoxical and fascinating: intuitively one would expect that the maximum superconducting gap or critical current manifests in an unperturbed sample, but it turns out to exist out of equilibrium exceptions.

Aside from this theoretical interest, one could simply wonder how much supercurrent can carry a superconductor. The study of out of equilibrium superconductivity can also be interesting for applications such as photon detection, where the absorption of a photon breaks Cooper pairs, leading to either an excess of quasiparticles or a transition to the normal state. Finally, there is recently a strong concern in the electronic devices made of superconducting materials, where the circuits are by construction driven out of equilibrium.

Thus, this chapter describes reported experiments on superconductors driven out of equilibrium by a supercurrent flow or by tunnel injection of quasiparticles.

3.1 Critical pair breaking current

Measurements of the critical current density J_c[1] of nanowires (narrow and thin strips) have first been reported in [93]. Aluminum had been chosen for its large London penetration depth λ_L and coherence length ξ. Indeed, in order to ensure uniform current distribution along the cross section, both width w and thickness t must be smaller than λ_L, otherwise the current piles up at the edges and overcome the critical current density only locally. Similarly, ξ should be larger than t and w to prevent vortex nucleation and therefore current induced vortex flow.

[1] In this PhD, the subscript c refers to the experimental critical current I_c or current density J_c whereas dp refers to the theoretical depairing current I_{dp} or current density J_{dp}.

Good agreement between Kupryanov Lukichev (KL) theory in the small mean free path limit and the critical current as a function of temperature has been observed. Notably, the best agreement was obtained for samples having λ_L comparable or larger than w, and was interpreted as an evidence of homogeneous current density limit (see Fig. 3.1). All samples were small enough to prevent vortex nucleation. KL theory fitted better the data than the phenomenological Bardeen formula [7] which is an extrapolation between the BCS result at zero temperature and the Ginzburg Landau behavior in the vicinity of T_c where an analytic treatment is possible:

$$J_{dp,GL}(T) = J^0_{dp,GL}\left(1-\left(\frac{T}{T_c}\right)^2\right)^{3/2} \tag{3.1a}$$

$$J^0_{dp,GL} = 0.68\Delta_0^{3/2}\sqrt{N_0\sigma_N/\hbar} \tag{3.1b}$$

$J^0_{dp,GL}$ differs slightly from the KL result with $l \ll \xi_0$[2]: $J^0_{dp} = 0.75\Delta_0^{3/2}\sqrt{N_0\sigma_N/\hbar}$ as evidenced on Fig. 3.1. Indeed, $(J^0_{dp}/(2\sqrt{2}J^0_{c,GL}))^{2/3} = 0.5 \times (0.75/0.68)^{2/3} \approx 0.53$, but this difference of about 10% is of the same order of magnitude than the uncertainty over J^0_c of all reported experiments. Finally, the ordinate axis of the figure was chosen to emphasize the critical behavior near T_c: $J_{dp,GL}(T \to T_c) \approx 2\sqrt{2}J^0_{dp,GL}\left(1-\frac{T}{T_c}\right)^{3/2}$.

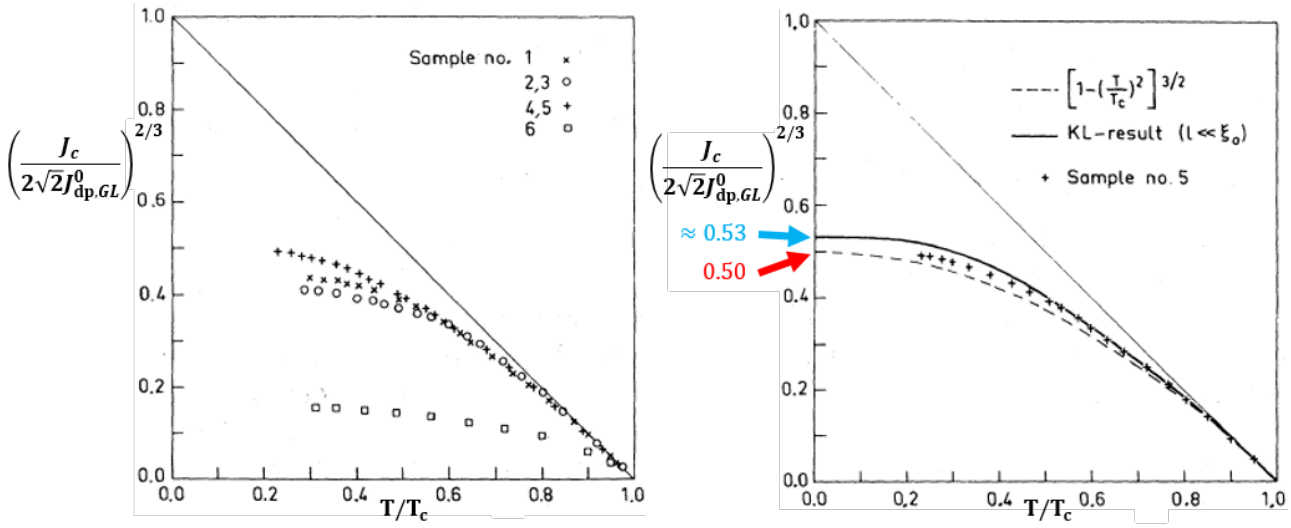

(a) (b)

Figure 3.1: Temperature dependence of the critical pair breaking current of narrow strips. Experimental critical current density J_c normalized to the Ginzburg Landau pair breaking current density as a function of reduced temperature for 300 nm wide aluminum strips. The effective penetration depth λ_L is tuned by the thickness. Straight line is the Ginzburg Landau result valid close to T_c. Adapted from [93]. (a) Illustration of the effect of non homogeneous current: samples with $w < \lambda_L$ (1,2,3,6) present lower J_c because the depairing current density is exceeded locally on the edges where current is piling up. (b) Comparison with theoretical predictions.

The depairing current predicted by Usadel theory of out of equilibrium superconductivity in diffusive superconductors accounts well for the critical current measured in narrow strips. However, the theory does not take into account the presence of vortices. **We address in this PhD work a different situation where vortex nucleation cannot be discarded.**

[2]The critical current obtained by solving Usadel equations in previous chapter (Eq. 2.19) is equivalent to the Kupryanov Lukichev result in the $l \ll \xi_0$ limit.

3.2 Density of states in the presence of supercurrent

Superconductivity is based on the pairing of electrons formed with mutually time reversed states (states with opposite spins and momenta). A supercurrent flow or a magnetic field breaks time reversal symmetry and therefore affects this pairing, resulting in a modification of the superconducting properties, among which is the Density Of States (DOS). This effect is described in the Usadel equations (Eq. 2.13) by a single parameter, the depairing energy. Similarly to the effect of a supercurrent introduced above (Eq. 2.18), a perpendicular magnetic field B also creates some depairing energy γ in a wire of width w with $w \ll \lambda_L$ so that [4]:

$$\frac{\gamma}{\Delta_0} = \left(\frac{I_s}{I_\gamma}\frac{\Delta_0}{U_s}\right)^2 + \left(\frac{B}{B_\gamma}\right)^2 \tag{3.2}$$

where $B_\gamma = \frac{\sqrt{6\hbar\Delta_0}}{ew\sqrt{D}}$.

Only one experiment addresses the effect of a supercurrent on the DOS [4]. The differential conductance of a current-biased superconducting wire placed in a perpendicular magnetic field was measured with a lithographed tunnel probe junction. The probe being metallic, the differential conductance is proportional to the density of states (disregarding Coulomb blockade and finite temperature effects introduced below). Fig. 3.2 shows the good agreement between experimental and theoretical behavior of the differential conductance upon application of both magnetic field B and supercurrent I_s.

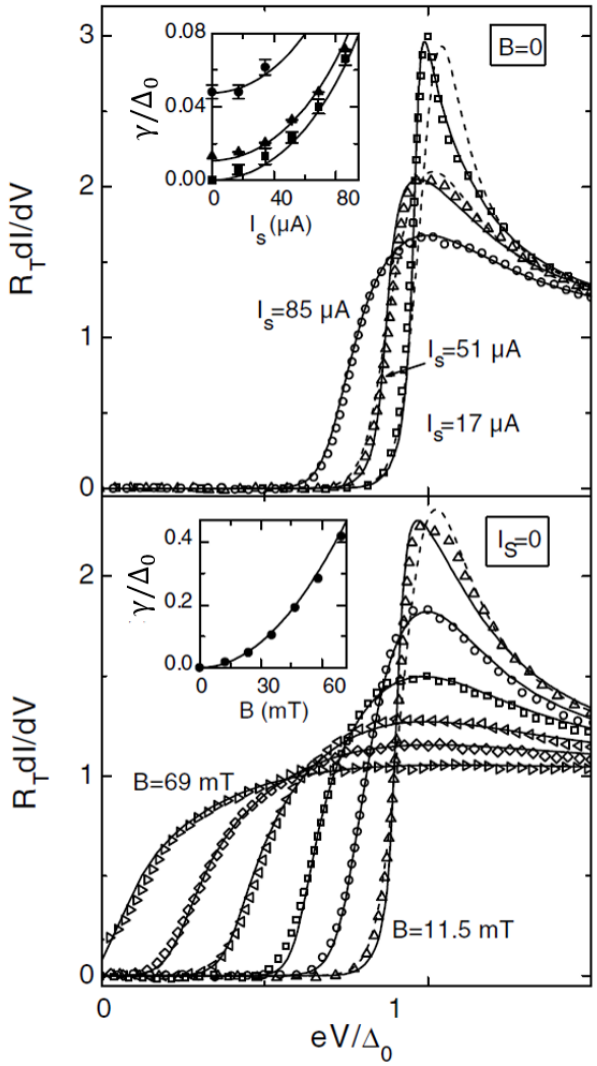

Figure 3.2: Superconducting density of states in the presence of depairing mechanisms. Normalized differential conductance $R_T dI/dV$ as a function of bias voltage V. *Top panel:* In the absence of magnetic field ($B = 0$) for different supercurrents I_s flowing in the wire. *Bottom panel:* At $I_s = 0$ for different magnetic fields. Solid lines are $dI/dV(V)$ fits. Insets: Depairing energy γ as a function of I_s and B, deduced from the fits. Solid lines: fits with Eq. 3.2. From [5]. In this sample, $I_c^0 = 106$ μA.

Usadel equations (Eq. 2.13) with the self consistent gap equation (Eq. 2.4) lead to the pairing angle θ, from which the DOS $N_s = N_0 \Re[\cos\theta]$ is deduced. Then, the depairing energy γ can be extracted from the experiment as a parameter depending on B and I_s. Eq. 3.2 gives the theoretical γ behavior (where U_s is given by Eq. 2.8). Good agreement between theoretical and experimental determination of the depairing energy is found, evidencing that the effect of both I_s and B can be accounted for by the single parameter γ.

Coulomb blockade and finite temperature effects are also taken into account [5]. Indeed, because of these two effects, the measured differential conductance slightly deviates from the DOS in the wire. First, Coulomb blockade results from the finite impedance of the electromagnetic environment: the tunneling electrons can absorb or emit some energy as mentioned in Subsection 1.2.2 and [88]. Then, the probe electrode and the superconducting wire exchange some energy through electron tunneling. Consequently, since the probe electrode is thermally isolated, its temperature depends on the bias voltage V, which affects the measured differential conductance.

Finally, the effect of supercurrent and magnetic field on the superconducting order is well described by the Usadel theory of out of equilibrium superconductivity in diffusive superconductors, and depends on a single parameter, the depairing energy. **In this PhD, the study of the effect of supercurrent on the density of states is extended up to (almost) the critical depairing current density with, in addition, a spatially resolved probe (see Section 5.2).**

3.3 Enhancement of superconductivity by quasiparticle injection

The possibility of an enhancement of superconductivity is contained in the BCS gap equation [8]:

$$\frac{1}{N_0 V_{eff}} = \int_{\Delta}^{\hbar\omega_D} dE \frac{1-2f(E)}{\sqrt{E^2-\Delta^2}} \tag{3.3}$$

with Δ the superconducting order parameter, f the distribution function, V_{eff} the electron pairing potential, ω_D the Debye frequency and N_0 the density of states at Fermi level. This equation is only valid for a symmetric distribution function. Because of the divergence of the denominator, the contribution of the numerator to the integral is larger for small energies. Then, lowering the distribution function f at these energies increases the integral and results in a larger superconducting order parameter Δ. This can be interpreted as follows: at finite temperature, quasiparticles close to the Fermi level block states that could be available for Cooper pairs, so removing them leads to an enhancement of superconductivity. This effect was first predicted by Parmenter [86]. Then, Eliashberg [33] proposed a mechanism, known as the *Eliashberg effect*, where quasiparticles are redistributed to higher energies where they are less effective in blocking states for the formation of additional Cooper pairs. Such an out of equilibrium distribution function can be achieved by tunnel injection and extraction of quasiparticles as in the experiments reported in this section, but also by absorption of microwave radiation [110, 62].

3.3.1 Enhancement of the critical temperature

A superconducting gap was measured in aluminum up to temperatures exceeding considerably its equilibrium critical temperature in [12]. The device consists in an aluminum film sandwiched between two tunnel junctions with niobium electrodes. A model was then developed in [50] to explain the gap enhancement in SIS'IS systems (S=superconductor, I=insulator).

In a symmetric double barrier structure, the junction voltage between left and right niobium electrodes is distributed equally over the two tunnel junctions. Thus, in the situation pictured in Fig. 3.3a, for junction voltages in a specific range, quasiparticle extraction from Al to Nb electrodes can be performed. It results in an out of equilibrium distribution function in Al leading to an enhancement of the Al superconducting gap Δ_{Al} as predicted by the Eliashberg effect. This is only possible because the niobium superconducting gap Δ_{Nb} is larger than the one of aluminum.

Since enhancement implies an out of equilibrium distribution function, its relaxation time is of particular importance as evidenced by the theoretical results plotted in Fig. 3.3b, where the balance between injection rate and relaxation time is the driving parameter. As long as quasiparticle extraction is sufficiently efficient to maintain Al out of equilibrium, a superconducting gap can be observed even if the equilibrium state is a normal metal. Finally, Δ_{Al} cannot exceed its equilibrium value at zero temperature.

The samples presented on Fig. 3.3c have equilibrium critical temperatures lower than 2.4 K. In the presence of tunneling enhancement of superconductivity, finite superconducting gaps have been measured well above critical temperature. The gap values at low temperature are close to the BCS prediction for the zero temperature superconducting gap[3].

This enhancement of the superconducting gap can also be interpreted as an enhancement of the critical temperature, since the material exhibits superconductivity for temperatures larger than its equilibrium critical temperature.

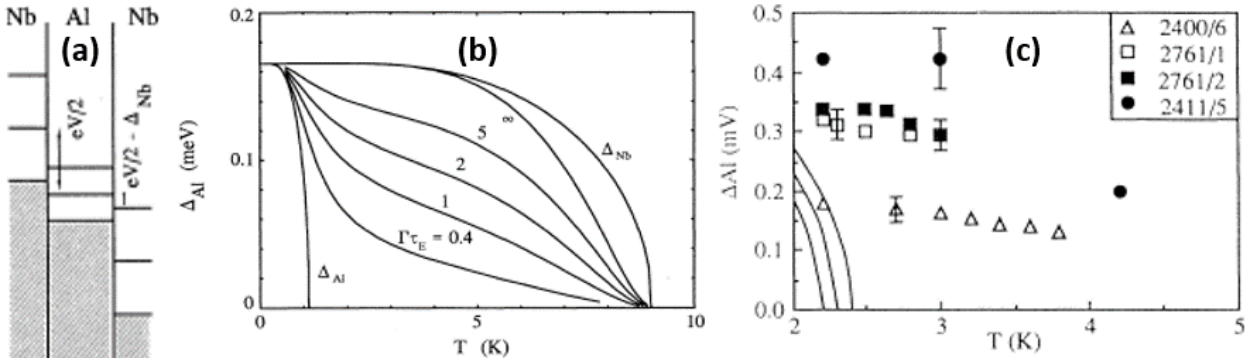

Figure 3.3: Enhancement of superconductivity far above the critical temperature in double-barrier tunnel junctions. (a) Energy diagram of the SIS'IS system. For a bias junction V in the range $2(\Delta_{\mathrm{Nb}} - \Delta_{\mathrm{Al}}) < eV < 2(\Delta_{\mathrm{Nb}} + \Delta_{\mathrm{Al}})$, quasiparticle extraction is sufficiently effective to develop a gap in the Al electrode. The quasiparticles close to the Fermi level are extracted to the right electrode while the quasiparticles injected from the left one to ensure current conservation in the junction remain far from the Fermi level. (b) Theoretical Al superconducting gap as a function of temperature at a bias corresponding to $eV = 2\Delta_{\mathrm{Nb}}(T)$ and for different products of the injection rate Γ and the relaxation time of the out of equilibrium distribution function τ_E. (c) Measured Al superconducting gap as a function of temperature for several devices with different thicknesses and critical temperatures (unlike in most other superconductors, the critical temperature of thin aluminum films increases with decreasing thickness). Solid lines are the BCS temperature dependence of the thermal equilibrium gap for the critical temperatures associated to the samples. From [50].

[3]Sample 2400/6 is the thickest and the measured gap corresponds to the gap value for Al. Samples 2761/1 and 2761/2 have a critical temperature of 2.2 and 2.3 K, and their gap corresponds to BCS prediction. Sample 2411/5 has the largest critical temperature (2.4 K) and its gap exceeds the BCS prediction. This large gap to critical temperature ratio has been reported in thin granular aluminum [72]

3.3.2 Enhancement of the critical current

An analytic perturbative treatment of the Eliashberg effect can be made close to the critical temperature [116]. An enhancement of the critical current is then predicted under quasiparticle injection, and was observed in [115]. Indeed, under quasiparticle injection, a critical current larger than the one in the absence of injection was measured as shown on Fig. 3.4c.

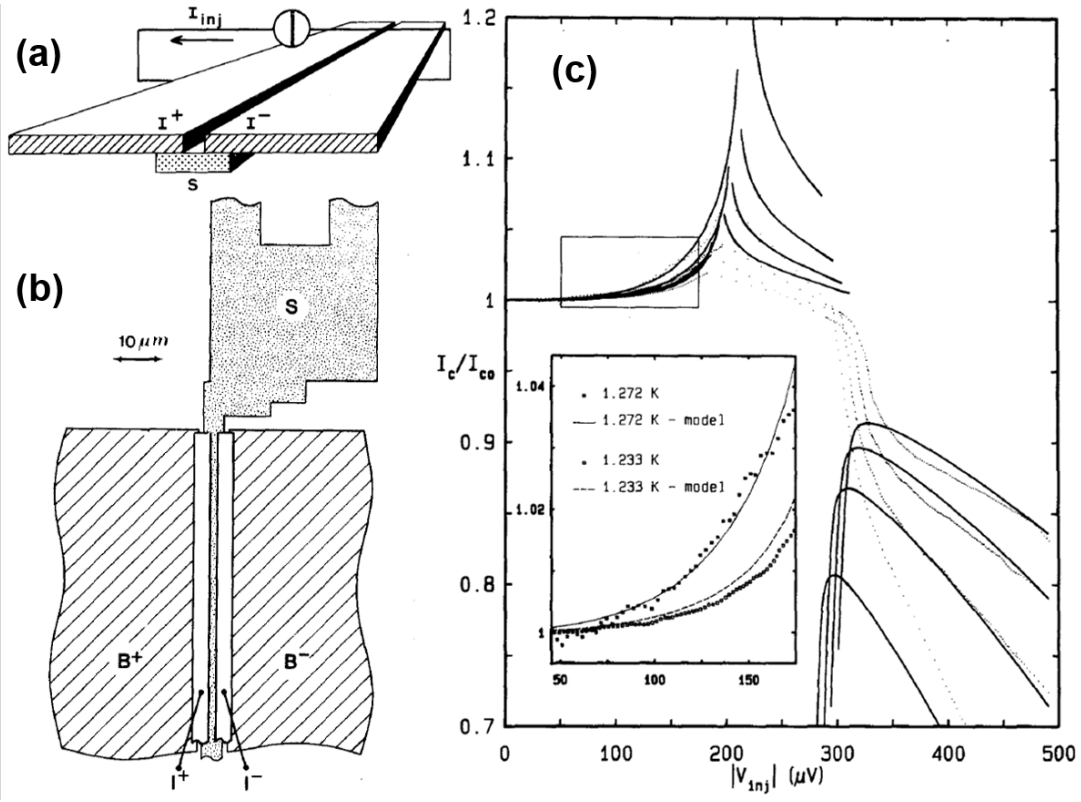

Figure 3.4: Enhancement of the critical current by quasiparticle injection close to the critical temperature. (a) Side and (b) top view of a narrow aluminum strip (S) subject to quasiparticle injection from side electrodes (I^+ and I^-). (c) Critical current normalized to its value in the absence of quasiparticle injection as a function of injection voltage for different temperatures (dots). Solid lines are fit with the model of [116]. From [115].

In this experiment, quasiparticles are injected in the superconducting strip S through a tunnel barrier from the two side electrodes I^+ and I^- which are also superconducting but with a larger critical temperature than S. A dual tunnel injection geometry was chosen in order to ensure both homogeneous distribution function within the cross section of the superconducting strip, and to discard charge imbalance[4]. However, the authors mention that their measurements are to be compared with theoretical predictions for a single junction (with a quasiparticle injection current I_{inj} flowing between one electrode, e.g. I^+, and S and without the second electrode represented on Fig. 3.4a and b). They are therefore also comparable to the experiments carried out in this PhD work except for the fact that our STM tip is not superconducting but normal.

The critical current is determined by the weakest section of the strip, which is unfortunately located within one of the two sections which are not covered by the injection junctions because of the proximity effect induced by the side electrodes. This makes the analysis more complex since one has to consider the diffusion of the injected quasiparticles between the injection junctions and the weakest section of the strip.

[4]Charge imbalance will be introduced in Chapter 8, but for now the absence of charge imbalance ensure a filling factor which is an even function of the energy so that Eq. 3.3 applies.

The agreement between theory and experiment is satisfactory for injection voltages lower than 200 μV and larger than 400 μV[5]. Both the enhancement of the critical current with respect to the unperturbed value at subgap injection voltages and its decrease when the injection voltage is increased far above the gap are unambiguously evidenced in Fig. 3.4. However, the sudden downturn of the critical current when the injection voltage is around 300 μV which is theoretically predicted is not experimentally observed in [115]. This is also an Eliashberg effect that we observed in this PhD work and which will be described and discussed in Chapter 8.

By comparison with the experiments carried out in this PhD by Scanning Critical Current Microscopy (SCCM), measurements from [115] are only performed very close to the critical temperature ($T_c = 1.291\ K$) of the strips. In addition, the injection current I_{inj} is comparable to the critical current. This is not the case in this PhD work as it will be shown in the next chapters, the tunneling current injected from the STM tip being many orders of magnitude smaller than the critical current. Also, the injection rate and energy of the quasiparticles cannot be set independently. Eventually, the use of lithographed junctions instead of a STM prevents from injecting quasiparticles locally and especially in the weakest section of the strip. Nevertheless, the use of superconducting injection electrodes allows to enhance superconductivity. Indeed, injection of quasiparticles with a normal electrode (or STM tip) can still create out of equilibrium distribution functions, but without leading to an enhancement of superconductivity.

The sharp decrease of the critical current for injection of quasiparticles with an energy close to the gap predicted but not observed in [115, 116] has been measured during this PhD and is presented in Chapter 8.

The enhancement effects presented in this section are due to out of equilibrium distribution functions.

The use of a STM instead of lithographed junctions in this PhD work allows to tune independently the injection rate and the energy of the injected quasiparticle, in addition to provide spatial resolution.

3.4 Modulation of the critical current by a gate voltage

Suppression of the critical current of a superconducting wire by an external electric field has first been reported in [27]. An electrostatic field is generated by a gate voltage V_b and modulates the critical current of the superconducting wire as shown on Fig. 3.5.

Technologically speaking, this result has applications in the field of superconducting electronics. Indeed, the device pictured in Fig. 3.5a acts as a superconducting field effect transistor (SuFET). The same modulation of the current have been investigated with SNS structures (SNS FET) [26] and Dayem-bridges playing the role of a Josephson weak link (JoFET) [85, 84, 89] instead of superconducting wires. In all cases, such a gate-tunable transistor is all metallic, and therefore takes advantage of the simplicity (in comparison with its semiconducting counterparts) and scalability of its fabrication process. Furthermore, it is believed to be faster and more energy efficient than current semiconductor devices.

On the fundamental physics side, the authors claim that this discovery deeply question our understanding of superconductivity. Indeed, according to conventional theory of electrostatic screening [6], electric fields in metals and superconductors are screened over the Thomas-Fermi screening length (typically smaller than 1 nm) so that it should not affect superconductivity.

Although a microscopic description has not been found yet, a phenomenological theory (based on the modification of Ginzburg Landau functional due to the electrostatic energy) is

[5] In between these values, the clear discrepancy is due to experimental issues preventing from biasing properly the injection voltage. The existence of several theoretical branches is due to the fact that there are several metastable solutions of the gap equation.

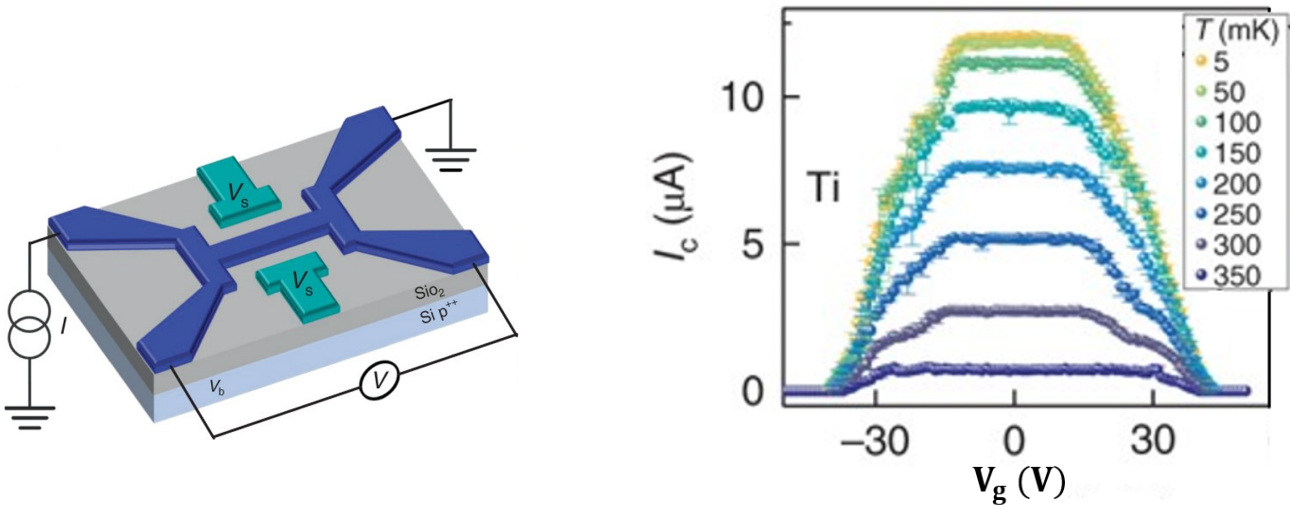

Figure 3.5: Electrostatic field dependence of the superconducting field effect transistor. Taken from [27]. (a) Schematic of a device. Back and side gate voltages (V_b and V_s) are used to apply electrostatic fields while the $I-V$ characteristics of the wire is recorded thanks to a conventional four probe measurement setup. In experiments, either $V_s = V_b \equiv V_g$ or $V_s = 0$ and $V_b \equiv V_g$ (b) Critical current I_c versus V_g at different bath temperatures T of a titanium wire.

developed in [27] to account for experimental results. Questioning of the validity of this theory is beyond the scope of this PhD work. Nevertheless, the superconducting field effect transistor reported in [27] and [89] is discussed in Section 6.8. **In light of the experimental results of this PhD work, we suggest that the modulation of the critical current by a gate voltage is rather due to quasiparticle overheating than to field effect.**

Chapter 4

Equilibrium properties of Nb\Au nanowires

Contents

As detailed in Section 1.4, the samples studied by STM in this PhD are 300 nm wide nanowires connected at both ends to wider leads, the whole sample consisting in an evaporated bilayer of niobium capped with gold. This chapter presents the dependence of the main equilibrium superconducting parameters on both width and thickness of the nanowires.

Firstly, both niobium and gold thicknesses t_{Nb} and t_{Au} have an influence on the superconducting properties. Notably, the critical temperature is strongly reduced due to disorder and low dimensionality when t_{Nb} becomes very thin. Incidentally, due to inverse proximity effect, the capping layer decreases further the critical temperature. Besides, capping the samples with gold prevents surface oxidation, preserving both the quality of the tunnel junction and the superconducting character of the samples: indeed, while a $\mathrm{Nb}_{5nm}\backslash\mathrm{Au}_{5nm}$ bilayer has typically a critical temperature of $\approx 2.5\ K$ (see Table 4.2.), an uncapped Nb_{5nm} sample does not become superconducting down to 50 mK. Finally, the width of the nanowires also turned out to play a role on the critical temperature despite its large value compared to other length scales.

4.1 Critical temperature

Specific samples have been fabricated to investigate the width dependence of the critical temperature. They consist in a series of three wires with different widths and lengths (300 nm wide × 20 μm long, 600 nm × 10 μm and 1.5 μm × 120 μm wires). The connections between the different wire parts are smooth widenings such as in the STM-designed samples to prevent current crowding effects. Eight contact pads allow to measure simultaneously the resistance of the different parts of the sample using the same current. Finally, such a design guarantees a constant thickness for all the three wires which rules out the thickness as a possible origin of critical temperature variations. Fig. 4.1 shows the resistance as a function of temperature of the three parts of a single wire with different widths. Both normal state resistivity and critical temperature present a monotonic dependency with the width (see Table 4.1).

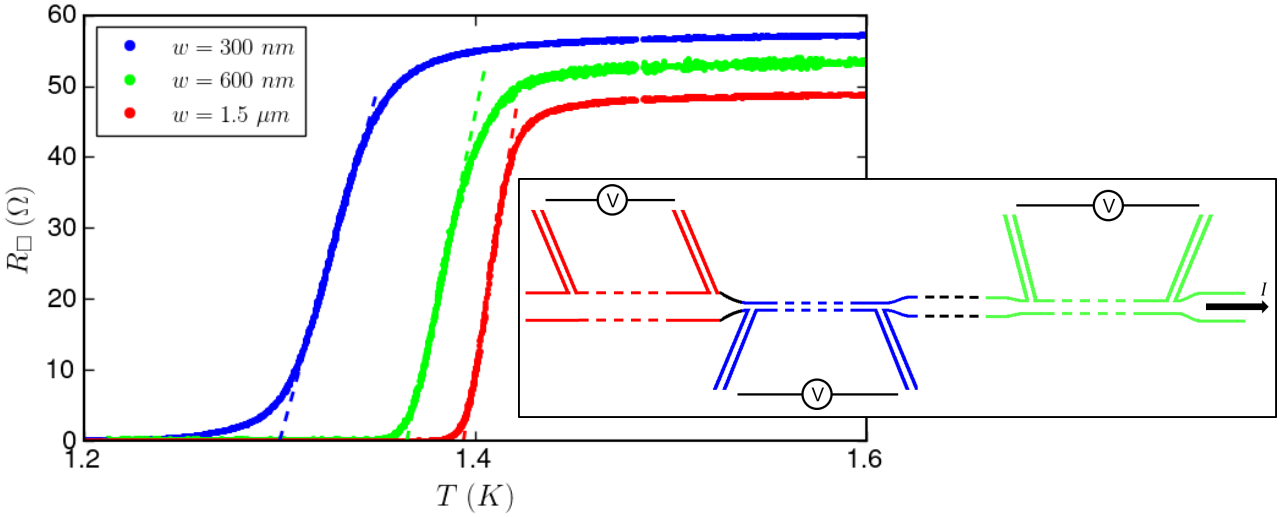

Figure 4.1: Square resistance $R_\square$ versus temperature for different widths w of sample T1. Dashed lines are linear extrapolations to extract the critical temperature T_c. *Inset:* Scheme of the sample (not to scale).

Sample	t_{Nb} (nm)	t_{Au} (nm)	w (nm)	T_c (K)	ρ_N ($\mu\Omega$.cm)	l (nm)	ξ_{GL} (nm)
T1	3	3	300	1.300	34.3	0.79	30
			600	1.365	32.2	0.84	31
			1500	1.394	29.3	0.92	32

Table 4.1: Parameters of the different sections of a $\mathrm{Nb}_{t_{\mathrm{Nb}}}\backslash\mathrm{Au}_{t_{\mathrm{Au}}}$ sample. t_{Nb} and t_{Au} are the nominal niobium and gold thicknesses, w is the width of the section, the critical temperature T_c is the extrapolation to $R = 0$ in linear scale of the resistance drop and ρ_N is the normal state resistivity. l is the mean free path computed from Eq. 4.1 and ξ_{GL} is the Ginzburg Landau coherence length computed from Eq. 2.32.

Consequently, the critical temperature is unambiguously lowered by a reduction of the wire width.

This behavior leads to a two step superconducting transition of the STM-designed samples because their geometry (detailed on Fig. 1.9) consists in a 300 nm wide nanowire connected at both ends to wider leads. Two examples are shown in Fig. 4.2. The incomplete superconducting transition with the higher critical temperature comes from the leads, whereas the resistance

drop to zero at lower temperature corresponds to the superconducting transition of the nanowire itself. Therefore the resistance of the sample at high temperature is given by $R_N^{nw} + R_N^{lead}$, where R_N^{nw} is the resistance of the nanowire and R_N^{lead} is the resistance of the leads, whereas the value of the resistance plateau in the middle of the transition is determined by R_N^{nw} alone. This scenario can be quantitatively confirmed by considering the aspect ratio of the nanowire and of the leads. They correspond respectively to a number of squares N^{nw} and N^{lead} in series. Accordingly we observe $R_N^{nw}/(R_N^{nw} + R_N^{lead}) = N^{nw}/(N^{nw} + N^{lead})$. Thus, we identify two transition temperatures: T_c^{lead} and T_c^{nw}, defined as the extrapolation to $R = 0$ in linear scale of the resistance drop from respectively R_N^{lead} to R_N^{nw} and R_N^{nw} to zero.

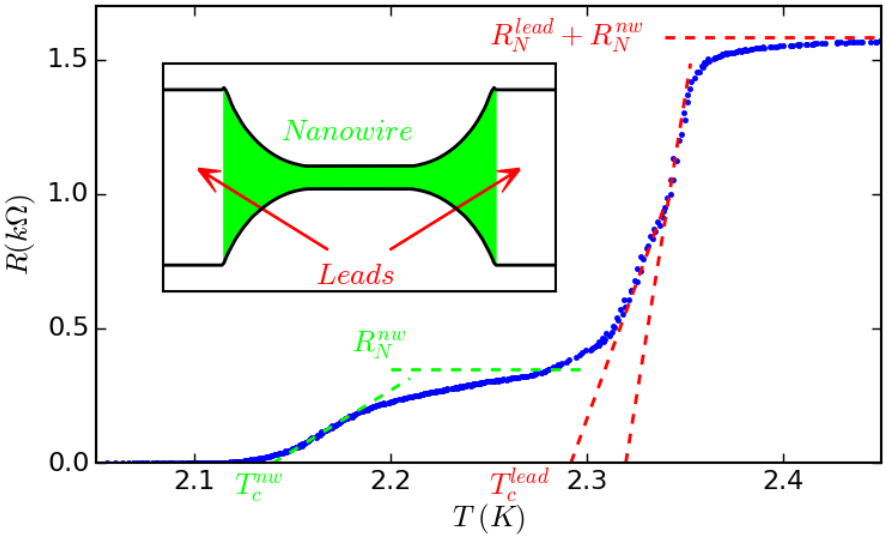

(a) N08.

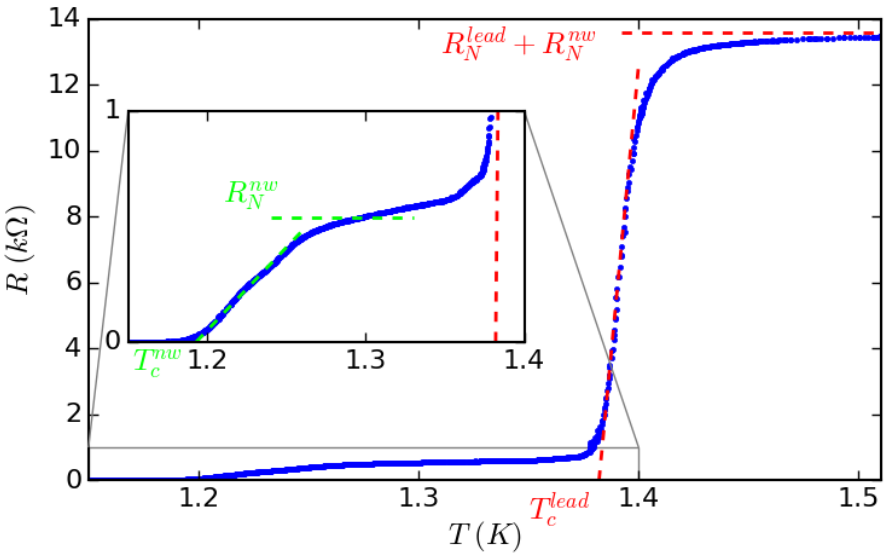

(b) N05.

Figure 4.2: Resistance versus temperature of typical samples. (a) N08. *Inset:* Scheme of the nanowire, with colored area used to compute N^{nw}. (b) N05. *Inset:* Zoom on the resistance plateau. N08 leads are wider (4 μm with respect to 2.3 μm) and shorter (smaller target) than those of N05, while the nanowire dimensions are the same, so their contribution to the total normal state resistance is smaller.

As we will see in Section 4.5, the critical temperature difference with respect to the width of the wire is too small compared to the energetic resolution to be revealed unambiguously by

Scanning Tunneling Spectroscopy through spectral gap variations. Besides, the determination of the slope of the leads transition can result in some uncertainty on T_c^{lead} (see Fig. 4.2a), so that two extreme values are extracted for some samples, but we will use the smallest one for all computations. Table 4.2 contains general experimental parameters about the Nb\Au nanowires studied by STM in this PhD, showing that the critical temperature is also lowered by a reduction of the thickness of the wire.

Then, one can notice in Table 4.2 that for the same niobium and gold **nominal thicknesses**, the critical temperature varies significantly from one sample to another. This is mainly attributed to **uncontrolled thicknesses variations due to the fabrication process**: for low thicknesses, the amount of material deposited relies only on the (short) evaporation time, which is calibrated with thicker deposits using a quartz microbalance. Therefore the calibration is not very accurate and may overlook a potential non superconducting seedlayer. Also, the metallic ingots of the sources are regularly removed from the evaporation chamber to change the materials available for the deposition, which does not help to maintain ultimate and constant purity, and therefore reproducible critical temperatures. Indeed, the bulk critical temperature of niobium is very sensitive to small oxygen contamination for instance [31].

Sample	t_{Nb} (nm)	t_{Au} (nm)	T_c^{lead} (K)	T_c^{nw} (K)	I_c^0 (μA)	ρ_N ($\mu\Omega$.cm)	l (nm)	ξ_{GL} (nm)	$k_F^{\mathrm{Nb}} l_{\mathrm{Nb}}$
N01	15	5	6.09	6.07	1000	18.2	1.1	16	2.1
N02	10	5	4.32	4.19	301	23.1	0.92	18	1.4
N03	5	5	2.66-2.68	2.43	96.3	18.5	1.5	29	1.4
N04	5	5	2.65	2.54	103	18.4	1.5	29	1.4
N05	3	3	1.38	1.19	15.7	24.8	1.1	35	1.0
N06	3	3	1.53	1.39	18.5	24.7	1.1	33	1.0
N07	3	3	2.01-1.95	1.72	-	31.3	0.87	26	0.8
N08	4	4	2.32-2.29	2.14	60	22.7	1.2	28	1.1
N09	3	3	1.72-1.68	1.55	-	30.2	0.90	28	0.8
N10	3	3	1.32-1.31	1.16	14.9	25.2	1.1	35	1.0
N13	3	3	0.820-0.810	0.790	6.8	31.2	0.87	40	0.8
N14	4	4	3.09	2.93	105	22.5	1.2	24	1.1
N15	3	3	1.44*	1.36*	18.3	36.8	0.74	28	0.7
N16	3	3	1.00-0.980	0.960	10.2	31.9	0.85	36	0.8

Table 4.2: Transport parameters of the samples studied by STM: t_{Nb} and t_{Au} are the nominal niobium and gold thicknesses, T_c^{lead} and T_c^{nw} are the critical temperature of the leads and the nanowire, I_c^0 is the zero temperature critical current, ρ_N is the bilayer normal state resistivity, l is the bilayer mean free path computed[1] from Eq. 4.1, ξ_{GL} the Ginzburg Landau coherence length computed from Eq. 4.4 and the $k_F^{\mathrm{Nb}} l_{\mathrm{Nb}}$ product is computed from the normal state properties of the Nb layer alone (see Section 4.2). For all the samples, the nanowire is 300 nm wide. All leads are 2.3 μm wide except N08's whose leads width is 4 μm. N07 critical current has not been measured down to very low temperatures before being damaged by the tip, and only transport measurements under magnetic field have been performed on N09. *The case of N15 is discussed in Appendix E.

The critical temperature of the nanowires is lowered by a reduction of either their width or their thickness. To better understand this dependence, we will then investigate the two characteristic lengths in a diffusive superconductor, namely the electron mean free path and the superconducting coherence length.

[1] Using T_c^{lead} and ρ_n.

4.2 Mean free path and normal state resistance

Within the Drude-Sommerfeld framework, valid in the normal (metallic) state, the normal state resistivity ρ_N gives information about the electron mean free path l. Indeed, Drude's law writes $\rho_N^{-1} = N_0 e^2 D$ with $D = v_F l/3$ the diffusion constant in three dimensions and N_0 the density of states at Fermi level, leading to:

$$l = \frac{3}{\rho_N N_0 v_F e^2} \tag{4.1}$$

Nevertheless, the electronic properties of the system differ between normal and superconducting states. As it will be demonstrated later, the transparency of the interface between Nb and Au is high and the coherence length is larger than the total thickness of the samples, so that superconductivity is sensitive to the *bilayer mean free path* l according to Eq. 2.30, considering the bilayer as a single material with averaged electronic properties. In the normal state however, the two layers behave as parallel resistors with different transport properties. The superconducting, metallic or even insulating character of the niobium layer alone disregarding the inverse proximity effect of gold is determined by its square resistance $R_\square^{\mathrm{Nb}}$ and mean free path l_{Nb} in the normal state and will be discussed in Subsection 4.7.1.

Computation of the bilayers mean free path

The bilayer normal state resistance directly stems from resistivity measurements of Fig. 4.2 through $\rho_N = (t_{\mathrm{Au}} + t_{\mathrm{Nb}}) R_\square^{\mathrm{Nb\backslash Au}}$ with $R_\square^{\mathrm{Nb\backslash Au}} = (R_N^{nw} + R_N^{lead})/(N^{nw} + N^{lead})$. The value $v_F = 1.4 \times 10^6$ m.s^{-1} will be used for the Nb\Au bilayer, since both materials have similar Fermi velocities [6]: $v_F^{\mathrm{Au}} = 1.4 \times 10^6$ m.s^{-1} and $v_F^{\mathrm{Nb}} = 1.37 \times 10^6$ m.s^{-1}. On the other hand, an averaged value weighted by the thicknesses t_{Au} and t_{Nb} will be taken for N_0:

$$\langle N_0 \rangle = \frac{t_{\mathrm{Nb}} N_0^{\mathrm{Nb}} + t_{\mathrm{Au}} N_0^{\mathrm{Au}}}{t_{\mathrm{Nb}} + t_{\mathrm{Au}}} \tag{4.2}$$

because **the density of states at Fermi level differs by one order of magnitude between gold and niobium:** $N_0^{\mathrm{Au}} = 5.8 \times 10^{46}$ J^{-1}.m^{-3} and $N_0^{\mathrm{Nb}} = 5.6 \times 10^{47}$ J^{-1}.m^{-3} [43], in agreement[2] with the values reported in [55].

This difference in the density of states at Fermi level can be attributed to different electronic interactions in these materials, which accounts for dissimilar effective masses m_*. Indeed, in a free electron gas model, $N_0 = m_*^2 v_F/(\pi^2\hbar^3)$, so that with comparable Fermi velocities, $m_*^{\mathrm{Nb}}/m_*^{\mathrm{Au}} = \sqrt{N_0^{\mathrm{Nb}}/N_0^{\mathrm{Au}}} \approx 3.1$. A thickness independent effective mass of $1.0 \pm 0.03\ m$ was measured for gold in [106] and although "niobium is a transition metal and its Fermi surface has a complicated topology", $m_*^{\mathrm{Nb}} = 3.2$ according to [60]. Consequently, these values give a starting estimate, but have to be taken with caution since they do not take into account possible variations with the thickness.

The mean free path l of the bilayer considered as a whole can be computed with the averaged density of states at Fermi level (Eq. 4.2). The results are reported in Table 4.2. The fact that **the mean free path l is only equal to a few lattice parameters** shows that the diffusion motion of the electron is quite reduced by some kind of disorder, which can have several origins, such as lattice defects or boundary scattering on the surface of the films so that $l \lesssim t$. Then, one should remind that the evaporation technique does not provide ultimately pure niobium and gold, neither a perfect interface between the two layers reducing again l.

Surprisingly, **the normal state resistivity ρ_N slightly increases when the width w is lowered at constant thickness t** (see Table 4.1), despite the fact that $l \ll w$. This may be

[2] Many studies reported in [55] give $N_0^{\mathrm{Nb}} \in [18; 30]$ Ry^{-1}.atom^{-1}, which leads to $N_0^{\mathrm{Nb}} \in [4.6; 7.6] \times 10^{47}$ J^{-1}.m^{-3} taking a molar mass $M_{\mathrm{Nb}} = 92.9$ g.mol^{-1} and a density of 8.57 for body-centered cubic niobium.

due to a small reduction of l (although boundary scattering on the wires sides sounds unlikely) and/or a modification of the Fermi surface. Nonetheless, this increase of ρ_N is compatible with an over etching leading to smaller effective widths: assuming a constant resistivity equal to the one measured in the widest part for sample T1 leads to effective widths of $\approx$ 250 nm and 550 nm for the narrow parts, while the nominal widths are respectively 300 nm and 600 nm. However, a bare reduction of the actual width of the samples could not explain the decrease of the critical temperature which is more likely related to a width dependence of the electronic properties.

Eventually, $\boldsymbol{l \ll w, t}$ **validates the three dimensional character of the electron gas** and that the electron diffusion constant writes $D = \frac{1}{3} v_F l$.

Computation of the normal state resistance of niobium only

Since the resistivity of gold is lower than the one of niobium, the measured bilayer square resistance in the normal state $R_\square^{\mathrm{Nb\backslash Au}}$ is essentially equal to the one of gold. Considering the two layers as parallel resistors, one can extract the square resistances of the two layers $R_\square^i = \rho_i / t_i$ where ρ_i is the resistivity and t_i the thickness of the layer for i=Nb, Au. Then,

$$R_\square^{\mathrm{Nb}} = R_\square^{\mathrm{Nb\backslash Au}} \left(1 + \frac{\rho_{\mathrm{Nb}} t_{\mathrm{Au}}}{\rho_{\mathrm{Au}} t_{\mathrm{Nb}}} \right) \tag{4.3}$$

The determination of the ratio $\rho_{\mathrm{Nb}}/\rho_{\mathrm{Au}}$ is subject to large uncertainties. As we already mentioned, the layers thicknesses are not well known because of the fabrication process. In addition to this, the resistivity strongly depends on thickness (as reported for instance in thin niobium samples [45]) and also probably on the deposition conditions. Thus, we will assume for simplicity that the ratio $\rho_{\mathrm{Nb}}/\rho_{\mathrm{Au}}$ is equal to its bulk value $\rho_{\mathrm{Nb}}/\rho_{\mathrm{Au}} \approx 5$ [6]. Then, $R_\square^{\mathrm{Nb}}$ allows to extract the mean free path in the niobium layer in the normal state l_{Nb} using Eq. 4.1. Since Fermi wavevector in Nb is about 0.5 $\mathrm{\AA}^{-1}$ [77, 47], this leads to the estimate of the $k_F^{\mathrm{Nb}} l_{\mathrm{Nb}}$ products of our samples given in Table 4.2.

4.3 Coherence length

4.3.1 Computation from resistivity and critical temperature

Given the theoretical values of Fermi velocity and density of states at Fermi level (Eq. 4.2), the normal state resistivity gives access to l (Eq. 4.1). Approximating[3] Δ_0 by $1.76 k_B T_c$, the critical temperature of a sample allows to compute $\xi_0 = \frac{\hbar v_F}{\pi \Delta_0}$. Therefore, the experimental parameters ρ_N and T_c leads to the Ginzburg Landau coherence length given in Table 4.2:

$$\xi_{GL}(\rho_N, T_c) = 0.855 \sqrt{\xi_0(T_c) l(\rho_N)} \tag{4.4}$$

In order to test the validity of such a computation, one can take advantage of the measurement of the upper critical field.

4.3.2 Determination by upper critical field measurements

The Ginzburg Landau coherence length can be extracted from the variations of the upper critical field B_{c2} near T_c. Indeed, using Eq. 2.32:

$$\frac{dB_{c2}}{dT}(T \to T_c) = -\frac{\phi_0}{2\pi \xi_{GL}^2 T_c} \tag{4.5}$$

[3] Such an approximation allows to compute ξ_{GL} for all samples with the same method, but one could replace Δ_0 by the superconducting gap measured by STS at low temperatures in the absence of depairing when it is available (see Table 4.3). This would only modify ξ_{GL} by a few percents.

Sample N06. In that respect, Fig. 4.3 shows the resistance of sample $N06$ as a function of temperature under different magnetic fields. The resistance is plotted in log scale to better distinguish the R_N^{nw} plateau which tends to disappear when the magnetic field is increased, but the same linear extrapolation than before is performed to extract the critical temperatures, leading to the $B_{c2}(T)$ dependence plotted in the inset. Values resulting from the linear behavior of $B_{c2}(T)$ near T_c are: $\xi_{GL,Bc2}^{lead} = 31$ nm and $\xi_{GL,Bc2}^{nw} = 32$ nm for the lead and the nanowire respectively. These values are in good agreement with the Ginzburg Landau coherence length computed from ρ_N and T_c^{lead}: $\xi_{GL}^{lead} = 33$ nm.

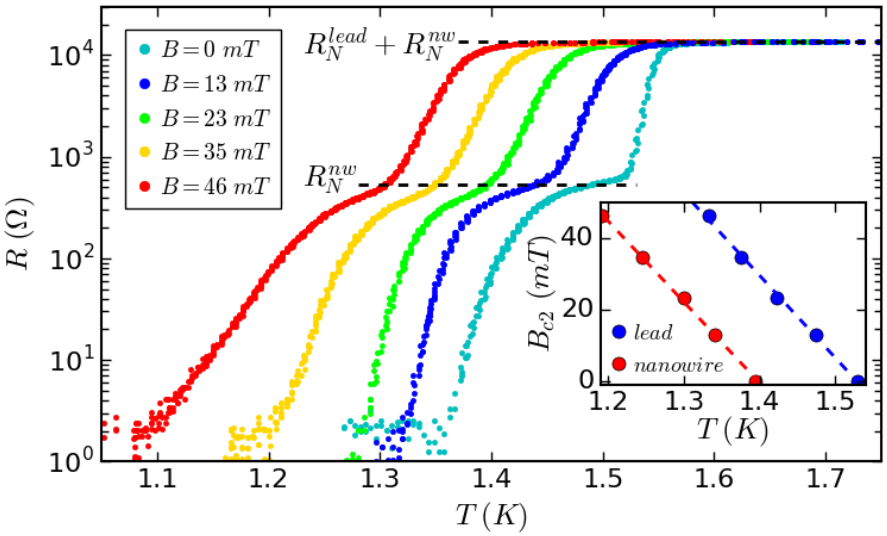

Figure 4.3: Resistance versus temperature under different magnetic fields of sample $N06$. Inset: Extracted upper critical fields as a function of temperature of the lead and the nanowire. The resulting coherence lengths (Eq. 4.5) are $\xi_{GL,Bc2}^{lead} = 31$ nm and $\xi_{GL,Bc2}^{nw} = 32$ nm.

Sample N09. Measurements up to larger magnetic fields have been performed on sample N09 and will be further discussed in Section 4.4. The behavior close to T_c leads to $\xi_{GL,Bc2} = 22$ nm using Eq. 4.5. This value is compatible with the coherence length computed from normal state resistivity: $\xi_{GL} = 28$ nm (see Table 4.2). The difference may be due to the uncertainties for instance over effective thicknesses, whose values affects the density of states and the resistivity of the samples which are used for the computation (an uncertainty of 1 nm over t_{Nb} results in a 20% change on ξ_{GL} for the present sample).

To summarize, upper critical field measurements were performed on two samples (N06 and N09). The extracted coherence length is in agreement with the above computation which depends on the averaged electronic properties of the samples through the bilayer mean free path. This confirms that the bilayer can be considered as a whole.

Since $\xi_{GL} \sim 30$ nm (see Table 4.1 and 4.2), $t \leq 20$ nm and $w \geq 300$ nm, it demonstrates that the characteristic length scale for the variations of the order parameter ξ is about one order of magnitude smaller than the nanowires width w. It is also larger than the total thickness t of the samples. Thus, **the nanowires can be considered as two dimensional superconductors.**

4.4 Low temperature upturn of the upper critical field

Within conventional BCS theory, the upper critical field $B_{c2}(T)$ is expected to saturate at low temperatures. The WHH [49, 118] theory adds a little distinction between clean and dirty superconductors, with a reduced collision parameter $\lambda \approx 0.88\xi_0/l$ varying from 0 (clean

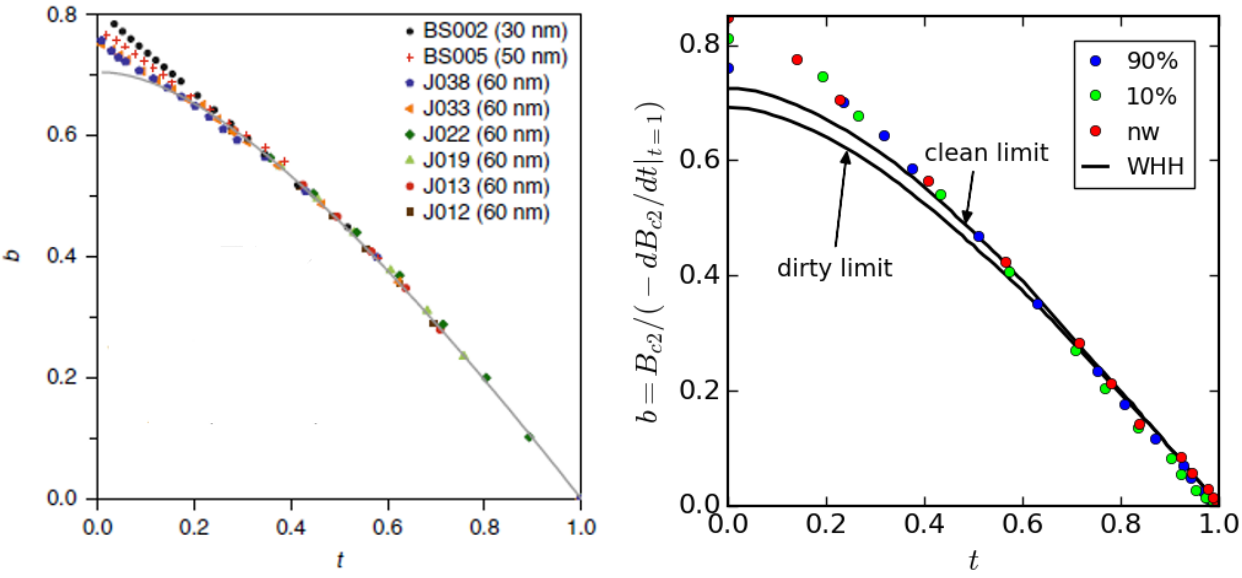

(a) (b)

Figure 4.4: Low temperature anomaly of the upper critical field B_{c2}. Reduced critical field $b = B_{c2}/(-dB_{c2}/dt|t = 1)$ versus reduced temperature $t = T/T_c$. (a) Indium oxide samples whose thickness is indicated in brackets. Solid line is the conventional BCS result. From [98]. (b) Nb\Au sample (N09) with different criterion to determine T_c: $90\%R_N^{lead}$ (blue), $10\%R_N^{lead}$ (green) and linear extrapolation to $R = 0$ for $R < R_N^{nw}$ (red). The three criteria lead respectively to $\xi_{GL,Bc2} = 20$; 21 and 22 nm and exhibit an anomalous temperature dependence of the upper critical field B_{c2}. Solid lines are the WHH theory in clean and dirty limits.

limit) to ∞ (dirty limit). Nonetheless, a larger upper critical field than the one predicted by conventional theory of superconductivity is measured at low temperature for sample N09 as shown on Fig. 4.4b. This non classical behavior has been observed in disordered superconductors made of InO_x and MoGe [98] (see Fig. 4.4a).

Upturns of the upper critical field at low temperature have already been reported in disordered superconductors and will be discussed in Subsection 4.7.1.

4.5 Superconducting gap

The STS technique presented in Section 1.2 allows to probe locally the DOS of the samples, since the differential conductance of the tunnel junction (Eq. 1.8) is proportional to the DOS convoluted with a function reflecting some broadening due to the finite energetic resolution.

Within the Usadel framework, the DOS is given by $N_s = N_0\Re[\cos\theta]$ where the pairing angle θ follows Eq. 2.20. In the absence of any supercurrent and magnetic field ($\gamma = 0$), the DOS is equivalent to the Dynes form (see Appendix B):

$$N_s(\epsilon) = \begin{cases} N_0 \left| \Re\left[\frac{\epsilon + i\Gamma_{in}}{\sqrt{(\epsilon+i\Gamma_{in})^2 - \Delta^2}} \right] \right| & \text{if } |\epsilon| > \Delta \\ 0 & \text{if } |\epsilon| < \Delta \end{cases} \tag{4.6}$$

Thus N_s is a function of the energy ϵ with respect to Fermi level, and depends on two parameters: Δ and Γ_{in}. The thermal broadening is characterized by an effective temperature T_{eff}.

Fig. 4.5 shows the differential conductance measured on different samples at low bath temperatures T in the absence of depairing ($\gamma = 0$). Fit of experimental data with the theoretical expression for the differential conductance allows to extract Δ_0, Γ_{in} and T_{eff} (see Table 4.3).

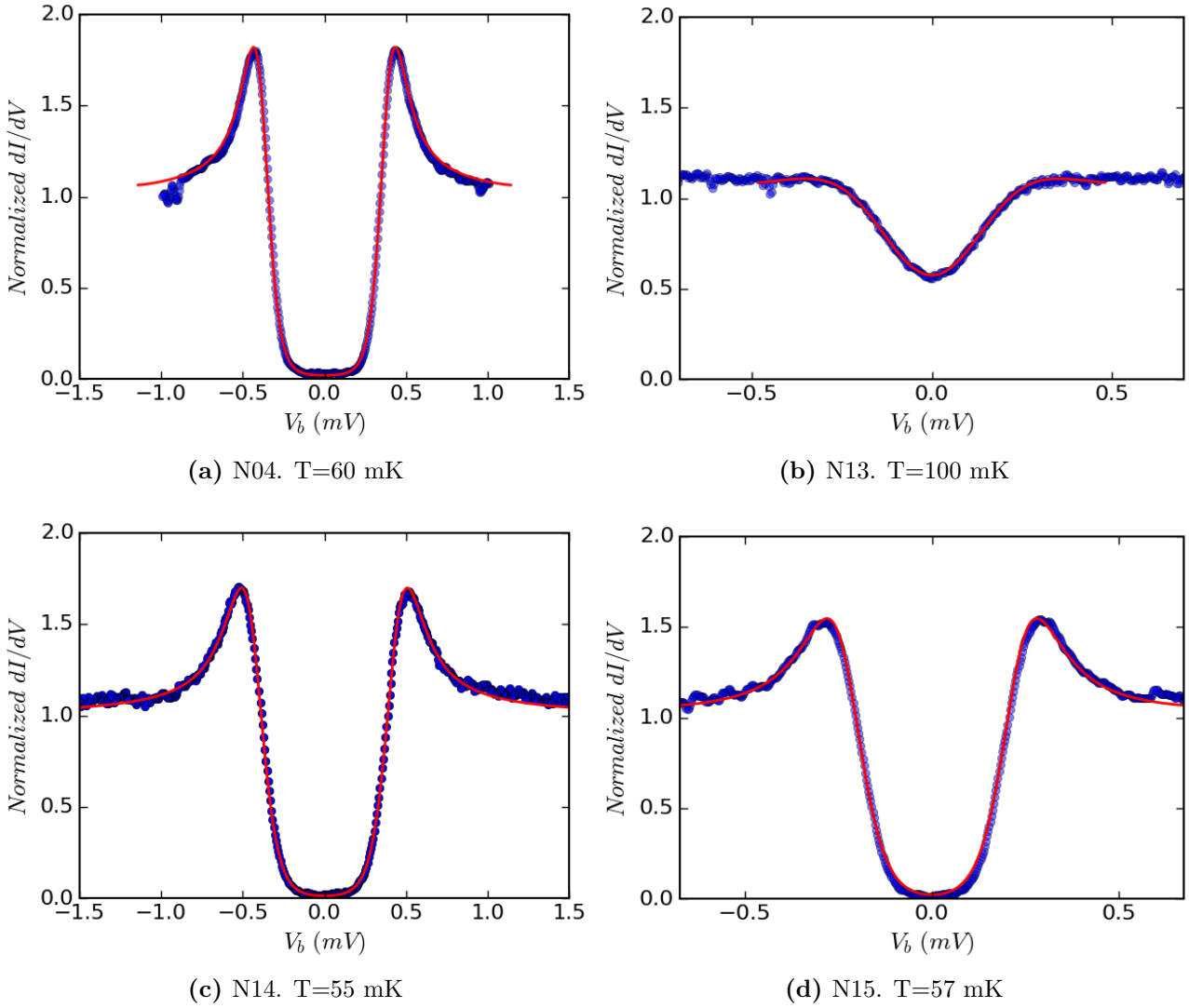

(a) N04. T=60 mK

(b) N13. T=100 mK

(c) N14. T=55 mK

(d) N15. T=57 mK

Figure 4.5: Normalized differential conductance as a function of bias voltage in the absence of depairing. T is the bath temperature. Solid red line is Eq. 1.8 with Δ_0, Γ_{in} and T_{eff} parameters given in Table 4.3.

Theoretical predictions for the DOS in a diffusive superconductor in the absence of depairing are in good agreement with experimental data using an effective electronic temperature T_{eff} larger than the bath temperature T (temperature of the sample holder).

The ratio $\Delta_0/(k_B T_c^{nw})$ - which is equal to 1.76 for a BCS superconductor - is plotted on Fig. 4.6 as a function of T_c^{nw}. The ratio $\Delta_0/(k_B T_c^{nw})$ slightly increases from the 1.76 BCS value to 2.4 as the critical temperature T_c^{nw} decreases from ~ 6 K to ~ 0.8 K.

Incidentally, only small spatial variations of the superconducting gap were detected in the nanowires. These variations (of about 10 μeV) are of the order of the energetic resolution (defined in Subsection 1.2.2 by $3.5k_BT$ and equal to 15 μeV at a bath temperature $T = 50$ mK) so that the DOS of the nanowires can be considered homogeneous within experimental accuracy. Furthermore, the critical temperature difference between leads and nanowires, which is typically ≈ 200 mK would result for a BCS superconductor in a 1.76 $k_B \times 200$ mK ≈ 30 μeV difference in the superconducting gaps. Therefore, variations in the DOS between the leads and the nanowire are difficult to detect due to our finite energetic resolution.

Besides, the effective energetic resolution is different than the theoretical $3.5k_BT$ value as discussed in Subsection 1.2.2. This is partly due to the fact that T_{eff} is larger than T: both

Sample	N01	N03	N04	N05	N06	N07	N08	N10	N13	N14	N15	N16
Δ_0 (μeV)	885	370	380	220	235	290	355	205	160	430	225	180
Γ_{in}/Δ_0	0	0.02	0.02	0.05	0.03	0.015	0.01	0	0.1	0.01	0.001	0.001
T_{eff} (mK)	385	556	450	570	540	680	660	430	1000	650	460	400
t_{Nb} (nm)	15	5	5	3	3	3	4	3	3	4	3	3
t_{Au} (nm)	5	5	5	3	3	3	4	3	3	4	3	3

Table 4.3: Spectral parameters of the samples: Δ_0 is the superconducting gap, Γ_{in} the inelastic scattering term and T_{eff} the effective temperature of the tip. t_{Nb} and t_{Au} are the nominal thicknesses of niobium and gold.

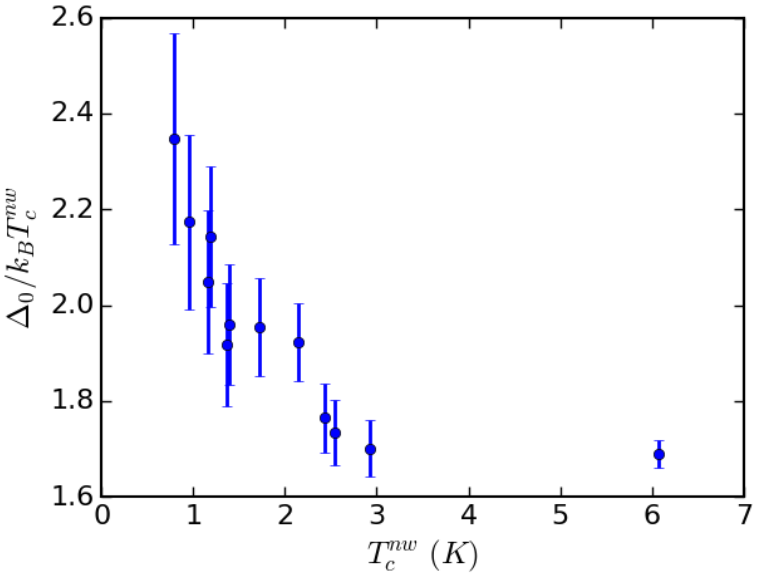

Figure 4.6: $\Delta_0/(k_BT_c^{nw})$ ratio versus T_c^{nw}. Error bars are given by the energetic resolution at 50 mK (15 μV, see text) leading to an uncertainty over Δ_0.

voltage fluctuations across the tunnel junction and poor thermalization of the STM tip electrons decrease the resolution by increasing T_{eff}. Nonetheless, since T_{eff} affects dI/dV, it also can account for deviations of the DOS from theory. In this respect, Fig. 4.6 suggests that a deviation from BCS theory goes together with a decrease of T_c^{nw}. As discussed in Subsection 4.7.1, this decrease is due to the combination of thickness reduction and proximity effect. Since these two effects weaken superconductivity, they are all reasons to alter the BCS character of the DOS with subgap states, leading to a smearing of the DOS coherence peaks which can be accounted for by large T_{eff} values.

Fig. 4.7 presents the temperature profile of the differential conductance $dI/dV(V_b)$. It evidences that the superconducting gap vanishes at T_c^{nw}.

The bilayers behave as BCS-like superconductors with nonetheless a smeared gap in the density of states.

4.6 Influence of the wire width

The present experimental work demonstrates that the critical temperature clearly depends on the wire width, but the explanation remains an open question. Possible interpretations include:

- Variations of evaporated films critical temperature have already been attributed to some strain due to differential thermal contractions between the substrate and the film [13, 56, 113]. One could imagine that down to small widths and thicknesses, the wire is subject to some width dependent strain affecting its critical temperature.

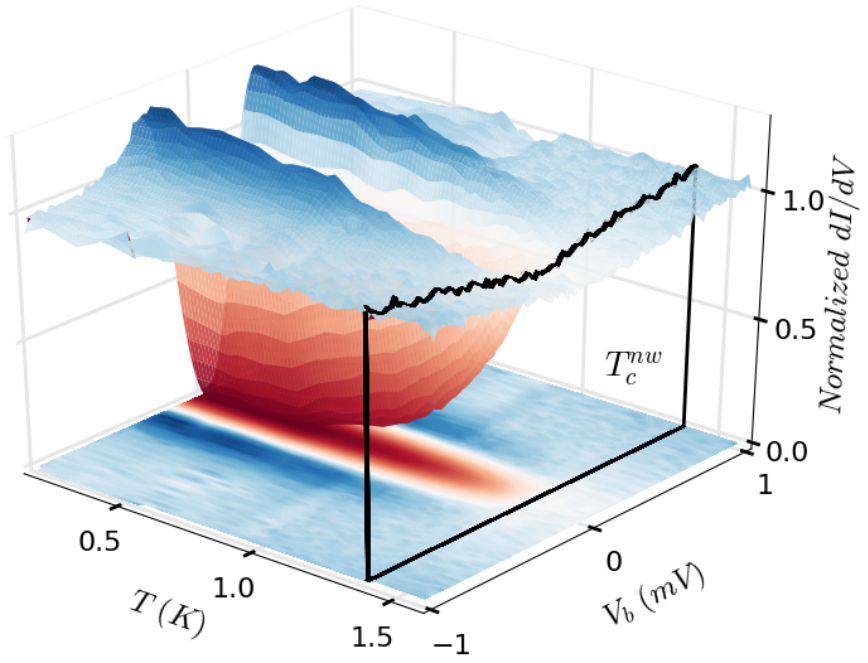

Figure 4.7: Temperature dependence of the density of states. Normalized differential conductance as a function of bias voltage V_b for different temperatures, measured in the center of the nanowire. Each spectrum is normalized to its large bias value. Black solid line corresponds to the nanowire critical temperature T_c^{nw}. Sample N06.

- The fact that the lowering of the critical temperature T_c goes together with an increase of the normal state resistivity ρ_N can be related to a modification of the density of states at Fermi level N_0. Indeed, $\rho_N^{-1} = N_0 e^2 D$ and BCS theory relates the critical temperature to the pairing potential V_{eff} and the density of states at Fermi level through Eq. 2.1. Then, an increase of ρ_N could be a manifestation of a lowering of N_0, which would also decrease the critical temperature T_c. However, further quantitative investigations are complex. The microscopical reasons leading to such a change in N_0 while the transverse dimension w is large compared to the mean free path are not understood, and are difficult to disentangle from the influence of other parameters such as l, v_F and V_{eff}. Finally, modifications of the Fermi surface are not independent from strain.

- At first sight, no dimensional crossover occurs when the width is lowered since one always have ξ_{GL} (the extension of a Cooper pair) much smaller than w, so that Cooper pair motion remains unaffected[4]. Nevertheless, because of the divergence of the coherence length near T_c, superconducting fluctuations can lead to such a crossover, as illustrated by the simple following computation:

  We note T_{2D} the critical temperature of an infinite two dimensional film of uniform thickness and $\xi(T) = \xi_{2D}\sqrt{\frac{T_{2D}}{T_{2D}-T}}$ its coherence length. Let's assume for simplicity that a wire of width w is in the normal state when $w \ll \xi$ and superconducting when $w \gg \xi$, the transition occuring when $\xi(T) \approx w/\alpha$ with α of order unity. Then, one obtains the following crossover temperature T_{cross}^{1D-2D} from a 1D metallic state to a 2D superconducting

[4]One may argue that the effective width could be reduced by side oxidation where the niobium is not protected by gold (see Fig. 1.9b), but probably not on more than ~ 10 *nm* thick since 15 nm thick uncapped niobium films coming from the same source turned out to be superconducting.

state:

$$\frac{T_{cross}^{1D-2D}}{T_{2D}} \approx 1 - \alpha^2 \left(\frac{\xi_{2D}}{w}\right)^2 \tag{4.7}$$

Approximating T_{2D} by T_c^{lead} for samples of Table 4.2 (the lead being the widest part of the wire for sample T1), one can plot T_c^{nw}/T_c^{lead} as a function of $(\xi_{GL}/w)^2$ (see Fig. 4.8). The experimental critical temperatures of our samples correspond approximately to the 1D to 2D crossover with $\alpha = 3$. This can be interpreted as follows: at low temperatures, the coherence length is smaller than w so the wire is two dimensional, and therefore superconducting. For $T_{cross}^{1D-2D} < T < T_c^{lead}$, the coherence length increases and when it approaches w, the wire becomes quasi one dimensional and therefore normal. It is worth noticing that the points which are the furthest from the crossover line in Fig. 4.8 correspond to the samples with the highest $\Delta_0/(k_B T_c^{nw})$ ratio. This may point out a non-BCS behavior of the thermal dependance of the coherence length in these bilayers.

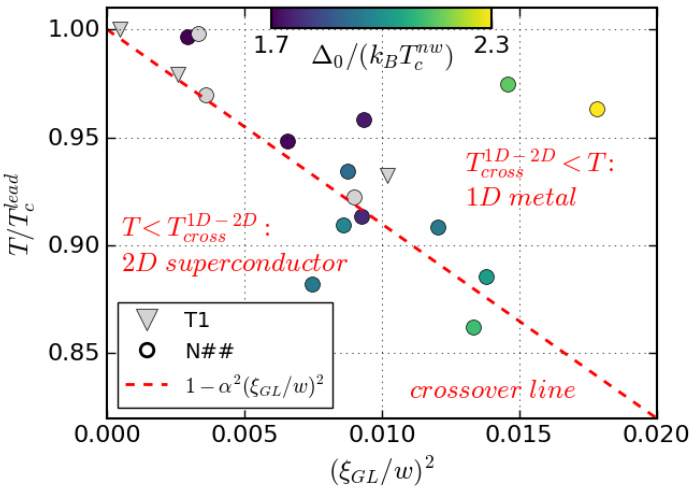

Figure 4.8: T_c^{nw}/T_c^{lead} ratio as a function of $(\xi_{GL}/w)^2$ of samples N01 to N16 (circles) and of sample T1 (triangles). The color corresponds to the $\Delta_0/k_B T_c^{nw}$ ratio when available. Dashed line is Eq. 4.7 with $\alpha = 3$.

Then, the simple model presented here shows that the superconducting fluctuations near critical temperature, manifested by the divergence of the coherence length near T_c, could explain the effect of the wire width on the superconducting critical temperature. Moreover, it is likely that these fluctuations only manifest close to the transition, affecting T_c^{nw} but leaving unchanged the low temperature properties such as the superconducting gap at $T = 0$. This is consistent with the fact that no variations of the latter have been measured between the leads and the nanowire in Section 4.5.

A size dependence of the transport properties of superconducting indium oxide nanowires has also been observed close to the disorder-driven superconductor-insulator transition [79]. Interestingly, thermally activated phase slips, i.e. one dimensional superconducting fluctuations, are invoked to explain the low temperature residual sheet resistance which value increases when the width of the nanowire is reduced. However, we think that this effect cannot explain the variations of the critical temperature with the wire width observed in our samples.

The width dependence of the critical temperature remains an open question.

4.7 Influence of disorder

To begin with, one should distinguish two different mechanisms which rule the superconducting properties of the Nb\Au bilayers: the inverse proximity effect of gold on niobium and the level of disorder in the niobium layer alone. In this section, we investigate the role of disorder disregarding the proximity effect.

4.7.1 Anderson localization and disorder-enhanced Coulomb repulsion

In the literature, the degree of disorder is usually defined by the $k_F l$ product, where k_F is the Fermi wavevector and l the mean free path. This parameter roughly makes the distinction between a metal and an insulator, the transition occurring when l is of the order of Fermi wavelength λ_F. **In weakly disordered systems ($k_F l \gg 1$), Anderson's theorem [3] states that superconductivity is not affected by weak disorder** as long as it is static and non magnetic (we already mentioned the sensitivity of niobium bulk critical temperature to oxygen contamination, we should also notice that eventual residuals of magnetic metals in the evaporation chamber would have the same effect). This thus extended the BCS framework to diffusive superconductors ($l \ll \xi_0$) by renormalizing the coherence length ($\xi_{GL} \approx \sqrt{\xi_0 l}$), before the development of Usadel equations [114].

However, Anderson's theorem does not hold in the strong disorder limit. Indeed, when $k_F l \approx 1$, electrons are localized over small length scales. In the worst case where $k_F l \ll 1$, k_F and l no longer make sense, the electrons are localized and do not participate to conduction: the material is insulating at $T = 0$. As for superconductivity, one may wonder how far in the insulating regime the overlap between localized wave functions of opposite spin and momenta is sufficient to allow the formation of Cooper pairs.

Besides localization, interactions can also play a role in the disorder-induced superconductor-insulator transition (SIT). One can distinguish two main classes of materials exhibiting distinct behaviors when the transition is approached depending on the range of Coulomb interaction:

- granular films (the granularity refers to their electronic phase, not necessarily to their morphology, and may be due to Anderson localization) are composed of superconducting islands coupled by tunnel junctions. The transition is interpreted as a competition between the inter-grains Josephson coupling, the charging energy and the thermal energy. They are characterized by a constant superconducting onset temperature, corresponding to the critical temperature of each grain. When the film disorder is increased, the superconducting transition first broadens due to phase fluctuations between the order parameter of each grain, and then the film become insulating, with an exponential increase of the resistance with decreasing temperature for the most disordered samples (Fig. 4.9a). In the vicinity of the critical disorder, these films also often exhibit re-entrance features of the resistance as the temperature decreases (see Fig. 4.9a, the resistance first start to drop when the temperature decreases as in a superconducting transition before rising again).

- homogeneously disordered superconductors exhibit a sharp transition, translated without broadening when the disorder is increased (Fig. 4.9b). The transition is interpreted as a competition between electron pairing and disorder-enhanced Coulomb repulsion, leading to a continuous destruction of the order parameter by the disorder. In this model, the mobility of electrons is affected so that dynamical charge screening is less efficient, enhancing Coulomb repulsion and so lowering the effective pairing potential and the critical temperature.

Experimentally, granular systems are generally metals deposited on a substrate at low temperature without any particular precaution regarding the film wetting. Homogeneously disordered systems include amorphous alloys (a-MoGe, a-NbSi,...) and metals deposited at low temperature on a thin a-Ge underlayer. Indeed, the a-Ge underlayer increases the films wetting allowing the materials to grow homogeneously: Pb films grown on two different substrates (SiO and a-Ge) exhibit either granular or homogeneous behavior [39]. To conclude, the deposition

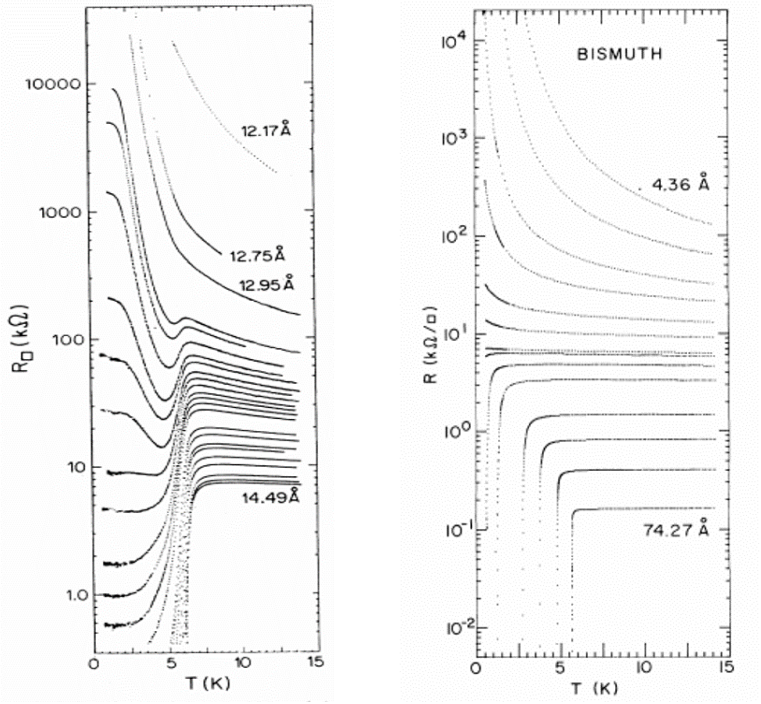

(a) **(b)**

Figure 4.9: Square resistance versus temperature for different thicknesses of granular and homogeneous films. (a) Granular films (granular gallium deposited on quartz, taken from [54]). (b) Homogeneous films (amorphous bismuth deposited on an a-Ge underlayer, taken from [48]).

process plays as well as the substrate an important role for pure metals, the low temperature deposition process providing highly disordered materials for instance.

When the thickness is sufficiently low as in our Nb\Au samples, it is reasonable to wonder whether the decrease of the critical temperature is due to Anderson localization or disorder-enhanced Coulomb repulsion. The resistance versus temperature curves of our samples do not show any characteristic of granular systems such as re-entrance or disorder-independent onset of a critical temperature, so they are believed to be homogeneously disordered (see Fig. 4.2). The broadening of the transition observed in some samples may be attributed to some thickness inhomogeneities (roughness) along the leads due to the evaporation process. Superconducting fluctuations can also broaden the transition because of the nucleation of superconducting domains of size $\sim \xi_{GL}$ in the metallic phase. The effect becomes non negligible when the coherence length is reduced, by disorder for instance, and in two dimensions the fluctuations occur on a temperature range $\delta T_c/T_c \approx R_\square e^2/(23\hbar)$ [68].

In any case, our Nb\Au films are neither granular nor highly inhomogeneous, so we will therefore discuss in the following the two remaining possible models: the fermionic scenario of homogenously disordered films with Coulomb repulsion, and the bosonic scenario of localized Cooper pairs without repulsive interaction.

The "Fermionic" scenario

The fact that in two dimensions the degree of disorder (usually defined by $k_F l$) is directly related to the square resistance $R_\square = h/(e^2 k_F l)$ led to consider the latest as a direct measurement of the disorder level in homogeneously disordered thin films. A full theoretical description of the competition between superconductivity and disorder embracing the homogeneous case and the pure granular case is still lacking, but Finkelstein explained the destruction of superconductivity in *two dimensional* homogeneously disordered superconductors ($t_s \ll \xi_{GL}$) as a function of the normal state square resistance $R_\square$ [36]. His theory gives $T_c(R_\square)$ as a function of only two parameters: the bulk critical temperature T_c^{bulk} and the elastic scattering time τ, while $R_\square$

captures the effect of the weakening of dynamical Coulomb screening:

$$T_c = T_c^{bulk}\ e^{\gamma}\left(\frac{1/\gamma - \sqrt{r/2} + r/4}{1/\gamma + \sqrt{r/2} + r/4}\right)^{1/\sqrt{2t}} \tag{4.8}$$

with $r = \frac{R_\square e^2}{\pi h}$ and $\gamma = \ln\left(\frac{h}{k_B T_c^{bulk}\tau}\right)$. Excellent agreement was found with the data measured previously on amorphous MoGe thin films [44] (see Fig. 4.10).

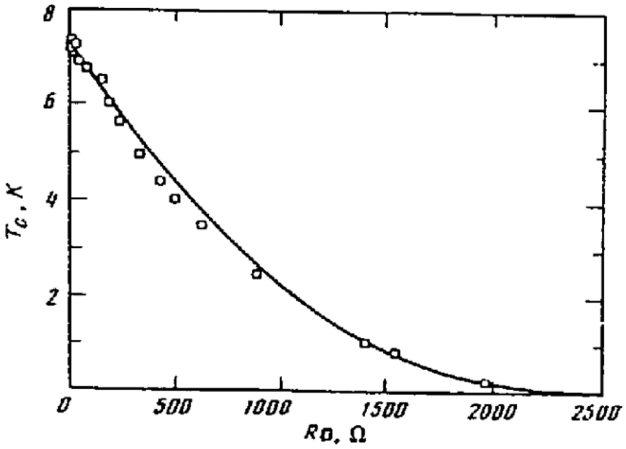

Figure 4.10: Destruction of superconducting transition temperature in amorphous $Mo_{79}Ge_{21}$ thin films as a function of $R_\square$. Solid line: result of Finkelstein's adjustment. From [36].

An increase of the normal state square resistance of the bilayers $R_\square^{\mathrm{Nb\backslash Au}}$ together with a decrease of the critical temperature T_c^{lead} was observed. Within Finkelstein theory, the level of disorder of the niobium layer is given by its square resistance $R_\square^{\mathrm{Nb}}$ extracted in Eq. 4.3 with non negligible uncertainties[5]. Fig. 4.11 gives a rough estimate of the $T_c^{lead}(R_\square^{\mathrm{Nb}})$ behavior, but the critical sheet resistance for which superconductivity is destroyed, $R_{\square,c}^{\mathrm{Nb}} \approx 500\ \Omega$, is comparable to the one given in [30] and [21] for pure Nb.

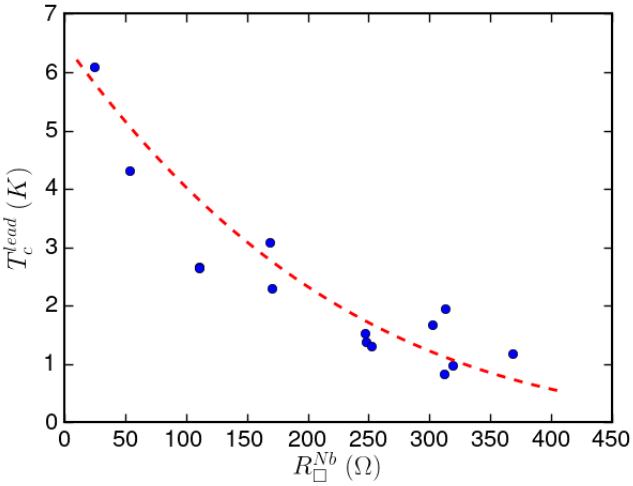

Figure 4.11: Nb\Au bilayers critical temperature as a function of the normal state square resistance attributed to the niobium layer $R_\square^{Nb}$. Dashed line is Eq. 4.8 with $\tau = 1.6\ 10^{-18}\ s$ and $T_c^{bulk} = 6.5\ K$.

Finkelstein analysis leads to the parameters $\tau = 1.6 \times 10^{-18}$ s and $T_c^{bulk} = 6.5\ K$. The obtained T_c^{bulk} is lower than the theoretical bulk value for Nb (9.2 K), but can be explained by the proximity effect of gold on niobium and by the deposition conditions (magnetic impurities or oxygen pollution). In contrast, the value of τ is unrealistic since it would lead to a mean free path $v_F\tau \sim 1$ pm far too low compared to the mean free path of the niobium layer l_{Nb} extracted in Table 4.2 ($k_F^{\mathrm{Nb}} l_{\mathrm{Nb}} \approx 1$ leads to l_{Nb} of the order of a few angstroms with $k_F^{\mathrm{Nb}} = 0.5\ \text{Å}^{-1}$). Thus, Finkelstein theory does not apply here, so **the enhancement of Coulomb repulsion is not the main cause for the destruction of superconductivity in our samples.** Some work on Nb [30], NbSi, [21] and TiN [46], where the disorder has also been tuned by the thickness, also report that although describing well the $T_c(R_\square)$ curves, Finkelstein theory provides unrealistic values of τ.

Besides, the scaling theory of localization [70] predicts a metal-insulator transition (MIT) for a value of $R_\square$ of the order of the quantum of resistance. Then, the fact that $R_{\square,c}^{\mathrm{Nb}}$ is lower than the quantum of resistance indicates that the most disordered samples are on the metallic side of the MIT. This is also confirmed by the fact that $k_F^{\mathrm{Nb}} l_{\mathrm{Nb}} \approx 1$ (see Table 4.2) for our samples.

It is interesting to specify that **Finkelstein theory accounts for the destruction of su-**

[5]Using more refined expressions for the resistivities $\rho_i \propto t_i^{-1}$ as in [45] does not change $R_{\square,c}^{\mathrm{Nb}}$ of more than a factor 2 neither the order of magnitude of the τ value extracted from Finkelstein analysis.

perconductivity by disorder-enhanced Coulomb repulsion, assuming that the bulk properties of the electron gas remain unchanged.

Incidentally, some work report the following counter-intuitive result in highly disordered superconductors (Pb, Bi or Ga) covered with a normal metal (Ag) [15, 67]: instead of weakening the superconductivity by proximity effect, the normal overlayer increases the critical temperature. This is attributed to an enhancement of the electron screening due to the quasiparticles brought by the normal metal, and reminds that the gold layer modifies the electronic properties of niobium. In addition to induce some inverse proximity effect, the presence of gold may also reinforce dynamical Coulomb screening.

The "Bosonic" scenario

In contrast with the Fermionic scenario, the SIT can be explained as a competition between localization and Cooper pairing disregarding Coulomb interactions [35]. At the transition, the superconducting order parameter is predicted to be inhomogeneous as observed through spatial variations of the spectral gap by STS [94]. Unusually large $\Delta/(k_B T_c)$ ratios are expected [94] (up to 4 or 5). Above critical temperature, a regime of superconducting fluctuations and of preformed Cooper pairs is also expected, resulting in a noticeable depression in the DOS, the pseudogap. Temperature evolution of the superconducting DOS revealed that such a pseudogap persists relatively far from the SIT [95].

Then, the $k_F^{\mathrm{Nb}} l_{\mathrm{Nb}} \approx 1$ products of our samples (see Table 4.2) show that the niobium layer in the normal state is strongly disordered. The slight increase of the $\Delta/(k_B T_c)$ ratio together with a decrease of the critical temperature suggests that the Bosonic scenario for the SIT could apply here. Moreover, the upturn of the upper critical field B_{c2} at low temperature described in Section 4.4 goes in this direction. Indeed, this effect has already been measured in indium oxide, a superconductor where Cooper pairs become localized by disorder on the verge of the SIT [97]. This upturn of B_{c2} is attributed to the thermal fluctuations of the vortex glass, strongly pinned by the spatial fluctuations of the order parameter due to disorder [98].

Nevertheless, STS measurements (see Section 4.5) revealed an homogeneous gap, suggesting that the fluctuations of the order parameter are relatively small. This could however be sufficient to account for the upturn of B_{c2} since the effect was observed in samples far from the disorder-tuned SIT [98]. Also, one can explain the upturn of the upper critical field of our samples in light of other mechanisms leading to vortex pinning as discussed in Subsection 7.3.2. Anyhow, the fact that no detectable spatial variations of the spectral gap are measured indicates that our samples are far from the SIT. This is also confirmed by the fact that $\Delta/(k_B T_c)$ remains relatively close to the BCS value and that no pseudogap is observed in our samples as shown on Fig. 4.7.

To conclude, we think that **regarding the SIT, the samples studied in this PhD are not in the vicinity of the transition so that electrons are not completely localized and Coulomb interactions are relatively well screened.**

4.7.2 Special role of thickness

Experimental evidence

Further investigation on the SIT is of particular interest in $\mathrm{Nb}_x\mathrm{Si}_{1-x}$ films, where the disorder can be tuned not only by the thickness but also by the stoechiometry (x) and an eventual annealing (the annealing temperature being the third disorder tuning parameter). Fig. 4.12 shows that T_c is not uniquely determined by $R_\square$ in $\mathrm{Nb}_{18}\mathrm{Si}_{82}$ samples. In fact, the complete

study demonstrates the specific role of the thickness: whereas a disorder change due to either composition or annealing relates one to one T_c and $R_\square$, the same reduction of T_c can be reached for a given stoechiometry through thickness or annealing whereas the corresponding $R_\square$ is completely different. Thereby, **there is no univocal parameter to measure the level of disorder.**

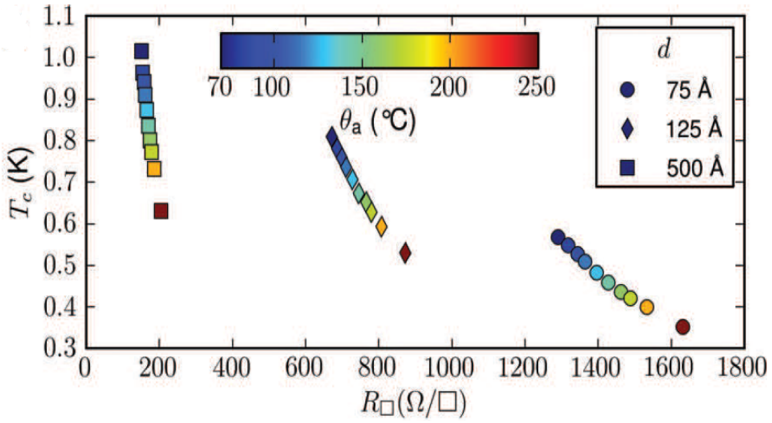

Figure 4.12: Critical temperature as a function of square resistance for several $Nb_{18}Si_{82}$ samples. Each symbol (set of aligned points) represents one thickness, and each color (from top to bottom) represents one annealing temperature θ_a. From [23].

Since neither the square resistance nor the thickness is an univocal parameter to measure the level of disorder, it is interesting to look for phenomenological models. By analyzing the data published over several decades on different materials, Ivry and coworkers [53] propose the following phenomenological scaling law for superconducting films:

$$t_s T_c = A R_\square^{-B} \tag{4.9}$$

which applies for several systems [53]. t_s is the superconducting film thickness and A and B are fitting parameters. This law confirms that the specific role of thickness on critical temperature is not enclosed in the square resistance.

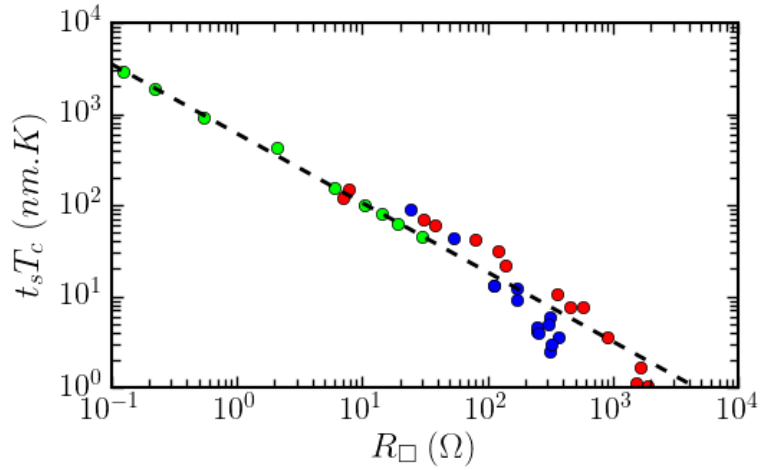

Figure 4.13: Niobium thickness t_s times critical temperature T_c versus square resistance $R_\square$ of: • Nb samples from [119] • Nb samples from [45] and • Nb\Au samples from this PhD work. Dashed line: scaling law of Eq. 4.9 with $A = 611$ and $B = 0.761$.

According to Ivry et al. [53], the fitting parameters for niobium are $A = 611$ and $B = 0.761$. We plot in Fig. 4.13 this fitting law together with experimental data taken from reported experiments ([45] which gave the fitting parameters according to Ivry *et al.* and [119]) and our own results with Nb\Au bilayers. As shown on Fig. 4.13, this scaling law applies similarly for Nb and Nb\Au samples. The small difference between these two materials suggests that the inverse proximity effect of gold slightly decreases the critical temperature of niobium. This effect will be discussed in Section 4.8.

Models for the depletion of critical temperature with thickness

It is well known experimentally that the critical temperature of a superconductor starts to decrease when its thickness becomes smaller than its coherence length, but only a few theories account for such an effect. An explanation consists in considering a non superconducting surface layer of thickness a, although there is no consensus since the existence of such a layer is neither experimentally confirmed or theoretically motivated in the literature. However in our case, one could imagine some diffusion of silicon from the substrate leading to a non superconducting NbSi alloy, or some boundary condition for the surface atoms where dynamical Coulomb screening is perturbed.

The first way to take into account such a layer consists in considering the induced proximity effect of the surface layer on the superconductor in the Cooper limit. The proximity effect is described theoretically in Subsection 2.2.3, and the relevant assumptions of the present description are as follows. The surface layer is assumed to be metallic (not insulating) at zero temperature. For the sake of symmetry, one usually considers two surface layers of thickness a on both sides of the film of total thickness t, so that the normal layer thickness is $t_N = 2a$. For simplicity, the density of states of the normal layer N_N is taken equal to the one of the superconductor N_S. Then, Eq. 2.26 leads to:

$$T_c = T_c^{bulk} e^{-\frac{d_c}{t-2a}} \tag{4.10}$$

with $d_c = \frac{2a}{N_S V_S}$, T_c^{bulk} the critical temperature of the infinitely thick superconductor and V_S its BCS pairing potential.

The second way developed by Simonin in [102] is a more general approach using Ginzburg Landau free energy with a modified boundary condition on the film surface. This leads to:

$$T_c = T_c^{bulk} \left(1 - \frac{d_c}{t}\right) \tag{4.11}$$

with $d_c = \frac{2a}{N_S V_S}$ and a approximately equal to Thomas-Fermi screening length. This result is consistent with the Cooper limit in the large thickness range and reproduces well the $T_c \propto t^{-1}$ behavior observed in different materials (see Fig. 4.14).

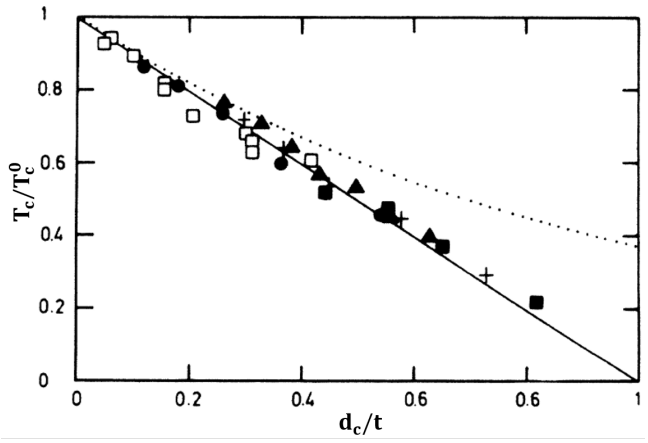

Figure 4.14: Reduced critical temperature versus reduced inverse thickness for different materials and substrates. Nb: □ ($d_c = 36$ Å) and ■ ($d_c = 22$ Å), Pb: • ($d_c = 8$ Å) and ▲ ($d_c = 20$ Å) and Bi: + ($d_c = 12$ Å). Solid line: Eq. 4.11. Dashed line: Cooper limit. From [102].

One should notice that the d_c value is substrate dependent, that is why two values are given for Nb and Pb (corresponding to two sets of experiments on different substrates). This is not surprising since disorder (through the deposition method, the substrate, etc...) can affect the critical temperature independently of the thickness. For instance, an increase of d_c together with an increase of the disorder (tuned through the composition and at constant thickness) was reported in NbSi [22].

Thereby, although there is no complete microscopical theory for this, **the thickness is a main knob to tune the critical temperature of Nb films.**

4.8 Influence of the inverse proximity effect

Since we have to deal with proximity effect, the relevant parameters are both niobium and gold thicknesses. It is important to note that **both niobium and gold thicknesses are small compared to the coherence length: $t_{\mathrm{Au}}, t_{\mathrm{Nb}} \ll \xi_{GL}$.** Then, the models presented in Subsection 2.2.3 to describe a normal metal-superconductor (NS) bilayer can be applied, and the order parameter should be nearly constant with respect to the perpendicular direction to the films.

The other parameter playing an important role in the proximity effect is the interface resistance between the layers. The two extreme limits of interlayer interface resistance correspond to the Cooper limit (perfect interface) and to a superconducting layer unaffected by the presence of the normal layer (opaque interface). Fominov model encloses the intermediate values of interface resistance.

Combined effect of thickness and proximity effect

Independently from the proximity effect, the thickness of the superconducting layer has an influence on its critical temperature (see Subsection 4.7.2). Thus, Simonin's theory gives the critical temperature of a bare niobium layer as a function of its thickness t_{Nb}:

$$T_c^{\mathrm{Nb}}(t_{\mathrm{Nb}}) = T_c^{bulk}\left(1 - \frac{d_c}{t_{\mathrm{Nb}}}\right) \tag{4.12}$$

From this, Cooper limit and Fominov model (see Subsection 2.2.3) give the critical temperature of the NS bilayer obtained by depositing a t_{Au} thick layer of gold on top of niobium. The superconducting layer critical temperature T_c^S in Eq. 2.26 (Cooper limit) and 2.28 (Fominov model) has to be replaced by the thickness dependent niobium critical temperature $T_c^{\mathrm{Nb}}(t_{\mathrm{Nb}})$.

In the Cooper limit, this leads to:

$$T_c^{\mathrm{Nb\backslash Au}} = T_c^{\mathrm{Nb}}(t_{\mathrm{Nb}})\ \exp\left(-\frac{N_{\mathrm{Au}}t_{\mathrm{Au}}}{N_{\mathrm{Nb}}t_{\mathrm{Nb}}}\frac{1}{N_{\mathrm{Nb}}V_{\mathrm{Nb}}}\right) \tag{4.13}$$

where N_{Nb} and V_{Nb} must fulfill the BCS relationship $T_c^{\mathrm{Nb}}(t_{\mathrm{Nb}}) = 1.13\Theta_D e^{-1/(N_{\mathrm{Nb}}V_{\mathrm{Nb}})}$ where Θ_D is the Debye temperature.

Finally, N_{Au} and N_{Nb} may depend respectively on t_{Au} and t_{Nb}. In the following, we will assume for simplicity that for samples where $t_{\mathrm{Au}} = t_{\mathrm{Nb}}$ the ratio $N_{\mathrm{Au}}/N_{\mathrm{Nb}}$ is constant and equal to the bulk value used to compute Eq. 4.1.

Fig. 4.15 displays the critical temperature as a function of the inverse thickness for samples where $t_{\mathrm{Au}} = t_{\mathrm{Nb}}$ and the theoretical predictions of Simonin's law, Cooper limit and Fominov model. Simonin's law gives an upper bound for the critical temperature of the NS bilayer (corresponding to the case where the S layer remains unaffected by proximity effect). Cooper limit gives a lower bound corresponding to the case of perfect interface between N and S layers (maximal influence of the proximity effect). In between these two extreme cases, Fominov model gives the critical temperature as a function of the interface resistance.

T_c^{bulk}, d_c and $\mathcal{T}$ (characterizing the interface transparency) are subject to fluctuations in the fabrication process. Additionally, t_{Nb} and t_{Au} probably deviate from their nominal values, that's why one can only conclude that the critical temperature of the samples is roughly determined by the niobium thickness through Simonin's law, from which it is slightly lowered by inverse proximity effect. This is confirmed by the comparison between the critical temperature of our samples and of Nb layers taken from the literature as shown on Fig. 4.13. Furthermore, this is also confirmed by our tunneling spectroscopy experiments. Indeed, in the limit of large

interface resistance, the gold (normal) layer must show a metallic density of states and the niobium (superconducting) layer must remain roughly unaffected by the proximity effect, while in the limit of small interface resistance, both layers must exhibit a superconducting DOS [38]. Thus, the **superconducting gaps of the order of $1.76k_BT_c$ probed by STS on the surface of gold** (for experimental data see Section 4.5), **are an evidence of small interface resistance.** Additionally, the compensation of a large $\Delta_0/(k_BT_c)$ ratio in the superconducting layer by a poor interface is excluded since $\Delta_0/(k_BT_c) = 1.83$ [81] in niobium.

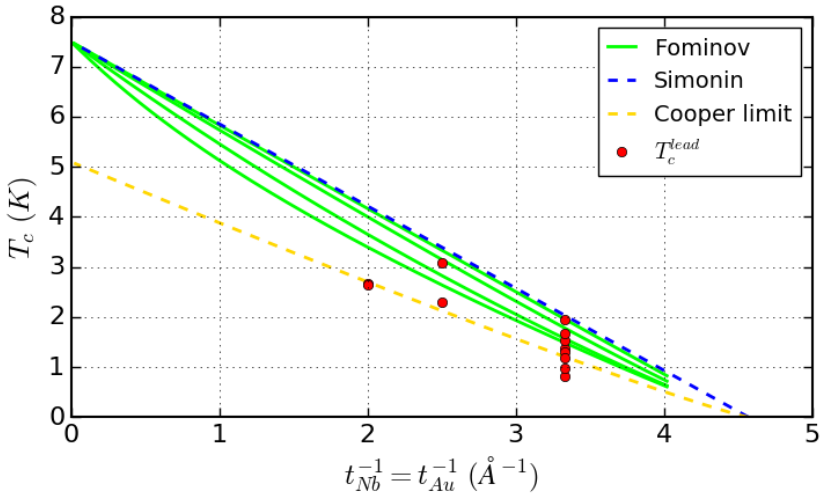

Figure 4.15: Critical temperature of the leads as a function of inverse niobium thickness for samples where $t_{\mathrm{Nb}} = t_{\mathrm{Au}}$. The blue dashed line is Simonin's curve for niobium computed with Eq. 4.12 with $d_c = 22$ Å and $T_c^{bulk} = 7.5\ K$. The yellow dashed line is the Cooper limit computed from Eq. 4.13 with $\Theta_D = 275\ K$ (typical value for Nb [43]). The solid lines represent Fominov model with intermediate interface resistance values computed from Eq. 2.28 with T_c^S given byEq. 4.12, $\Theta_D = 275\ K$, $N_0^{\mathrm{Au}} = 5.8\ 10^{46}\ J^{-1}.m^{-3}$, $N_0^{\mathrm{Nb}} = 5.6\ 10^{47}\ J^{-1}.m^{-3}$, $\lambda_F = 5\ \mathring{A}$ and $\mathcal{T} = 0.001$; 0.005 ; 0.02 and 0.05 from top to bottom.

The inverse proximity effect slightly decreases the critical temperature of the Nb layer alone, which depends on the Nb thickness in first approximation.

4.9 Conclusion

Disorder, geometry and inverse proximity effect have an influence on the critical temperature of the nanowires studied in this PhD. Specifically, the superconducting properties of the samples are efficiently tuned by their thickness. Because the latter is small compared to the coherence length and the interface resistance between gold an niobium is also small, the bilayers behave as one superconducting material as confirmed by upper critical field and spectroscopy measurements. Disorder induces mechanisms weakening superconductivity but the samples remain far from the superconductor-insulator transition so that the DOS is spatially homogeneous. Finally and unexpectedly, the nanowire width turns out to affect the critical temperature.

Chapter 5

Out of equilibrium superconductivity driven by a supercurrent flow in Nb\Au nanowires

Contents

The ability to tune the superconducting properties with the width and the thickness of the nanowires was introduced in the previous chapter. On the one hand, the total thickness t had to be small for several reasons. Firstly, whether to probe or modify the properties of superconducting nanowires by STM/STS or Scanning Critical Current Microscopy (SCCM), the tunneling junction is located on the surface of the sample so lowering t allows to be more sensitive to the bulk and not only to the surface properties. Furthermore, it helps to prevent overheating when the critical current is reached (a Joule power $R_N I_c^2$ is then dissipated in the normal wire of resistance R_N). Indeed, the superconducting gap Δ_0 decreases with t (Table 4.3) and according to Ginzburg Landau (Eq. 3.1b) and Kupryanov Lukychev (Eq. 2.19) depairing current densities, $R_N I_c^2 \propto \Delta_0^3 t$, so lowering t reduces Joule overheating. On the other hand, a small width compared to London penetration depth ensures homogeneous current density.

This chapter describes measurements of thin superconducting nanowires critical current. The results are then compared to Usadel theory in the limit of uniform current density. Then, the modification of the superconducting order by a supercurrent flow is investigated by STS, up to values as close as possible to the critical current.

5.1 Evolution of the critical current with temperature

Fig. 5.1 shows typical current-voltage characteristics for different temperatures T near the nanowire critical temperature T_c^{nw}. The wire current I_{wire} is successively ramped up and down while the wire voltage V_{wire} is monitored. For $T < T_c^{nw}$, during the rising ramp, a first voltage jump occurs for a I_{wire} value defined as the nanowire critical current I_c. Then, a resistive behavior is observed ($V_{wire} \approx R_N^{nw} I_{wire}$ where R_N^{nw} is the nanowire normal state resistance, see

Fig. 4.2). A second voltage jump occurs at a higher current that corresponds to the leads critical current. For larger I_{wire}, V_{wire} equals $(R_N^{lead} + R_N^{nw})I_{wire}$ where R_N^{lead} is the leads normal state resistance. During the decreasing ramp, the wire voltage goes down to zero for a I_{wire} value defined as the retrapping current $I_r \leq I_c$. For temperatures close to T_c this hysteretic behavior is washed out, $I_c = I_r$ and the jump at I_c becomes less steep.

For $T \ll T_c^{nw}$, the $I_{wire}(V_{wire})$ characteristics is very difficult to monitor as soon as I_c is exceeded, because the bath temperature T (temperature of the sample holder) cannot be maintained at a constant value since Joule overheating overcomes the cooling power at the sample holder. Near T_c^{nw}, the currents at play and therefore the power dissipated are far smaller, and the cooling power is also higher. In this respect, I_r quickly saturates when the temperature is lowered because the local temperature is higher than T during the decreasing ramp. I_c however, can be measured down to low temperatures: I_{wire} is ramped up and when V_{wire} overcomes a threshold value (slightly above noise level), the current is immediately set back to zero and the operation is repeated several times to perform statistical averaging.

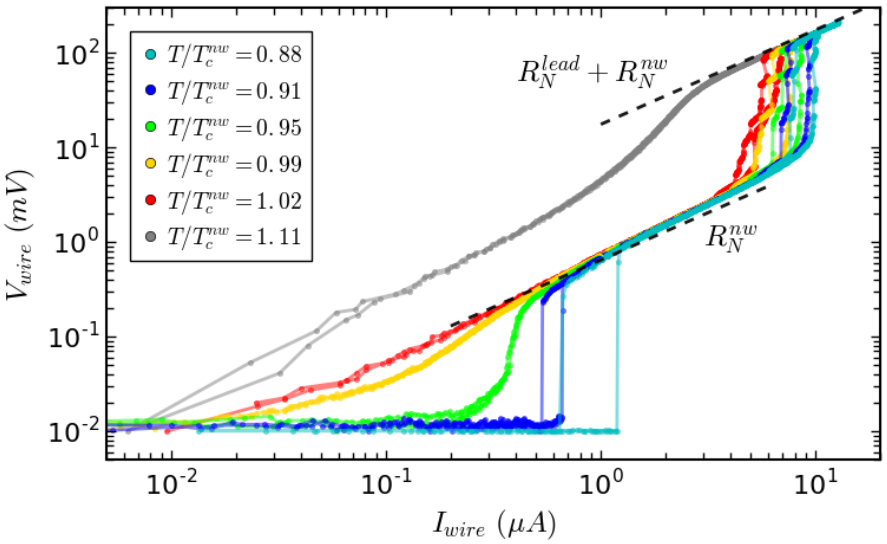

Figure 5.1: Current-voltage characteristics for different temperatures near T_c^{nw}. The current is raised and decreased in order to show the hysteretic loop. Black dashed lines correspond to the resistive behaviors associated to the total normal state resistance $R_N^{lead} + R_N^{nw}$ and the resistance attributed to the nanowire R_N^{nw}. Sample N07.

In the following we will only consider the critical temperature of the nanowire and we define $T_c = T_c^{nw}$. Fig. 5.2 presents the reduced critical current I_c/I_c^0 (where I_c^0 is the extrapolation of I_c to $T = 0$) versus reduced temperature T/T_c in the absence of any perturbation due to the STM (withdrawn tip). The numerical solution of Usadel equations in the presence of inelastic scattering Γ_{in}, whose model is presented in Subsection 2.2.2, fits well the measured temperature dependence of I_c for finite Γ_{in}. In addition, experimental data for all samples merge on an universal curve, which makes the measurement of the critical current a thermometer for the electronic temperature.

One should thus discuss the validity of the model presented in Subsection 2.2.2 leading to the numerical computations performed here. Both homogeneous current distribution and absence of dissipation due to vortex flow must be ensured. London penetration depth is given by $\lambda_L = \sqrt{\hbar/(\pi\mu_0\sigma_N\Delta_0)}$. For films much thinner than λ_L, the effective penetration depth is

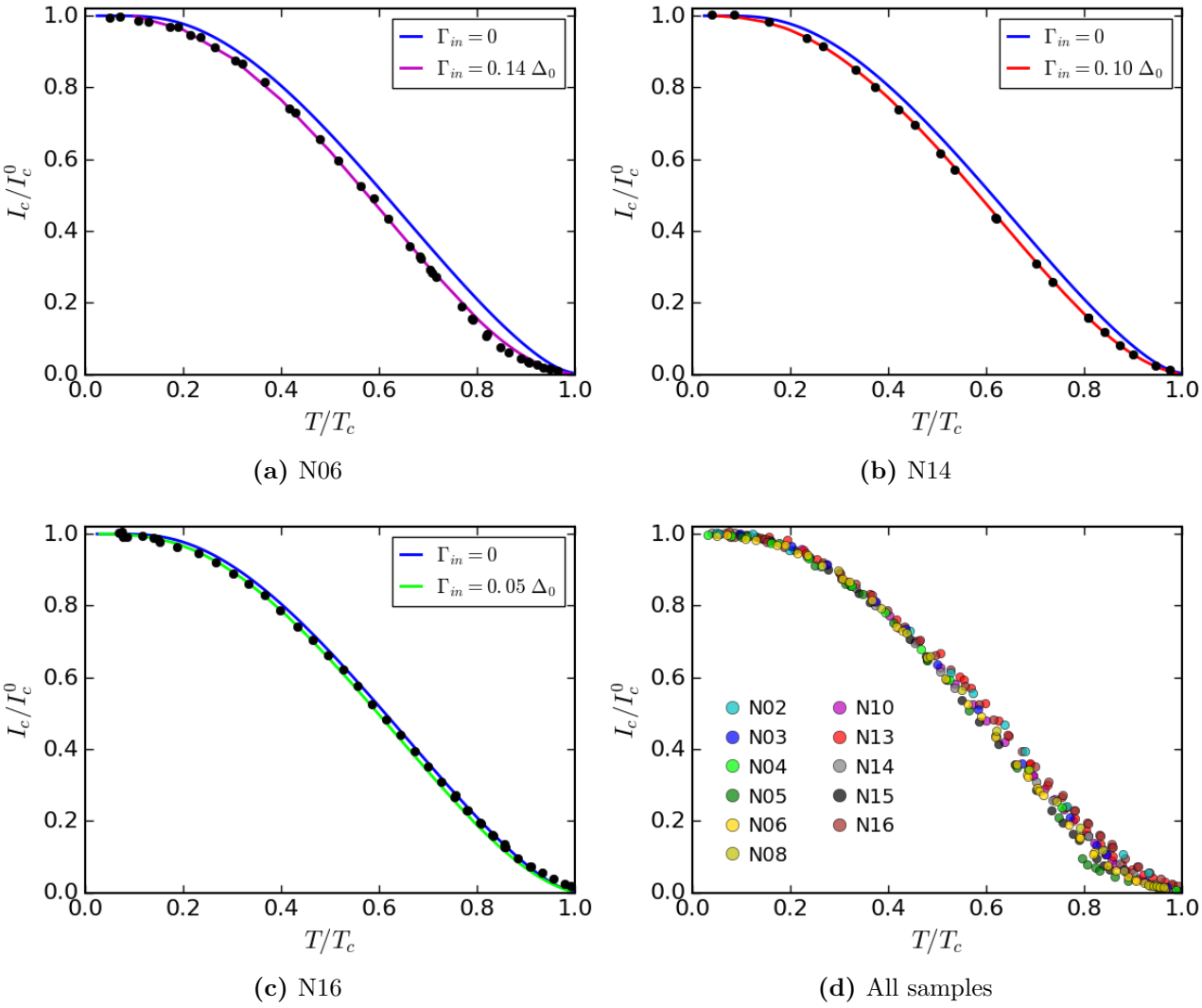

(a) N06 **(b)** N14 **(c)** N16 **(d)** All samples

Figure 5.2: Reduced critical current I_c/I_c^0 versus reduced temperature T/T_c. Solid lines: numerical solution of Usadel equations for several values of inelastic scattering Γ_{in}.

increased by a factor λ_L/t [63]:

$$\begin{aligned} \lambda_{eff} &= \lambda_L \coth\left(\frac{t}{\lambda_L}\right) \\ &\approx \frac{\lambda_L^2}{t} \quad \text{if } t \ll \lambda_L \end{aligned} \tag{5.1}$$

Table 5.1 contains computed values for all the samples. The effective penetration depth is well larger than both width and thicknesses of all samples, ensuring homogeneous current distributions.

In contrast, the theoretical critical width below which no vortex can penetrate in an infinitely long wire is $4.4\xi_{GL}$ [73] (this result valid for long wires with respect to ξ_{GL} is known as the *Likharev limit*). Although the model developed in [73] is subject to deviations depending on whether the vortices are generated by an external magnetic field or by a supercurrent (in the latter case the critical width becomes larger than $4.4\xi_{GL}$), our 300 nm wide nanowires fulfill the inequation $w > 4.4\xi_{GL}$ (see the estimation of the coherence lengths in Table 5.1) so the nucleation of vortices under the action of current cannot be fully discarded.

Besides, the values of Γ_{in} required to fit the $I_c(T)$ curves ($\Gamma_{in} \sim 0.1\Delta_0$) are larger than the values extracted from the Density Of States (DOS) probed by STS ($\approx 0.05\Delta_0$, see Section 4.5).

Moreover, on Fig. 5.1 and when T/T_c approaches 1, V_{wire} increases with current before the transition ($T/T_c = 0.91$ and $T/T_c = 0.95$ curves), which suggests some dissipation in the superconducting state below I_c. If such dissipation lowers the measured I_c, this would be compatible with an overestimate of Γ_{in} since the predicted depairing current density decreases together with Γ_{in}. One could therefore blame vortex flow and this topic will be discussed in Subsection 7.3.2.

Sample	N01	N02	N03	N04	N05	N06	N08	N10	N13	N14	N15	N16
J_c^0 (MA.cm^{-1})	17	6.7	3.2	3.4	0.87	1.0	2.5	0.83	0.38	4.4	1.0	0.57
J_c^0/J_{dp}^0	0.82	0.68	0.75	0.75	0.69	0.63	0.74	0.67	0.62	0.85	0.80	0.70
λ_{eff} (μm)	1.65	4.04	8.37	7.96	38.2	32.5	14.6	40.0	72.3	10.5	51.4	60.9
ξ_{GL} (nm)	16	18	29	29	35	33	28	35	40	24	28	36

Table 5.1: Critical current parameters: J_c^0 is the experimental critical current density at low temperatures, J_{dp}^0 is the theoretical depairing current density at zero temperature (Eq. 2.19), λ_{eff} is the effective penetration depth (Eq. 5.1) and ξ_{GL} the coherence length (Eq. 4.4). For all samples, the nanowire width is 300 nm. All leads are 2.3 μm wide except N08's whose leads width is 4 μm.

The measured critical current allows to extract the critical current density J_c with non negligible uncertainty since thickness is not very accurately known[1]. The experimental critical current density at low temperatures J_c^0 is close to the zero temperature theoretical depairing current density J_{dp}^0 for all samples as shown in Table 5.1. Indeed, J_c^0 is in the range $[0.62; 0.85] \times J_{dp}^0$. Firstly, the uncertainty over thickness explains the scattering of this value: for instance an uncertainty of ≈ 0.5 nm over the two layers thicknesses of a $Nb_{3nm}\backslash Au_{3nm}$ leads to an uncertainty of about 17 % over J_c^0. On the other hand, the fact that J_c^0 is always smaller than J_{dp}^0 is often explained in the literature by fluctuations of the minimum cross section of the wire, since both width and thickness are subject to fluctuations due to roughness. This explanation can account for an experimental J_c^0 value smaller than the depairing current density J_{dp}^0 because in this case the critical current density is only reached locally in the minimum cross section. Then, if such a weak link was present in the nanowire, the reduction of the critical current by quasiparticle injection must be driven by the distance between the injection position and the weak link. Nonetheless, this does not correspond to experimental observations, since what matters in Fig. 6.4 is the distance between the injection position and the leads. The hypothesis of homogeneous current distribution made from the estimate of the penetration depth will be confirmed by measurements of the DOS at different positions (see Fig. 5.5). Then, the difference between J_c^0 and J_{dp}^0 cannot be explained either by a current density locally larger at the edges. By contrast, a systematic overestimate of the thickness due to an eventual seedlayer during the deposition could account for such a difference.

The temperature dependence of the reduced critical current merge on an universal curve which provides a reliable thermometer for the electronic temperature. It is also in good agreement with Usadel predictions for the depairing current.

[1]To get rid of this uncertainty, the authors of [93] use the resistance ratio between room and cryogenic temperatures. Because of the gold capping layer, this ratio is close to 1 in Nb\Au samples and is therefore unexploitable. Furthermore, the uncertainty over thickness mainly concerns the niobium layer: because it is a refractory metal, its evaporation is performed at very high temperatures and also faster than for other materials, which makes the evaporation time very short and therefore lowers the accuracy over the thickness. One would then be interested in the resistance ratio of the niobium only, which is difficult to disentangle from the one of the bilayer.

5.2 Modification of the density of states by a supercurrent flow

5.2.1 Local measurement close to the critical current

The superconducting order is affected by a supercurrent flow, so that when the critical current is reached superconductivity is destroyed. Usadel equation (Eq. 2.20) predicts how the superconducting properties determined by the pairing angle θ are altered by some depairing energy γ. In the superconducting state and in the absence of external magnetic field, Δ is related to θ by Eq. 2.4 and the wire current I_{wire} is related to γ through Eq. 2.18.

The dependence of the DOS as a function of the wire current is investigated here to test the validity of this model. Fig. 5.3a shows the differential conductance for different wire currents of sample N03 at $T = 100$ mK. The low noise and the quality of the junction allowed here to perform measurements for values of I_{wire} very close to I_c^0 (the critical current in the absence of tunnel current between the STM tip and the sample).

Within Usadel framework, the differential conductance depends on four parameters: γ, Δ, Γ_{in} and T_{eff}. Indeed, the density of states of the sample is proportional to $\Re[\cos\theta]$ and is determined by a set of γ, Δ and Γ_{in} solution of the self consistent equations Eq. 2.20 and 2.4. The differential conductance (Eq. 1.8) is then the convolution of the density of states with a thermal broadening function depending on the effective temperature T_{eff} of the tunnel junction. For $I_{wire} = 0$, γ can be set to 0 and one recovers the same analysis than in Section 4.5, leading to $\Delta_0 = 370$ μV, $\Gamma_{in} = 0.02\Delta_0$ and $T_{eff} = 556$ mK. As discussed before, T_{eff} is larger than T and this can be related to both a finite energetic resolution or a non BCS behavior. However, we will assume in the following that T_{eff} is independent of I_{wire}. Similarly, whether it reflects some inelastic scattering of the quasiparticles or some interaction with the electromagnetic environment (see Subsection 1.2.2 and [88]), Γ_{in} will be taken constant. Then, only γ and Δ

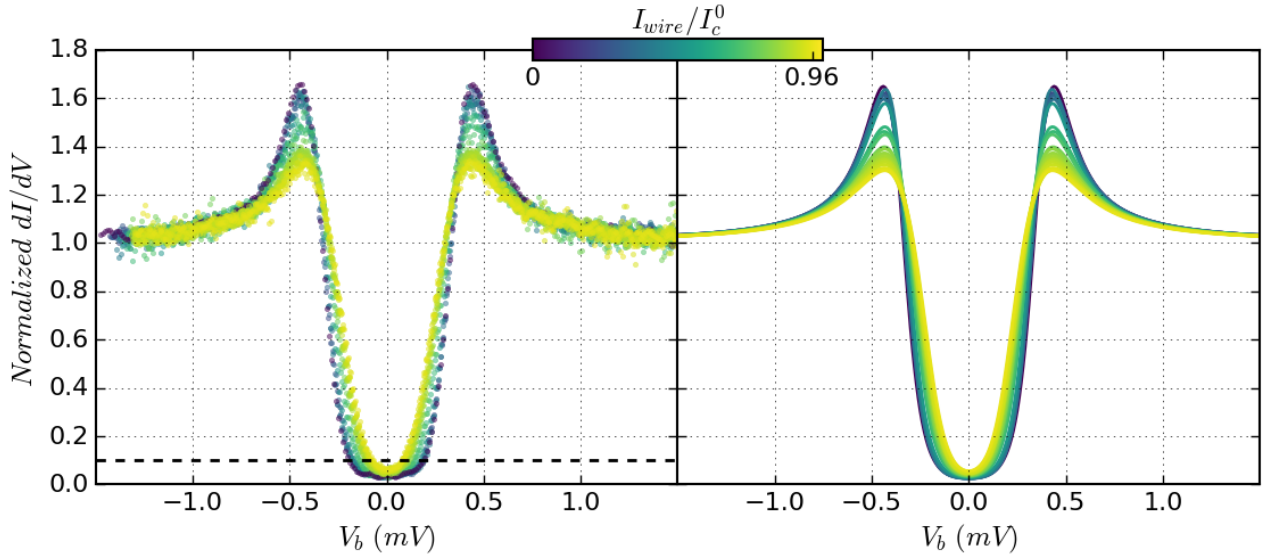

Figure 5.3: DOS as a function of the supercurrent flow. *Left panel:* Normalized differential conductance as a function of bias voltage of sample N03 for different wire currents I_{wire} at 100 mK. Dashed horizontal line: threshold used to extract Δ_G plotted in Fig. 5.4b. *Right panel:* Theoretical fits: the $I_{wire} = 0$ spectrum (for which γ is set to 0) leads to $\Gamma_{in} = 0.02\Delta_0$ and $k_B T_{eff}/\Delta_0 = 0.13$. Γ_{in} and T_{eff} are then fixed to fit all the spectra with γ and Δ as free parameters. I_c^0 is the zero temperature critical current in the absence of any perturbation due to the STM tip.

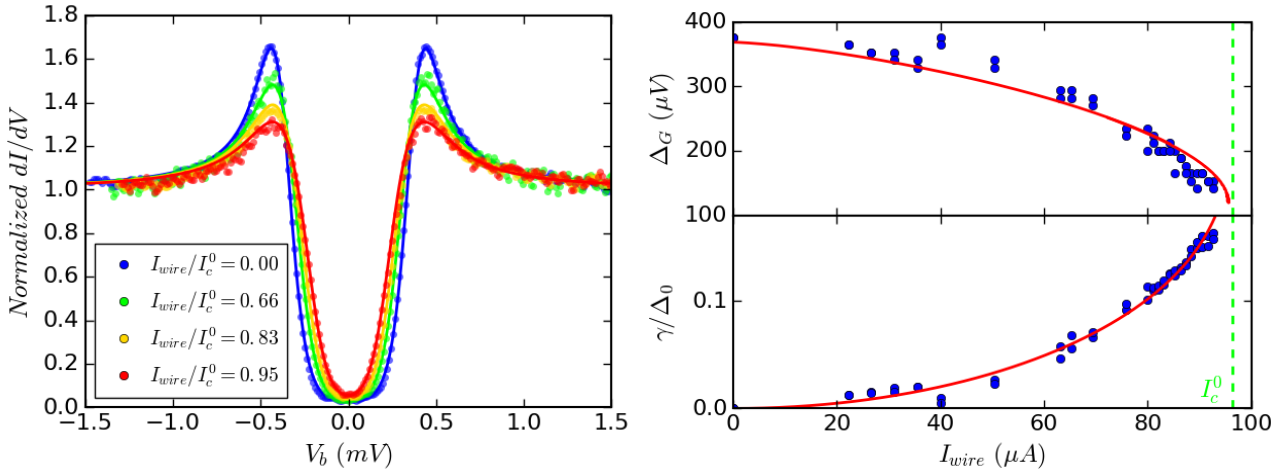

(a) (b)

Figure 5.4: Depairing energy and spectral gap as a function of the supercurrent flow. (a) Dots: Normalized differential conductance as a function of bias voltage of sample N03 for different wire currents. Solid line: Theoretical fits (see legend of Fig. 5.3). (b) *Top panel:* Spectral gap Δ_G as a function of wire current I_{wire}. Solid line: theoretical behavior (Eq. 2.16). *Bottom panel:* Depairing energy γ as a function of wire current. Solid line: Eq. 2.18 with $\Gamma_{in}/\Delta_0 = 0.02$, $T = T_{eff} = 556$ mK and $I_\gamma = 186$ μA. Dashed vertical line: zero temperature critical current in the absence of tunnel current $I_c^0 = 96.3$ μA.

will be taken as free parameters to fit the experimental data for $I_{wire} \neq 0$. The inferred fits reproduce well the $dI/dV(V_b)$ measurements as shown on Fig. 5.3 and Fig. 5.4a.

The $\gamma(I_{wire})$ dependency extracted from the fits is shown on bottom panel of Fig. 5.4b. Usadel prediction is given by Eq. 2.18 and depends notably on Γ_{in} and on the temperature of the sample T. Since the function $U_s(\gamma)$ is almost independent of temperature and inelastic scattering in the range $k_B T \ll \Delta_0$ and $\gamma < 0.2$ (as is Δ), the solution presented here takes the values given by the $I_{wire} = 0$ fit: $\Gamma_{in} = 0.02\Delta_0$ and $T = T_{eff}$. By contrast, Usadel prediction of Eq. 2.18 is sensitive to the value of I_γ and compares well to experimental data for $I_\gamma = 186$ μA. For $\Gamma_{in} = 0.02\Delta_0$ as deduced by the DOS measurements when $I_{wire} = 0$, the numerical solution of Usadel equations leads to $I_c^0 = 0.51 I_\gamma$, which corresponds to $0.51 I_\gamma = 94.9$ μA. Consequently, this value extracted from fits of the normalized conductance in the presence of supercurrent is in very good agreement with the measured critical current at low temperatures $I_c^0 = 96.3$ μA.

Finally, one can extract the spectral gap Δ_G (which is different from Δ in the presence of depairing). To do so, we define Δ_G as the energy range for which the DOS is lower than the threshold plotted in dashed line on Fig. 5.3a. The chosen threshold leads to $\Delta_G = \Delta_0$ for $I_{wire} = 0$ as predicted by theory and the resulting $\Delta_G(I_{wire})$ dependency is plotted on top panel of Fig. 5.4b. The numerical solution of Usadel equations and Eq. 2.16 give the theoretical dependency of Δ_G. This simple experimental determination of the spectral gap follows well the expected behavior.

5.2.2 Dependence on the position across the section

The STS technique is especially interesting to probe locally the DOS at different positions across the width of the nanowire. We will therefore perform the above experiment at two different positions to extract the local depairing energy.

Fig. 5.5a shows the differential conductance as a function of wire current at two different positions. First of all, one can notice that the superconducting gap is slightly larger at the

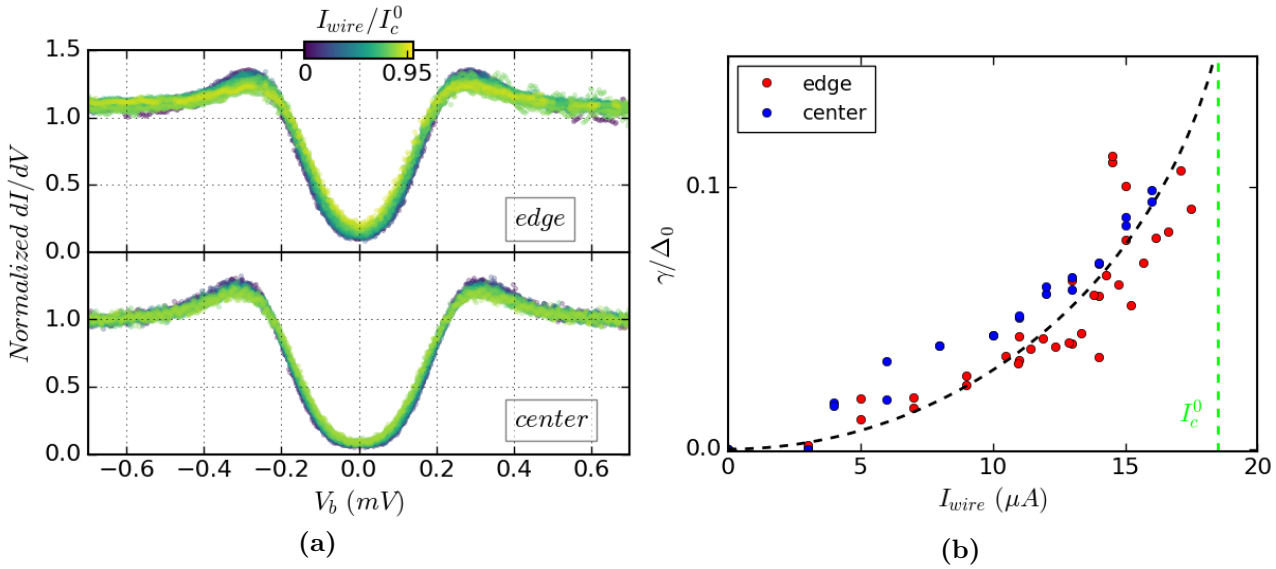

Figure 5.5: Influence of the position across the wire width. (a) Normalized differential conductance as a function of bias voltage of sample N06 at 100 mK at two different positions. *Top panel:* edge of the nanowire where $\Delta_0 = 205$ μeV. *Bottom panel:* center of the nanowire where $\Delta_0 = 230$ μeV. (b) Depairing energy γ as a function of wire current. Solid line: Eq. 2.18 with $\Gamma_{in}/\Delta_0 = 0.03$, $k_BT/\Delta_0 = 0.21$ and $I_\gamma = 39$ μA. Dashed vertical line: zero temperature critical current $I_c^0 = 18.5$ μA.

center of the nanowire ($\Delta_0 = 230$ μV) than at the edge ($\Delta_0 = 205$ μV). As discussed in Section 4.5, althoug remaining rather small (comparable to the energetic resolution), such a difference is probably due to local inhomogeneities of the DOS. Here, such an inhomogeneity may be caused by a thickness difference between the center and the edge of the nanowire, since both the etching and deposition processes can lead to round edges.

Unfortunately, it revealed more difficult to perform the experiment than in previous paragraph. For wire currents close to critical current, the superconducting state is metastable, so the sample switches quickly to the normal state while measuring the $dI/dV(V_b)$. To overcome this difficulty, we used another measurement strategy. Instead of acquiring the full $dI/dV(V_b)$ curve at a fixed I_{wire}, we recorded the differential conductance at a given bias voltage value for all wire currents.[2] Finally, this sample (N06) is thinner than the one of previous paragraph (N03), so that the DOS presents lower coherence peaks and more rounded DOS shape at subgap energies. Therefore, the wire current affects less the differential conductance, which provides less features for the fit and the extraction of γ.

Despite the Δ_0 difference between the center and the edge of the nanowire, the extracted depairing energy versus wire current dependency is similar. This confirms that the current distribution is homogeneous. Indeed, if it was not the case, one would expect that current piles up at the edges, so that the depairing energy would be larger there, which is not what we observe.

Furthermore, the similar evolution of the depairing energy at different positions shows that there is no weak link within the nanowire: within experimental accuracy, when the transition to the normal state driven by a supercurrent occurs, the depairing current density is reached everywhere. This observation will be interesting when we will trigger such a transition with

[2]This is done by applying an initial tunneling setpoint before freezing the feedback loop (to keep constant tunneling resistance) like in a conventional spectroscopy measurement. The bias voltage is then changed and set to the value at which the dI/dV will be recorded while ramping I_{wire}. The limitation of this technique is now the response time of the lock-in used to record the differential conductance.

the STM tip, the weak link being in this case under the tip.

We found a excellent agreement with Usadel predictions for the DOS in our Nb\Au nanowires. In particular, the agreement persists up to the depairing current and at different positions.

5.2.3 Discussion of the results and future prospects

By contrast with Anthore experiment [5] presented in Section 3.2, Coulomb blockade has been neglected. Also, finite temperature effects are not taken into account. On the one hand, Anthore *et al.* performed measurements at a lower phonon bath temperature (the temperature given by the thermometer): 25 mK while in our case it is 100 mK. Thus, the cooling of electrons is more efficient in our experiment, especially since the effective temperature of the STM tip electrons is more likely to be around 300 mK as discussed in Subsection 1.2.2. On the other hand, while the probe electrode is thermally isolated from the larger contact pads by superconducting connections in [5], our STM tip is metallic and therefore well thermally coupled to the cold parts of the cryostat. Finally, our energetic resolution is probably not good enough to be sensitive to a dependence of T_{eff} on V_b due to Coulomb blockade (because T_{eff} is large and also because STS is much more sensitive to mechanical vibrations than lithographed tunnel junctions employed in [5]).

Anthore *et al.* demonstrated the consistency of Usadel theory upon both the application of a magnetic field and a supercurrent flow. Moreover, they also accounts for Coulomb blockade and finite temperature effects. Their experiment was performed on aluminum with larger thickness, larger mean free path ($l \approx 10$ nm) and larger coherence length (approximately equal to the width) than in our case. Unfortunately, they were not able to record differential conductance for I_{wire} larger than $80\% I_c^0$, and the use of lithographed tunnel junction prevent from measuring the DOS at different positions. Thus, our experiment extends the experimental validity of Usadel theory to wire current values closer to I_c^0. What's more, we introduced finite values of Γ_{in} which account well for the measured $dI/dV(V_b)$ curves and I_γ. Finally, the spatial resolution allowed to probe the DOS in different positions. Then, a future prospect could be to probe the DOS in different positions where a change is expected: either because of an non homogeneous current distribution (for instance in a wire wider than λ_L) or because of variations of Δ_0 (for instance in a disordered superconductor or in the presence of vortices[3]).

5.3 Computation of the thermal dependence of the spectral gap at critical current

The numerical solution of Usadel equations gives the order parameter Δ as a function of T, γ and Γ_{in}. Eq. 2.18 translates the depairing energy in wire current and Eq. 2.16 gives the spectral gap as experimentally checked in previous paragraphs.

A striking behavior is then foreseen by Usadel equations when extracting Δ_G for $I_{wire} = I_c(T)$. As shown on Fig. 5.6, **the spectral gap at critical current is predicted to be non monotonous as a function of temperature.** In the absence of depairing however, $\Delta_G = \Delta$ and ones recover the conventional BCS behavior.

Unfortunately, this theoretical behavior could not be experimentally addressed during the course of this PhD. Although such a measurement is complex to perform (because of the

[3]Vortices would indeed induce the largest Δ_0 variations (since $\Delta_0 = 0$ in the core), but it makes the theoretical description more complex.

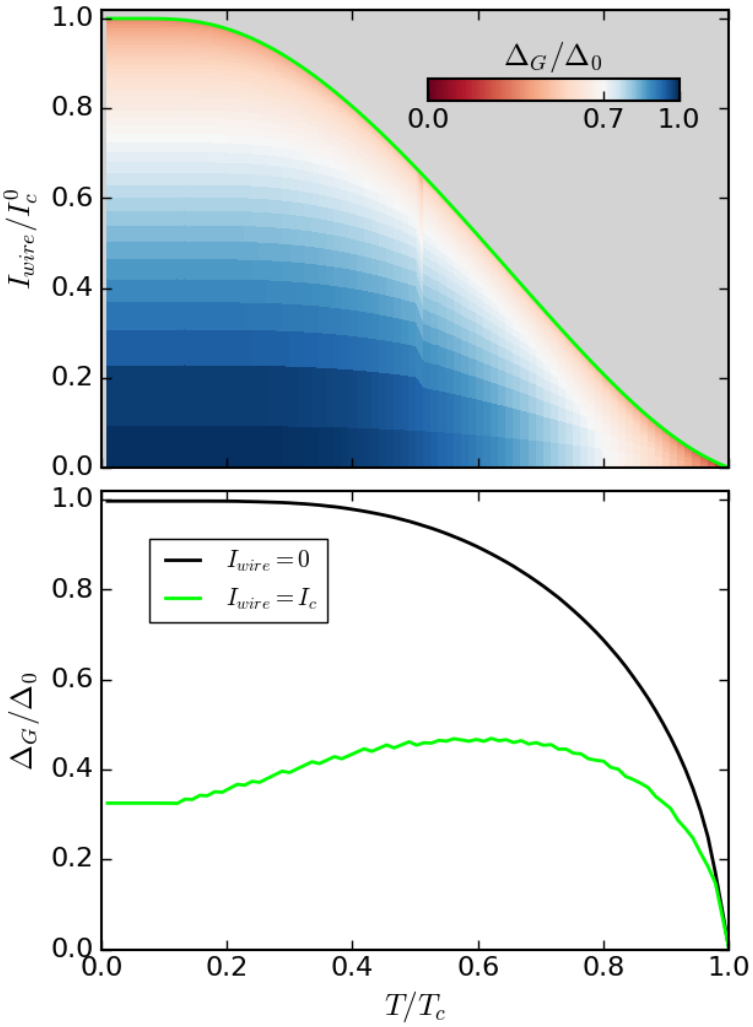

Figure 5.6: Non monotonicity of spectral gap at critical current. Numerical solution of Usadel equations for $\Gamma_{in} = 0$. *Top panel:* Spectral gap as a function of wire current and temperature. *Bottom panel:* Spectral gap as a function of temperature in the absence of wire current (Δ_G is then equal to the order parameter) and at critical current.

metastability of the superconducting state close to critical current and the good tunnel junction quality required to get exploitable data), forthcoming experiments could check this prediction.

Chapter 6

Out of equilibrium superconductivity driven by tunnel injection of quasiparticles in Nb\Au nanowires

Contents

In addition to allow spatially resolved tunneling spectroscopy, the STM technique provides a three dimensional control of the tunnel junction with an atomic resolution. The STM tip height modifies the tunnel resistance allowing to tune independently the setpoints parameters I_t and V_b. The control of its position on the surface of the sample provides a spatially resolved injector of quasiparticles. Notably, in thin and narrow wires, the density of quasiparticles injected by the tip is sufficiently high to cause measurable perturbations. This chapter addresses the role of the perturbations induced by the STM on the critical temperature and the critical current of superconducting Nb\Au nanowires. Then, a model of heat diffusion by quasiparticles and phonons is developed. Finally, the physical interpretation of superconducting field effect transistors is discussed.

6.1 Modulation of the critical temperature

Fig. 6.1 shows the resistance as a function of temperature of a $Nb_{3nm}\backslash Au_{3nm}$ nanowire for different tunneling currents injected by the tip. The blue curve corresponds to the case where

the tip is withdrawn and therefore no tunneling current is injected. As the tunneling current I_t injected in the central part of the nanowire (point A of the image) is increased, while maintaining a constant voltage bias V_b, the superconducting transition is shifted to lower temperatures. Note that the tunneling quasiparticle injection only affects the lowest temperature transition. When the injection is realized in a less constrained area (point B of the image) almost no change is observed compared to without injection. As a consequence, it first confirms that the plateau corresponds to the nanowire normal resistance (as discussed in Fig. 4.2) and further that the injection occurs only under the tip, making it a perfect tool to study the diffusion of quasiparticles. Finally, this shows that the leads can be considered as good reservoirs, and this approximation will be discussed later.

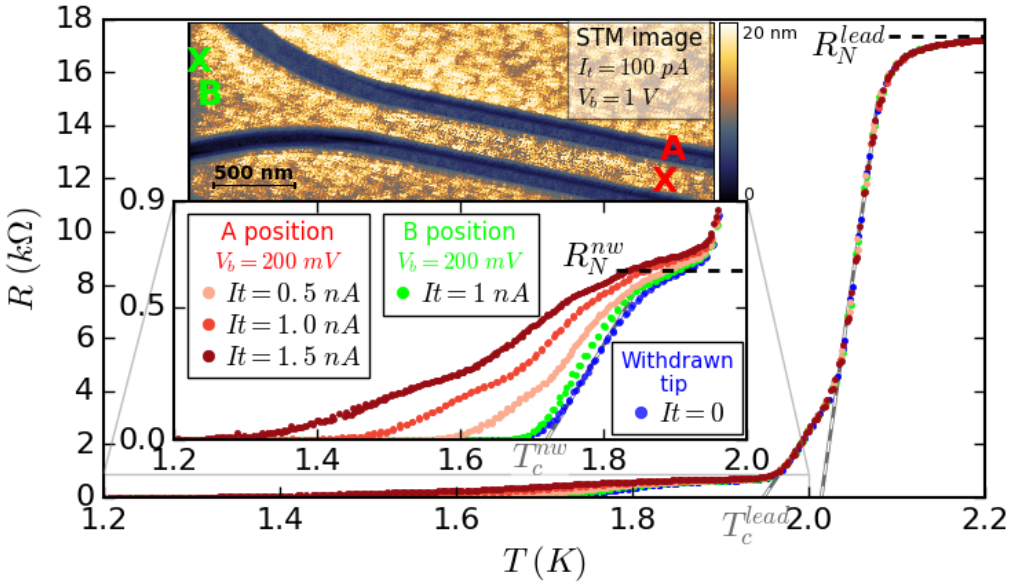

Figure 6.1: Resistance versus temperature for different tunneling currents. *Inset:* STM image of the nanowire for $I_t = 100$ pA and $V_b = 1$ V tunneling setpoint. A and B indicate the positions of the tunneling current injection I_t. *Curves:* Resistance versus temperature of sample N07 for no current injection in blue and injection at B-position in green (superimposed right curves), and for current injection at A-point (red) from left to center: $I_t = 1.5$ nA, 1.0 nA and 0.5 nA. For all curves, $V_b = 200$ mV.

Here, T is the temperature of the sample holder measured by the RuO thermometer glued on it. The fact that the measured T_c^{nw} is lowered under quasiparticle injection suggests that if a temperature can be defined in the nanowire (assumption of quasi equilibrium), it is locally higher than T when quasiparticles are injected in it. Therefore we will call T the *bath temperature* in the following. We will write it T_b in order to stress that its value only gives information about the temperature of the sample holder. Indeed, under certain conditions (as in Fig. 6.1) the nanowire is not in thermal equilibrium with the sample holder.

Tunneling injection of quasiparticles reduces the nanowire critical temperature.

6.2 Drastic decrease of the critical current

Fig. 6.2a displays the critical current measured under quasiparticle injection at one fixed position (in the middle of the nanowire) for various tunneling setpoints (I_t, V_b). Increasing either V_b (x axis direction) or I_t (from top to bottom) reduces I_c. One should notice the impressive

effect of quasiparticle injection: the critical current is substantially decreased even when I_t is 6 orders of magnitude lower than I_c^0.

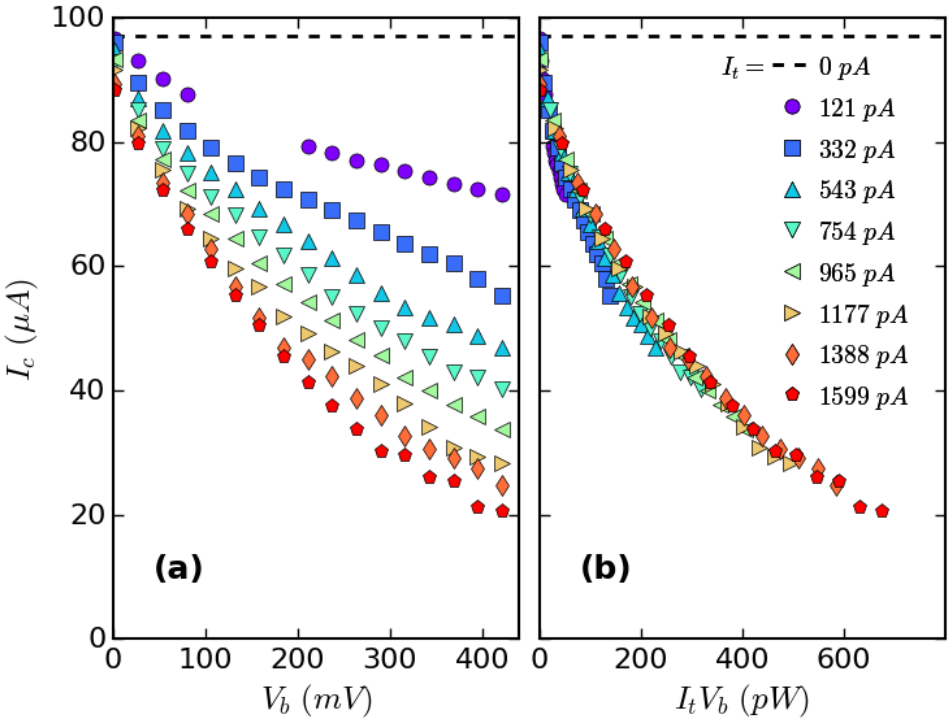

Figure 6.2: Critical current as a function of bias voltage and injected power. (a) Critical current as a function of bias voltage V_b for different tunneling currents I_t at $T = 250$ mK. Sample N03. Without injection current, $I_c^0 = 96.3$ μA. (b) Same data as a function of I_tV_b. For large eV_b compared to the superconducting gap $\Delta_0 = 370$ μeV, the injected power equals $P = I_tV_b/2$.

Fig. 6.2b evidences that the critical current is controlled by the injected power $P = I_tV_b/2$: all the data merge onto an universal curve when displayed as a function of I_tV_b. The injected power acts as a heating source reducing the critical current from its thermal equilibrium value $I_c(T_b)$ to $I_c(T_e)$ with $T_e > T_b$.

The critical current is substantially decreased even when the tunneling current is six orders of magnitude lower than the critical current in the absence of injection.

The critical current is controlled by the injected power.

6.3 Interpretation with an electronic temperature

On the one hand and as already discussed in Section 5.1, at thermal equilibrium and in the absence of quasiparticle injection, the normalized critical current I_c/I_c^0 as a function of reduced bath temperature $t_b = T_b/T_c$ collapse on an universal curve for every sample (see Fig. 6.3a). On the other hand, the critical current under injection of tunnel current is the same as if the nanowire was at an higher *electronic temperature* T_e. Moreover, the fact that T_e is fully determined by the injected heating power $P = I_tV_b/2$ and not by the average energy of the injected quasiparticles (equal to $eV_b/2$ at large V_b) suggests that some kind of relaxation towards a *quasi equilibrium* characterized by T_e occurs. Then, T_e is the local electronic temperature of the nanowire where the transition to the normal state first occurs, i.e. below the STM tip where the quasiparticles are injected (we will discuss later other situations where the transition

does not occur at the injection location). As a consequence, the critical current plays the role of a thermometer: an electronic temperature T_e can be associated to the out of equilibrium reduced critical current $I_c(T_e)$ measured when quasiparticles are injected.

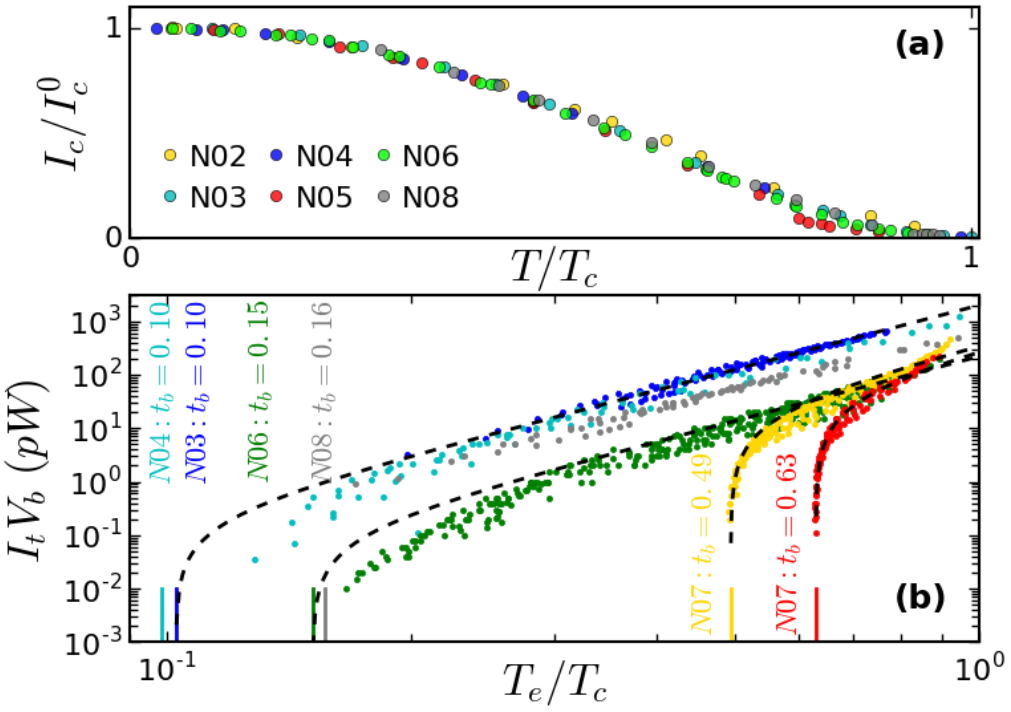

Figure 6.3: Effect of the power injected by quasiparticles on the electronic temperature. (a) Normalized critical current as a function of reduced temperature without quasiparticle injection. (b) $I_t V_b$ as a function of the reduced electronic temperature of the nanowires. Vertical bottom lines represents the reduced bath temperature t_b. Dashed lines correspond to $\kappa(t_e^4 - t_b^4)$ with $\kappa = 57, 59, 34, 41$ pW.K^{-4} from left to right.

Hence, Fig. 6.3b shows the effect of the power $P = I_t V_b/2$ injected by the tip on the reduced electronic temperature $t_e = T_e/T_c$ for different samples and reduced bath temperatures $t_b = T_b/T_c$. The curves are fitted by a $\kappa(t_e^4 - t_b^4)$ equation. For all samples, κ is of the order of 50 pW.K^{-4} and is independent of the thickness within our experimental accuracy. The accuracy on the extracted value of κ is notably due to the scattering of the data, because of uncontrolled fluctuations of the tunneling current during the measurement. Close to T_c, the voltage jump at the transition is less sharp (see previous chapter) and the shape of the $I_c(T)$ curve (see Fig. 6.3a) induces more uncertainty on T_e. Indeed, just like at low temperatures, a small variation in I_c results in a larger variation of T_e than for intermediate temperatures.

An universal power law is obtained for the power-electronic temperature characteristics for all samples.

6.4 Influence of the injection position along the nanowire

So far, all the results presented in this section have been measured for quasiparticle injection at a fixed position. In the present section however we will vary the injection position. This is achieved since by contrast with lithographed tunnel junctions, the STM technique allows to control the injection position of the quasiparticles with high spatial resolution. Fig. 6.4 shows the effect of the injection position on the critical current. The STM tip scans the surface of the nanowire with a fixed tunneling setpoint, and stops at different positions to measure the critical

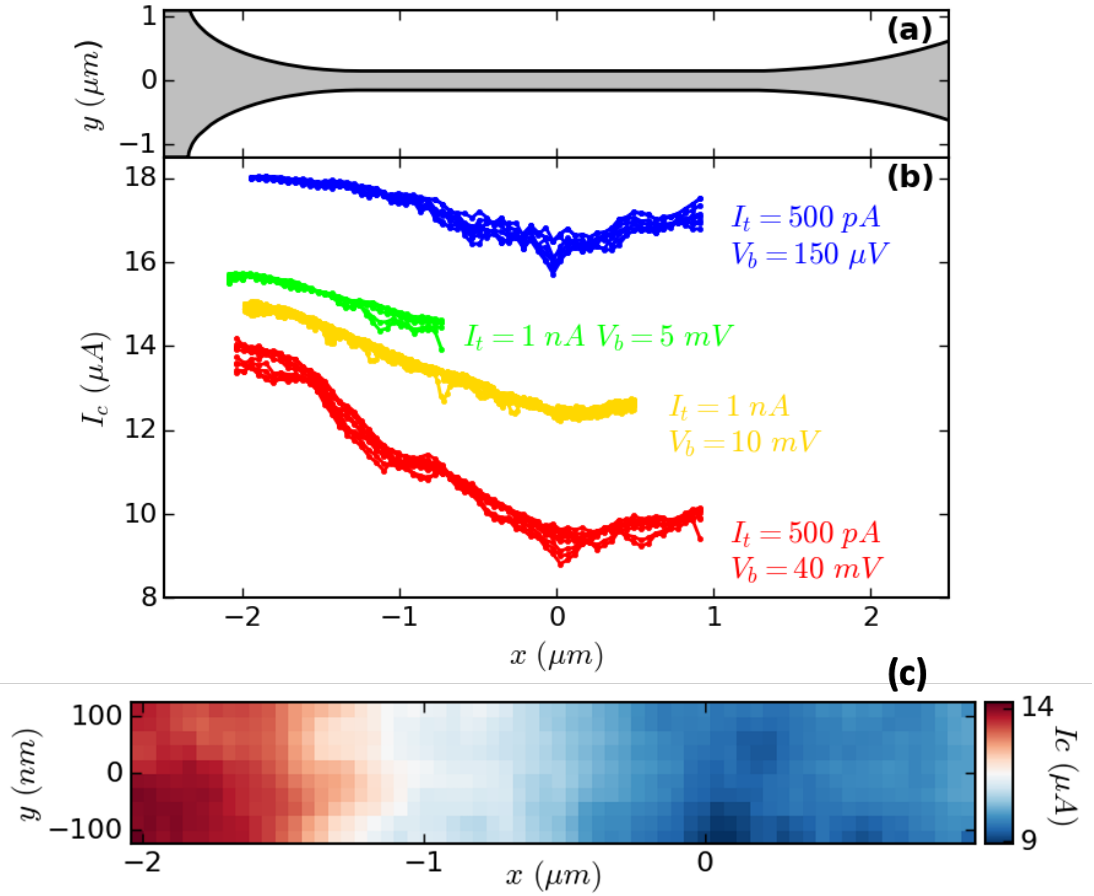

Figure 6.4: Influence of the injection position. (a) Nanowire shape. (b) Critical current as a function of the STM tip position along the nanowire for different tunneling conditions at $T = 180\ mK$. (c) Map of the critical current as a function of the injection position at a fixed tunneling setpoint ($I_t = 500$ pA and $V_b = 40$ mV; same data than bottom curve of (b)). Without injection current, $I_c^0 = 18.5\ \mu A$. Sample N06.

current. The direction of scan is parallel to the wire, and several lines are scanned, from one lateral border of the nanowire to another. Panel (a) sketches the nanowire shape. Panel (b) presents the critical current as a function of the x-position at various y-positions for different tunneling conditions (I_t, V_b). Panel (c) shows a map of the critical current as a function of the injection position $(x,\ y)$ for a fixed tunneling setpoint. At first glance, while the x-position modulates the critical current, the y-position has almost no influence (collapse of the curves for a given color on panel (b)). However, looking more in detail, the SCCM technique allows to detect small variations of the critical current on the injection position along y as shown on panel (c). For a given tunneling condition, the critical current is further reduced as the quasiparticle injection occurs close to the center of the nanowire.

Hence, the distance between the tip position and the leads matters and suggests that significant heat conduction occurs from the injection position to the leads acting as reservoirs. Indeed, if it was not the case, heat would only be evacuated through the substrate, and one would expect a constant reduction of the critical current for a fixed setpoint as soon as the injection occurs in the central (constant width) part of the nanowire.

The spatial dependence of the critical current on the injection position along the nanowire evidences thermal diffusion towards the leads.

6.5 Heat diffusion model in the quasi equilibrium limit

In this section, we develop a theoretical description of the quasiparticle diffusion process in thin films reaching the *quasi equilibrium* limit.

6.5.1 Two temperatures model

Quasi equilibrium limit

Thermodynamically speaking, the thin superconducting films studied in this PhD can be divided into two interacting systems: the electrons and the phonons (see Fig. 6.5). The heating power coming from the tip is first injected locally to the electrons. Since the films are deposited on insulating substrates, only the phonons are coupled to them. In contrast, heat conduction can occur through the electron and phonon channels in the superconductor.

In the quasi equilibrium limit, the local distribution function for both electrons and phonons always reaches thermal equilibrium, so that an electronic T_e and a phonon T_{ph} temperatures can be defined at all points in space. We will assume that the substrate acts as a reservoir with fixed bath temperature T_b, and that the system is in a steady state.

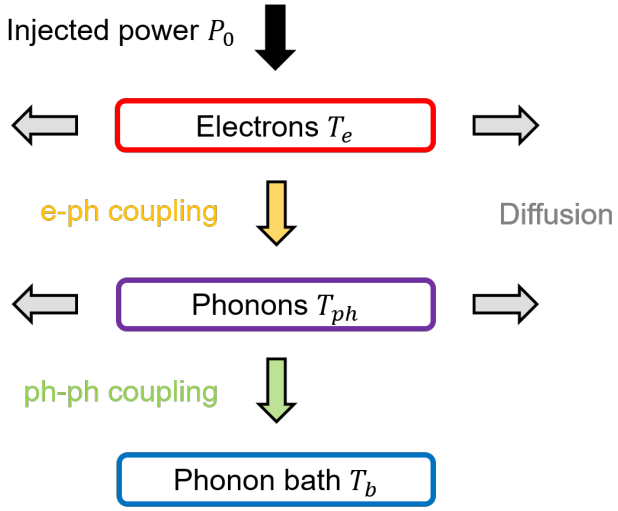

Figure 6.5: Schematics of the quasi equilibrium model.

Injected power

A power P_0 is injected locally by the STM tip at a position x_0 along the wire. Assuming perfect spatial resolution for the STM tip, the power P injected in the wire at a position x is:

$$P(x) = P_0\ \delta(x - x_0) \tag{6.1}$$

where δ is the Dirac delta function. The characteristic time scale for this process is the electron injection rate τ_{inj}^{-1}. For $I_t = 1$ nA, $\tau_{inj} = e/I_t \approx 100$ ps.

Electron phonon coupling

The electron and phonon subsystems are coupled by electron-phonon scattering and the net power exchanged in a volume V is:

$$P_{e-ph} = \Sigma V (T_e^p - T_{ph}^p) \tag{6.2}$$

where Σ is the electron-phonon coupling constant and $p = 5$ in the clean limit [117] corresponding to $\lambda_{ph} \ll l$ with λ_{ph} and l respectively the phonon wavelength and the electron mean free path. In the opposite disordered limits [101], $p = 4$ for a static disorder and $p = 6$ for a vibrating disorder (dragged by phonons).

In the clean case ($p = 5$), and in the presence of static disorder ($p = 4$), only longitudinal phonons interact with electrons [101]. We will thus use the longitudinal phonon velocity in niobium [58] $c_s^l = 5.1$ km.s^{-1} in the following for numerical computations. For vibrating disorder (dragged by phonons), $p = 6$ and both transverse and longitudinal phonons interact with electrons.

For most metals including gold [42], the order of magnitude of the coupling constant Σ is $\sim 10^9$ W.K^{-5}.m^{-1} for $p = 5$. Nevertheless, Karvonen et al. [61] found that Σ increases when the thickness decreases. As for the exponent p, it depends notably on the ratio between the electron mean free path l and the phonon wavelength λ_{ph}. The order of magnitude of the phonon wavelength strongly varies with the phonon energy E since $\lambda_{ph} \sim hc_s/E$. Indeed, E is typically equal to k_BT for thermal phonons and to eV_b for phonons resulting from scattering of the injected electrons in our experiments. Therefore, λ_{ph} ranges from about 2 μm for a thermal phonon at $T = 100$ mK to a few lattices parameters (the Debye cutoff wavelength) when eV_b reaches hundreds of millivolts. In our samples, $l \approx 1$ nm so that $\lambda_{ph} \approx l$ for $E \approx 20$ meV. Since in our experiments eV_b can vary from the gap energy (typically 200 μeV) to hundreds of meV the ratio between l and λ_{ph} can vary. For all of these reasons, the value of p cannot be presumed.

Thermal conductivity

For both electron and phonon subsystems, we will assume Fourier's law to be valid:

$$\overrightarrow{J_{th,i}} = -k_i \overrightarrow{\nabla} T_i \tag{6.3}$$

where $\overrightarrow{J_{th}}$ is the heat flux density, k the thermal conductivity and $i = e, ph$ stands for electron and phonon subsystem, respectively.

- The thermal conductivity of phonons writes [14]:

$$k_{ph} = \frac{1}{3} C_{ph} c_s \Lambda \tag{6.4}$$

  where $C_{ph} = \frac{2\pi^2}{5} \frac{k_B^4 T_{ph}^3}{\hbar^3 c_s^3}$ is the specific heat of phonons at low temperature, c_s the sound velocity and Λ the phonon mean free path. As a result, k_{ph} goes as T_{ph}^3: $k_{ph} = \alpha_{ph} T_{ph}^3$.

  When Λ becomes larger than the sample's dimensions (here the thickness t), boundary scattering becomes more important. This is particularly true at low temperatures when all the other scattering processes become more scarce, so one can make the assumption $\Lambda \approx t$ (Casimir theory). In this case, for $c_s = 5.1$ km.s^{-1} and 5 nm$< t <$ 10 nm, $\alpha_{ph} \sim 10^{-5}$ W.K^{-4}.m^{-1}.

- The electronic thermal conductivity can be inferred from Usadel equations. In the quasi equilibrium limit (see Appendix C), the thermal current carried by the electrons reads $\overrightarrow{J_{th,e}} = -k_e \overrightarrow{\nabla} T_e$ where:

$$k_e = \frac{\sigma_N}{2e^2} \int_{-\infty}^{\infty} d\epsilon \, \frac{\epsilon^2}{2k_B T_e^2} \left(1 - \tanh^2\left(\frac{\epsilon}{2k_B T_e}\right)\right) \cos(\Re[\theta]) \tag{6.5}$$

  is the electronic thermal conductivity, with θ the pairing angle. Due to the condensation of Cooper pairs in a superconductor, k_e vanishes at low temperatures as shown on Fig. 6.6.

In the normal state ($\theta = 0$), one recovers the Wiedemann-Franz law[1]:

$$\frac{k_e}{\sigma_N T_e} = \frac{\pi^2}{3}\left(\frac{k_B}{e}\right)^2 \tag{6.6}$$

which also reads similarly to the case of phonons $k_e = D\ C_e$ with $C_e = \frac{\pi^2}{3} N_0 k_B^2 T_e$ the electronic specific heat and $D = \frac{1}{3} v_F l$ the diffusion constant[2].

Finally, using the normal state resistivity of Table 4.2, Eq. 6.6 leads to the following order of magnitude for the electronic thermal conductivity at critical temperature: $k_e(T_c)\alpha_e \times T_c$ with $\alpha_e \approx 0.1$ W.K^{-2}.m^{-1}.

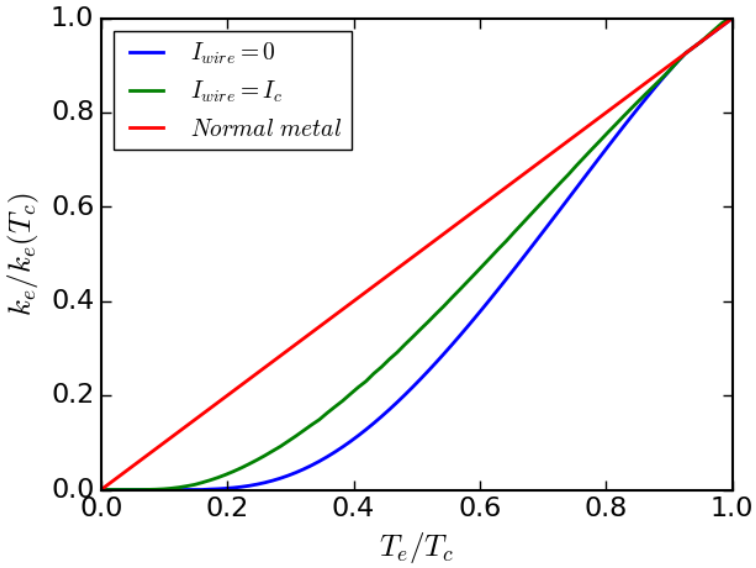

Figure 6.6: Electronic thermal conductivity as a function of temperature. In the Usadel framework, the thermal conductivity depends on the pairing angle, which is affected by supercurrent. The $I_{wire} = 0$ curve corresponds to the absence of any current in the wire, while the $I_{wire} = I_c$ is the thermal conductivity when the current driven transition from superconducting to normal state occurs. Computed by S. Sankhar*. The normal metal curve corresponds to the Wiedemann-Franz law (for a normal metal T_c is any arbitrary value of temperature). *Université Grenoble Alpes, CEA, IRIG, PHELIQS, 17 Av. des Martyrs, 38000 Grenoble, France.

Kapitza coupling

The interface between film and substrate is characterized by the power transferred from the phonon system to the substrate [74]:

$$P_K = KA\left(T_{ph}^4 - T_b^4\right) \tag{6.7}$$

where A is the interface area, $K = \frac{2\pi^5}{15}\frac{k_B^4 \eta}{\hbar^3 c_s^2}$ and η is the interface transparency. For a Nb-Si interface, $\eta \approx 0.1$ [74, 58] and with $c_s = 5.1$ km.s^{-1}, $K \sim 5 \times 10^3$ W.K^{-4}.m^{-2}.

[1] Using $\int_{-\infty}^{\infty} dx\ \frac{x^2}{cosh^2(x)} = \frac{\pi^2}{6}$.

[2] At critical temperature, the electron specific heat is discontinuous as expected for a second order transition. The magnitude of this jump is given by BCS theory [8]. Paradoxically, the relation $k_e = C_e D$ is always valid but the thermal conductivity is continuous at the transition [9]. Indeed, the effective speed of the electrons in the diffusion constant falls off rapidly because of Cooper pairs condensation: the group velocity decreases because of the opening of a gap in the dispersion relation.

Electron temperature

In the following we investigate the case of quasi one dimensional diffusion along the nanowire axis (see Fig. 6.7). Indeed, Fig. 6.4 evidences that heat conduction occurs in this direction towards the leads.

Let's consider a nanowire slice of length dx, width w and thickness t. Its volume is then $V = t \times w \times dx$ and its section $S = w \times t$. In steady state, the electron temperature is time independent and therefore the heat balance for the electron system writes:

$$S(J_{th,e}(x) - J_{th,e}(x+dx)) - \Sigma V(T_e^p(x) - T_{ph}^p(x)) + \int_x^{x+dx} P(x')dx' = 0 \tag{6.8}$$

where the first term corresponds to the heat flow carried by electrons through the wire section, the second term is the net heat exchange with phonons in the volume V and the last term represents the heat brought by quasiparticles injected with the STM tip. Rearranging the terms and taking the limit $dx \to 0$ one obtains:

$$\frac{d}{dx}\left(wtk_e\frac{dT_e}{dx}\right) = \Sigma wt(T_e^p - T_{ph}^p) - P(x) \tag{6.9}$$

Phonon temperature

The same nanowire slice has an interface with the substrate of area $A = w \times dx$. In steady state, the heat balance for the phonon system writes:

$$S(J_{th,ph}(x) - J_{th,ph}(x+dx)) + \Sigma V(T_e^p(x) - T_{ph}^p(x)) - KA(T_{ph}^4(x) - T_b^4) = 0 \tag{6.10}$$

where the first term is the heat flow carried by phonons through the wire section, the second term corresponds to the net heat exchange with electrons and the last term represents the heat flux through the interface with the substrate. Rearranging the terms and taking the limit $dx \to 0$ one obtains:

$$\frac{d}{dx}\left(wt\alpha_{ph}T_{ph}^3\frac{dT_{ph}}{dx}\right) = -\Sigma wt(T_e^p - T_{ph}^p) + Kw(T_{ph}^4 - T_b^4) \tag{6.11}$$

6.5.2 Discussion of analytically soluble limiting cases

The heating power is injected locally by the tip at a position $x = x_0$ and we will assume that both electron and phonon temperatures tends towards the bath temperature in the reservoirs at a distance x_R: $T_e(\pm x_R) = T_{ph}(\pm x_R) = T_b$.

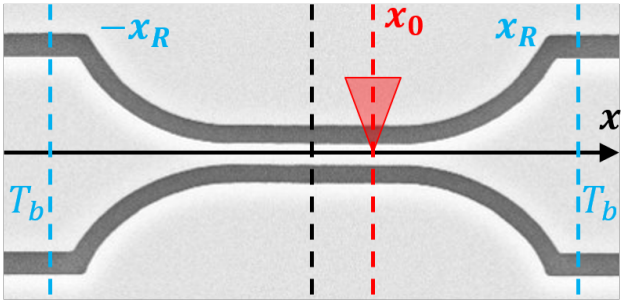

Figure 6.7: Schematics of the nanowire geometry (Scanning Electron Micrograph).

Electron diffusion only

To begin with, one can consider for simplicity only the electron diffusion process, by neglecting the power transferred to the phonons ($P_{e-ph} = 0$). In addition, assuming a normal-like electronic thermal conductivity $k_e = \alpha_e T_e$, Eq. 6.9 becomes:

$$\frac{d}{dx}\left(wt\alpha_e T_e \frac{dT_e}{dx}\right) = -P_0\delta(x - x_0) \tag{6.12}$$

which is analytically soluble (see Appendix D). It leads to $T_e^2(x) - T_b^2 = P_0\ f(x, x_0)$ where f is a function of positions x and x_0 (tip position). In the case of constant width and when the injection occurs in the middle of the nanowire, one gets the temperature at the tip position:

$$P_0 = \frac{wt\alpha_e}{x_R}(T_e^2(x_0) - T_b^2) \tag{6.13}$$

In this case, the tip position is also the hottest location in the nanowire and is therefore where the critical current is the most reduced.

This result does not correspond to the experimental behavior of Fig. 6.3 where $P_0 \propto (T_e^4 - T_b^4)$. Consequently, one should either release the assumption of normal like electronic thermal conductivity, either consider the influence of phonons.

Phonon diffusion only

By contrast with the previous paragraph, one can consider the limit of strong coupling between electrons and phonons. In this toy model, $T_e = T_{ph} = T$. By adding Eq. 6.9 and Eq. 6.11 one obtains:

$$\frac{d}{dx}\left((k_e + \alpha_{ph}T^3)wt\frac{dT}{dx}\right) = -P_0\delta(x - x_0) + Kw(T^4 - T_b^4) \tag{6.14}$$

If $k_e \ll \alpha_{ph}T^3$ and in the case of a constant width this leads to (see Appendix D):

$$P_0 \approx \frac{\alpha_{ph}wt}{2x_R}\exp\left(\frac{|x - x_0|}{x_R}\right)(T^4(x) - T_b^4) \tag{6.15}$$

This could account for the observed $P_0 \propto (T_e^4 - T_b^4)$ behavior of Fig. 6.3.

However, the order of magnitude of κ is not consistent with theory: for the typical values $\alpha_{ph} \sim 10^{-5}$ W.K^{-4}.m^{-1}, $t = 10$ nm, $w = 300$ nm and with $T_e = T(x_0)$, the experimental $\kappa \sim 50$ pW.K^{-4} values of Fig. 6.3 lead to $x_R < 1$ nm. This is not coherent with the lengthscale over which variations of the critical current are observed in Fig. 6.4.

Nevertheless, this is not really surprising since the assumption $k_e \ll \alpha_{ph}T^3$ is not valid over the full temperature range. Indeed, although the function $k_e(T_e)$ vanishes exponentially at low temperature in a superconductor, the electron contribution to the thermal conductivity $k_e = \alpha_e T$ in a normal metal widely exceeds the contribution of the phonons (given the above orders of magnitude, $\alpha_e T = \alpha_{ph}T^3$ for $T \sim 100$ K). The situation for a superconductor with an electronic temperature close to 1 K is therefore more complicated and requires further investigation.

Then, the two limiting cases studied above show that a closer look to both the electron-phonon coupling and the electronic thermal conductivity in the superconducting state must be taken into account. In particular, no analytical solution can be found and we will have to perform numerical computations.

6.5.3 Discussion of the other cases

Phonon temperature

For a constant width w, Eq. 6.11 reads in adimensional units $u = (T_e/T_b)^2$ and $v = (T_{ph}/T_b)^4$:

$$\frac{d^2v}{dx^2} = -\frac{1}{l_{ph-e}^2}(u^{p/2} - v^{p/4}) + \frac{1}{l_{ph-s}^2}(v-1) \tag{6.16}$$

- $l_{ph-s} = \sqrt{\alpha_{ph} t/(4K)}$ is the characteristic lengthscale of heat diffusion by phonons before dissipation to the substrate. The resulting characteristic lifetime of a diffusive phonon in the film is then $\tau_{ph-s} = l_{ph-s}^2/(\frac{1}{3}c_s\Lambda) = \frac{3}{4\pi^3} \times \frac{t}{c_s\eta}$. For $c_s = 5.1$ km.s^{-1}, $\eta = 0.1$, $K = 5.10^3$ W.K^{-4}.m^{-2}, $\alpha_{ph} = 10^{-5}$ W.K^{-4}.m^{-1} and $t = 5$ nm we get $\tau_{ph-s} \approx 0.2$ ps and $l_{ph-s} \approx 1$ nm.

- $l_{ph-e} = \sqrt{\alpha_{ph}/(4\Sigma T_b^{p-4})}$ is the characteristic distance over which heat is carried by phonons before being transferred to the electrons by scattering. Equating this to the phonon electron scattering length $\sqrt{\frac{1}{3}c_s\Lambda\tau_{ph-e}}$ one gets for typical values ($\Lambda = t = 5$ nm; $p = 5$; $\Sigma \sim 10^9$ W.K^{-5}.m^{-3}; $T_b = 100$ mK; $c_s = 5.1$ km.s^{-1} and $\alpha_{ph} \sim 10^{-5}$ W.K^{-4}.m^{-1}) a phonon electron scattering time $\tau_{ph-e} \approx 3$ ns and $l_{ph-e} \approx 150$ nm.

Then, the escape time of phonons from the film to the substrate τ_{ph-s} is smaller than the phonon electron scattering time τ_{ph-e}, so the "hot" phonons emitted by electrons leave the film before interacting with the electron system via phonon-electron scattering. However, the situation is less clear for the phonon lifetime against pair breaking τ_B. Indeed in Nb and at low temperatures, $\tau_B \approx 4$ ps for phonons with an energy 2Δ (which is just enough to break a Cooper pair) and τ_B decreases for higher energy phonons [59]. Thus, it is very likely that "hot" phonons (especially at high energies) can create quasiparticles by breaking Cooper pairs before leaving the film.

Nevertheless, in order to distinguish the phonon population in the film from the one of the substrate, the phonon wavelengths must be at least as short as the film thickness t. The dominant phonon wavelength [14] (maximum spectral density of phonon black body radiation obeying Planck's law) being $\lambda_{dom} = hc_s/(2.82k_BT_{ph})$, $\lambda_{dom} < t$ implies that the local phonon temperature T_{ph} must be larger than $hc_s/(2.82k_Bt) \approx 17$ K for $t = 5$ nm (typical thickness of our samples). In our experiments, the external heat is deposited by the tip in the electron system and we measure electronic effective temperatures smaller than a few Kelvins. It is therefore unlikely that the phonon system of the film reaches much higher local temperatures.

Thus, either the phonon bath is not in quasi equilibrium (this case will be discussed below), either it is at thermal equilibrium with the substrate and $T_{ph} = T_{sub}$ where T_{sub} is the temperature of the substrate at the interface with the film. In this latter situation, either the substrate really acts a reservoir and $T_{ph} = T_{sub} = T_b$ are by definition independent of the position, either the substrate has a spatially varying temperature which can be locally hotter than the base temperature of the sample holder T_b (then, the diffusion problem in the substrate becomes three dimensional and will not be investigated in this PhD work).

Electron temperature

We investigate here the case where an electron is injected by the STM tip with an energy $E \approx eV_b$. Typically, $E \gg \Delta_0$ and $\Delta_0 \approx 200$ μeV in our samples. The quasiparticle energy relaxation rate τ_{rel}^{-1} is the result of several processes:

- inelastic electron-electron scattering. At low temperatures ($k_BT \ll E$), electron-electron scattering rate τ_{e-e}^{-1} varies as $E^2/(\hbar E_F)$ where E_F is Fermi energy [2].

- electron-phonon scattering. This represents scattering processes of an electron with the absorption or emission of a phonon. The associated scattering lifetime τ_{e-ph} increases as the temperature is lowered owing to the decrease of the phonon population[3]. In a superconductor, a quasiparticle at the gap edge cannot emit a phonon because it is in the lowest energy state and we have $\tau_{e-ph}^{-1} \propto E^3/(\hbar\omega_D)^2$ for $E \gg \Delta_0$ [59].

- recombination to Cooper pairs. The timescale for recombination of two quasiparticles to form a pair and whose excess energy is emitted as a phonon is noted τ_r.

Firstly, $\tau_{e-e} \gg \tau_{e-ph}$ when $E \gg (\hbar\omega_D)^2/E_F \approx 100$ μeV for Nb [59]. This corresponds to our experimental conditions since $k_BT < \Delta_0 \ll E$ and $E \gg 100$ μeV, so electron-electron scattering can be neglected with respect to electron-phonon scattering[4].

Thus, quasiparticles relax by transferring their excess energy to the crystal lattice by electron-phonon and recombination processes. The emitted phonons have an energy of the order of the one of the injected electron $E \approx eV_b \gg \Delta_0$. Because these phonons have a large energy compared to the superconducting gap, they break Cooper pairs before leaving the film (see previous paragraph), creating more quasiparticles which emit other phonons and so on. Consequently, this avalanche scattering process continues until the resulting quasiparticles reach low energy states so that the electron bath reaches a quasi equilibrium with an electronic temperature T_e. In addition, energy relaxation is ensured by electron-phonon scattering although recombination processes still occur. Indeed, on the one hand electron-phonon scattering is faster than recombination process [59] except for quasiparticles with an energy E lower than $\approx 2\Delta_0$ and $T/T_c > 0.2$. On the other hand, phonons resulting from recombination of high energy quasiparticles are quickly reabsorbed by Cooper pairs, so they do not contribute to the relaxation of energy. Finally, on top of these relaxation mechanisms one should keep in mind that low energy phonons are escaping in the substrate without breaking Cooper pairs.

The quasiparticle energy relaxation time τ_{rel} is therefore governed by the electron-phonon scattering time τ_{e-ph} and the phonon lifetime against pair breaking τ_B. As mentioned above, τ_B decreases with E so that $\tau_B \leq 4$ ps for Nb [59]. Similarly, $\tau_{e-ph} \propto E^{-3}$ and $\tau_{e-ph}(E = 2\Delta_0) \approx 70$ ps for Nb. As a result, τ_{rel} is of the order of a few picoseconds or less for $E \gg \Delta_0$. During this time scale, quasiparticles diffuse over a distance $(\tau_{rel} v_F l/3)^{1/2} \lesssim 10$ nm with $l \approx 1$ nm and $v_F \approx 10^6$ m.s^{-1}. This is small compared to the dimensions of the nanowire (300 nm wide and 2 μm long) and to the lengthscale of the variations of the critical current (see Fig. 6.4). Therefore, **the assumption of local quasi equilibrium for the electron system is valid when $eV_b \gg \Delta_0$ in our experimental situation.**

Finally, since we inject quasiparticles with a tunnel junction, we are initially in a situation where the branches of the quasiparticle excitation curve corresponding to quasiparticle wave vectors less and greater than the Fermi wave vector are not equally occupied. In the present case of injection of quasiparticles with large energies compared to the superconducting gap, there is no branch imbalance since quasi equilibrium is reached (the distribution function is Fermi Dirac with a local electronic temperature). The opposite limit is investigated in Chapter 8.

[3] In quasi equilibrium, $\tau_{e-ph} \propto T^{p-2}$ and a power $P = \Sigma V T^p$ is dissipated to the lattice in a volume V (see Eq. 6.2) where $p = 5$ in the clean limit [117] and $p = 4$ or $p = 6$ depending on the nature of the disorder [101].

[4] The model of [59] considers the clean limit ($\lambda_{ph} \ll l$) of electron-phonon scattering with λ_{ph} the phonon wavelength and l the electron mean free path. However, [57] gives τ_{e-e} and τ_{e-ph} for a disordered metal corresponding to the case $p = 4$ in Eq. 6.2 and we still have $\tau_{e-e} \gg \tau_{e-ph}$ in the case of phonon-mediated superconductivity (non negligible electron-phonon coupling).

Numerical results

In the following, we will consider that there is no high energy out of equilibrium phonons, meaning that the avalanche process described above is instantaneous and the quasi equilibrium is established. As also discussed above, in these conditions the temperature of the phonon system cannot be disentangled from the one of the substrate. We will then consider for simplicity that the latter acts as a reservoir, so that $T_{ph} = T_{sub} = T_b$ everywhere. We will numerically solve Eq. 6.9 and compare our results to experimental observations.

To begin with, one can extract from Eq. 6.9 a typical relaxation length for the electron temperature (see Eq. D.10 in Appendix D) $l_R = \sqrt{\alpha_e/(\Sigma T_b^{p-2})}$. In our experimental conditions l_R depends on the values of the electron-phonon parameters p and Σ and on the bath temperature T_b at which the experiment is performed but l_R is typically equal to 100 μm at 100 mK and 10 μm at 1 K. This is larger than the nanowire dimensions and reflects the strong influence of the electrons thermal conductivity $k_e(T_e)$.

The numerical resolution of Eq. 6.9 (or equivalently Eq. D.10 in adimensional units) will be performed as follows. The critical temperature T_c, the geometry of the wire (thickness t and function $w(x)$), the bath temperature T_b and the value of the electronic thermal conductivity at critical temperature $k_e(T_c) = \alpha_e T_c$ (given by the normal state resistivity using Eq. 6.6) are set constant and equal to nominal experimental parameters (see Table 4.2). The temperature dependence of k_e in the superconducting state is given by Usadel equations at critical current (through Eq. 6.5). For simplicity we neglect its current density dependency and assume that the critical current density is reached everywhere. This is an approximation which slightly affects k_e for two reasons. First, when the critical current is reached in the nanowire, a smaller current density flows in the leads. Secondly, the current density is homogeneous in the nanowire, but the local critical current density depends on the local electronic temperature. Therefore when the current density is equal to the critical current density of the hottest part, it is however smaller than the critical current density of the cooler parts. In any case, the error made on the thermal conductivity is small since no matter the value of the current the thermal conductivity at a given temperature T_e is comprised between the blue and green curves of Fig. 6.6. The boundary conditions are given by $T_e \to T_b$ at infinity (see Appendix D for details). Finally, we will adjust the parameters Σ and p and confront our theoretical solution to experimental data.

First, we address the situation where heat injection takes place at the middle of the nanowire. The electronic temperature extracted from critical current measurements corresponds here to the electronic temperature at the tip position $T_e(x_0)$. Fig. 6.8a compares experimental data of sample N03 with our numerical solution of Eq. 6.9 for several values of p. In contrast with Fig. 6.3 whose axis scale is larger, one can notice some scattering of the data measured for different I_t. This probably reflects two limitations to the thermal behavior discussed above. On the one hand, the substrate does not always behave as a reservoir (this effect is investigated in Section 6.7). On another hand, tunnel injection of electrons is not rigorously equivalent to the deposition of a constant power when the injection rate I_t/e is small compared to the energy relaxation time over the nanowire width. Indeed, in this limit electron injection rather corresponds to power "pulses" and therefore to a temporarily larger effective temperature. This interpretation is consistent with the larger scattering of low I_t experimental data (see $I_t = 121$ pA), but is however beyond the scope of this manuscript. Nevertheless, it is possible to notice that better agreement is obtained for $p = 5$ and $\Sigma = 6 \pm 2 \times 10^9$ W.K^{-5}.m^{-3}. It is important to emphasize here that the slope of the experimental $P(T_e)$ data in logarithmic scale (i.e. the exponent 4 in the $P = \kappa(T_e^4 - T_b^4)$ behavior) is different from the exponent p which corresponds to the microscopic electron-phonon process. This is the numerical resolution of Eq. 6.9 which indicates that the experimental behavior is better described by $p = 5$.

Data scattering is even more important for sample N06 as evidenced by Fig. 6.8b, and is also related to the value of I_t. Our numerical solution reproduces well experimental data for fixed values of I_t as shown on Fig. 6.8c and d, except at the lowest temperatures. Two experimental biases could explain such a discrepancy. First, a poor local thermalization of the substrate under the nanowire with the sample holder[5] would result in a poorer cooling of the electrons. Secondly, at low temperatures a small reduction of the critical current due to excess noise on the tunnel current (discussed above) results in a large variation of the electronic temperature because of the shape of the $I_c(T)$ curve (used to extract T_e from the measured I_c). Better agreement is obtained for $p = 6$ although the solutions for $p = 5$ cannot be fully discarded. The value of Σ depends on the tunnel current considered. If one restricts to the larger values of tunnel current which are believed to be less sensitive to experimental offsets as discussed above, the value $\Sigma = 9 \pm 3 \times 10^9$ W.K^{-6}.m^{-3} reproduces well experimental data (see Fig. 6.8b and d).

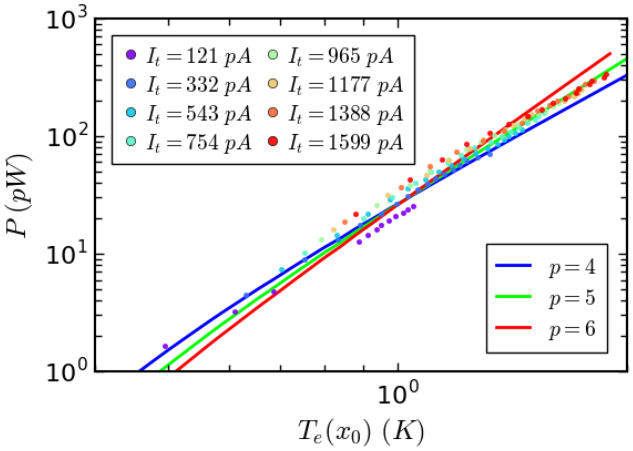

(a) Sample N03 with $\Sigma = 6 \times 10^9$ W.K^{-p}.m^{-3}.

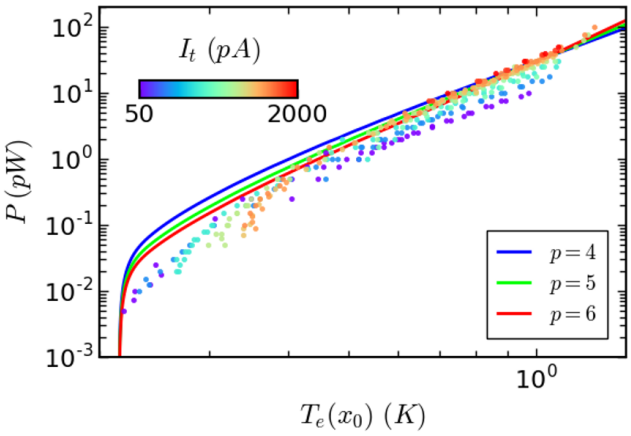

(b) Sample N06 with $\Sigma = 9 \times 10^9$ W.K^{-p}.m^{-3}.

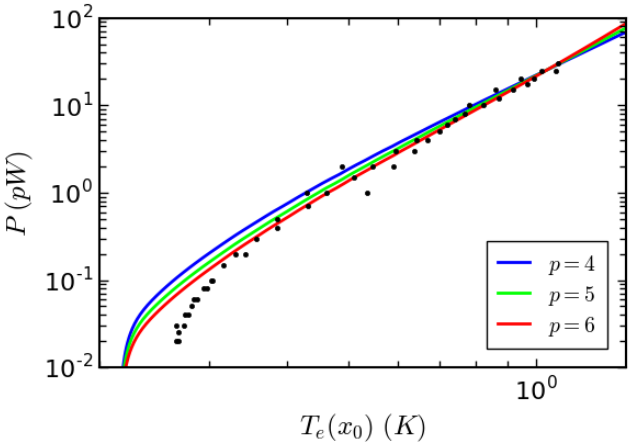

(c) $I_t = 200$ pA curve of sample N06 with $\Sigma = 4 \times 10^9$ W.K^{-p}.m^{-3}.

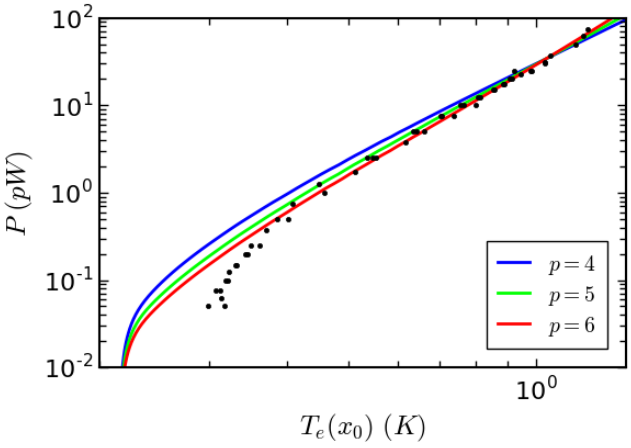

(d) $I_t = 500$ pA curve of sample N06 with $\Sigma = 9 \times 10^9$ W.K^{-p}.m^{-3}.

Figure 6.8: Confrontation of the heat diffusion model to experimental power-electronic temperature characteristics. Dots: Injected power $P = I_t V_b/2$ versus effective temperature for samples N03 and N06 (same data than Fig. 6.3). Solid lines: temperature at the tip position inferred from numerical solutions of Eq. 6.9.

[5] One the one hand, this could be due to the fact that at each current driven transition to the normal state, a Joule power is locally dissipated for a short period of time before the current is set back to zero. On the other hand, the substrate does not act as a perfect reservoir, which can manifests in a larger effective bath temperature (see Section 6.7).

The difference in Σ between N03 and N06 can be related to their thicknesses (respectively 10 and 6 nm), since it has been measured experimentally that Σ increases when the thickness decreases [61], which is what we observe. For sample N03, the value $p = 5$ corresponds to the clean case (phonon wavelength smaller than the electron mean free path). This is consistent with our experimental conditions (which correspond here to values of V_b larger than 20 mV, see Fig. 6.2a) and with the discussion below Eq. 6.2. For sample N06, the determination of p is not enough accurate to draw any definitive conclusions.

Then, the numerical solution of Eq. 6.9 also provides a theoretical prediction for the spatial dependence of the critical current on the injection position along the nanowire. Here, the critical current is determined by the nanowire section with the largest electronic temperature (which does not corresponds to the tip position when the latter is in the leads). We use the values $p = 6$ and $\Sigma = 9 \times 10^9$ W.K^{-6}.m^{-3} extracted from the power-electronic temperature characteristics of N06 in order to compute the spatial dependence of the critical current of the same sample. Confrontation to experimental measurements on Fig. 6.9 shows that the lowest bias voltage V_b curve (in blue) does not fit at all experimental data, but this corresponds to the low energy regime ($eV_b \approx \Delta_0$) which will be treated in Chapter 8. In contrast, as evidenced by the three other curves of Fig. 6.9 (for which $eV_b \gg \Delta_0$), excellent agreement is found between experimental measurements and our theoretical prediction while we do not use any adjustable parameter for this computation. Notably, our model reproduces the absolute value of the critical current both at the center and at the entrance of the nanowire, such as the difference between the different curves measured for different injected powers. In particular, the value of I_c at the entrance of the nanowire is not trivial given the value of l_R: the electronic temperature exceeds T_b over a larger lengthscale that the nanowire dimensions.

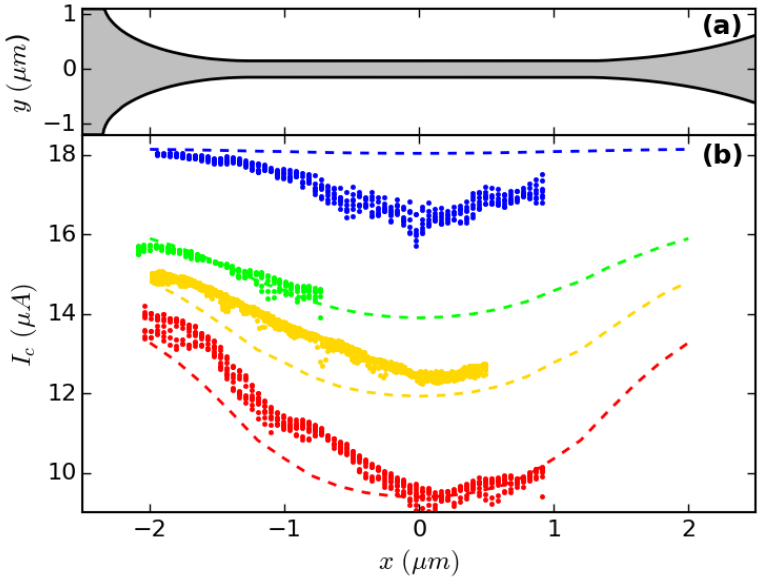

Figure 6.9: Confrontation of the heat diffusion model to the spatial dependence of the critical current on the injection position. (a) Nanowire shape. (b) Dots: critical current as a function of the STM tip position along the nanowire for different tunneling conditions at T=180 mK: • $I_t = 500$ pA and $V_b = 150$ μV • $I_t = 1$ nA and $V_b = 5$ mV • $I_t = 1$ nA and $V_b = 10$ mV • $I_t = 500$ pA and $V_b = 40$ mV (same data than Fig. 6.4). Dashed lines: critical current obtained from the numerical solutions of Eq. 6.9 for $p = 6$, $\Sigma = 9 \times 10^9$ W.K^{-6}.m^{-3}, $T_b = 180$ mK and for an injected power $P = I_t V_b/2$. The relation between electronic temperature T_e and critical current I_c is obtained through the $I_c(T)$ curve in the absence of injection (see Section 6.3). Sample N06 ($\Delta_0 = 235$ μeV).

In summary, the heat diffusion model developed in this section reproduces the $P_0 \propto (T_e^4 - T_b^4)$ behavior (see Fig. 6.3) while the analytical solutions considered in Eq. 6.13 and 6.15 failed. Indeed, heat diffusion by electrons is important (given the value of l_R) so the thermal dependence of the electrons thermal conductivity k_e in a superconductor plays a major role. Thus, our model where Usadel predictions for $k_e(T_e)$ are considered is in agreement with experimental measurements. In addition, our numerical solution of the heat diffusion model accounts consistently for two types of measurements with the same parameters, namely the power and spatial dependence of the critical current. Finally, it also allows to probe the microscopic electron-phonon mechanism by extracting the values of p and Σ.

The heat diffusion model in a superconductor with an electronic thermal conductivity given by Usadel equations and in the presence of electron-phonon coupling accounts for all experimental observations under local injection of quasiparticles.

6.6 Nanowires with a dead-end strip

Nanowires with a dead-end strip have been fabricated to investigate the diffusion process in a different geometry. They consist in a 300 nm × 2.5 μm nanowire connected in its center to a 600 nm × 8.5 μm dead-end strip as pictured on Fig. 6.10. The left side furrows with different lengths are landmarks for the STM images at low temperature.

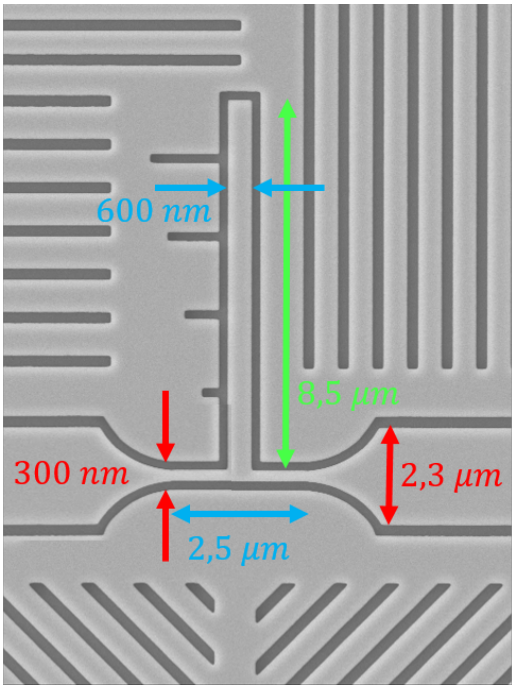

Figure 6.10: Scanning Electron Micrograph of a dead-end strip geometry sample.

The influence of quasiparticle injection in the dead-end strip with different tunneling setpoints and at different positions has been investigated as shown on Fig. 6.11. Similarly to the result of Fig. 6.1, for a fixed injection position, the superconducting transition of the nanowire is shifted to lower temperatures by the injection of quasiparticles while the leads remain unaffected. However, superconducting properties are not probed at the STM tip position but rather at the junction between the nanowire and the dead-end strip. Therefore, by moving the tip in the y direction, one can now study the energy relaxation of the quasiparticles when they diffuse along the dead-end strip. The effect of injected quasi-particles on T_c is shown in Fig. 6.11c and 6.11d for five different injection positions. As expected, for a given position, the critical temperature is all the more weakened that the injected power is increased (Fig. 6.11c). But this effect is less effective when the STM tip is moved away from the nanowire as shown in Fig. 6.11d. This means that some of the injected power is lost and never reaches the nanowire.

Then, this experiment gives some boundary conditions to the heat diffusion process: for given heating conditions (injected power and tip position), the temperature T of the sample holder has to be reduced down to $T_c(I_t \neq 0)$ (lower than its value in the absence of injection $T_c(I_t = 0)$) so that the temperature at the intersection between the dead-end strip and the nanowire reaches $T_c(I_t = 0)$.

Similarly to Fig. 6.4, the injection position of quasiparticles has also an influence on the critical current I_c as evidenced on Fig. 6.12. Firstly, I_c is less reduced when the injection occurs

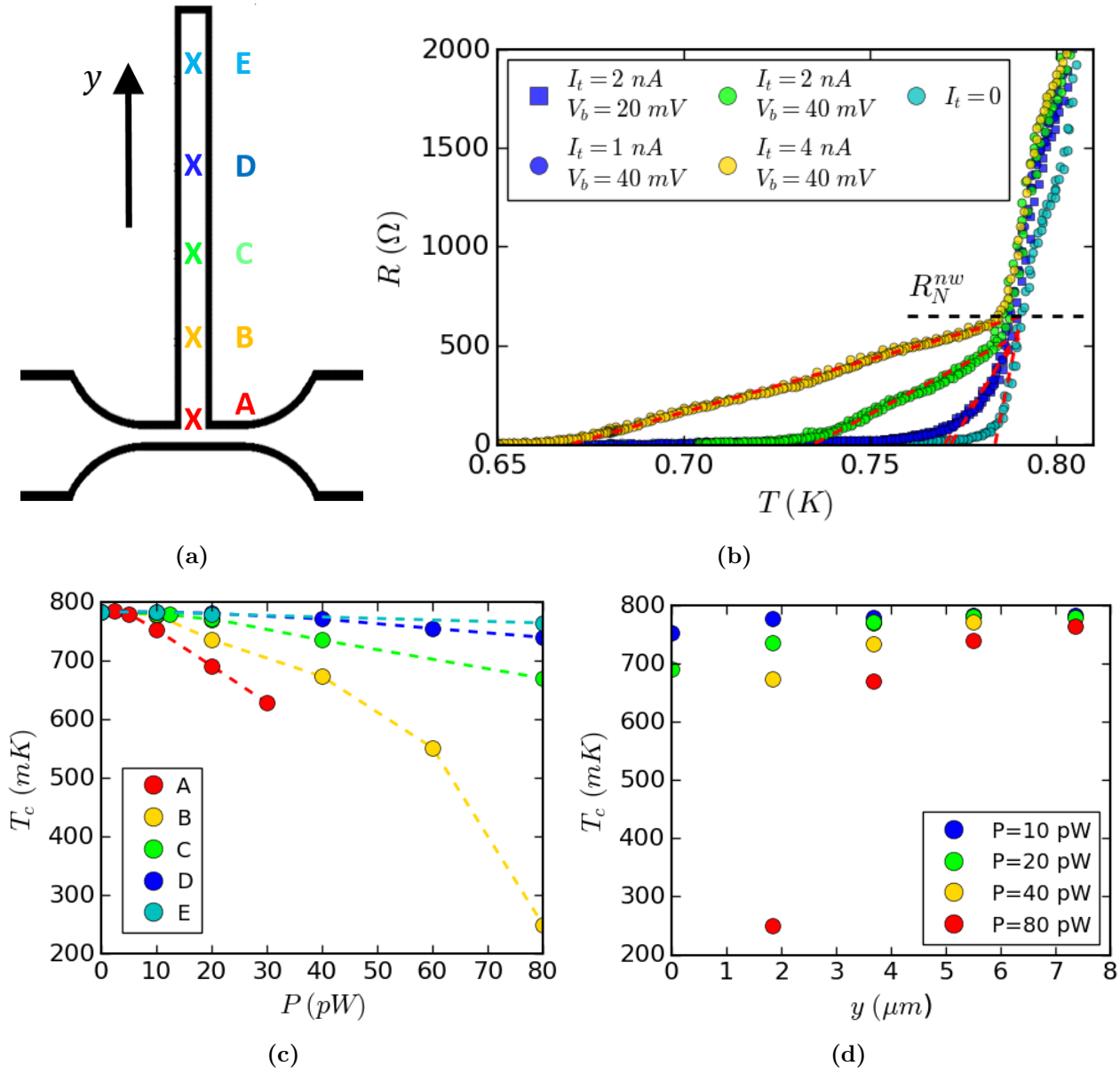

Figure 6.11: Resistance versus temperature for different injection positions and setpoints. (a) Schematics of the sample with indicated injection positions. y is the direction perpendicular to the nanowire whose origin is located at the intersection between the nanowire and the dead-end strip. (b) Resistance versus temperature for no current injection and for different tunneling conditions at position C. R_N^{nw} is the nanowire normal state resistance. Dashed red lines are the linear extrapolations used to extract the critical temperatures. (c) Measured critical temperature as a function of injected power $P = I_t V_b/2$ for injection positions A to E: respectively 0, 1.8, 3.7, 5.5 and 7.4 μm above the nanowire from bottom to top. (d) Measured critical temperature as a function of position along y for different injected powers. Sample N13.

further away along the dead-end strip. Since the value of the critical current is determined by the electronic temperature in the nanowire, this provides spatially dependent boundary conditions for the heat diffusion process at stake in our Nb\Au thin bilayers. Furthermore, for the same injected power, the relative reduction of the critical current depends on the bath temperature, i.e. the sample holder temperature tuned with a resistive heater and monitored by a RuO thermometer. The fact that in our samples the critical current is less affected by a given injected power as the temperature increases will be compared to literature experiments in Section 6.8.

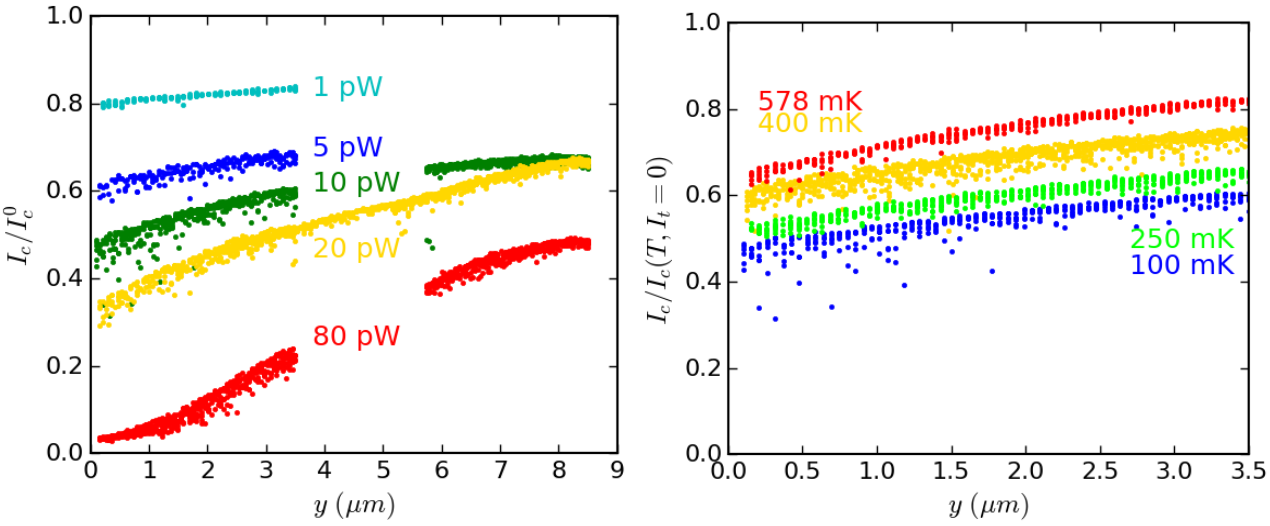

(a) Fixed temperature. **(b)** Fixed power.

Figure 6.12: Critical current as a function of injection position. y is the ordinate of the injection position with origin located on the nanowire axis. (a) Critical current normalized to its value in the absence of quasiparticle injection at $T_b = 100$ mK as a function of injection position for different injected powers. (b) Critical current normalized to the value in the absence of quasiparticle injection as a function of position at different temperatures and for constant injected power $P = 10$ pW. Sample N13.

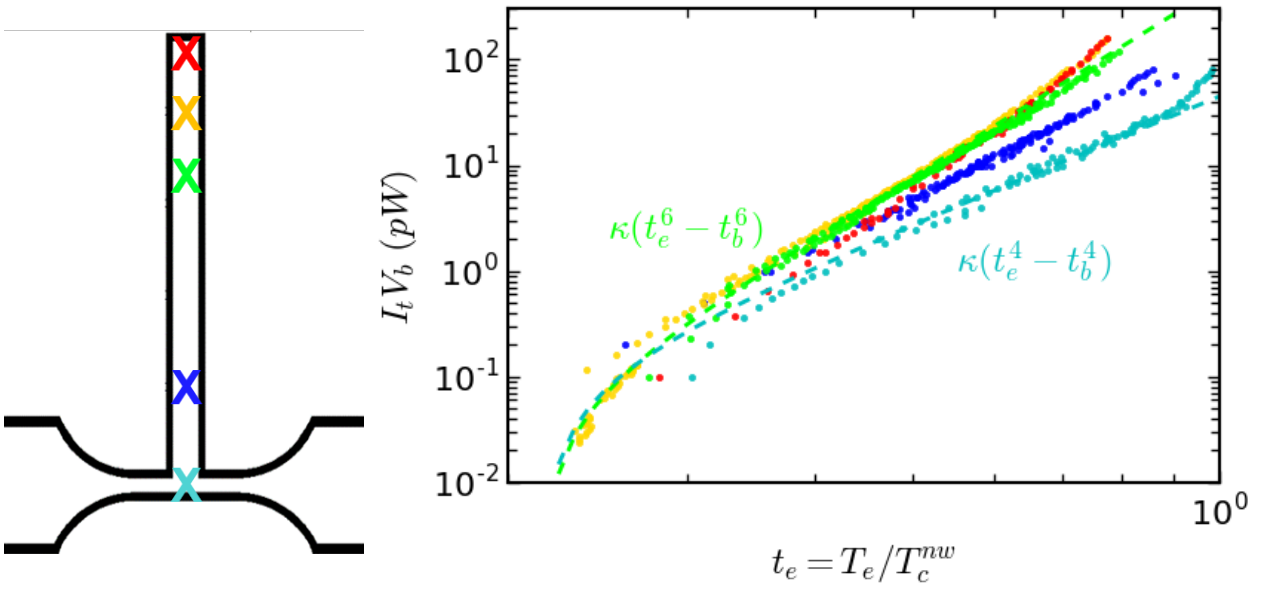

(a) **(b)**

Figure 6.13: Effective electronic temperature as a function of power for different injection positions. (a) Schematics of the sample with indicated injection positions. (b) $I_t V_b$ as a function of the reduced electronic temperature. Dashed lines indicate the $I_t V_b = \kappa(t_e^m - t_b^m)$ curves with $m = 4$ and $m = 6$ for respectively $\kappa = 118$ pW.K^{-4} and $\kappa = 2137$ pW.K^{-6}. Sample N13.

Finally, Fig. 6.13 presents the effect of the power $P = I_t V_b/2$ on the reduced electronic temperature t_e for different injection positions. As expected for a diffusion mechanism, for a given power the electronic temperature in the nanowire decreases as the injection occurs fur-

ther from the intersection between the dead-end strip and the nanowire. The observed behavior corresponds to a $\kappa(t_e^m - t_b^m)$ with a value of m increasing with the distance between the tip and the nanowire. Consistently with the behavior observed in the previous experiments with no dead-end strip, $m = 4$ when injection occurs at the intersection between the dead-end strip and the nanowire.

The power-electronic temperature characteristic shows a power law dependence with an exponent depending on the injection position in the dead-end strip.

Confrontation to the heat diffusion model

Firstly, the fact that $P_0 = \kappa(T_e^m - T_b^m)$ with a value of m increasing with the distance between the tip and the nanowire confirms the analysis made in the straight nanowires geometry (see below Eq. 6.15) where we discarded that heat could be carried out by phonons only. In the present geometry, we address a different situation where the critical current probes the electronic temperature at a position different from the tip position. However, Eq. 6.15 still predicts a constant $m = 4$ value and an increase of κ together with $|x - x_0|$ (which corresponds here to the tip to sample distance y). Since we observe experimentally in Fig. 6.13 that the exponent m varies with the distance y, we can again reject the mechanism of heat transport carried by phonons only.

We will now solve numerically Eq. 6.9 with $T_{ph} = T_{sub} = T_b$ (same model than above). As in the previous section, the critical temperature T_c and the value of the electronic thermal conductivity at critical temperature $k_e(T_c) = \alpha_e T_c$ will be taken equal to nominal experimental parameters. Since no supercurrent is flowing between the tip and the nanowire, we will use the temperature dependence of k_e in the absence of supercurrent (see Fig. 6.6). This is however an approximation since in the nanowire itself a current is flowing and k_e may be different. We will transpose for simplicity the two dimensional dead-end strip geometry to a quasi one

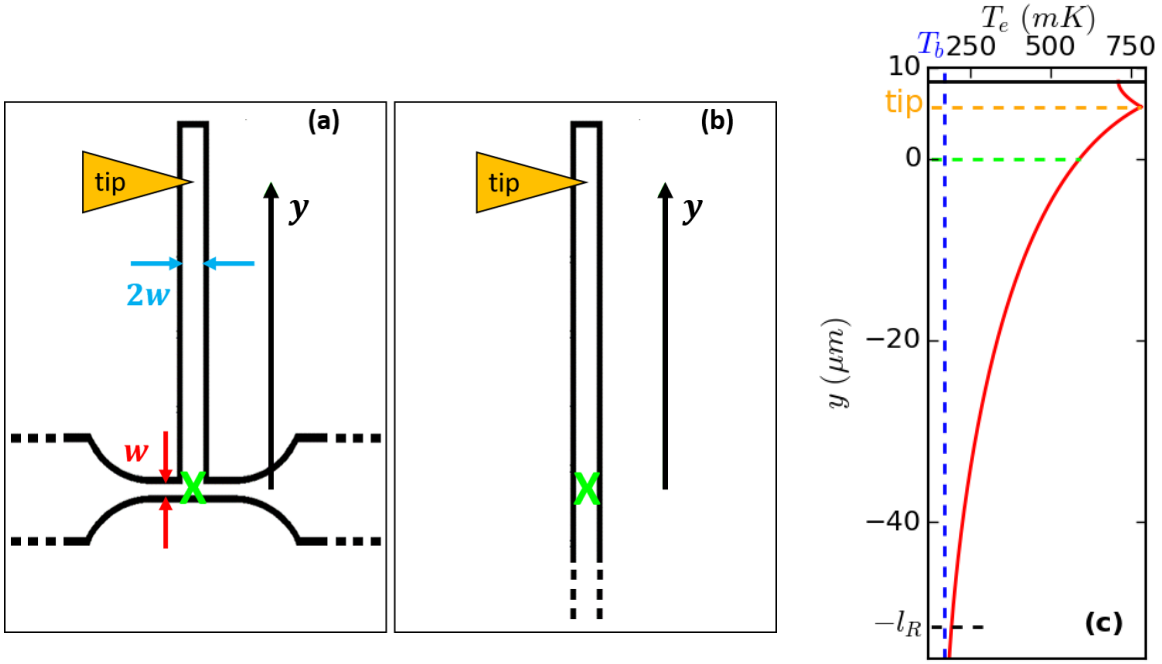

Figure 6.14: (a) Dead-end strip geometry. (b) Simplified geometry for numerical resolution of the heat equation. (c) Example of numerical solution taken from Fig. 6.15b ($P = 30$ pW and tip in $y = 5.7$ μm). l_R is the characteristic relaxation length of Eq. 6.9 (see Eq. D.10).

dimensional case (see Fig. 6.14). The boundary conditions are the following. At the top of the dead-end strip ($y = 8.5$ μm), the heat flux density is zero ($\overrightarrow{J_{th,e}} = \overrightarrow{0}$). Far away in the reservoirs ($y \to -\infty$) the electronic temperature T_e equals the bath temperature T_b. Finally, the superconducting properties (critical temperature and critical current) will be given by the value of T_e at the intersection between the nanowire and the dead-end strip ($y = 0$ and green cross of Fig. 6.14).

Fig. 6.15b compares experimental data and theoretical predictions of the power versus electronic temperature dependency for different injection positions along the dead end strip in sample N13. By contrast with the previous section, adjusting only the values of p and Σ was not sufficient to provide a satisfactory fit. Indeed, the solution presented here is computed for $T_b = 170$ mK and $t = 4$ nm while the temperature of the sample holder during the experiment was 110 mK and the nominal thickness of the sample is 6 nm. Nonetheless, an effective thickness smaller than the nominal one is consistent with the relatively low critical temperature measured for N13 when compared to other samples with same nominal thicknesses (see Table 4.2). Such an overestimate of the effective thickness is very possible given the uncertainty over thickness during the deposition process. The discrepancy in T_b may be related to a poor local thermalization of the substrate below the nanowire with the sample holder (because of the heat briefly released by Joule effect when the critical current is reached, and because the substrate is not a perfect reservoir as discussed in Section 6.7). However, the present set of parameters $T_b = 170$ mK, $t = 4$ nm, $p = 5$ and $\Sigma = 6 \times 10^9$ W.K^{-5}.m^{-3} accounts for the main experimental feature observed in the dead-end strip geometry, being the dependence on the injection position of the slope of the power-electronic temperature characteristic. For large injected powers, the increase of T_e saturates. Indeed, when injection is performed at the top of the dead-end strip and the temperature in the nanowire approaches T_c, the dead-end strip is almost entirely in the normal state, and electronic cooling becomes then much more efficient than when it was in the superconducting state. The values of p and Σ are consistent with the ones extracted in previous section for similar samples.

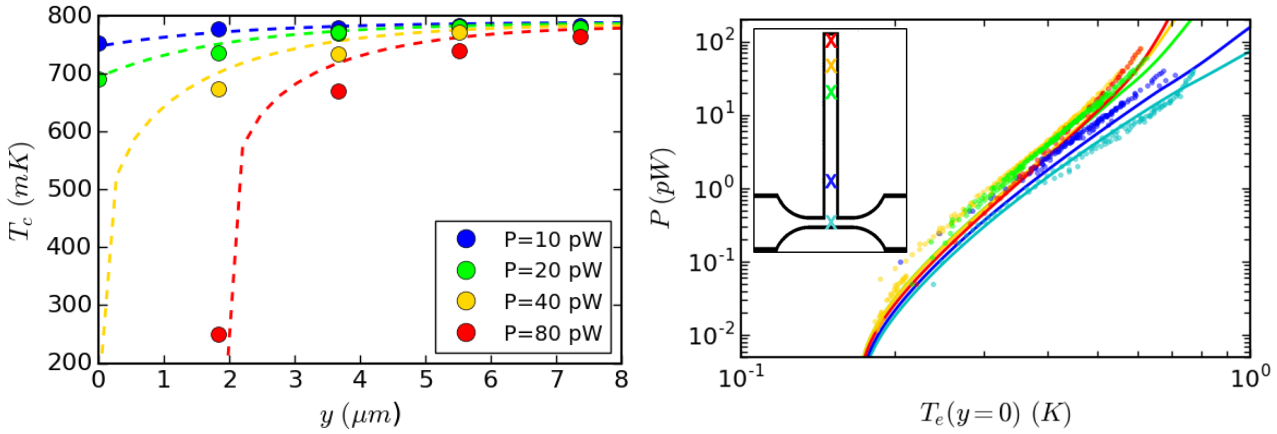

(a) (b)

Figure 6.15: Confrontation of the heat diffusion model to dead-end strip geometry experimental results. (a) Dots: critical temperature as a function of injection position along y for different injected powers. Dashed lines: theoretical predictions of Eq. 6.9 with $p = 5$, $\Sigma = 6 \times 10^9$ W.K^{-5}.m^{-3} and $t = 4$ nm. (b) Dots: injected power $P = I_t V_b/2$ as a function of electronic temperature for different injection positions along y (respectively y =0, 1.7, 5.7, 7.1 and 8 μm) displayed in the inset. Dashed lines: theoretical predictions with $p = 5$, $\Sigma = 6 \times 10^9$ W.K^{-5}.m^{-3}, $T_b = 170$ mK and $t = 4$ nm. Sample N13, whose nominal thickness is $t = 6$ nm.

Good agreement between experimental data and theoretical predictions for the modulation of the critical temperature with quasiparticle injection with the STM tip is found as shown on Fig. 6.15a. We do not use any adjustable parameter for this computation: the values of p and Σ are the same than the ones extracted for the same sample from critical current measurements (Fig. 6.15b) Data are extracted from the resistance versus temperature curves of Fig. 6.11, and $T_c(P)$ is defined as the bath temperature T_b for which $T_e(y = 0)$ is equal to the sample critical temperature in the absence of injection $T_c(I_t = 0) = 790$ mK.

Therefore, as in previous section, the heat diffusion model provides consistently quantitative predictions for two type of measurements (resistivity and critical current under quasiparticle injection) in the same sample. However, we extended in this section the validity range of the model. Indeed, in contrast with the straight nanowires geometry the temperature under the tip can exceed T_c when quasiparticle injection is performed at large injected powers in the dead-end strip. Furthermore, while the critical current measurements are performed at low bath temperatures, the resistance versus temperature curves are measured close to T_c. Nonetheless, the model still accounts well for experimental observations, notably thanks to the consistency of Usadel prediction for the electronic thermal conductivity in the normal and superconducting states.

The model of heat diffusion is also in good agreement with experimental observations in the dead-end strip geometry, and this even when the electronic temperature exceeds the critical temperature.

6.7 Injection through the substrate

Thanks to the sample design, it is possible to perform STM for any position of the tip on the surface of the sample, although the nanowire (and the dead-end strip) is electrically isolated

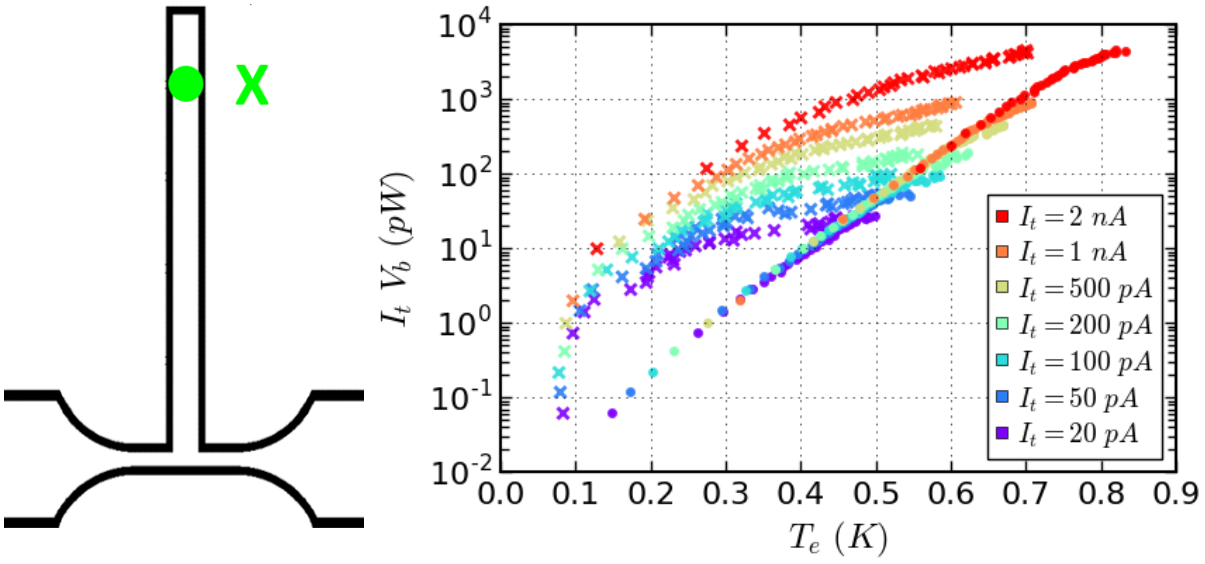

(a) (b)

Figure 6.16: Effect of the injected power on the effective temperature for injection of quasiparticles in the dead-end strip and in the ground plane. (a) Schematics of the sample with indicated injection positions. (b) I_tV_b as a function of effective temperature for injection in the dead-end strip (circles) and in the ground plane (crosses) at $T = 70$ mK. Sample N16.

from the surrounding ground plane. Fig. 6.16 shows the effect of the injected power on the effective temperature for quasiparticle injection in the dead-end strip and in the ground plane. Interestingly, even though there is no electrical contact between the injection position and the nanowire, we observe that quasiparticle injection in the ground plane affects the nanowire electronic temperature. Then, the heat conduction mechanism necessarily goes through the substrate, which is therefore locally not in thermal equilibrium with the thermometer of the sample holder ($T_{sub} \neq T_b$). In addition, this behavior is not driven by the injected power $P = I_t V_b/2$ but by both bias voltage V_b and tunneling current I_t: at a given power, larger effective temperatures are reached for low I_t and large V_b than for high I_t and low V_b. As for the case of injection in the dead-end strip, one recovers the thermal behavior presented in previous sections, except for very large bias voltages (here the experiment is performed up to $V_b = 900$ mV whereas in the previous experiments described in Section 6.5 and 6.6 the maximum bias voltage was typically $V_b = 50$ mV for samples with a similar thickness and lower than 400 mV for all the samples). In this regime, the electronic temperature T_e is driven by both I_t and V_b and is close to the one measured when injection is performed in the ground plane. This means that for very large V_b, heat conduction through the substrate becomes non negligible: for a given tunneling setpoint both conduction through the dead-end strip and through the substrate contribute to the nanowire overheating.

Fig. 6.17 shows the effect of the injected power on the effective electronic temperature in the nanowire for different injection positions in the ground plane. For a given tunneling setpoint, the effective electronic temperature in the nanowire is only slightly affected by the injection position and therefore by the tip-nanowire distance (see Fig. 6.17a and b). In addition, although heat conduction between the injection position and the electrons of the nanowire occurs through the substrate, the presence of the ≈ 500 nm deep furrows on the left side of the dead-end branch (low temperature STM landmarks) does not result in any detectable difference between the two injection positions of Fig. 6.17c.

For large bias voltages, the substrate cannot be considered as a reservoir with fixed temperature. The associated effect on the critical current is not driven by the injected power but by both bias voltage and tunnel current, and is only slightly dependent on the injection position.

Discussion

These experiments show that when quasiparticle injection occurs in the ground plane, the nanowire is still overheated through its interface with the substrate. This means that some phonons emitted during the energy relaxation process of the injected quasiparticles and transmitted to the substrate reach the nanowire before being thermalized by the substrate phonon bath (whose temperature T_b is fixed). There, they overheat the nanowire electron system by creating excess quasiparticles. Therefore, our measurements allow to probe the dynamics of the above phonons.

First, the fact that this overheating effect is only slightly dependent on the injection position shows that the diffusion of phonons from the tip position to the nanowire is fast compared to their thermalization with the sample holder at T_b. The relaxation lengthscale of the phonons l_{rel}^{ph} is therefore larger than the dead-end strip dimensions so that $l_{rel}^{ph} \gtrsim 10$ μm. Assuming a ballistic motion at $c_s = 3-5$ km.s^{-1} for the phonons in the bulky substrate (the phonon mean free path in the bulk is not limited by the thickness) this leads to a characteristic thermalization time for the substrate phonons $\tau_{rel}^{ph} \gtrsim l_{rel}^{ph}/c_s \sim 10$ ns.

Then, since the presence of deep furrows has no influence at all it is likely that the wavelength of the phonons traveling in the substrate and reaching the nanowire is larger than the depth

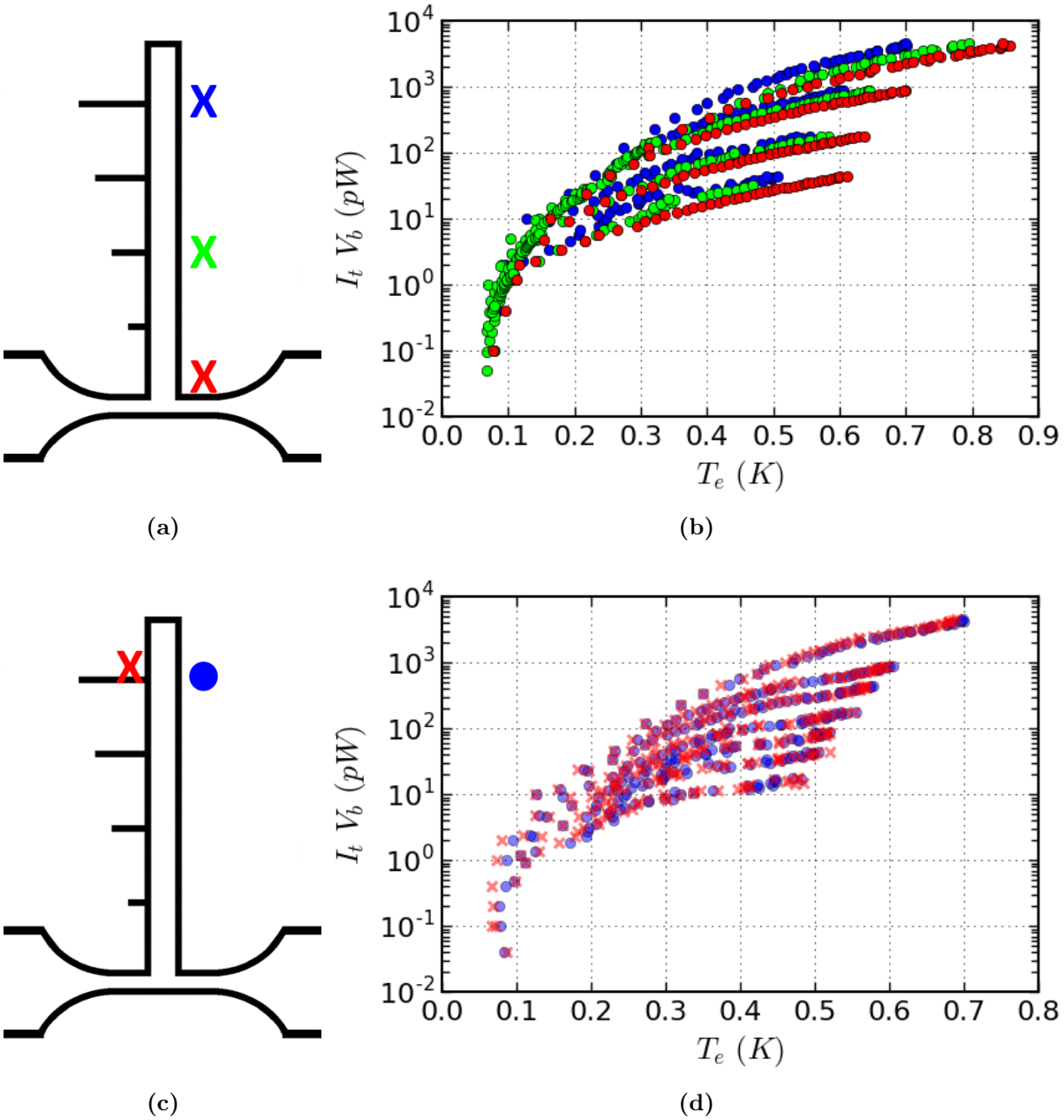

Figure 6.17: Effect of the injected power on the effective electronic temperature in the nanowire for injection of quasiparticles at different positions in the ground plane. (a) Schematics of the sample with indicated injection positions of (b). (b) $I_t V_b$ as a function of effective temperature for injection at different positions in the ground plane at $T = 70$ mK. From top to bottom, $I_t = 5$ nA, 1 nA, 200 pA and 50 pA. (c) Schematics of the sample with indicated injection positions of (d). (d) $I_t V_b$ as a function of effective temperature for injection at different positions in the ground plane at $T = 70$ mK. From top to bottom, $I_t = 5$ nA, 1 nA, 500 pA, 200 pA, 100 pA, 50 pA and 20 pA. Sample N16.

of the furrows (≈ 500 nm) otherwise they would be partially reflected. Because $\lambda_{ph} \sim \hbar c_s/E$, it corresponds to low energy phonons ($E \lesssim 40$ μeV). This is consistent with the quasiparticle relaxation process considered in Section 6.5, according to which high energy phonons are quickly absorbed by Cooper pairs in the vicinity of the injection position.

Notably, the electronic temperature in the nanowire is not governed by the injected power but both by the injection rate (through I_t) and the energy (through V_b) of the injected quasi-

particles. Indeed at fixed power, it is more efficient in overheating the nanowire to increase the injected quasiparticles energy rather than the injection rate. This probably allows to probe the energy dependence of the phonon scattering processes creating excess quasiparticles in the nanowire, such as the phonon-electron scattering and pair breaking process. We are however not aware of any theoretical model available for such a discussion.

Finally, these measurements clearly demonstrate that the substrate cannot be considered as a reservoir with a fixed temperature equal to the one of the sample holder T_b. This therefore reconsiders the model discussed in Section 6.5 and 6.6 where we assumed that $T_{ph} = T_{sub} = T_b$. This is all the more interesting since in the thin films considered in this PhD, the phonon population of the film cannot be disentangled from the one of the substrate in the vicinity of its interface with the film as discussed in Section 6.5. Whether the phonon system of the substrate is locally in quasi equilibrium (with a spatially varying temperature $T_{ph} = T_{sub}$ larger than T_b), or whether the temperature of the substrate (and therefore of the phonons of the film) is not defined is not known. In any case, the electron system of the film should be sensitive to the presence of out of equilibrium phonons in the substrate.

However, although we assumed the substrate to act as a reservoir in our model, the theoretical predictions made in previous sections reproduce well experimental measurements. This could be explained as follows. First, as discussed above, it is believed that only few high energy phonons are dissipated to the substrate because of their short lifetime against pair breaking. Under this condition, the phonon population is therefore close to quasi equilibrium. Then, in quasi equilibrium the electron-phonon coupling power is proportional to $T_e^p - T_{ph}^p$ with $p \approx 5$, so that the error made on the phonon temperature only has a small influence on the exchanged power when T_e is larger than T_{ph}. Furthermore, the small spatial dependence of the overheating effect through the substrate (see Fig. 6.17) supports the above claim. Indeed, this suggests that the phonon population of the substrate is independent of the position on the nanowire scale. In this case, the substrate can be considered in first approximation as a reservoir but with a larger temperature than the one of the sample holder. Finally, as experimentally evidenced on Fig. 6.16, the substrate contribution to the heat diffusion between the tip and the nanowire is negligible except at very large V_b. This means that in the typical experimental conditions of this PhD work, the heat diffusion model developed in Section 6.5 accounts for the main diffusion channel and is therefore accurate in its predictions.

The substrate phonon system carries heat over a larger lengthscale than the nanowires dimensions before reaching equilibrium. Nevertheless, the phonon system carries a negligible heat flow compared to the electron system of the superconducting film.

6.8 Discussion of field effect versus quasiparticle overheating

The modulation of the critical current by quasiparticle injection with a STM tip has to be compared with the results introduced in Section 3.4. To begin with, **there is no doubt that the modulation of the critical current in our experiments is due to quasiparticle overheating and not to field effect.** Indeed, a major benefit of the STM technique is the ability to tune independently the tunneling current I_t and the bias voltage V_b, by contrast with lithographed junctions where the tunnel barrier width is fixed. Small variations of the tip height (smaller than 1 Å) at fixed bias voltage result in an exponential modification of the tunneling current while the electric field between the tip and the sample remains essentially

constant (since the tip to sample distance is almost unchanged and the bias voltage is fixed). Then, the data presented in Fig. 6.2a shows that for a fixed bias voltage (and therefore electric field), the critical current I_c strongly depends on the tunneling current (the injection rate of quasiparticles). Moreover, Fig. 6.2b demonstrates that the reduction of I_c is driven by the power injected in the nanowire. Another big advantage of the STM is its spatial resolution. Thus, the evolution of the critical current with respect to the injection position of quasiparticles with a given power (Section 6.4) evidences the diffusion process of the injected quasiparticles to the leads. A field effect would not involve heat diffusion and therefore the critical current would not depend on the distance between the STM tip and the reservoirs (leads) and should result in a constant I_c plateau in the nanowire, by contrast with the behavior observed in Fig. 6.4.

As for the suppression of the critical current of superconducting wires or weak links reported in [27, 85, 84, 26, 89], it is attributed to field effect. In each experiment, a gate electrode is used to apply a gate voltage V_g which controls the critical current of the device (see Fig. 3.5a, 6.18a, 6.19a and 6.20a). The arguments given by the authors to discard the quasiparticle overheating due to injection of electric current in the samples are discussed below. Comparisons with the results obtained in this PhD work by SCCM are made. Finally, the alleged field effect reported in literature is interpreted by quasiparticle overheating.

Argument of negligible leakage current and power

Some leakage current in the field effect transistors (FETs) upon biasing the gate electrodes is measured in the reported experiments. However, the authors claim that the leakage currents I_L (as low as a few tens of pA) and the resulting dissipated powers (as low as hundreds of pW), are too low to be considered as the origin of the suppression of I_c. In particular, the leakage currents are typically $I_L \sim 10^{-6} I_c(V_g = 0)$ where $I_c(V_g = 0)$ is the critical current in the absence of perturbation.

Yet, **our experiments demonstrate that such leakage currents as low as $10^{-6} I_c^0$ affect the critical current.** Indeed, the injection of tunneling currents I_t as low as $10^{-6} I_c^0$ allow to reduce the critical current of Nb\Au wires as shown on Fig. 6.2. Also, the injection of hundreds of pW is sufficient to strongly reduce the critical current (see Fig. 6.2b) or even completely suppress superconductivity for the samples with the lowest critical temperatures (see Fig. 6.3). Additionally, most of the devices in which the field effect transistor is investigated are made of titanium, which critical temperature (about 500 mK) is lower than that of all the samples studied in this PhD. For the few aluminum ($T_c \approx 1.5$ K) devices [27], the modulation of the critical current by a backgate voltage is less efficient. Consequently, the orders of magnitude of leakage powers and currents are sufficient to affect significantly the FETs critical current. Besides, although $I_L \sim 10^{-6} I_c(V_g = 0)$, one should remind that the injected quasiparticles have an energy of the order of $eV_g \sim 30$ eV, that is to say orders of magnitude larger than the superconducting gap ($\Delta_0 \approx 60$ μeV for Ti), so that $eV_g \sim 10^6 \Delta_0$. By comparing the characteristic energy of the superconductor and the injected quasiparticles energy, the argument of negligible power does not stand.

Argument of independence of critical temperature upon application of backgate voltage

Measurements of the critical temperature T_c under the application of a backgate voltage V_g high enough to lead to almost full suppression of the critical current I_c showed that T_c was independent of V_g within the experimental error [85]. Then, the authors assert that if quasiparticle overheating occured, if some injected power led to a strong suppression of I_c it should also reflect into a sizable decrease of T_c ([27] Supplementary).

As a comparison, considering the modulation of the critical temperature of sample N07 presented in Fig. 6.1, an injected power $P = I_t V_b/2 = 500$ pA×200 mV / 2 = 50 pW is required to shift the critical temperature to lower values. Such an injected power strongly reduces I_c at low temperature since it raises the effective temperature of the nanowire to $\approx 0.9T_c$ (see Fig. 6.3b). Lower powers (a few pW) still reduce I_c but do not affect T_c within experimental accuracy. Then, **our experiment proves that for relatively small quasiparticle overheating powers, the critical temperature can remain unchanged while the low temperature critical current is affected.** This is not surprising since at low temperature, the electronic thermal conductivity of the superconductor is vanishing whereas near T_c, it approaches the normal metal value. Thus, the injected power is a small perturbation near critical temperature since it is easily carried away (by heat diffusion to the leads) by contrast with low temperatures.

Besides, in another experiment [84], the resistance of the FET does not go to zero upon application of large backgate voltage (see Fig. 6.18). The authors develop a model responsible for the emergence of an inhomogeneous superconducting state under the application of an electric field. Nevertheless, this could be a more trivial heating effect. The onset of the transition in Fig. 6.18b is indeed independent of V_g, but this curve looks like the one measured with our Nb\Au nanowires (Fig. 6.1): the critical temperature of the leads (530 mK in Fig. 6.18b) is not affected by quasiparticle injection and the critical temperature of the Dayem bridge could be below 480 mK. The value of the resistance plateau below 530 mK is governed by the normal part of the Dayem bridge which increases together with the gate voltage.

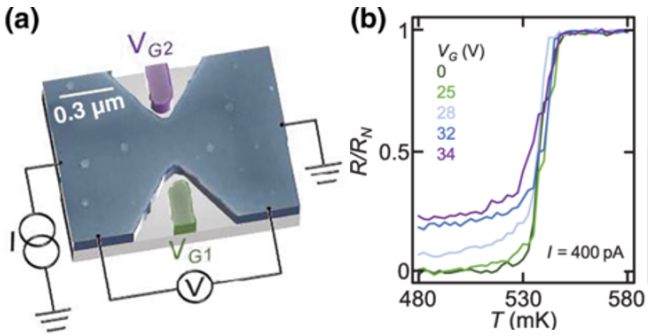

Figure 6.18: Effect of gate voltage on superconducting Dayem-bridge field effect transistor. (a) Scheme of the superconducting Dayem-bridge. The titanium device (blue) is current biased and the voltage drop is measured while the gate voltages V_{g1} and V_{g2} are applied to the bottom (green) and top (violet) lateral gate electrodes. (b) Normalized resistance R/R_N as a function of temperature T for different gate voltages $V_g = V_{g1} = V_{g2}$. I is the bias current used for the measurement. From [84].

Argument of the temperature evolution of the shape of the field effect transistor $I_c(V_g)$ characteristics

As in all FET experiments [27, 85, 84, 26, 89], the critical current of the superconducting transistor (or the switching current of the Josephson junction for SNS transistors) monotonically decreases for large values of V_g as shown in Fig. 3.5b for a SuFET and Fig. 6.19b for a SNS FET. Increasing the value of the temperature increases the range of ineffectiveness of the electric field on I_c (or I_s), so that **the plateau of constant critical current widens with temperature.** The same effect is observed upon increasing magnetic field[6].

[6]For superconducting FETs only. A slight non monotonic narrowing of the plateau is measured in SNS FETs under magnetic field [26].

Furthermore, **the effect of V_g on I_c disappears at large temperatures as shown on Fig. 6.19c:** for $T > 350$ mK, V_g has no influence on I_s. Notably, the disappearance of the effect of V_g on critical current occurs at $\sim 85\%T_c$ for devices made of titanium and at $\sim 40\%T_c$ for similar devices made of aluminum [27]. The authors interpret this observation as a damping of the electrostatic effect in the devices as they approach the normal state [26].

Finally, **the critical backgate voltage V_g^c leading to complete suppression of I_c is independent of temperature** for titanium FETs[7] as shown on Fig. 3.5b.

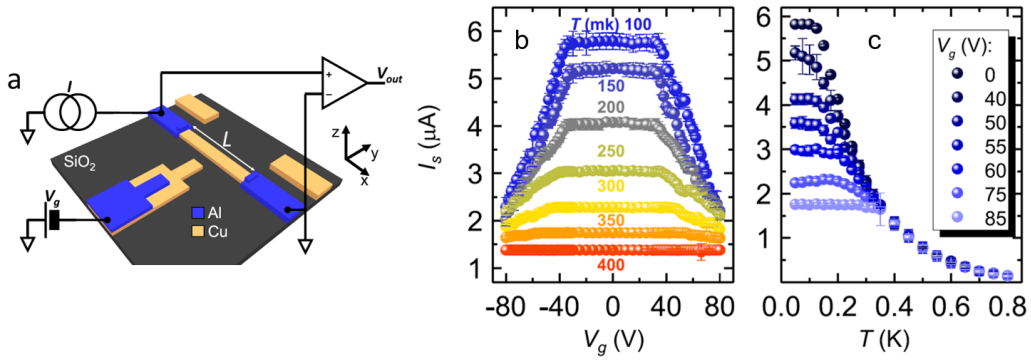

Figure 6.19: Critical current plateau of a SNS FET. (a) Scheme of the SNS FET. The Josephson junction consists in a copper wire proximitized at both ends by superconducting aluminum. A voltage V_g can be applied to the side electrode. (b) Josephson switching current I_s as a function of V_g for different temperatures T. (c) I_s versus T for different V_g. From [26].

The widening of the constant I_c plateau with temperature observed in FETs can be compared to the data measured by SCCM and presented in Fig. 6.3b. When the bath temperature at which quasiparticle injection is performed is increased, the required power to reduce the critical current increases. Fig. 6.12b also shows that a given heating power affects less the critical current when the temperature raises. Similarly to the discussion on the independance of the critical temperature versus V_g, this is expected since we are dealing with overheating effects: a given injected power is a bigger perturbation for the wire as the bath temperature decreases. In addition, the weakening of superconductivity, whether due to an increase of temperature or magnetic field, lowers the thermal resistance with the contacts(or leads). Then, the sample is less sensitive to heating. That is also probably why I_c becomes unaffected by V_g at large temperature. As for the independence of V_g^c on temperature, the same result is obtained by SCCM in Nb\Au wires: whatever the bath temperature, the effective temperature of the wire (reflecting the reduction of I_c) follows a power law at large injected powers and is also bath temperature independent. Eventually, the fact that the reduction of I_c is more efficient in titanium than in aluminum supports the above claim: the leakage power is probably sufficient to raise the temperature of the devices up to a few hundreds of mK, which almost completely destroys superconductivity in titanium ($T_c \approx 500$ mK) but has a limited impact on aluminum ($T_c > 1$ K). Consequently, **the evolution of the shape of the $I_c(V_g)$ characteristics with temperature can be explained by quasiparticle overheating.**

Interpretation of the alleged field effect by quasiparticle overheating

Similarly to the analysis presented in Fig. 6.3 for our Nb\Au nanowires, one can plot the leakage power dissipated in the FETs as a function of an effective temperature reflecting the bath temperature required to observe the same critical current when $V_g = 0$. This curve computed on the basis of experimental data extracted from [89] is shown on Fig. 6.20d. It presents a trend $P_L = kT_{eff}^2$.

[7] V_g^c is not always within the accessible V_g range as for example in Fig. 6.19b

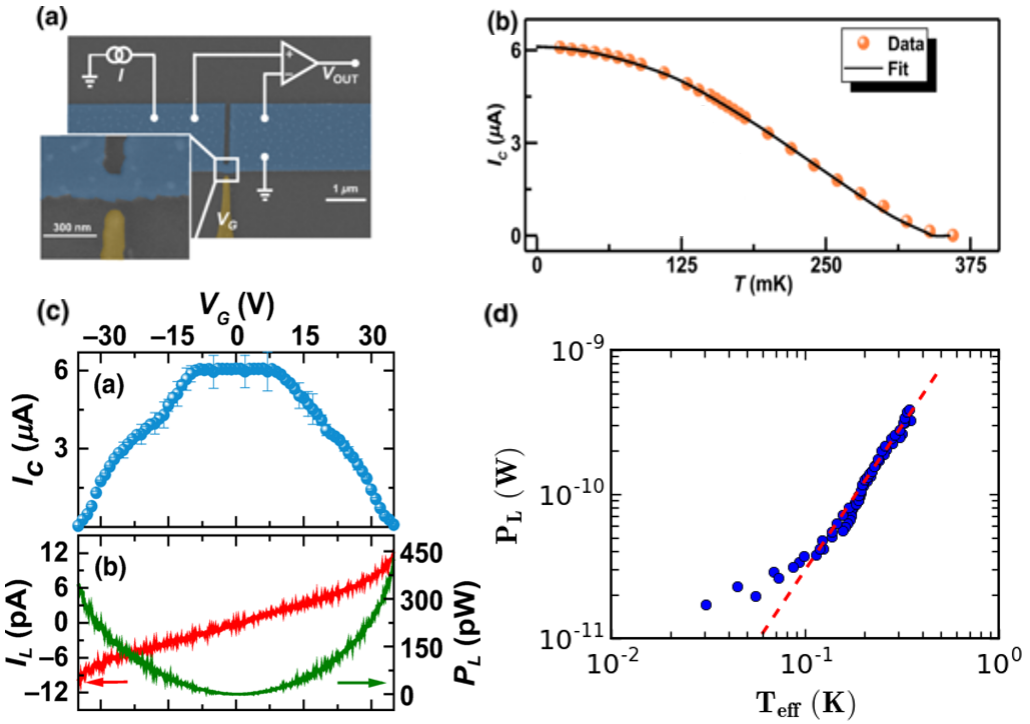

Figure 6.20: Possible quasiparticle overheating of a superconducting Dayem-bridge field effect transistor. (a) Scheme of the superconducting Dayem-bridge (blue) and side gate electrode (yellow). (b) Critical current I_c as a function of temperature T (dots). Solid line is a fit with Bardeen's formula [7] presented in Eq. 3.1a. (c) *Top panel*: I_c vs gate voltage V_g applied to the side electrode at $T = 20$ mK. *Bottom panel:* Leakage current (red) and corresponding Joule leakage power (green) as a function of V_g at the same temperature. (d) Leakage power versus effective temperature extracted from data of top panel of (c) (dots). Dashed line corresponds to $P_L = \kappa\, T_{eff}^2$ with $\kappa = 3$ nW.K^{-2}. (a), (b) and (c) are taken from [89]. (d) is computed from these data.

Since the lithographed junctions do not allow to adjust independently V_g and I_L, one cannot assert that some quasi equilibrium is reached by contrast with our SCCM study (see Fig. 6.2). However, the fact that data are compatible with a power law trend suggests an overheating of the sample. Furthermore, the $P_L = \kappa T_{eff}^2$ trend corresponds to the mechanism of power dissipation by quasiparticle diffusion only (see Eq. 6.13). The extracted $\kappa = 3$ nW.K^{-2} goes in this direction. Indeed, according to Eq. 6.13, the value of κ corresponding to diffusion of heat by quasiparticles for punctual power injection in the middle of a wire with constant width w is $\kappa = wt\alpha_e/x_R$ where t the thickness, $\lambda_e = \alpha_e \times T$ the electronic thermal conductivity and x_R the distance to the reservoirs. Naturally, deviations are expected since neither the wire has a constant width nor the power is injected punctually (the side gate electrode has a finite width as shown on Fig. 6.20a). Yet, the theoretical value for κ is of the same order of magnitude than the extracted one: taking $w = 120$ nm, $t = 30$ nm, x_R equal to the length of the constriction (150 nm) [89] and[8] $\alpha_e = 0.1$ W.K^{-2}.m^{-1} one finds $\kappa = 2.4$ nW.K^{-2}.

To conclude, these arguments do not reject the potential existence of some unexpected field effect, but they show that **quasiparticle overheating can explain all experimental features observed in superconducting FETs.**

[8]This typical value for a metal at low temperature (the same as the one found in our Nb\Au samples) is taken since the resistivity of the Ti samples of [89] is not given in the paper (this would have provided α_e with Wiedemann-Franz law).

6.9 Conclusion

The tunnel injection of quasiparticles with a STM allows to vary both position and tunnel resistance of the junction. Then, the ability to inject the same power with different tunneling setpoints demonstrates the existence of some quasiparticle overheating and that a quasi equilibrium characterized by an electronic temperature is reached for a broad range of tunneling setpoints in Nb\Au nanowires. Furthermore, the spatial resolution of the SCCM technique helps to probe the diffusion processes at stake. A heat diffusion model in the quasi equilibrium limit is then developed and accounts quantitatively for the all experimental features. It also allows to extract microscopical parameters of the electron-phonon interaction. Further investigation of the out of quasi equilibrium regime paves the way to the study of several processes of quasiparticle dynamics such as electron-electron, electron-phonon, phonon-electron and phonon-phonon interactions. Finally, these results reconsider the physical interpretation of superconducting FETs given in literature.

Chapter 7

Vortices in Nb\Au nanowires

Contents

In a type II superconductor, magnetic vortices are one of the strongest inhomogeneity of the density of states that can be found. In addition, at low temperatures the thermal conductivity is expected to vary significantly between the vortex core and the superconducting regions. Consequently, it is of fundamental interest to study the local injection of quasiparticles and its influence on the critical current in type II superconducting nanowires under magnetic field. Moreover, the magnetic field also allows to reduce the critical current in the absence of quasiparticle injection. This reduction of the critical current helps to prevent overheating due to Joule effect at the transition, and reduces the maximum Lorentz force exerted on vortices so they are more likely to remain motionless when a supercurrent is flowing.

The presence of excess quasiparticles can be characterized by an effective electronic temperature that exceeds the temperature of the phonon bath as discussed in the previous chapter. In the field of superconducting electronics, this overheating limits the performances of mesoscopic devices, causing for instance decoherence in qubit systems [76, 91] or decrease of the quality factor in superconducting resonators [87, 29]. Since vortices are believed to act as quasiparticle traps [109, 82], their physics is of particular interest for who wants to improve the performances of superconducting circuits.

In this chapter we investigate the influence of magnetic vortices on the out of equilibrium properties of our superconducting nanowires. We first explain how to locate by STM vortices induced by a magnetic field and how to detect when a vortex is unpinned by the supercurrent. Then we present Scanning Critical Current Microscopy (SCCM) experiments in the presence of vortices. We interpret our results in terms of quasiparticle trapping by vortices. We also interpret the influence of the magnetic field on the electronic thermal conductivity as a confirmation of the heat diffusion model developed in the previous chapter. Finally we discuss the effect of vortex flow on the critical current in the absence of quasiparticle injection.

7.1 Observation of vortices by STM

Fig. 7.1 shows images of vortex lattices in a Nb\Au nanowire for different magnetic fields. The experimental technique of differential conductance measurement is described in Subsection 1.2.3. During a scan with the STM tip, both the topographic (Fig. 7.1a) and spectroscopic (Fig. 7.1b) image of the same area are recorded. Here, the AC modulation for the spectroscopy is only applied on the nanowire. Then, when the tip scans the ground plane on the left area of Fig. 7.1b, no modulation of the tunneling current is recorded. However, when the tip is in the right furrow separating the nanowire from the ground plane, a tunnel current flows between the tip and the nanowire, so some differential conductance is measured. This difference between the left and right part of the image is due to the asymmetrical shape of the STM tip. When it is above a furrow, the tip apex cannot reach its bottom but the tunneling current is rather established on the side of the tip with either the ground mass or the nanowire depending on the sharpness of the tip on its right and left sides. This effect is however much less visible in the topographic image because the tip is significantly lower above both furrows than when it scans the nanowire or the ground plane.

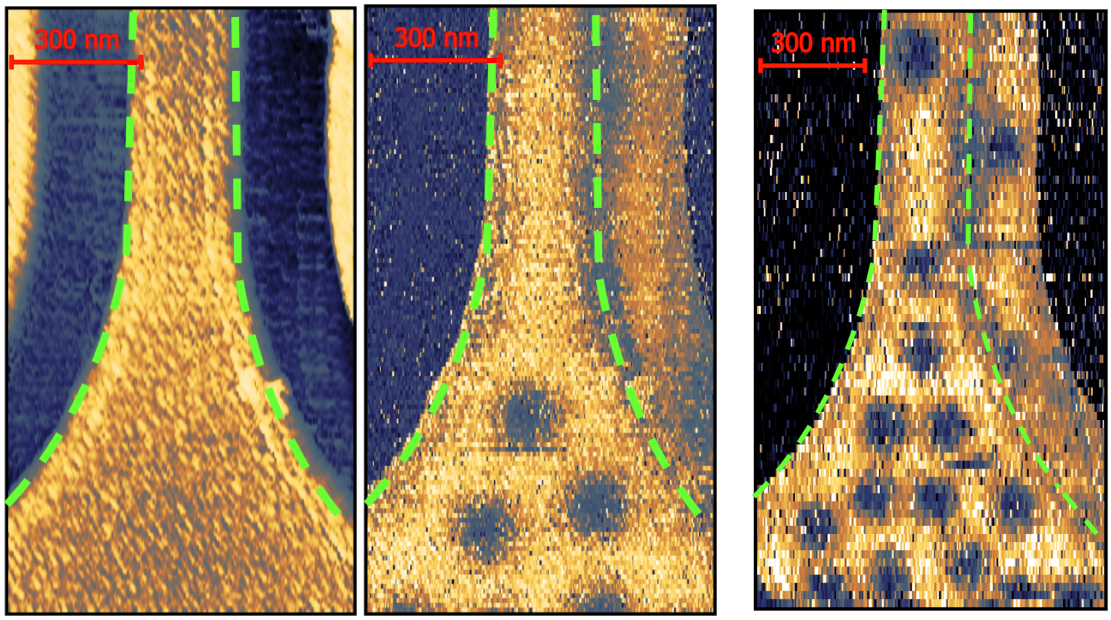

(a) B=23 mT **(b)** B=23 mT **(c)** B=34 mT

Figure 7.1: Penetration of vortices in a nanowire. (a) and (b) Topographic and spectroscopic images (I_t = 500 pA ; V_b = 400 μV) of the same area for a perpendicular magnetic field B = 23 mT. The color scale is in arbitrary units with light - respectively dark - colors corresponding to large - respectively small - values of tip height and differential conductance. Green dashed line indicates the (geometric) edges of the nanowire. (c) Spectroscopic image of the same sample for a larger magnetic field B = 34 mT. Sample N04.

Fig. 7.1c shows the spectroscopic image of the same region than Fig. 7.1a, but recorded with a larger magnetic field. The same effect than above occurs when the tip scans the right furrow area. For both magnetic fields, a vortex lattice appears in the leads, whereas vortices penetrate in the nanowire only for the larger magnetic field. Indeed, the critical field B_{pen} below which no vortex can penetrate in a strip of width w varies as ϕ_0/w^2 (see Eq. 7.5). For the present sample, B_{pen} = 28 mT in the 300 nm wide nanowire, in agreement with the observed behavior. When B increases, the lattices becomes denser, but the size of the vortices remains unchanged[1].

[1]The color scale is chosen to provide the best contrast, but rigorously speaking the vortex core does not

Fig. 7.2 shows the DOS in a vortex core for different wire currents I_{wire}. For $I_{wire} = 0$ the DOS is flat, as expected, but when I_{wire} overcomes a value I_{pin} the DOS becomes gaped, as in a superconducting region. This indicates that the vortex has moved under the effect of the current flow. When one wants to measure the critical current of the nanowire while performing quasiparticle injection in a vortex core this effect must be avoided. Then, one can look for another vortex with a higher I_{pin} - the different forces governing vortex motion and therefore the value of I_{pin} are discussed below in Subsection 7.3.2. Another strategy consists in increasing the magnetic field to reduce the critical current to a value lower than I_{pin}.

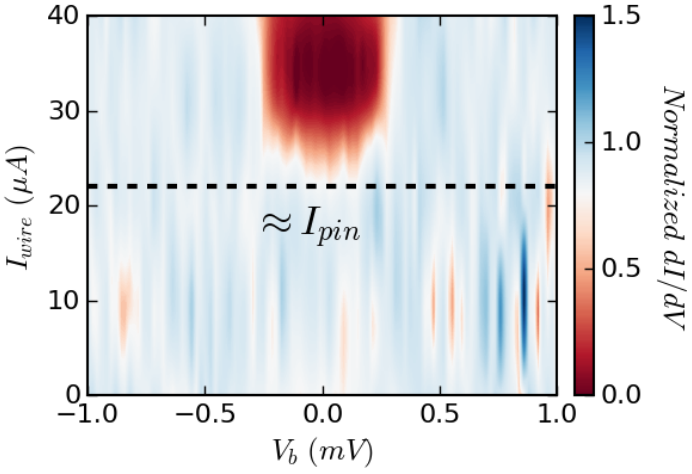

Figure 7.2: Unpinning of a vortex under the effect of a supercurrent flow. Normalized differential conductance as a function of bias voltage for different wire currents measured in a vortex core. When the current overcomes the value I_{pin} the DOS goes from a normal to a superconducting shape, indicating the disappearance of the vortex at the position of the tip. $B = 23$ mT. Sample N04.

Vortices can be imaged by STM. They nucleate more easily in the leads than in the nanowire. Their motion can be detected by STS.

7.2 Influence on critical current

In this section, we investigate how the DOS at the injection position - modulated by the presence of vortices - affects the critical current. Since injected quasiparticles have an energy comprised between 0 and eV_b, we address the high and low quasiparticle energy regimes by adjusting the bias voltage to $eV_b \gg \Delta_0$ and $eV_b \approx \Delta_0$. Finally, we probe how the diffusion and relaxation processes in the dead-end strip geometry are affected by the presence of vortices.

7.2.1 Injection of low energy quasiparticles

Fig. 7.3 shows the influence of the injection position around a vortex on the critical current of the nanowire, for a constant tunneling setpoint. The vortex is located in the nanowire, and it has first been ensured that I_{pin} is larger than the critical current in the absence of quasiparticle injection by performing the same experiment than in Fig. 7.2 and observing a flat DOS up to the critical current. Then, the tip scans the surface of the sample with the tunneling setpoint ($I_t = 1$ nA; $V_b = 400$ μV) and both tip height and differential conductance are recorded to provide Fig. 7.3a and 7.3b. The tip stops regularly at positions corresponding to the grid of Fig. 7.3c (with a lower resolution). The setpoint is shifted to ($I_t^{I_c} = 1$ nA; $V_b^{I_c} = 500$ μV) and the critical current is measured several times to perform statistical averaging.

corresponds to the whole dark circles. Indeed, the spectroscopic image reflects the height of the coherence peaks, which weakens in the vicinity of the vortex because of the screening currents around the vortex core. However, only a smaller part of diameter $2\xi \sim 60$ nm inside the dark spot corresponds to the vortex itself, i.e. a normal region with a nearly flat DOS.

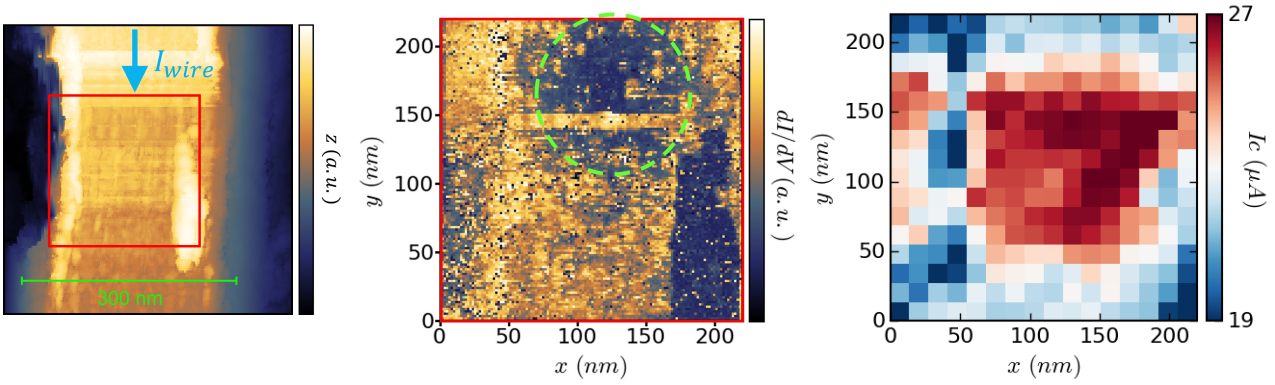

Figure 7.3: Tunneling injection of low energy quasiparticles in the vicinity of a vortex. (a) STM topographic image of the nanowire with in red inset the area of the SCCM measurement. The blue arrow indicates the direction of the current. (b) Spectroscopic image at $I_t = 1$ nA and $V_b = 400$ μV recorded during the SCCM measurement. Dashed green line indicates the position of the vortex. (c) Critical current as a function of injection position for a constant tunneling setpoint $I_t^{I_c} = 1$ nA and $V_b^{I_c} = 500$ μV. $B = 46$ mT, $T = 100$ mK and $\Delta_0 = 380$ μeV. Sample N04.

There is a correlation between the spectroscopic image and the critical current map: when the injection is performed in the vortex region, the critical current is higher than when the injection occurs in the superconducting regions. Nonetheless, the area of higher critical current is slightly shifted in the direction of the current flow with respect to the vortex position. In this experiment, quasiparticles are injected in the energy range $[0; eV_b^{I_c} = 500$ μeV$]$ for an energy gap equal to $\Delta_0 = 380$ μV.

7.2.2 Injection of high energy quasiparticles

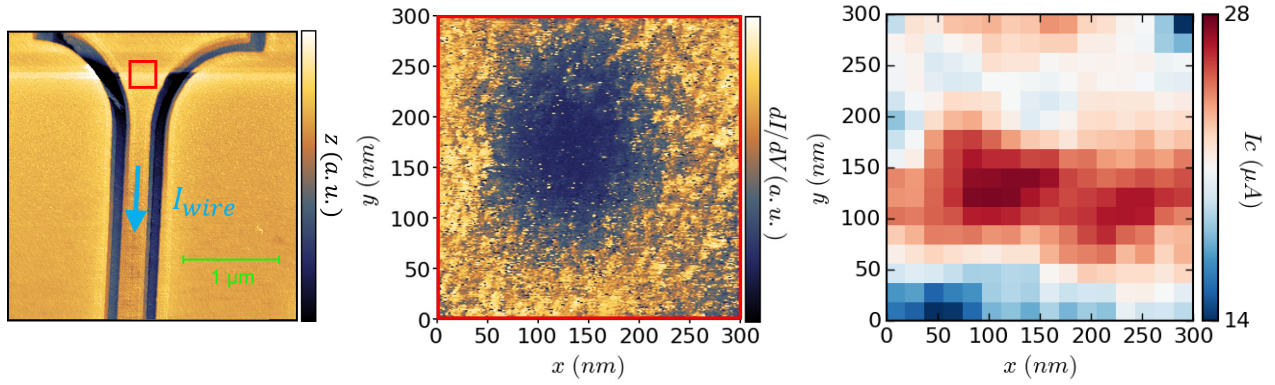

Figure 7.4: Tunneling injection of high energy quasiparticles in the vicinity of a vortex. (a) STM topographic image of the nanowire with in red inset the area of the SCCM measurement. The blue arrow indicates the direction of the current. (b) Spectroscopic image at $I_t = 1$ nA and $V_b = 400$ μV recorded during the SCCM measurement. (c) Critical current as a function of injection position for a constant tunneling setpoint $I_t^{I_c} = 1$ nA and $V_b^{I_c} = 400$ mV. $B = 23$ mT, $T = 100$ mK and $\Delta_0 = 380$ μeV. Sample N04.

The same experiment than above is performed here with $eV_b^{I_c} = 400$ meV$\gg \Delta_0 = 380$ μeV (see Fig. 7.4). The injected quasiparticles have therefore on average an energy much larger than the gap. Nevertheless, a correlation between the DOS at the injection position and the measured critical current is still observed. Notably, the critical current is higher when the injection occurs in a strip perpendicular to the current flow at the level of the vortex, and this region is also slightly shifted in the same direction than I_{wire} with respect to the vortex position.

7.2.3 Injection in the dead-end strip

In the dead-end strip geometry, the critical current is determined by the excess of quasiparticles reaching the nanowire. When the injection occurs in the dead-end strip, where no supercurrent is flowing, the determining processes are the relaxation and the diffusion of injected quasiparticles in the path leading to the nanowire.

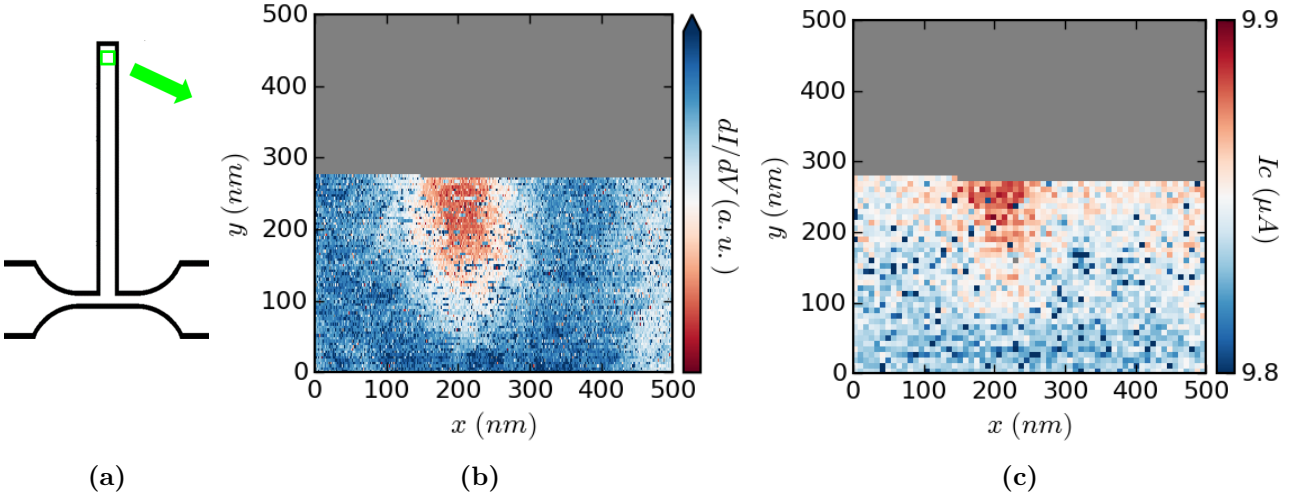

Figure 7.5: Influence of the DOS at the injection position in the dead-end strip on the nanowire critical current. (a) Scheme of the sample with the scan area located approximately 8 μm above the nanowire in green. (b) Recorded spectroscopic image during the scan at $I_t = 500$ pA and $V_b = 320$ μV. (c) Critical current as a function of injection position for a constant tunneling setpoint $I_t^{I_c} = 500$ pA and $V_b^{I_c} = 735$ μV. $B = 16$ mT, $T = 100$ mK and $\Delta_0 = 255$ μeV. Sample N15.

The influence of the DOS at the injection position is evidenced on Fig. 7.5. The remarkable low noise conditions on this experiment show that the effect of DOS persists even when the injection occurs far (≈ 8 μm) from the nanowire. Interestingly, no shift between the critical current map and the spectroscopic image is detected, and no supercurrent is flowing in this region because of the sample geometry. The long acquisition time did not allow to finish the measurement in between two helium fills (the tip is then retracted and the measurement stopped because of the induced noise).

In Fig. 7.6, injection of quasiparticles at large energies compared to the superconducting gap is performed at the same position in the absence ($B = 0$) and in the presence of vortices ($B = 16$ mT) in between the tip position and the nanowire. For $B = 16$ mT, vortices are only present in the dead-end strip and not in the nanowire[2]. The injection position is located 7 μm

[2]Accordingly to vortex penetration critical fields, since for sample N16 $B_{pen} = 24$ mT for the 300 nm wide nanowire and $B_{pen} = 9$ mT for the 600 nm wide dead-end strip (see Eq. 7.5).

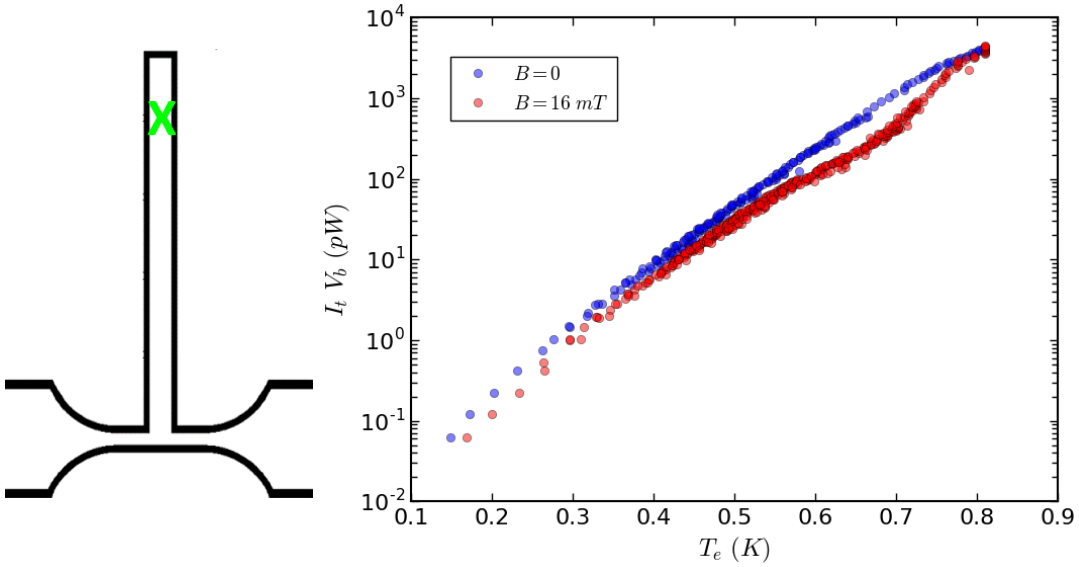

(a) **(b)**

Figure 7.6: Influence of the presence of vortices on heat diffusion. (a) Scheme of the sample with injection position (green cross). (b) I_tV_b as a function of electronic temperature for two different magnetic fields. For B=16 mT vortices are present in the dead-end strip. Sample N16 ($T_c = 960$ mK).

above the nanowire, and is chosen to be in a superconducting region (not in a vortex) for the finite magnetic field measurement. The two $I_c(T)$ curves in the absence of tunnel injection by the tip for B=0 and B=16 mT allow to extract the associated electronic temperatures from the measured critical currents (as explained in Section 6.3). Then, we observe that for the same injected power $I_tV_b/2$, the electronic temperature of the nanowire is higher in the presence of vortices than in their absence. This effect is present at low electronic temperatures, and becomes stronger in an intermediate regime ($T_e/T_c^{nw} \approx 0.7$). Finally, the difference disappears when T_e approaches T_c^{nw}.

For the same tunneling setpoint, the critical current is less reduced when quasiparticle injection occurs in the vicinity of a vortex.

Overheating of the nanowire by injection of quasiparticles in the dead-end strip is enhanced by the presence of vortices.

7.3 Discussion

Here we discuss how vortices affect the physical properties of our samples, depending on whether vortices are generated by an external magnetic field or by a supercurrent flow.

7.3.1 Vortices induced by a magnetic field

To begin with, the fact that some vortices generated by a magnetic field can be unpinned by a supercurrent flow lower than the critical current density as evidenced by Fig. 7.2 can be related to the low temperature upturn of the upper critical field observed in similar samples (see Section 4.4). Indeed, this upturn has been observed in dirty superconductors and explained by the pinning of vortices by the spatial fluctuations of the order parameter due to disorder [98]. In this model, the transition to the normal state occurs when the vortex glass melts, but for a

larger magnetic field than the one predicted by the mean field theory which does not take into account the strong pinning of the vortices by disorder. In our Nb\Au samples, we observe a regime where the vortex glass has at least partially melted since vortex motion is evidenced by Fig. 7.2. Yet, perfect conductivity is not lost and the sample is still superconducting. Therefore, this regime corresponds to vortex glass fluctuations in the superconducting state such as those at the origin of the upturn of the upper critical field.

Influence on the critical current

To interpret the dependence of the critical current on the DOS at the injection position for a constant tunneling setpoint, one should pay special attention to the power effectively deposited by the tip into the nanowire. Indeed, the two situations where tunneling occurs in a vortex core and in a superconducting region are very different at low bias energy. For instance, when the bias voltage V_b is equal to Δ_0/e in a superconducting region with a hard gap, only electrons with an energy Δ_0 can tunnel, whereas in a vortex core (with a nearly flat DOS), tunneling is allowed for all electrons in the energy range $[0;\ \Delta_0]$ and the average energy of tunneling electrons is $\Delta_0/2$.

In the following we assume the tip to be perfectly metallic and therefore having a flat DOS over the full energy range under consideration. The DOS is also assumed to be metallic in the vortex cores and is be given by Usadel equations (see Subsection 2.2.2) in the superconducting regions. We will consider elastic tunneling with a transmission coefficient independent of the electron energy (see Section 1.2). Then, the tunnel current is given by Eq. 1.5 which simplifies under our assumptions to:

$$I_t(V_b) = \frac{1}{eR_T}\int_{-\infty}^{\infty} dE\ N_s(E)(f_s(E) - f_{tip}(E - eV_b)) \tag{7.1}$$

with R_T the resistance of the tunnel junction, N_s the DOS of the sample and f the Fermi-Dirac distribution where the subscripts *tip* and s refer respectively to the tip and the sample. Using the same tunneling rates than in Section 1.2 leading to Eq. 1.5, but considering the energy and not the charge transferred by the tunneling electrons, one obtains the net power transfer from the tip to the sample [80]:

$$P_{cool}(V_b) = \frac{1}{e^2R_T}\int_{-\infty}^{\infty} dE\ (E - eV_b)N_s(E)(f_{tip}(E - eV_b) - f_s(E)) \tag{7.2}$$

The subscript *cool* is used since this power is extracted from the tip to the sample and therefore cools the tip. This effect will be addressed in Section 8.2. Since the source applying the bias voltage dissipates a power I_tV_b in the tip-sample system, the power dissipated in the sample[3] equals:

$$P = I_tV_b + P_{cool} \tag{7.3}$$

Then, we define P_S and P_V as the powers effectively deposited in the sample when the tip is located respectively in a superconducting region and a vortex region for the same tunneling setpoint. Thus, for every value of V_b, R_T in Eq. 7.2 has to be adjusted to provide the same I_t in both cases (see Fig. 7.7a). Experimentally, this corresponds to the variations of the tip height. Fig. 7.7b shows the ratio P_S/P_V as a function of bias voltage. As expected, a larger power is injected in the superconducting regions than in the vortex regions for low bias voltages V_b. The difference disappears for large V_b, where in both cases $P_S \approx P_V \approx I_tV_b/2$ as it was defined in previous chapter. We took the base temperature of the fridge (50 mK) as the effective temperature for the Fermi-Dirac distributions. This value has an influence on the divergence of

[3] In the case of a normal metal-normal metal junction the power is dissipated equally in both electrodes.

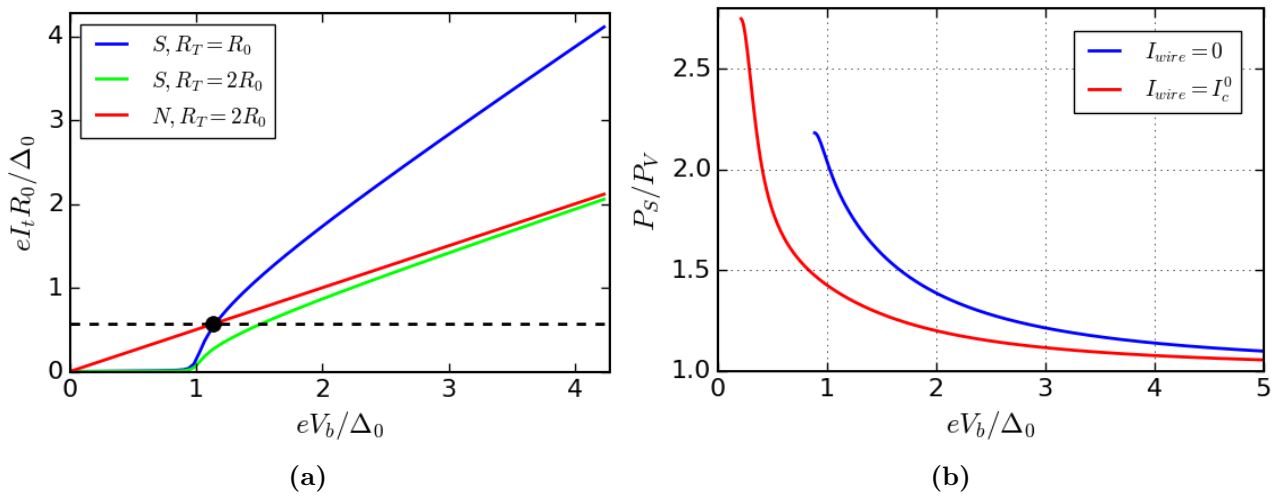

Figure 7.7: Influence of the DOS of the sample on the power injected by a normal tip. (a) Illustration of the constant tunneling current mode: $I_t - V_b$ characteristics of a tunnel junction with a normal (N) and a superconducting (S) sample for different tunneling resistances R_T computed from Eq. 7.1. For a given setpoint (I_t, V_b) (black circle), the tunneling resistance R_T (driven by the tip height) has to be adjusted to different values depending on whether the sample is normal (red) or superconducting (blue). In the example shown in the figure, the tunneling resistance is doubled when the sample is normal. (b) Ratio between the power injected in a superconducting region P_S and the power injected in a vortex core (normal region) P_V as a function of bias voltage, for two different currents flowing in the superconductor. P_V and P_S are computed from Eq. 7.2 for the same tunneling setpoint, and therefore for different tunneling resistances R_T. The sample DOS is flat in the vortex and is given by Usadel equations in the presence of supercurrent in the superconducting region. An electronic temperature of 50 mK for the Fermi-Dirac distributions and a typical $\Delta_0 = 380$ μeV are used (for larger electronic temperatures, P_S/P_V is smaller). At low bias voltages, the tunneling current is exponentially suppressed in the case of a superconducting sample, so P_S is not defined unless R_T vanishes, which does not make sense in tunnel regime.

P_S/P_V when $eV_b < \Delta_0$ but not in the $eV_b > \Delta_0$ region which is the interesting regime for our experimental conditions[4].

In the experiment of Fig. 7.3, $eV_b^{I_c} \approx 1.3\Delta_0$. For this value, $P_S \approx 1.4P_V$ when the critical current is reached, so one cannot rigorously state that the experimental conditions are the same since the average injected power is not constant. However, in this regime of injected powers ($P \approx 0.5$ pW), a change of 40% in P is not sufficient to explain a 30% difference in critical current (for instance see Fig. 6.2b). Furthermore, such a correlation between the DOS and the critical current as a function of the tip position persists even when the difference between P_S and P_V is negligible (see below).

For $eV_b \geq 3\Delta_0$, P_S and P_V differ by less than 10% at critical current. Since such a difference corresponds roughly to the fluctuations of the tunneling current during the experiment, one can consider that for $eV_b \geq 3\Delta_0$ P_S and P_V are equal within our experimental accuracy. This corresponds to the experimental situations of Fig. 7.4 and Fig. 7.5, so the higher critical

[4]To measure the critical current I_c under quasiparticle injection one needs to ramp I_{wire} from zero to I_c in tunnel regime. For $I_{wire} = 0$, the absence of subgap states prevents a tunnel current to flow for too low bias voltages values.

current measured for quasiparticle injection in a vortex cannot be attributed to a smaller injected power.

Then, this experimental observation must be due to the fact that the quasiparticle dynamics depends on the local density of states. In contrast with the superconducting regions, the energy gap is locally suppressed in the vicinity of the vortices, so that states with an energy below the superconducting gap Δ are available. Thereby some quasiparticles can loose energy (by any inelastic process described in Section 6.5) and end up being trapped in the vortex region where they are Andreev reflected at its boundaries and converted into Cooper pairs in the condensate. This quasiparticle trapping therefore reduces the quasiparticle density in the superconducting regions where the supercurrent flows so that the transport properties (such as the critical current) are less affected.

It is interesting to notice that the correlation between the DOS at the injection position and the critical current has been observed in the two completely different energy regimes where $eV_b^{I_c} \sim \Delta_0$ and $eV_b^{I_c} \gg \Delta_0$. In the case where $eV_b^{I_c} \sim \Delta_0$, a significant fraction of the quasiparticle is directly injected by the tip in "bound" states (where quasiparticles are trapped). By contrast, when $eV_b^{I_c} \gg \Delta_0$ the trapping of the quasiparticles injected in the vicinity of the vortex involves relaxation processes. The relaxation time τ_{rel} is expected to be of the order of the diffusion time towards the outside of the vortex since a non negligible fraction of the quasiparticles is trapped. The diffusion time can be approximated by L^2/D where L is the vortex size and D the electron diffusion constant. With $L \approx 2\xi_{GL}$ this leads for our samples[5] to $\tau_{rel} \sim 10$ ps. This is consistent with our estimation of the relaxation time made in Section 6.5 (p. 80) where we estimated τ_{rel} to be of the order of a few picoseconds when $eV_b \gg \Delta_0$.

The problem of vortex trapping was addressed theoretically in [99]. The quasiparticle trapping rate of a single vortex is predicted to scale as $\gamma^{1/3}$ where γ is the local depairing energy. For an isolated vortex, $\gamma = \frac{1}{2}\Delta(\frac{\xi}{r})^2$ where r is the distance to the vortex core and Δ the superconducting gap far from the vortex. Because of this smooth spatial dependence, the contribution of trapping in the peripheral regions may dominate the one in the vortex core because these peripheral regions can be large. Their radius R is determined by the condition $\Delta - \Delta_g(R) \approx k_B T$ where Δ_g is the spectral gap. Indeed, beyond this distance thermally activated quasiparticle escape overcomes quasiparticle trapping since the energy "depth" of the trap (approximated here by a potential well of height $\Delta - \Delta_G$) is too low.

Despite the refinement of the model, the authors of [99] could not account quantitatively for experimental measurements of vortex trapping, the predicted "vortex trapping power" being too small by two orders of magnitude. Therefore, we think that the experimental results presented in this PhD could provide further information about the trapping mechanism. Indeed, since up to now experimental measurements probing vortex trapping are transport measurements carried on with mesoscopic samples, the authors of [99] summed up the different contributions to vortex trapping over the whole sample. In our experimental setup however, quasiparticle injection is performed locally, which allows to distinguish between core and peripheral contributions. On the other hand, the problem is here theoretically more complex than the one treated in [99] since both magnetic field and supercurrent are present. This requires new theoretical developments which are beyond the scope of this PhD work.

Finally, we think that the shift between the vortex position and the trapping area, where quasiparticle injection is less efficient in reducing the critical current, (see Fig. 7.3 and 7.4) could be due to Doppler effect. This shift has been observed in the direction of the supercurrent flow, and is absent in regions where there is no supercurrent (see Fig. 7.5). It is therefore probably related to the supercurrent flow and its direction.

[5] For which $\xi_{GL} \approx 30$ nm, $l \approx 1$ nm and $v_F = 1.4 \times 10^6$ m.s^{-1}, see Table 4.2 and Section 4.2.

In order to get a qualitative understanding of the situation, let's consider the ballistic case (mean free path larger than the coherence length). The effect of an uniform supercurrent flow on the excitation spectrum can then be written as:

$$E_p = \sqrt{\epsilon_p^2 + \Delta^2} + E_{dop} \tag{7.4}$$

with E_p the quasiparticle excitation energy, ϵ_p the kinetic energy of an electron in the state described by its momentum $\overrightarrow{p}$ and $E_{dop} = \overrightarrow{p}.\overrightarrow{V_s}$ the Doppler energy where $\overrightarrow{V_s}$ is the superfluid velocity [40]. The supercurrent density writes $\overrightarrow{J_s} = en_s\overrightarrow{V_s}$ where n_s is the density of superconducting electrons. Since the charge of the electron is negative, the Doppler energy E_{dop} is positive for quasiparticle states with a momentum in the opposite direction to the current flow, and negative for states with a momentum in the same direction than the current. Thereby the normalized single electron density of states $d\epsilon_p/dE_p$ depends on the direction of the momentum $\overrightarrow{p}$ (through the sign of E_{dop}) as shown on Fig. 7.8a. In particular, electrons (quasiparticles with a positive energy $E \sim \Delta$) occupying states with a momentum going in the direction of the current ($E_{dop} < 0$) can relax their energy and reach states with an energy slightly smaller than the gap Δ. In contrast, electrons occupying states with a momentum in the opposite direction to the current cannot. Reminding the definition of the spectral gap Δ_G (energy below which no energy states are available), this can be interpreted by a smaller spectral gap for electrons going in the direction of the current.

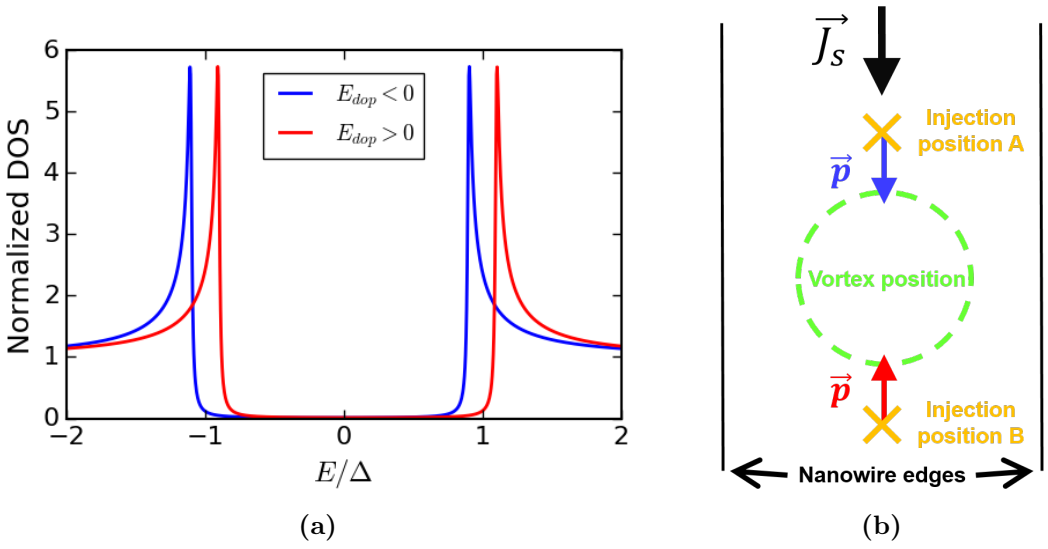

Figure 7.8: Influence of the Doppler energy on the trapping of electrons injected in the vicinity of a vortex. (a) Normalized single electron density of states (DOS) computed from Eq. 7.4 versus quasiparticle energy E for positive and negative values of the Doppler energy E_{dop}. For both curves, $|E_{dop}| = 0.1\Delta$. (b) Schematics of a vortex in a current carrying nanowire. The injection positions A and B are at the same distance to the vortex core. Two available electron states are sketched by their momentum $\overrightarrow{p}$. These two states have opposite Doppler energies because of the different orientations of their momentum with respect to the direction of the supercurrent flow (represented by the supercurrent density $\overrightarrow{J_s}$).

Then, let's consider vortex trapping. Quasiparticles are trapped in a vortex when they occupy energy states which are not available outside the vortex. This can be approximated by a potential well, which "depth" is the spectral gap far from the vortex Δ_G. Therefore, assuming that the trapping efficiency is proportional to the "depth" of the potential well, electrons moving in the direction of the current are less likely to be trapped than the ones moving in the opposite

direction due to their spectral gap difference. Fig. 7.8b sketches electron injection by a STM tip at two symmetric positions with respect to the vortex core. Electrons moving towards the vortex are more efficiently trapped when injected in B than in A because of the orientation of the current flow. Then, electron injection in B is less efficient in reducing the critical current because of vortex trapping. This corresponds to the shift observed in Fig. 7.3 and 7.4.

Note that the local density of states probed by STS is an average over all momentum. That is why as long as the Doppler energy is small compared to Δ, the main effect on the density of states is a reduction of the peak height [64]. When the Doppler energy is large, this also results in a modification of the order parameter and the situation is more complex [40]. This corresponds to the suppression of superconductivity by a supercurrent flow in the ballistic limit. In contrast, our experiment corresponds to the diffusive case so the above analysis cannot be straightforwardly applied. Indeed, the modification of the superconducting properties by a supercurrent flow in the diffusive case is described by the depairing energy (see Subsection 2.2.2 for a theoretical description and Section 5.2 for experimental observation) instead of the Doppler energy. By contrast with the Doppler energy, the depairing energy is proportional to the square of the superfluid velocity, and is in our case of the order of $0.2\Delta_0$ at critical current. This manifests by a significant modification of the density of states under a supercurrent flow. Consequently, the influence of the Doppler effect on quasiparticle trapping in the diffusive case rely on the following hypothesis. The electrons should be sensitive to a quasiparticle density of states which depends on the direction towards which they are moving. This is not straightforward since during a diffusive motion an electron often scatters and change its momentum (at least its direction in the elastic case). However one can imagine than during his displacement, the electron occupies energy states with a momentum which is in average oriented in the direction of its displacement. Eventually, if this hypothesis is valid this would explain the observed shift between the vortex position and the trapping area.

Influence on thermal conductivity

Fig. 7.6 shows that the nanowire overheating by quasiparticle injection in the dead-end strip is enhanced by the presence of vortices in between the tip position and the nanowire. As in the experiments described in Chapter 6, for large bias voltages[6] the critical current is determined by the electronic temperature where the transition driven by the current occurs, namely the intersection between the nanowire and the dead-end strip in the present geometry. Since the electronic thermal conductivity at a given temperature is higher when superconductivity is destroyed as drawn in Fig. 6.6, the magnetic field increases the average electronic thermal conductivity of the dead-end strip. Both the presence of normal regions (vortices) and the finite depairing energy due to the magnetic field in the superconducting regions contribute to this increase. Consequently, heat diffuses more easily from the tip to the nanowire, resulting in a higher electronic temperature [17]. This also confirms the interpretation of our experiments made in Section 6.5 according to which the contribution of the electrons to heat diffusion plays a major role and exceeds the one of the phonons. Indeed, the phonon thermal conductivity is rather decreased in the mixed state with regard to the zero field state, because the fluxoids act as scatterers for the phonons [75]. Therefore, the increase of the total thermal conductivity can only be due to the electrons contribution.

At intermediate temperatures ($T \sim 700$ mK), the difference in electronic temperature with and without magnetic field is larger. This suggests that the thermal conductance of the dead-end strip further increases. This may be due to the decrease of the upper critical field B_{c2} when temperature increases. This would result to a larger fraction of the dead-end strip in the

[6]For low bias voltages, one does not always observe a thermal behavior. The quasi equilibrium is then not reached and the electronic temperature not defined. This is the subject of the following chapter.

normal state, and therefore in a higher average thermal conductance.

Finally, when the electronic temperature approaches T_c, the difference disappears. In this situation the local temperature between the tip and the nanowire probably exceeds T_c, so that the dead-end strip is in the normal state no matter the value of B.

As expected, the magnetic field increases the electronic thermal conductivity.

Quasiparticle trapping by vortices has been evidenced at the microscopic scale for the first time. This is of particular interest since the microscopic trapping mechanisms remain not well understood theoretically.

The experiments revealing the motion of vortices under the action of a supercurrent while remaining in the superconducting state can be explained as a manifestation of vortex glass fluctuations such as the upturn of the upper critical field observed in Section 4.4.

7.3.2 Vortices induced by a supercurrent

As discussed in Section 5.1, the numerical solution of the Usadel equations in the presence of inelastic scattering Γ_{in} presented in Subsection 2.2.2 fits well the experimental critical current versus temperature behavior. Nevertheless, the values of Γ_{in} required to account for the critical current thermal dependence are slightly larger than the ones extracted from STS. In addition, at low temperatures the measured critical current density is about 20% smaller than the depairing current density. In Section 5.1, we attributed this discrepancy to the uncertainty over the thickness of the films. Since the presence of vortices induced by a supercurrent in our samples cannot be discarded considering Likharev limit, we will consider here the possible influence of vortex dissipation.

In order to cause such a dissipation, vortices must nucleate and be set in motion under the effect of a supercurrent flow.

Vortex motion

Vortex motion is a complex topic since many interactions compete:

- The screening currents circulating around vortices create repulsive forces between them. However, at fields above the lower critical field of a type II superconductor H_{c1}, it is energetically favorable to keep the flux density constant, so the balance between these two effects tend to create a vortex lattice.
- The disorder present in the system tends to pin the vortices on pinning centers (lattice defects for instance) as the order parameter is already depressed there and the creation of a normal core is less costly.
- When a current is flowing, the Lorentz force pushes the vortices in a direction perpendicular to the current flow and the vortex axis (in the widthwise direction of the wire in our geometry). When the current density overcomes a critical value J_{pin}, it sets the vortices in motion.
- A viscous drag opposes the vortex flow, giving a constant velocity to the vortices.
- Finally, thermal energy helps the Lorentz force to overcome pinning.

The depairing critical current density J_{dp} computed in Subsection 2.2.2 is the ultimate value for the supercurrent, at which the velocity of Cooper pairs becomes too high to carry any additional current without dissipation. If $J_{pin} < J_{dp}$, when the current density overcomes

J_{pin}, vortex flow induces an electric field parallel to the direction of the current, causing power dissipation. Therefore perfect conductivity is lost and the measured J_c is not equal to J_{dp}.

Near critical temperature, the voltage across the wire V_{wire} increases with current before the transition as discussed in Section 5.1 (see $T/T_c = 0.91$ and $T/T_c = 0.95$ curves of Fig. 5.1). Besides, Fig. 7.9 displays the temperature dependence of the critical current density for several samples together with theoretical curves computed with typical inelastic scattering rates Γ_{in} as deduced from the DOS measurements (see Table 4.3: $0 < \Gamma_{in}/\Delta_0 < 0.1$). The inset shows the critical behavior of I_c near T_c: $J_c \propto (1 - T/T_c)^{3/2}$ but J_c is approximately half the value given by Ginzburg Landau theory. One could rationally blame vortex flow dissipation for these two observations. Indeed, Likharev [73] predicts that vortex flow should occur at about half the depairing current.

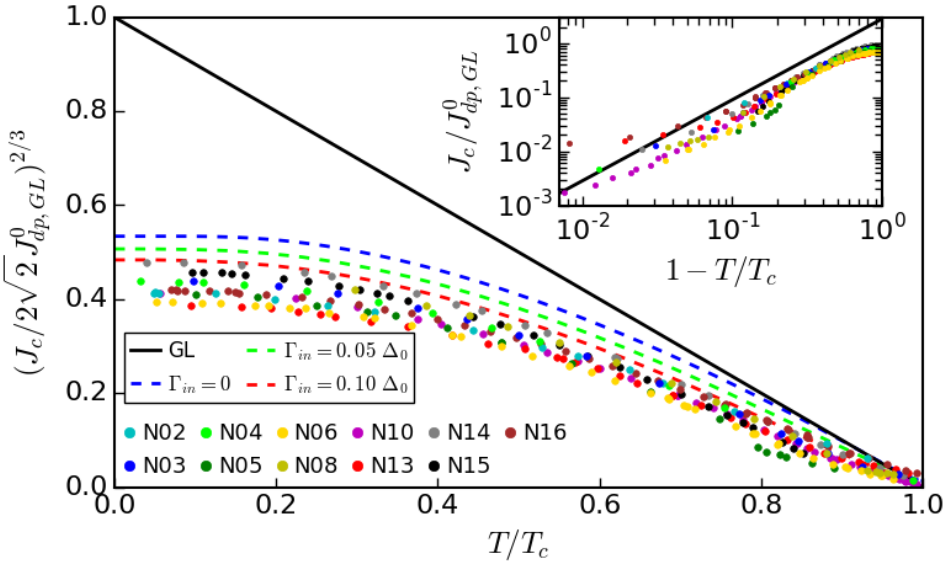

Figure 7.9: Comparison between experimental critical current density and theoretical models. Normalized critical current density ($J^0_{dp,GL} = 0.68\Delta_0^{3/2}\sqrt{N_0\sigma_N/\hbar}$ is the Ginzburg Landau result) versus reduced temperature T/T_c^{nw}. Dashed lines: numerical solutions of Usadel equations for several values of inelastic scattering Γ_{in}. Solid line: Ginzburg Landau (GL) result valid only near T_c: $J_{dp}(t) = 2\sqrt{2}J^0_{dp,GL}(1 - T/T_c)^{3/2}$. Inset: $J_c/J^0_{dp,GL}$ versus $1 - T/T_c$ in log scale.

However at low temperatures and within experimental accuracy, the measured critical current density is close to the theoretical depairing current density for all samples[7]. Furthermore, no detectable change in V_{wire} is observed at low temperatures (see Fig. 5.1) before the voltage jump at I_c.

One should then distinguish two regimes for vortices: at low temperature vortex flow is not detectable by contrast with high temperature (T/T_c close to 1). Nonetheless, if vortices were present over the whole temperature range, their effect should be more dramatic at low temperature where electronic cooling is weak (because of the low electronic thermal conductivity at low temperature) and depinning force is strong (large current density). Experimental data do not go in this direction. Furthermore, although the experiment described in Fig. 7.2 shows that I_{pin} is smaller than I_c, no sign of vortex flow is detected at low temperature as opposed to

[7]The ratio between measured and theoretical critical current densities at low temperature is close to 1 as evidenced by Fig. 7.9. The scattering of these values is attributed to the uncertainty over thickness and the fact that the nominal thicknesses may include an eventual seedlayer could account for a systematic underestimate (see Section 5.1).

the vicinity of T_c. This suggests that vortices can penetrate under the action of a supercurrent only near critical temperature.

Vortex nucleation

First of all, one should keep in mind that the stability of a vortex in a constrained geometry depends on what it is originated from. Indeed, vortices induced by a supercurrent are theoretically less stable than the ones created by an external magnetic field [73]. This explains the counter intuitive statement that at low temperature vortices can nucleate under the action of an external magnetic field while they cannot under the action of a current.

As expected by the Likharev limit, vortices turned out to nucleate much more easily in the leads than in the nanowire under the action of a magnetic field (see Section 7.1). Since Likharev limit is a bit versatile with respect to the vortex generation mechanism, another criterion can be interesting. In narrow strips, a potential barrier opposes the vortex nucleation from the edges (Bean-Livingston model). Thus, complete vortex expulsion occurs when the field is lower than a barrier penetration field B_{pen} [105, 65]:

$$B_{pen} = \frac{2\phi_0}{\pi w^2} \ln\left(\frac{2w}{\pi\xi}\right) \tag{7.5}$$

with $\phi_0 = \frac{h}{2e}$ the superconducting flux quantum, w the strip width and ξ its coherence length[8]. Without external magnetic field, the current density resulting in such a field on the edge of the wire with $\lambda_L \gg w, t$ and homogeneous distribution is[9]: $J_s = 2B_{pen}/(\mu_0 w)$, leading to the current density required for vortex penetration:

$$J_{pen} = \frac{4\phi_0}{\pi\mu_0 w^3} \ln\left(\frac{2w}{\pi\xi}\right) \tag{7.6}$$

In the nanowires ($w = 300$ nm), one obtains $J_{pen} = 14$ MA.cm^{-2} using the typical value $\xi = 30$ nm. For the 2.3 μm wide leads $J_{pen} = 0.067$ MA.cm^{-2}.

In the nanowires, J_{pen} is about one order of magnitude larger than J_{dp} (see J_c^0 values in Table 5.1). This estimation tends to confirm that current induced vortex flow does not occur in the nanowire at low temperature since no vortex can nucleate.

As for the leads however, since their width is larger the current density reaches only about 10% J_c^0 but this value is close to J_{pen}. So, although we cannot exclude the nucleation of vortices in the leads under the action of current, it is very unlikely that they are unpinned by the Lorentz force because we observed in the nanowire that J_{pin} is of the order of J_{dp}. In any case, the leads are behaving as thermostats and the dissipation due to the vortex motion would not increase significantly the electronic temperature in the nanowire.

Near critical temperature, vortex flow induced by the supercurrent in the nanowire can explain the slight difference between the measured critical current and the theoretical depairing current. Although vortex nucleation in the leads cannot be excluded, it does not affect the nanowire critical current.

[8] In the literature, the prefactor of B_{pen} varies since the critical field for complete vortex expulsion can correspond to the field above which a vortex is absolutely stable (present result) or in a metastable equilibrium. In any case, $B_{pen} \sim \phi_0/w^2$.

[9] The vector potential within these conditions has already been computed using Maxwell-Ampere law and Coulomb gauge: Eq. 2.21. The definition of the vector potential $\vec{B} = \vec{\nabla}\vec{A}$ leads to the present equation.

Chapter 8

Tunnel injection of quasiparticles close to the gap energy

Contents

As discussed in Chapter 6, the decrease of the critical current of our Nb\Au nanowires under quasiparticle injection is driven by the injected power when the bias voltage is large compared to the superconducting gap. A heat diffusion model in the quasi equilibrium limit accounts quantitatively for the experimental observations.

In the present chapter, we investigate the case where the bias voltage is close to the gap energy. In particular, we observe a non monotonic behavior of the critical current with respect to the injected power when the bias voltage approaches the gap energy. This result is interpreted by an out of equilibrium distribution function for the injected low energy quasiparticles due to their slow energy relaxation rate.

8.1 Anomaly of critical current at low energy

Fig. 8.1 shows the measured critical current under injection of low energy quasiparticles in the nanowire. Panels (a) and (b) correspond to two different positions. Data are displayed as a function of bias voltage. For both panels, the left axis is the critical current for different tunneling currents and the right axis is the measured normalized differential conductance (which is proportional to the local DOS). For large bias voltages and a constant tunneling current, we observe the same behavior than in Fig. 6.2: the critical current increases as V_b is lowered. This is expected within the heat diffusion model developed in Section 6.5 since when the bias voltage is reduced at constant tunneling current the power deposited in the sample and therefore the overheating decreases. In contrast, when V_b becomes smaller than the energy gap we observe a sharp decrease of the critical current despite the fact that the injected power continues to decrease. Indeed, lowering V_b decreases the upper bound of the energy range over which quasiparticles are injected, and the injection rate is fixed since the tunneling current is kept constant. This non monotonous behavior of the critical current with V_b is all the more marked

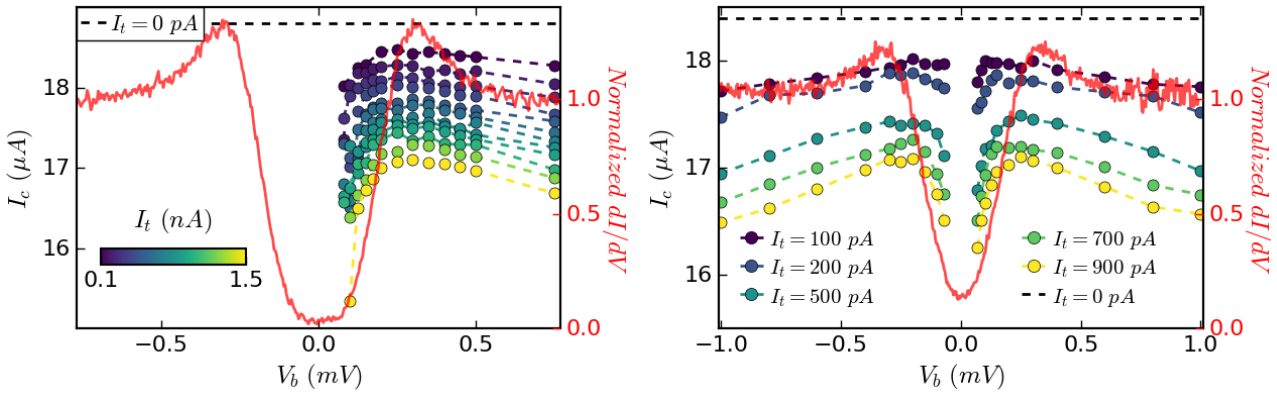

(a) (b)

Figure 8.1: Low energy anomaly. Left axis: critical current as a function of bias voltage for different tunneling currents at $T = 200$ mK. Right axis: normalized differential conductance versus bias voltage. (a) and (b) corresponds to two positions in the nanowire of sample N06.

that the tunneling current I_t is high. The observed behavior is symmetric with respect to the sign of V_b, i.e. injecting electrons or holes with the STM tip as shown in Fig. 8.1b.

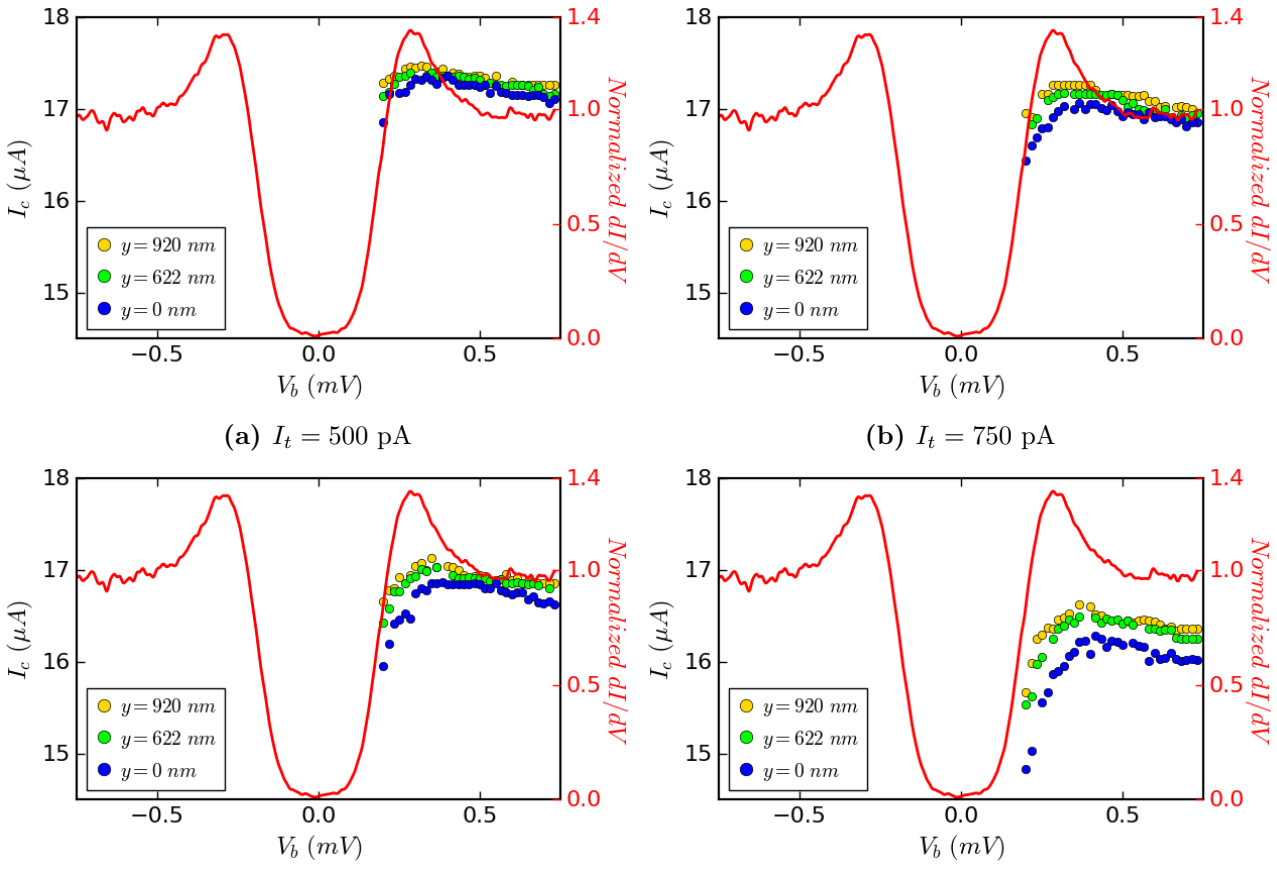

(a) $I_t = 500$ pA (b) $I_t = 750$ pA

(c) $I_t = 1$ nA (d) $I_t = 2$ nA

Figure 8.2: Low energy anomaly in the dead-end strip geometry. Left axis: critical current as a function of bias voltage for quasiparticle injection at different positions. Right axis: normalized differential conductance as a function of bias voltage. y is the distance between the tip and the intersection between the dead-end strip and the nanowire. Panel (a) to (d) correspond to different tunneling currents I_t (500 pA, 750 pA, 1 nA and 2 nA). Sample N15.

In the dead-end strip geometry, we observe the same behavior as shown on Fig. 8.2. Nevertheless, the anomaly weakens as the injection occurs further from the nanowire. Recent measurements (not shown) show that the anomaly, although strongly weakened, is still visible at the top of the dead-end strip. From this spatial dependence of the low energy anomaly, we estimate the typical lengthscale for the disappearance of the anomaly to be comparable to the dead-strip length (~ 10 μm).

For injection of quasiparticles with an energy close to the gap, we observe a low energy anomaly: the critical current sharply decreases when the bias voltage is lowered although the injected power decreases.

8.2 Discussion of the fast thermalization regime

In this section, we discuss the anomaly in the fast thermalization regime. This corresponds to the same assumption of quasi equilibrium than in Section 6.5, valid in the limit of a fast energy relaxation rate for the injected quasiparticles: the electron system can be described by an electronic temperature T_e, corresponding to the measured critical current $I_c(T_e)$. We therefore expect the temperature T_e to be governed by the power deposited by the tip in the sample consistently with our heat diffusion model of Section 6.5.

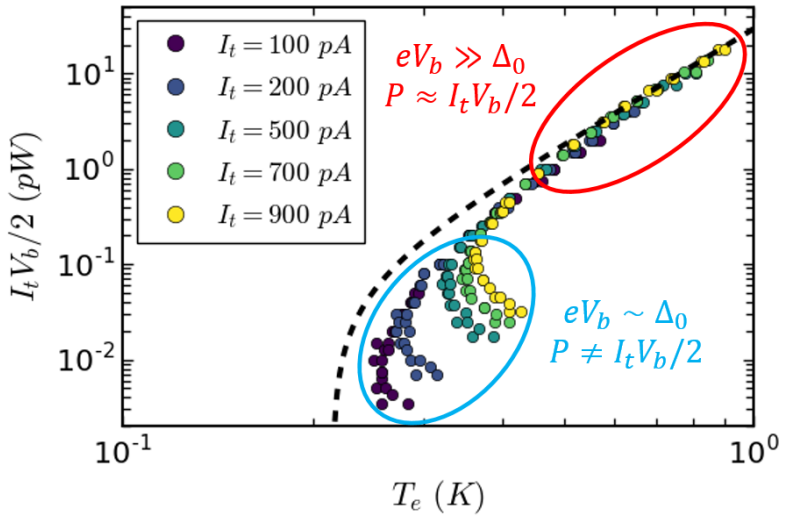

Figure 8.3: $I_t V_b/2$ as a function of electronic temperature T_e. Dashed line is the large bias thermal behavior $I_t V_b = \kappa(T_e^4 - T_b^4)$. Same experimental data than Fig. 8.1b.

Fig. 8.3 presents the same experimental data than in Fig. 8.1b by plotting the product $I_t V_b/2$ as a function of T_e. The dashed line is the large bias thermal behavior discussed in Chapter 6: $I_t V_b = \kappa(T_e^4 - T_b^4)$ with $\kappa = 59$ pW.K^{-4} and $T_b = 215$ mK (see Fig. 6.3). For $eV_b \gg \Delta_0$, the injected power is in good approximation equal to $I_t V_b/2$ and one recovers the thermal behavior. In contrast, for $eV_b \sim \Delta_0$ the power effectively deposited by the normal tip in the superconducting sample differs from $I_t V_b/2$. Indeed, according to Eq. 7.2, this power depends on the DOS N_s of the sample and on the tip and sample temperatures T_{tip} and T_s. As illustrated by Fig. 8.4, when V_b approaches the energy gap Δ, only the most energetic electrons of the tip can tunnel, resulting in an excess power deposited in the sample and a cooling of the normal tip. Since this low bias voltage regime also corresponds to the low energy anomaly, one has to take into account the heat flow in the normal-insulator-superconductor (NIS) junction to correctly interpret the anomaly. We will also address the effect of inelastic tunneling on the power deposited in the sample.

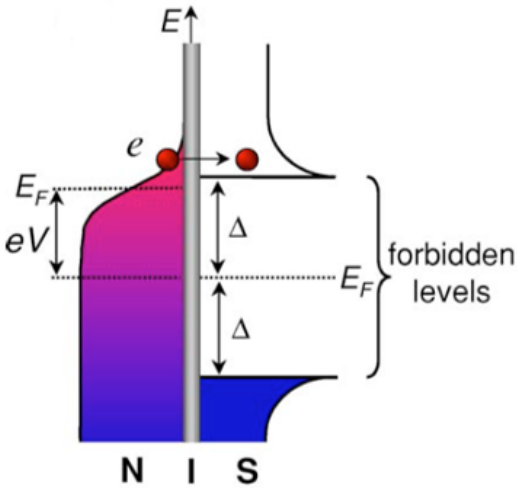

Figure 8.4: Principle of NIS cooling. Sketch of the energy-band diagram of a Normal-Insulator-Superconductor (NIS) junction biased by a voltage V. When $eV < \Delta$, only the most energetic electrons (e) can tunnel into the superconductor, thus cooling down - respectively heating up - the electron gas of the N - respectively S - electrode. Taken from [42].

Contribution of the heat flow in the NIS junction

To account for such an effect, one needs to compute the power P effectively injected in the sample as a function of the tunneling setpoint (I_t, V_b) when the critical current is reached. This can be done using Eq. 7.2 and 7.3 given the density of states of the sample at critical current N_s, the tip and sample temperatures T_{tip} and T_s, and the tunneling resistance of the junction R_T. Indeed, the latter is adjusted experimentally by varying the tip height to keep the tunnel current I_t constant when V_b is changed. Then, Usadel equations (see Subsection 2.2.2) give N_s at critical current. Eq. 7.1 provides the tunneling resistance R_T corresponding to the tunneling setpoint (I_t, V_b), N_s, T_{tip} and T_s. By definition, T_s is taken equal to the electronic temperature T_e corresponding to the measured critical current $I_c(T_e)$. Finally, T_{tip} is the only adjustable parameter.

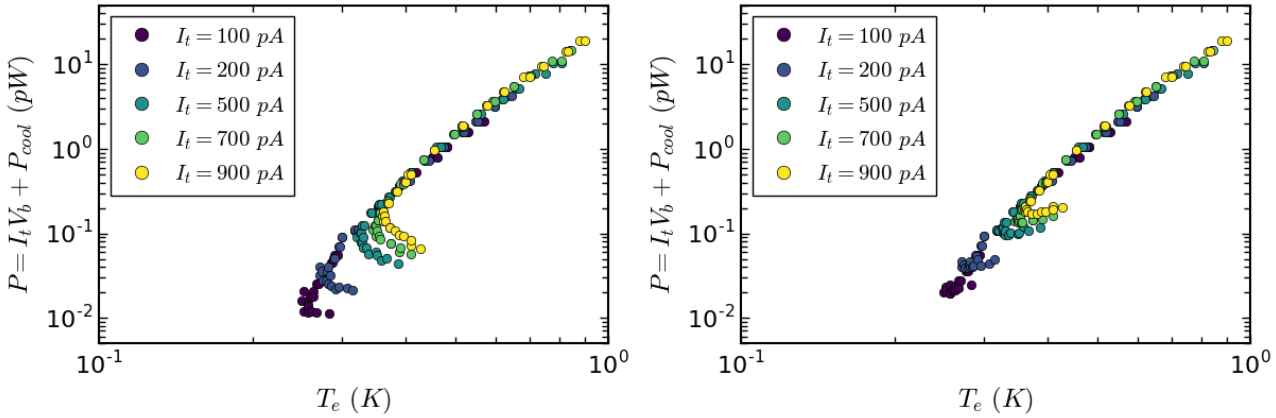

(a) $T_{tip} = 400\ mK$ **(b)** $T_{tip} = 900\ mK$

Figure 8.5: Effective power deposited in the sample P versus electronic temperature T_e for different tip temperatures T_{tip}. Same experimental data than Fig. 8.1b.

Fig. 8.5 presents the same experimental data than in Fig. 8.1b by plotting P as a function of T_e for different tip temperatures. As suggested by Fig. 8.4, the hotter the tip, the greater the excess power deposited in the sample. Nevertheless, the electronic temperature is not controlled by P since experimental data do not merge on an universal curve on Fig. 8.5, even for very large values of the tip temperature T_{tip}. Although the value of T_{tip} is not well known experimentally (see Subsection 1.2.2), it is for sure lower than 900 mK otherwise the energetic resolution would not allow to probe the superconducting gap by STS. In addition, the anomaly

persists for every value of tunneling current I_t and appears specifically for low bias voltages V_b, suggesting that the energy of the injected quasiparticles plays a role independently from the injection rate.

Electronic heating by the NIS junction made by the STM-sample system cannot explain the anomaly.

Contribution of inelastic tunneling

As discussed in Section 1.2, the expressions used above for the current and heat flowing in a tunnel junction (Eq. 7.1, 7.2 and 7.3) are valid in the case of elastic tunneling. In the inelastic case, the critical ingredient is the probability $P(E)$ for a tunneling electron to exchange an energy E with its environment. We will try to understand here whether the absorption of energy by the tunneling electrons can explain the anomaly. We will first try to quantify the average energy that can be absorbed and then estimate its influence.

It can be shown both theoretically and experimentally[1] that the tunnel current versus bias voltage $I_t(V_b)$ characteristic of a NIS tunnel junction in the inelastic case is strictly equivalent to the one obtained in the elastic case (without coupling to its environment) with a modified density of states for the superconducting electrode. This modified density of states $n_{mod}(E)$ is equal to the convolution between the effective density of states of the sample $n_s(E)$ and the $P(E)$ function. When measuring experimentally the density of states by tunneling spectroscopy, it is therefore impossible to distinguish between the influence of the coupling with the environment (through $P(E)$) and the intrinsic properties of the superconductor (through $n_s(E)$), such as deviations from the BCS theory. In particular, photon assisted tunneling due to a hot electromagnetic environment can be described[2] by a Lorentzian form for $P(E)$. The convolution with this $P(E)$ function transforms the BCS density of states into the Dynes form of Eq. 4.6, where Γ_{in} is the half width maximum of $P(E)$.

Consequently, in our case one cannot disentangle the possible origins of the finite inelastic scattering term Γ_{in} necessary to fit the spectroscopy measurements (see Section 4.5). However, these values of Γ_{in} allow to put an upper bound for the average energy that can be deposited into the sample by inelastic tunneling due to the coupling with a hot environment. Indeed, in the case where the only origin of the term Γ_{in} is then inelastic tunneling, the full width at half maximum of the function $P(E)$ characterizing the energy transfer from the environment is equal to Γ_{in}. Since the intrinsic properties of the superconductor can also contribute to a finite value of Γ_{in}, the value extracted from spectroscopy measurements is the largest possible value of the full width at half maximum of the function $P(E)$. Therefore, the average energy exchanged by an electron during a tunneling event is at most of the order of the extracted $\Gamma_{in} \sim \Delta_0/100$ (see Table 4.3).

Then, in order to understand whether such an additional heat flow from the environment can result in the low bias anomaly, we will consider the most favorable case: for each tunneling event an additional energy of the order of the full width at half maximum of the function $P(E)$ ($\sim \Gamma_{in}$) coming from the environment is deposited in the sample. This consists in adding Γ_{in} to the term $E - eV_b$ in the expression of the power transferred from the tip to the sample (Eq. 7.2). Using the expression of the tunneling current (Eq. 7.1), the contribution of the environment on the deposited power is equal to $I_t\Gamma_{in}/e \sim 10^{-15}$ W with the typical values $I_t = 1$ nA and $\Delta_0 = 200$ μeV. The power coming from the environment by inelastic scattering is therefore

[1] Under the assumption of symmetric distribution function $f(E) = 1 - f(-E)$ and probability $P(E) = P(-E)$, see [88] supplementary.

[2] Under the assumption of a purely resistive environment in thermal equilibrium at T_{env}, in parallel with the capacitance of the junction. The energy exchanged during the tunneling event must also be smaller than $k_B T_{env}$, see [88].

negligible compared to the total power deposited in the sample (see Fig. 8.5). Although this argument is not a rigorous demonstration[3], it addresses the influence of a hot environment and suggests that it cannot explain the anomaly.

Finally, **the anomaly cannot be explained by overheating effects in the quasi equilibrium limit.**

8.3 Discussion of the slow thermalization regime

By contrast with the previous section and Section 6.5, we discuss the case where a local electronic temperature cannot be defined because the distribution function of the electrons is out of quasi equilibrium.

To begin with, when the energy of the injected quasiparticles E is approaching the gap energy Δ, the energy relaxation process described in Section 6.5 becomes slower. In particular, both electron phonon scattering and recombination times diverge for $E \to \Delta$ [59]. Therefore the relaxation rate τ_{rel}^{-1} becomes too small to ensure quasi equilibrium. Notably, this is in agreement with the observation made in previous section: the critical current anomaly at low bias voltages cannot be simply explained by the heat balance of the sample in quasi equilibrium.

Then, one should discuss the value of the bias voltage V_b corresponding to the crossover from the quasi equilibrium regime (at large V_b) to the out of equilibrium regime (at low V_b). Such a crossover occurs when the relaxation rate is not sufficient to ensure that quasi equilibrium is reached over the lengthscale corresponding at least to the critical transition region which typical scale is given by the nanowire width w. This leads to the inequation $(\tau_{rel} v_F l/3)^{1/2} \gtrsim w$. Using typical values: $l \approx 1$ nm, $v_F = 1.4 \times 10^6$ m.s^{-1} and $w = 300$ nm one obtains $\tau_{rel} \gtrsim 200$ ps. Moreover, quasiparticles mainly relax their energy through electron-phonon scattering[4]. The associated rate τ_{e-ph}^{-1} vanishes for energies close to the gap energy Δ: for Nb, $\tau_{e-ph}(E = 2\Delta) \approx 70$ ps while $\tau_{e-ph}(E = 1.5\Delta) \approx 500$ ps and $\tau_{e-ph}(E \to \Delta) \to \infty$. Consequently, one expects the crossover to occur for $E = eV_b \approx 1.5\Delta_0$. Qualitatively, this corresponds to the emergence of the critical current anomaly observed in Fig. 8.1 and 8.2. Quantitatively, the upturn is experimentally observed for values closer to Δ_0. This discrepancy can be understood by considering the origin of the divergence of τ_{e-ph}. Indeed, at the gap edge the quasiparticles cannot scatter and relax their energy by emitting a phonon because they are in the lowest energy state. However, in the presence of depairing due to the supercurrent, additional low energy states are available (see Section 5.2) and the coherence peaks of the DOS are weakened. One therefore expect the divergence of τ_{e-ph} to be less sharp and to occur at lower energies than predicted in [59], as measured experimentally here.

We will now investigate the role of the out of quasi equilibrium distribution function on the superconducting properties of the samples. Two types of non-equilibrium can be realized depending on the nature of the quasiparticles, which continuously changes from holes (far

[3]This would require to compute the power transferred to the sample in the inelastic tunneling framework given the exact $P(E)$ function. Nevertheless, the $P(E)$ function is difficult to calibrate. Indeed, it depends on the choice made to model the environment, and requires to perform spectroscopy measurements knowing the density of states of both the tip and the sample. The environment characteristic can then be deduced from the fit of Coulomb blockade effects for example. For a superconducting sample, one could imagine performing the measurement above critical temperature or above upper critical field in order to obtain a flat density of states. Unfortunately our energy resolution is not good enough to detect Coulomb blockade at high temperatures and our experimental setup does not provide large enough magnetic fields.

[4]At low temperatures, both recombination time and electron-electron scattering times are larger than the electron-phonon scattering time (see Section 6.5 and [59])

from the Fermi level) to electrons (far above the Fermi level). Note the fractional charge of quasiparticles within the range of the energy gap around the Fermi level.

The first type of non-equilibrium is referred to as charge imbalance and corresponds to the case where populations of the electron-like and the hole-like quasiparticles branches do not coincide. This results in a net quasiparticle charge density Q^*.

The second type of non-equilibrium is referred to as energy imbalance and is characterized by a distribution function which is particle-hole symmetric. If this state can be approximated by a quasiparticle temperature, one recovers the quasi equilibrium limit investigated in Section 6.5.

8.3.1 Branch imbalance

At low temperatures, injection of tunnel current in a superconductor induces an imbalance in the population of electrons and holes[5]. The associated charge imbalance per unit volume Q^* is defined[6] by:

$$\begin{aligned} Q^* &= eN_0 \int_{-\infty}^{\infty} d\epsilon \; q(\epsilon) f(\epsilon) \\ &= eN_0 \int_{0}^{\infty} d\epsilon \; \frac{\epsilon}{E} \left(f(\epsilon) - f(-\epsilon) \right) \end{aligned} \tag{8.1}$$

where N_0 is the density of states at Fermi level, $E = \sqrt{\epsilon^2 + \Delta_0^2}$ is the quasiparticle excitation energy, ϵ is the normal state electron energy, $q(\epsilon) = \epsilon/E$ is the effective quasiparticle charge in units of the charge of the electron e and $f(\epsilon)$ is the quasiparticle distribution function [19]. This charge or branch imbalance relaxes over a timescale τ_Q called branch mixing time. Note that charge neutrality is not broken since a variation of the Cooper pair density compensates it.

Near critical temperature, relaxation of the branch imbalance is dominated by inelastic processes involving a phonon: inelastic scattering of a quasiparticle from one branch to another and pair breaking or recombination processes involving two quasiparticles of the same branch. At low temperatures however, the associated timescale τ_Q^{in} diverges for quasiparticles close to the gap edge [59]. Then, some elastic processes can also contribute to branch mixing. For instance, at low temperature charge imbalance relaxation resulting from elastic impurity scattering in the presence of pairing anisotropy dominates charge imbalance relaxation resulting from inelastic processes [107]. External perturbations leading to pair breaking such as magnetic field or supercurrent also contribute to branch mixing [71]. The associated rate for elastic pair breaking expresses [52]:

$$\frac{1}{\tau_Q^{el}} \approx \frac{\gamma}{\hbar} \frac{\Delta_0^2}{E\sqrt{E^2 - \Delta_0^2}} \tag{8.2}$$

where γ is the depairing energy[7]. In the case of an homogeneous supercurrent flow γ is related to the current through Eq. 2.18. One can give an estimate for the branch mixing time τ_Q^{el} in our samples since typically $\gamma \sim 0.2\Delta_0$ (see Fig. 2.3) and $\Delta_0 \approx 200$ μeV: $\tau_Q^{el}(E = 2\Delta_0) \approx 0.2\Delta_0/\hbar \approx 60$ ps and this time decreases as E approaches Δ_0. Thus, for E close to Δ_0 branch imbalance is suppressed over a timescale τ_Q^{el} of a few picoseconds corresponding to a quasiparticle diffusion time of a few tens of nanometers.

[5] This is only possible in the presence of a superconductor and when $k_B T \ll \Delta$, so that for instance when $eV > \Delta$ (see Fig. 8.4), only electrons and no holes can be injected.

[6] As pointed out in [19], one can define Q^* with or without weighting the branch imbalance effect by the fractional effective charge of the quasiparticle $q(\epsilon)$. In the latter case, one gets $Q^* = eN_0 \int_0^\infty d\epsilon (f(\epsilon) - f(-\epsilon))$.

[7] As discussed in previous note, the definition of Q^* depends on whether we are considering the net charge imbalance or the occupation number branch imbalance. Then, [108] gives a sightly different expression: $1/\tau_Q^{el} = \frac{4\gamma}{\hbar} \frac{\Delta_0^2 E}{(E^2 - \Delta_0^2)^{3/2}}$. One still recovers both the same order of magnitude at large energies and the divergence at the gap edge.

Consequently, **branch imbalance is negligible in our samples whatever the values of bias voltage.** Indeed, at large V_b the fast energy relaxation of the injected quasiparticles ensures that quasi equilibrium is locally reached (see Section 6.5), and at low V_b, branch imbalance is prevented by elastic quasiparticle scattering due to the supercurrent flow.

8.3.2 Energy imbalance

As discussed above, $Q^* = 0$ and the electron-like ($\epsilon > 0$) and hole-like ($\epsilon < 0$) branches of the quasiparticle spectrum are equally populated because of the fast (elastic) branch mixing time. However, quasi equilibrium is not reached over the lengthscale of the nanowire width w because of the slow (inelastic) energy relaxation time and this manifests experimentally by a non thermal behavior of the critical current.

Then, the out of equilibrium state is characterized by an energy imbalance, which enters the superconducting properties via the self consistent gap equation:

$$1 = N_0 V_{eff} \int_0^{\hbar\omega_D} d\epsilon \frac{1 - f(\epsilon) - f(-\epsilon)}{\sqrt{\epsilon^2 + \Delta^2}} \tag{8.3}$$

where V_{eff} is the BCS pairing potential, ω_D the Debye frequency and f the distribution function which can deviate from the usual Fermi Dirac distribution [8]. This equation is valid in the absence of depairing energy and within the approximation that the distribution function is symmetric in electrons and holes with respect to the Fermi surface, which is a stronger approximation that simply $Q^* = 0$. It gives however a good qualitative understanding of the situation. Indeed, the system is driven out of quasi equilibrium when $f(\epsilon) + f(-\epsilon) - 2f_{FD}(\epsilon) \neq 0$ where f_{FD} is the Fermi Dirac distribution. In particular, Δ is all the more affected as f differs from f_{FD} close to the Fermi level because of the energy denominator. This can either result in an enhancement (see Section 3.3)[8] or a destruction of superconductivity depending on whether low energy quasiparticles are extracted or injected. The latter case corresponds to the regime of injection of quasiparticles by the STM tip close to the gap energy and explains qualitatively the low energy anomaly presented in Fig. 8.1.

For a quantitative understanding, we will deal with the more general gap equation given by Eq. 2.10 where θ obeys Usadel equations (Eq. 2.2). Since branch imbalance has been discarded, we will assume for simplicity that the distribution function f is symmetric with respect to hole and electron like excitations ($f(\epsilon) = f(-\epsilon)$ or equivalently $f(E) = 1 - f(-E)$ where E and ϵ are respectively the quasiparticle and normal-state electron energies). The gap equation therefore follows:

$$\Delta = N_0 V_{eff} \int_0^{\hbar\omega_D} dE \ (1 - 2f(E)) \Im[\sin\theta] \tag{8.4}$$

We will investigate the situation where a constant tunneling current is injected by the tip (Eq. 7.1). This results in an excess population rate at each energy level equal to the current at that level divided by the electronic charge:

$$\frac{1}{e^2 R_T} N_s(E)(f(E) - f_{tip}(E - eV_b)) \tag{8.5}$$

where $N_s = \Re[\cos\theta]$ is the normalized density of states of the superconductor, f_{tip} the distribution function of the tip and V_b and R_T respectively the bias voltage and the normal state

[8] Eq. 8.3 keeps track of the electron or hole like character of the quasiparticles using ϵ instead of $E = \sqrt{\epsilon^2 + \Delta^2}$ as a variable. One can however recover Eq. 3.3 by making the associated variable change.

resistance of the tip-sample tunnel junction. The inelastic relaxation of the injected electrons is simply treated by a decay rate given by:

$$\mathcal{V}N_0N_s(E)\frac{f(E)-f_{FD}(E)}{\tau_{rel}} \tag{8.6}$$

where $\mathcal{V}$ is the characteristic relaxation volume, N_0 the density of states at Fermi level, f_{FD} the quasi equilibrium distribution function and τ_{rel} the energy relaxation time. The steady state occupation of the levels at energy E is determined by the balance between Eq. 8.5 and Eq. 8.6:

$$f(E)=\frac{f_{FD}(E)+\Gamma_{neq}f_{tip}(E-eV_b)}{1+\Gamma_{neq}} \tag{8.7}$$

where $\Gamma_{neq}=\tau_{rel}/(\mathcal{V}N_0e^2R_T)$.

Finally, we are interested in the value of the critical current. Assuming an homogeneous current density (which is a reasonable approximation in our samples as discussed in Section 5.1), the Usadel equation is given by Eq. 2.20, and the supercurrent writes $I_s=J_sS$ with S the wire section and J_s the supercurrent density. The latter is given by Eq. 2.11 and this simplifies to:

$$\frac{I_s}{I_\gamma}=\sqrt{\frac{\gamma}{\Delta_0}}\frac{U_s^{neq}}{\Delta_0} \tag{8.8}$$

where I_γ is given by Eq. 2.18b and $U_s^{neq}=\int_0^\infty d\epsilon\ (1-2f)\Im[\sin^2\theta]$. Eventually, the critical current is given by the maximum of the function $I_s(\gamma)$.

Then, the above set of equations can be solved self consistently as follows. For a given V_b, Eq. 8.7 gives the out of equilibrium distribution function f, which enters into the determination of Δ and θ through the gap (Eq. 8.4) and the Usadel (Eq. 2.20) equations. Since I_t (given by Eq. 7.1) is set constant, R_T has to be adjusted according to the variations of the density of states $N_s=\Re[\cos\theta]$ and finally, R_T affects again f through Eq. 8.7.

The resolution can be performed for any of the following remaining parameters:

- The distribution function of the tip f_{tip}. This distribution is taken equal to the equilibrium Fermi-Dirac distribution at a temperature T_{tip}. The temperature of the tip is equal to T_{eff} extracted from spectroscopy measurements (see discussion of Subsection 1.2.2 and values in Table 4.3).

- The distribution function f_{FD}. This distribution is taken equal to the equilibrium Fermi-Dirac distribution at a temperature T_e. The temperature T_e is the quasi equilibrium temperature towards which the electron system relaxes by inelastic scattering.

- The inelastic scattering term Γ_{in} appearing in Usadel equation (Eq. 2.20). It is necessary to account for the experimental tunnel current versus bias voltage $I_t(V_b)$ and differential conductance dI/dV measurements (see Section 4.5 and 5.2). It will be taken equal to the value extracted by tunneling spectroscopy given in Table 4.3. Its physical interpretation will be discussed below.

- The parameter Γ_{neq}. Physically, Γ_{neq} is related to the energy relaxation time τ_{rel} which can be energy dependent.

  Introducing the relaxation length of the out of equilibrium quasiparticles $\sqrt{D\tau_{rel}}$, one can approximate the volume $\mathcal{V}$ explored by these out of quasi equilibrium quasiparticles by $\sqrt{D\tau_{rel}}wt$ (valid when $\sqrt{D\tau_{rel}}>w,t$) where $D=v_Fl/3$ is the diffusion constant and w and t are the width and thickness of the nanowire. This leads to $\Gamma_{neq}=\sqrt{\tau_{rel}}/(\sqrt{D}R_Twt N_0e^2)$. Therefore, using $N_0=10^{47}$ J^{-1}.m^{-3}, $v_F=1.4\times10^6$ m.s^{-1} and $l=1$ nm (see Section 4.2), we will deal in the following with the parameter τ_{rel}.

First of all, we will check that this model can account for the measured critical current with reasonable values for the relaxation time τ_{rel}. As discussed in Chapter 6, the quasi equilibrium temperature of the sample T_e is related to the injected power and drives the critical current dependency for $eV_b > \Delta_0$ (see Fig. 8.1 and 8.3). In order to investigate the $eV_b \leq \Delta_0$ regime, we will set for simplicity, and only for the next computation, T_e constant and equal to the temperature of the sample holder. The numerical prediction of the model is compared to experimental data on Fig. 8.6. Experimental results correspond to $I_t = 1250$ pA curve of Fig. 8.1a (sample N06). The parameters $T_{tip} = 540$ mK, $\Gamma_{in} = 0.03\Delta_0$, $\Delta_0 = 235$ μeV (see Table 4.3) and $T_e = 200$ mK are used in our model as already determined quantities. The numerical solution is plotted for $\tau_{rel} = 40$ and 90 ns[9] (solid lines). The model predicts the essential feature of the low energy anomaly, being the decrease of the critical current together with V_b. The $eV_b > 1.5\Delta_0$ region is not investigated here since it is related to variations of T_e.

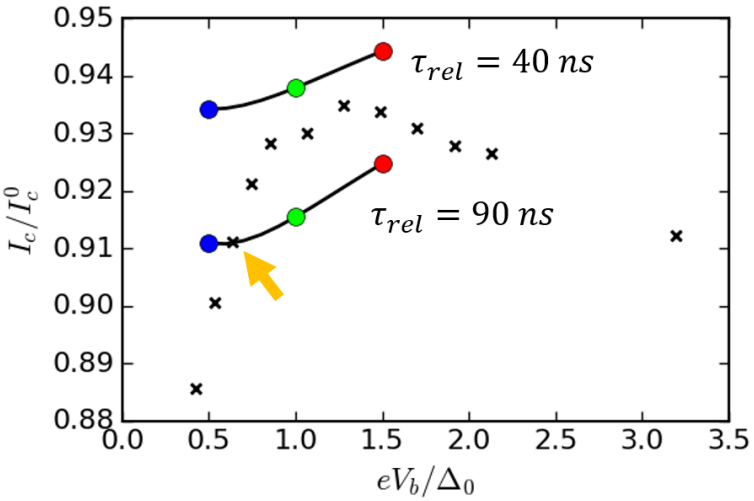

Figure 8.6: Predictions for the low energy anomaly with energy independent relaxation time and fixed quasi equilibrium temperature. Crosses: experimental data. $I_t = 1250$ pA. Sample N06. Solid lines: numerical solution for two values of the relaxation time τ_{rel}. Circles correspond to the curves extracted in Fig. 8.7. Yellow arrow is an indicator for the following discussion.

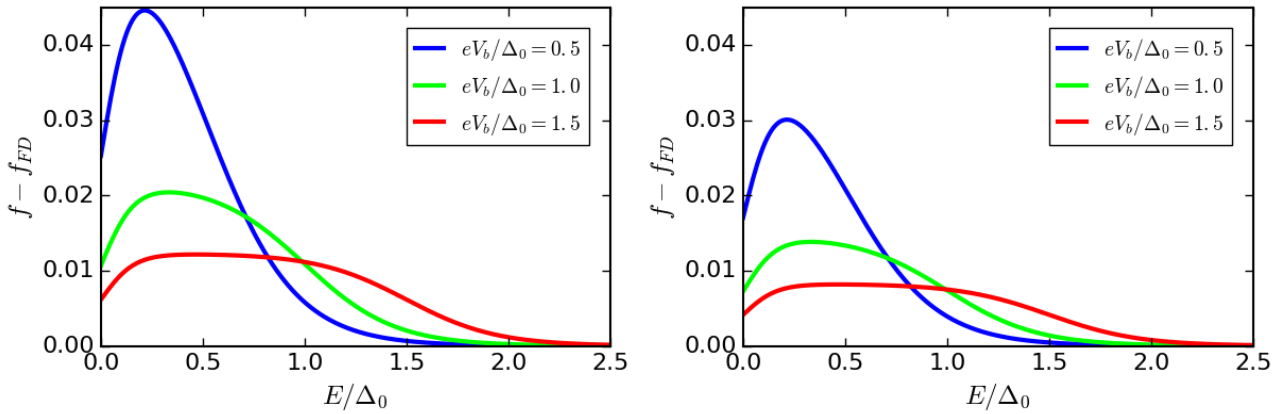

(a) $\tau_{rel} = 90$ ns **(b)** $\tau_{rel} = 40$ ns

Figure 8.7: Deviations of the distribution function from quasi equilibrium due to quasiparticle injection. $f - f_{FD}$ as a function of quasiparticle excitation energy E. f is the distribution function at critical current and in the presence of tunnel injection of quasiparticles at a constant tunneling current $I_t = 1250$ pA and different bias voltages V_b. The two panels correspond to two values of the relaxation time τ_{rel}. Extracted from the numerical computation of Fig. 8.6.

[9]For these values, the assumption $\sqrt{D\tau_{rel}} > w, t$ is readily checked.

Selected distribution functions f obtained during the numerical computation of Fig. 8.6 are plotted in Fig. 8.7. The two panels correspond to two values of the relaxation time τ_{rel}. f is the distribution function of the sample at critical current and in the presence of quasiparticle injection. Injection is performed at a fixed tunneling current and for different bias voltages corresponding to the colored circles of Fig. 8.6. The longer the relaxation time τ_{rel}, the larger the distribution function deviates from its quasi equilibrium value f_{FD}. In addition, when the bias voltage V_b decreases, the deviations from quasi equilibrium correspond to energy levels closer to the Fermi energy. Accordingly to the discussion below Eq. 8.3, this results to a weakening of superconductivity (which manifests here as a reduction of the critical current) together with a decrease of the bias voltage V_b.

As a comparison, Fig. 8.2 shows that the low energy anomaly is smoothed when the injection position is moved along the dead-end strip further away from its intersection with the nanowire. This is therefore an indirect measurement of the energy relaxation time: as the injected quasiparticles diffuse in the direction of the nanowire, they relax towards a quasi equilibrium. When the quasi equilibrium is reached, the energy imbalance described above is absent and the critical current recovers its thermal equilibrium value. We estimated from Fig. 8.2 the typical lengthscale for the disappearance of the anomaly with the injection position to be of about 10 μm. By equating this to the relaxation lengthscale $\sqrt{D\tau_{rel}}$, one can estimate τ_{rel} to be of the order of one hundred of nanoseconds. This order of magnitude is consistent with the values given by our crude model described above.

As discussed in the beginning of this section, we theoretically expect τ_{rel} to diverge at the gap energy, the divergence being smoothed by the depairing due to the supercurrent flow. For Nb, we estimated $\tau_{rel}(E = 1.5\Delta) \approx 500$ ps, but τ_{rel} must be much larger at lower energies, in line with the values of τ_{rel} estimated above. Consequently, **the model developed in this section can reasonably account for the anomaly.**

Now that we have demonstrated that a non thermal distribution function can account qualitatively for the downturn of the critical current, it is time to refine our model for a better description of our measurements. We will adjust the quasi equilibrium temperature T_e consistently with the expected behavior of the quasi equilibrium limit investigated in Chapter 6, using the law $I_t V_b = \kappa(T_e^4 - T_b^4)$. This will account for the critical current dependency in the $eV_b > \Delta_0$ region, and provide an extrapolation of the quasi equilibrium temperature T_e towards which the system relaxes in the $eV_b < \Delta_0$ region (see Fig. 8.3). Then, we will fit the experimental critical current with our model at each voltage bias V_b as a function of the only parameter τ_{rel}. This will provide the energy dependence of the relaxation time τ_{rel}. As an example, for $T_e = 200$ mK, we would find that $\tau_{rel} = 90$ ns at an injection voltage $V_b = 650$ μV since the theoretical curve hits the experimental data point $(V_b,\ I_c/I_c^0) = (650\ \mu\text{V},\ 0.91)$ as shown by the yellow arrow in Fig. 8.6.

Fig. 8.8 shows the relaxation time versus bias voltage dependency extracted from Fig. 8.1a data (sample N06). Consistently with the thermal behavior observed at large bias voltages on the same sample (see Fig. 6.3 and 8.3), we set T_e so that $I_t V_b = \kappa(T_{neq}^4 - T_b^4)$ with $\kappa = 59$ pW.K^{-4} and $T_b = 215$ mK. For large bias voltages ($eV_b > \Delta_0$), the extracted relaxation time is almost constant. In contrast, for $eV_b < \Delta_0$ we observe a clear raise of the relaxation time τ_{rel} when V_b is lowered. It must be emphasized here that $\tau_{rel}(V_b)$ is not rigourously equivalent to $\tau_{rel}(E = eV_b)$, the relaxation time of a quasiparticle at an energy $E = eV_b$. Indeed, in the experimental measurements quasiparticles are injected in an energy window $[\Delta_G^{I_c^0},\ eV_b]$ with $\Delta_G^{I_c^0}$ the spectral gap at critical current.

As discussed above, we think that the low energy anomaly is related to the divergence of the electron-phonon scattering time at the superconducting gap edge, because of the absence of lower energy states available for the quasiparticles. It manifests here by an increase of the

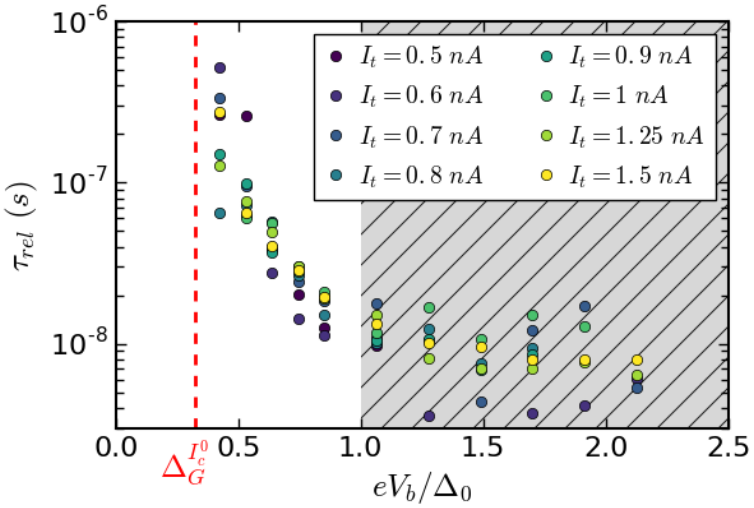

Figure 8.8: Extracted relaxation time versus bias voltage. Dashed vertical line corresponds to the spectral gap at critical current $\Delta_G^{I_c^0}$ (see Section 5.2) Grey hatched region corresponds to a regime where the out of quasi equilibrium model does not apply. Sample N06.

relaxation time τ_{rel} when eV_b is close to the spectral gap at critical current $\Delta_G^{I_c^0}$. Indeed, $\Delta_G^{I_c^0}$ corresponds to the energy below which the density of states vanishes. In addition, we also think that the contribution of impurity scattering should result in a saturation of τ_{rel}. However, our experimental setup does not allow to probe τ_{rel} for values of the bias voltage arbitrarily close to $\Delta_G^{I_c^0}/e$. Indeed, when the density of states of the sample between the Fermi energy and eV_b is too small, it is impossible to reach tunnel regime without damaging the tip.

Eventually, for $eV_b \gtrsim \Delta_0$ the extracted τ_{rel} is constant. This corresponds to a regime where the injected power governs the quasi equilibrium temperature T_e and the critical current I_c. The deviations of the distribution function of the sample from quasi equilibrium are negligible in this regime. Therefore the values of τ_{rel} computed in the gray hatched area of Fig. 8.8 are not physically relevant. They simply palliate the discrepancy between the phenomenological law obeyed by the quasi equilibrium temperature T_e ($I_t V_b = \kappa(T_e^4 - T_b^4)$) and the experimental critical current dependency. This puts an accuracy in our determination of $\tau_{rel}(V_b)$ in the low bias regime of about 10 ns. This is significantly more than the relaxation time in the quasi equilibrium regime.

Finally, we used in this section the inelastic scattering term Γ_{in} as a phenomenological parameter to describe the experimental tunnel current versus bias voltage $I_t(V_b)$ characteristics. However, as mentioned above (see Section 8.2), a finite Γ_{in} term (appearing in Eq. 2.20 or equivalently in Eq. 4.6 and affecting the effective density of states) can have several origins.

Among them is the finite quasiparticle lifetime against inelastic scattering, hence its name. We already discussed in Chapter 6 and in the present section the fact that this time depends on the energy of the quasiparticles. However, when Γ_{in} is extracted from spectroscopy measurements, it is adjusted to fit the coherence peaks features of the density of states, and should therefore correspond to the quasiparticle lifetime at the gap energy. This time is of the order of h/Γ_{in}. In our samples, the values extracted from spectroscopy measurements (see Table 4.3) lead to $h/\Gamma_{in} \approx 1$ ns.

This value of 1 ns is smaller than the expected relaxation lifetime at the gap energy in the absence of supercurrent. Indeed, this time is supposed to diverge (see the discussion at the beginning of the present section and [59]). This discrepancy may lie in the other potential origins of Γ_{in}. As discussed in Section 8.2, deviations from standard superconducting theory and inelastic tunneling can contribute to a finite value of Γ_{in}, resulting in an overestimate of the contribution of inelastic scattering to Γ_{in}. In this case, the value h/Γ_{in} is therefore smaller than the quasiparticle relaxation lifetime.

The low energy anomaly can be explained with a non Fermi Dirac out of equilibrium distribution function within Usadel framework.

Experimental data allow to probe the relaxation rate of the distribution function, and its dependency with the quasiparticles injection voltage.

8.4 Conclusion

We evidenced experimentally a low energy anomaly in the critical current dependency of our samples when injection of quasiparticles is performed at an energy close to the superconducting gap. Indeed, the reduction of the critical current turned out to be larger when reducing the energy of the quasiparticles while the rate is kept constant. First, we discarded overheating effects by considering the influence of inelastic tunneling and additional electronic heating due to the difference in the density of states of the sample and the tip. This signals the breakdown of the heat diffusion model in the quasi equilibrium limit developed in Chapter 6. We demonstrated that describing the quasiparticles with an out of equilibrium distribution can account for the anomaly. Finally, using a simple model describing the injection of quasiparticles and their relaxation we extracted an energy dependent relaxation time for the out of equilibrium quasiparticles. Ongoing theoretical developments may probe more accurately the microscopic mechanisms at stake, being the competition between diffusion and relaxation in the presence of a depairing mechanism.

Conclusion

The goal of this PhD work was to study superconductivity driven out of equilibrium with a STM. To this aim, substantial efforts were made to fabricate, contact, and locate with a STM a superconducting nanowire. Measurements of the critical current were performed to probe the superconducting state. The STM tip was used as a spatially resolved quasiparticle injector to drive the superconductivity out of equilibrium. The STM also enables to vary independently the quasiparticle energy and the injection rate through the bias voltage or the tunneling current. This new Scanning Critical Current Microscopy technique allowed, for the first time, to map the critical current tuned by local injection of quasiparticles and evidenced two remarkable behaviors:

- the critical current is substantially reduced by the tunnel injection of a quasiparticle current that is six orders of magnitude lower
- the critical current is less affected when quasiparticle injection is performed in the vicinity of a vortex

We prove that, for injection at bias voltages larger than the superconducting gap, the reduction of the critical current is due to a local overheating scaling with the injected power. We developed a heat diffusion model that accounts quantitatively well for our measurements and allows to estimate the electron-phonon coupling in our superconducting nanowires. We showed that heat is mainly carried by the electrons and partly by the phonons. Our quasi equilibrium model no longer applies when the energy of the injected quasiparticles is close to the superconducting gap energy. In this regime, the critical current reduction does not scale with the injected power, but it is even further reduced as the bias voltage is lowered at constant injection rate. We explained these observations as an out of quasi equilibrium energy distribution of the quasiparticles. The model we developed for this regime allows to estimate the relaxation rate of the quasiparticles as a function of the injection energy. Eventually, we showed that vortices modify the electronic thermal conductivity and act as quasiparticle traps.

We studied in this thesis superconducting nanowires made of thin bilayers of niobium capped with gold. We chose a conventional superconductor with a homogeneous density of states to valid our new technique, and to be able to use standard theories. The study of other materials with significantly different electron-phonon timescales or electron diffusion constants could be interesting in several respects. First, the difference in timescales could result in completely different behaviors. Second, this would further characterize other materials used in superconducting circuits. This could for instance allow to discriminate between the different mechanisms proposed to account for the operation of superconducting photon detectors [90].

Besides, our development of the Scanning Critical Current Microscopy technique paves the way to the study of inhomogeneous systems at the mesoscopic scale. Disordered superconductors might be interesting since their peculiar quasiparticle dynamics is believed to account for anomalous electrodynamics responses [16, 41]. In addition, percolative models of current distributions are also predicted in strongly disordered two dimensional systems [34] and could be tested by Scanning Critical Current Microscopy..

We focused in this PhD work on devices with geometries ensuring homogeneous supercurrent density because of the large London penetration depth. It would be probably interesting to study different geometries with the Scanning Critical Current Microscopy technique. For instance the use of a wider nanowire could allow to investigate the spatial dependence of the current and of the density of states generated by an inhomogeneous current distribution. Peculiar nanowires shapes with sudden expansions of the wire lead to the fascinating current crowding effect [20, 51] which may also be studied by Scanning Critical Current Microscopy.

Finally, the presence of magnetic vortices in our nanowires led to the interesting phenomena that are quasiparticle trapping and modulation of the electronic thermal conductivity. We hope that further investigations could give a better understanding of the vortex trapping mechanism which is not yet well understood since discrepancies between theory and experiments persist [99].

Appendix A

Depairing due to the magnetic field induced by a supercurrent

With an homogeneous current density and in a cylindrical geometry of diameter w, the vector potential created by the supercurrent I_s can be taken as[1]:

$$\overrightarrow{A} = \frac{\mu_0 I_s}{\pi w^2} r^2 \overrightarrow{u_z} \tag{A.1}$$

where r is the distance from the center of the wire and z axis is directed in the direction of the current.

When $w \ll \lambda_L$, only an average effect of the vector potential is seen, and the associated depairing energy averaged over the cross section is:

$$\begin{aligned} \gamma_A =& \frac{2De^2}{\hbar} \frac{1}{\pi(w/2)^2} \int_0^{w/2} dr \int_0^{2\pi} r d\theta |\overrightarrow{A}(r,\theta)|^2 \\ =& \frac{De^2 \mu_0^2 I_s^2}{24\hbar\pi^2} \end{aligned} \tag{A.2}$$

For wider wires, γ_A and therefore θ and $\overrightarrow{J}$ are not homogeneous, and the depairing energy is maximum on the side of wire.

The ratio between the depairing due to an homogeneous supercurrent and the one due to the induced magnetic field is (writing that $U_s \simeq \frac{\pi}{2}\Delta_0$ and $\lambda_L = \sqrt{\frac{\hbar}{\mu_0 \pi \sigma_N \Delta}}$):

$$\frac{\gamma_A}{\gamma_I} \simeq \frac{1}{48\pi^2} \left(\frac{w}{\lambda_L}\right)^4 \tag{A.3}$$

It is therefore negligible under the assumption of $w \ll \lambda_L$ (homogeneous current density).

NB: The calculation of Anthore [4] is a bit different for the averaging (the formula for the vector potential in a cylinder geometry is used but the cross section average is done in a parallelogram geometry accordingly to the related experiment).

[1] The study of the invariances and symmetries lead to $\overrightarrow{A} = A(r)\overrightarrow{u_z}$. The equation $\nabla^2 \overrightarrow{A} = -\mu_0 \overrightarrow{J}$ and the choice $A(r \to +\infty) = 0$ leads to the equation given in text.

Appendix B

BCS superconductor in the Usadel framework

Starting from the simplified Usadel equation valid in the case of a bulk superconductor (constant superconducting phase and no magnetic field) or of a wire with transverse dimensions smaller than London penetration depth (ensuring an uniform superfluid velocity):

$$\begin{aligned} \epsilon + i\gamma\cos\theta &= \Delta\frac{\cos\theta}{\sin\theta} \\ \nabla\theta &= 0 \end{aligned} \tag{B.1}$$

One can recover the BCS results in the absence of supercurrent and magnetic field ($\gamma = 0$ and therefore $\Delta(T=0) = \Delta_0$):

$$\tan(\theta) = \frac{i\Delta}{\epsilon} \tag{B.2}$$

leading to:

$$\theta = \begin{cases} \frac{\pi}{2} + i\ \mathrm{arctanh}\left(\frac{\epsilon}{\Delta}\right) & \text{if } |\epsilon| < \Delta \\ i\ \mathrm{arctanh}\left(\frac{\Delta}{\epsilon}\right) & \text{if } |\epsilon| > \Delta \end{cases} \tag{B.3}$$

$$\Longrightarrow \begin{cases} \cos(\theta) = \frac{|\epsilon|}{\sqrt{\epsilon^2-\Delta^2}} \\ \sin(\theta) = \frac{\Delta}{\sqrt{\Delta^2-\epsilon^2}} \end{cases} \tag{B.4}$$

- One recovers the BCS **density of states:**

$$N_s(\epsilon) = N_0\ \Re(\cos(\theta)) = \begin{cases} N_0\frac{|\epsilon|}{\sqrt{\epsilon^2-\Delta^2}} & \text{if } |\epsilon| > \Delta \\ 0 & \text{if } |\epsilon| < \Delta \end{cases} \tag{B.5}$$

  Note: This result is also valid with a Dynes parameter ($\epsilon \to \epsilon + i\Gamma$).

- Besides, the quantity $\Im[\sin^2\theta] = \frac{\Delta^2}{\Delta^2-\epsilon^2}$ is non zero only for $|\epsilon| \to \Delta$ yielding to: [38]

$$\Im[\sin^2\theta] = \frac{\pi}{2}\ \Delta\ \delta(\epsilon - \Delta) \tag{B.6}$$

  So that for $k_BT \ll \Delta$:

$$\begin{aligned} U_s &= \int_0^\infty d\epsilon\ \tanh\left(\frac{\epsilon}{2k_BT}\right)\Im[\sin^2\theta] \\ \boldsymbol{U_s} &= \boldsymbol{\frac{\pi}{2}\Delta} \end{aligned} \tag{B.7}$$

- Using the properties of the function arccosh[1], the gap writes in the low temperature limit $k_BT \ll \Delta$:

$$\begin{aligned}
\Delta &= N_0 V_{eff} \int_0^{\hbar\omega_D} d\epsilon \ \tanh\left(\frac{\epsilon}{2k_BT}\right) \Im[\sin\theta] \\
&= N_0 V_{eff} \int_\Delta^{\hbar\omega_D} d\epsilon \ \tanh\left(\frac{\epsilon}{2k_BT}\right) \frac{\Delta}{\sqrt{\epsilon^2-\Delta^2}} \\
&= N_0 V_{eff} \Delta \int_1^{\hbar\omega_D/\Delta} dx \ \frac{1}{\sqrt{x^2-1}} \\
&= N_0 V_{eff} \Delta \ \ln\left(\sqrt{\left(\frac{\hbar\omega_D}{\Delta}\right)^2 - 1} + \frac{\hbar\omega_D}{\Delta}\right)
\end{aligned} \tag{B.8}$$

  Leading to the BCS result (since $\hbar\omega_D \gg \Delta$):

$$\boldsymbol{\Delta = 2\hbar\omega_D e^{-1/N_0 V_{eff}}} \tag{B.9}$$

- Finally, the critical temperature T_c is defined by $\Delta(T \to T_c) \to 0$. Using the fact that $\hbar\omega_D \gg k_BT_c$:

$$\begin{aligned}
\Delta(T_c) &= N_0 V_{eff} \int_{\Delta(T_c)}^{\hbar\omega_D} d\epsilon \ \tanh\left(\frac{\epsilon}{2k_BT_c}\right) \frac{\Delta(T_c)}{\sqrt{\epsilon^2-\Delta(T_c)^2}} \\
1 &= N_0 V_{eff} \int_0^{\hbar\omega_D} d\epsilon \ \tanh\left(\frac{\epsilon}{2k_BT_c}\right) \frac{1}{\epsilon} \\
1 &= N_0 V_{eff} \int_0^{\hbar\omega_D/2k_BT_c} dx \ \frac{\tanh(x)}{x} \\
1 &= N_0 V_{eff} \left(\Big[\tanh(x)\ln(x)\Big]_0^{\hbar\omega_D/2k_BT_c} - \int_0^\infty dx \ \frac{\ln(x)}{\cosh(x)^2} \right) \\
1 &= N_0 V_{eff} \left(\ln\left(\frac{\hbar\omega_D}{2k_BT_c}\right) - \alpha \right)
\end{aligned} \tag{B.10}$$

  with $\alpha = \int_0^\infty dx \ \frac{\ln(x)}{\cosh(x)^2} \approx -0.81878$. Using the above result of Eq. B.9 one finally get:

$$\begin{aligned}
\frac{\Delta}{k_BT_c} &= 4e^\alpha \\
\boldsymbol{\frac{\Delta}{k_BT_c}} &\boldsymbol{= 1.764}
\end{aligned} \tag{B.11}$$

[1] $\text{arccosh}(x) = \ln(\sqrt{x^2-1}+x)$ and $\text{argcosh}'(x) = \frac{1}{\sqrt{x^2-1}}$

Appendix C

Out of equilibrium physical quantities in the Usadel framework

The development of the quasiclassical theory of superconductivity starting from non equilibrium Green functions in the Keldysh formalism is presented in [18]. The diffusive limit leads to the Usadel equations which merge in an unified formalism both equilibrium and out of equilibrium properties. The physical quantities of interest can be computed from retarded and advanced Green functions R and A (which are 2×2 matrices depending on position and energy) and filling factor h.

The filling factor can be decomposed in an odd h_{od} and an even h_{ev} functions of the energy, and is related to the distribution function of electrons f through $h = 1 - 2f$. At equilibrium, f is given by Fermi-Dirac distribution so $h_{od}^{eq}(\epsilon) = \tanh(\epsilon/(2k_BT))$ and $h_{ev}^{eq}(\epsilon) = 0$.

The retarded and advanced Green functions R and A must obey some normalization conditions, which allow to parametrize it for practical purposes. Then [104, 18]:

$$R = \begin{pmatrix} \cos\theta & \sin\theta e^{i\phi} \\ \sin\theta e^{-i\phi} & -\cos\theta \end{pmatrix} \tag{C.1}$$

From which A can be obtained through:

$$A = -\tau_3 R^\dagger \tau_3 \tag{C.2}$$

where $\dagger$ denotes the Hermitian conjugate, and the τ matrices are equal to the identity and Pauli matrices:

$$\tau_0 = \mathbb{1}, \quad \tau_1 = \begin{pmatrix} 0 & 1 \\ 1 & 0 \end{pmatrix}, \quad \tau_2 = \begin{pmatrix} 0 & -i \\ i & 0 \end{pmatrix}, \quad \tau_3 = \begin{pmatrix} 1 & 0 \\ 0 & -1 \end{pmatrix} \tag{C.3}$$

so that:

$$A = \begin{pmatrix} -\cos\theta^* & \sin\theta^* e^{i\phi^*} \\ \sin\theta^* e^{-i\phi^*} & \cos\theta^* \end{pmatrix} \tag{C.4}$$

Thus, the single particle density of states is given by:

$$\begin{aligned} N_s &= N_0 \frac{1}{4} \mathrm{Tr}\left\{\tau_3 (R - A)\right\} \\ \boldsymbol{N_s} &= \boldsymbol{N_0 \Re[\cos\theta]} \end{aligned} \tag{C.5}$$

where Tr denotes the trace of the matrix.

The superconducting order parameter reads:

$$\begin{aligned}\Delta &= \frac{N_0 V_{eff}}{8i}\int_{-\hbar\omega_D}^{\hbar\omega_D} d\epsilon\ \mathrm{Tr}\left\{(\tau_1 - i\tau_2)\left(h_{od}(R-A) + h_{ev}(R\tau_3 - \tau_3 A)\right)\right\}\\ \boldsymbol{\Delta &= \frac{N_0 V_{eff}}{4i}\int_{-\hbar\omega_D}^{\hbar\omega_D} d\epsilon\left(h_{od}(\sin\theta e^{i\phi} - \sin\theta^* e^{i\phi^*}) - h_{ev}(\sin\theta e^{i\phi} + \sin\theta^* e^{i\phi^*})\right)}\end{aligned} \tag{C.6}$$

leading to Eq. 2.10, and Eq. 2.4 at equilibrium for a bulk superconductor ($\Im[\phi] = 0$).

Defining the quantities

$$\begin{aligned}Q &= \frac{1}{4}\mathrm{Tr}\left\{\tau_3\left(R\overrightarrow{\nabla}R - A\overrightarrow{A}\right)\right\}\\ Q &= \Im\left[\sin^2\theta\overrightarrow{\nabla}\phi\right]\end{aligned} \tag{C.7}$$

and

$$M_{ij} = \frac{1}{4}\mathrm{Tr}\left\{\delta_{ij}\tau_0 - R\tau_i A\tau_j\right\} \tag{C.8}$$

where δ_{ij} is the Kronecker delta, the current density can be written as:

$$\overrightarrow{J_s} = \frac{\sigma_N}{2e}\int_{-\infty}^{\infty} d\epsilon\ \left(M_{33}\overrightarrow{\nabla}h_{ev} + Qh_{od} + M_{03}\overrightarrow{\nabla}h_{od}\right) \tag{C.9}$$

leading to Eq. 2.11 and Eq. 2.6 at equilibrium for a bulk superconductor ($Im[\phi] = 0$).

The thermal current is given by:

$$\overrightarrow{J_{th}} = \frac{\sigma_N}{2e^2}\int_{-\infty}^{\infty} d\epsilon\ \epsilon\left(M_{00}\overrightarrow{\nabla}h_{od} + Qh_{ev} + M_{30}\overrightarrow{\nabla}h_{ev}\right) \tag{C.10}$$

When the system is at local thermal equilibrium, $h_{od}(x,\epsilon) = \tanh(\epsilon/2k_BT(x))$ and $h_{ev}(x,\epsilon) = 0$. Then:

$$\begin{aligned}\overrightarrow{\nabla}h_{od} =& \frac{dh_{od}}{dT}\overrightarrow{\nabla}T\\ =& \frac{-\epsilon}{2k_BT^2}\left(1 - \tanh^2\left(\frac{\epsilon}{2k_BT}\right)\right)\overrightarrow{\nabla}T\end{aligned} \tag{C.11}$$

Note:

$$\begin{aligned}M_{00} &= \frac{1}{2}\left\{1 + \cos\theta\cos\theta^* - \sin\theta\sin\theta^*\cosh(2\Im[\phi])\right\}\\ M_{33} &= \frac{1}{2}\left\{1 + \cos\theta\cos\theta^* + \sin\theta\sin\theta^*\cosh(2\Im[\phi])\right\}\\ M_{03} &= \frac{1}{2}\sin\theta\sin\theta^*\sinh(2\Im[\phi])\\ M_{03} &= -M_{30}\end{aligned} \tag{C.12}$$

When ϕ is real, $M_{03} = M_{30} = 0$, $M_{33} = \cos(\Im[\theta])$ and $M_{00} = \cos(\Re[\theta])$.

Finally, in the quasi equilibrium limit $\boldsymbol{\overrightarrow{J_{th}} = -k_e\overrightarrow{\nabla}T}$ with:

$$\boldsymbol{k_e = \frac{\sigma_N}{2e^2}\int_{-\infty}^{\infty} d\epsilon\ \frac{\epsilon^2}{2k_BT^2}\left(1 - \tanh^2\left(\frac{\epsilon}{2k_BT}\right)\right)\cos\left(\Re[\theta]\right)} \tag{C.13}$$

Appendix D

Diffusion equations

D.1 Analytical resolution

Normal electrons channel

For practical reasons, one needs to solve the following equation (heat diffusion by electrons in the absence of electron-phonon coupling or heat diffusion by phonons in the case $T_e = T_{ph}$ and in the absence of Kapitza coupling):

$$\frac{d}{dx}\left(wt\alpha T^n \frac{dT}{dx}\right) = -P_0\delta(x - x_0) \tag{D.1}$$

which gives:

$$wt\alpha T^n \frac{dT}{dx} = \begin{cases} C_l & \text{if } x < x_0 \\ C_r & \text{if } x > x_0 \end{cases} \tag{D.2}$$

where by integrating Eq. D.1 between $x_0 - \epsilon$ and $x_0 + \epsilon$ one gets $C_l - C_r = P_0$. Finally, integrating Eq. D.2 between x_0 and the left and right reservoirs where $T = T_b$ and subtracting these two equations one finally gets:

$$\frac{\alpha t}{n+1}\left[T^{n+1}(x) - T_b^{n+1}\right]\left(\frac{1}{\int_{x_L}^{x} dx/w(x)} + \frac{1}{\int_{x}^{x_R} dx/w(x)}\right) = P_0 \frac{\int_a^{x_0} dx/w(x)}{\int_a^{x} dx/w(x)} \tag{D.3}$$

where $a = x_L$ if $x > x_0$ and $a = x_R$ if $x < x_0$.

Phonons channel

One also needs to solve (heat diffusion by phonons in the case $T_e = T_{ph}$ and in the presence of Kapitza coupling):

$$\frac{d}{dx}\left(\alpha_{ph} T^3 wt \frac{dT}{dx}\right) = -P_0\delta(x - x_0) + Kw(T^4 - T_b^4) \tag{D.4}$$

For a constant width and using the variable change $v = (\frac{T}{T_b})^4$ one obtains:

$$\frac{d^2v}{dx^2} = -\gamma\delta(x - x_0) + \frac{1}{l_{ph-s}^2}(v - 1) \tag{D.5}$$

with $\gamma = \frac{4P_0}{wt\alpha_{ph}T_b^4}$ and $l_{ph-s} = \sqrt{\alpha_{ph}t/(4K)}$. Defining $v(k) = \frac{1}{\sqrt{2\pi}}\int_{-\infty}^{\infty} dx\ v(x)e^{-ikx}$ the Fourier transform of $v(x)$, we have:

$$
\begin{aligned}
-k^2 v(k) &= -\frac{\gamma}{\sqrt{2\pi}} e^{-ikx_0} + l_{ph-s}^{-2}(v(k) - \sqrt{2\pi}\delta(k)) \\
v(k) &= \frac{\gamma}{\sqrt{2\pi}} \frac{e^{-ikx_0}}{k^2 + l_{ph-s}^{-2}} + \sqrt{2\pi}\delta(k) \frac{l_{ph-s}^{-2}}{k^2 + l_{ph-s}^{-2}} \\
v(x) &= 1 + \frac{l_{ph-s}\gamma}{2} \exp\left(-\frac{|x - x_0|}{l_{ph-s}}\right) \\
T^4(x) - T_b^4 &= \frac{2P_0 l_{ph-s}}{wt\alpha_{ph}} \exp\left(-\frac{|x - x_0|}{l_{ph-s}}\right)
\end{aligned}
\tag{D.6}
$$

In the case of weak Kapitza coupling compared to phonon diffusion, $l_{ph-s} \ll |x - x_0|$ and l_{ph-s} is actually the distance to the reservoirs x_R. One then recovers the result of previous paragraph with $n = 3$ and $x = x_0$:

$$
P_0 = \frac{\alpha_{ph} wt}{2x_R}(T^4(x) - T_b^4) \tag{D.7}
$$

D.2 Numerical resolution

The aim is to solve Eq. 6.9 with $T_{ph} = T_b$ and $k_e(T_e)$ given by Eq. 6.5 (see Fig. 6.6). This quasi one-dimensional equation also depends on the geometry through the function $w(x)$. Using the variable change $s = T_e/T_b$ one gets:

$$
\frac{d}{dx}\left(wtk_e \frac{ds}{dx}\right) = \Sigma wtT_b^{p-1}(s^p - 1) - P_0\delta(x - x_0) \tag{D.8}
$$

To begin with, we will solve this equation separately on the left $x \in [-\infty; x_0^-]$ and right $x \in [x_0^+; +\infty]$ side of the singularity (Dirac delta function), which we will treat as a boundary condition. Then, solving Eq. D.8 will be equivalent to solve this same equation without the last right hand term but with the boundary condition in x_0. Integrating between $x_0 - \epsilon$ and $x_0 + \epsilon$ and considering that the integral of the first term of the right hand of the equation is necessarily equal to 0 when $\epsilon \to 0$ since it corresponds to the heat transfer between electrons and phonons in a vanishing volume one obtains:

$$
\left[wtk_e(s)\frac{ds}{dx}\right]_{x_0^-}^{x_0^+} = -P_0 \tag{D.9}
$$

which provides a relation between the boundary conditions of the derivative of s on the left and right side of the tip position x_0.

Defining the function g such as $k_e(T_e) = \alpha_e T_b\, g(T_e)$ Eq. D.8 writes:

$$
\frac{d^2 s}{dr^2} + \frac{1}{w(r)}\frac{dw}{dr}\frac{ds}{dr} + \frac{1}{g(s)}\frac{dg}{ds}\left(\frac{ds}{dr}\right)^2 = \frac{1}{l_R^2}(s^p - 1) \tag{D.10a}
$$

$$
l_R = \sqrt{\frac{\alpha_e}{\Sigma T_b^{p-2}}} \tag{D.10b}
$$

In order to numerically solve the problem on a domain, we will solve the above equation with two boundary conditions: one over the derivative of s in x_0^+ or x_0^- and another on s to infinity (we will then set $s \to 1$ or equivalently $T_e \to T_b$). We will also take advantage of the symmetry when the injection position is at the center of the nanowire, while when the problem becomes asymmetric because of the tip position we will solve separately the equation on both domains until it converges to a solution where s is continuous in x_0.

Appendix E

Determination of N15 critical temperature

For some reason not completely understood, the superconducting transition of sample N15 is unusual compared to previous samples.

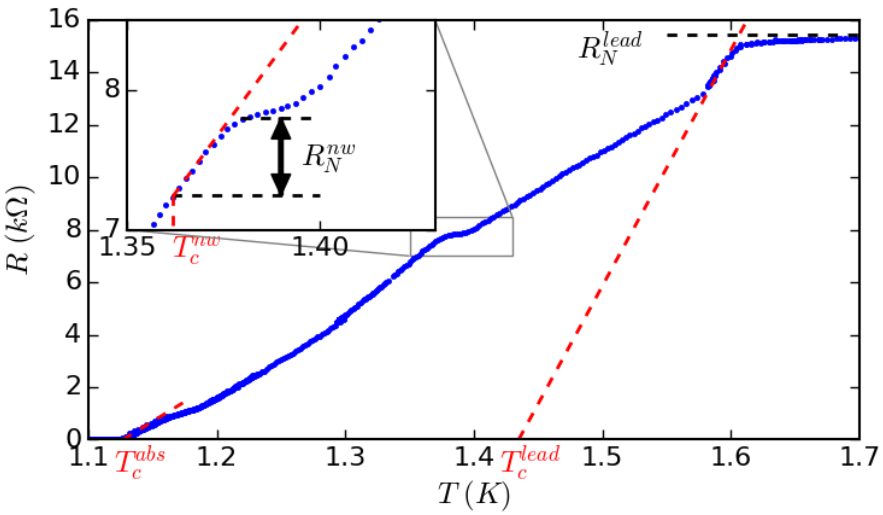

Figure E.1: Resistance versus temperature of sample N15 *Inset:* Zoom on the resistance plateau attributed to the nanowire.

The resistance versus temperature curve of sample N15 is wide by contrast with other samples. We define T_c^{lead} and T_c^{abs} as the extrapolation to $R = 0$ in linear scale of respectively the beginning and the end of the transition as shown on Fig. E.1. We attribute the resistance plateau in the middle of the transition to the nanowire (this assumption will be discussed), and thus define T_c^{nw} as the temperature for which the resistance drops of R_N^{nw} from the plateau. This method is of course less accurate than for the other samples, but the value of T_c^{nw} is consistent with the extrapolation of the $I_c(T)$ curve as explained below.

The $I_{wire}(V_{wire})$ curves near T_c^{abs} are shown on Fig. E.2a. For $T < T_c^{abs}$, during a rising ramp of I_{wire}, the first voltage jump defines the critical current (in blue), and for larger values of I_{wire}, V_{wire} increases exponentially (probably because of overheating) and we think that it prevents from measuring the voltage jump corresponding to the nanowire. For $T \geq T_c^{abs}$, a voltage jump appears while some dissipation already occurs ($V_{wire} > 0$). The associated resistance jump is equal to R_n^{nw}, so we attribute this transition to the nanowire critical current.

Fig. E.2b confirms this assumption. Indeed, the $I_c(T)$ curve corresponding to the first voltage jump (the blue curve jump of Fig. E.2a) is represented in blue points on Fig. E.2b and

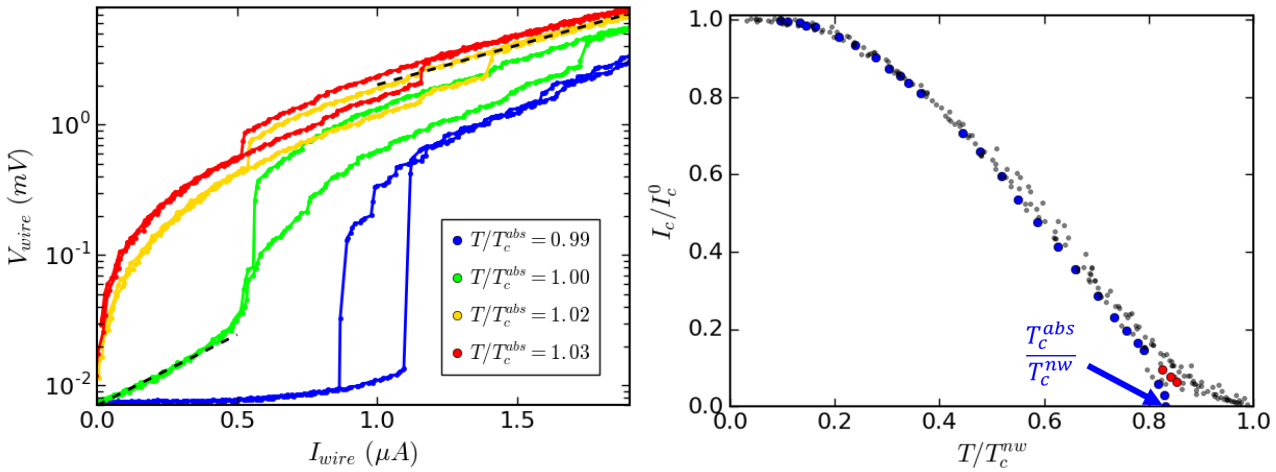

Figure E.2: (a) Current voltage characteristics of sample N15 near T_c^{abs}. The dashed lines indicates exponential increase of the resistance. (b) Reduced critical current versus reduced temperature. All the samples except N15 are in black. The critical current corresponding to the first voltage jump (in blue) vanishes at $T = T_c^{abs}$. The critical current attributed to the nanowire (in red, for more details see text) collapses with other samples data.

does not collapse with the other samples data. In contrast, the $I_c(T)$ curve corresponding to the second voltage jump attributed to the nanowire (the red, yellow and green curve jumps of Fig. E.2a) is represented in red in Fig. E.2b and collapse on an universal curve with other samples data.

Let's now discuss the possible reasons for such a difference with other samples.

Some inhomogeneity in the leads could create a weak link with a lower critical temperature that T_c^{nw}. Then, at low temperatures, the leads section being larger, the measured critical current would correspond to the one of the nanowire. At larger temperatures however, when the leads become resistive they dissipate some heat preventing to measure I_c up to T_c^{nw}.

Even if some inhomogeneities in the leads could explain a widening of the $R(T)$ transition, it is not very likely that this would lead to such a large one. Thus, another hypothesis would be that one part of the leads is warmed up (by some electrical short or thermal leak in the fridge). The cooling would therefore be inhomogeneous, the lead which is not heated up being first superconducting, then the nanowire, and finally the lead being warmed up. The point reaching effectively T_c^{lead} would move in the wire direction as the bath temperature T is lowered, so the total resistance decreases. When this point reaches the nanowire, no further reduction of the resistance is observed since the critical temperature of the nanowire T_c^{nw} is lower than T_c^{lead}. When the temperature in the nanowire reaches T_c^{nw}, the R_N^{nw} resistance drop occurs and the plateau ends, and the other lead transition starts. This also explains why the resistance plateau corresponds to half the normal state resistance. In this scenario, near critical temperature, because of the uncontrolled additional heat flux in one of the leads, the current flow triggers the transition of the latter in the normal state before the nanowire critical current is reached, explaining the observed reduction of the critical current near T_{abs}.

To conclude, the exact reason for such a weird transition is not well understood, but the small width of the nanowire ensures that at low temperatures ($T \leq 0.8T_c^{nw}$) the transition driven by the current occurs in the nanowire. The critical current cannot be measured up to temperatures arbitrarily close to T_c^{nw}, but **the $I_c(T)$ curve still provides a thermometer for the electronic temperature in the nanowire.**

Bibliography

[1] Abrikosov, A. On the Magnetic Properties of Superconductors of the Second Group. *Zh. Eksp. Teor. Fiz. 32* (Dec. 1957), 1442–1452. [JETP Letters 5(6), 1174 (1957)]. (p. 14)

[2] Abrikosov, A. A. *Fundamentals of the Theory of Metals.* Courier Dover Publications, Sept. 2017. (pp. 1, 80)

[3] Anderson, P. W. Theory of dirty superconductors. *Journal of Physics and Chemistry of Solids 11*, 1 (Sept. 1959), 26–30. (p. 51)

[4] Anthore, A. *Mécanismes de Decohérence Dans Les Conducteurs Mésoscopiques / Decoherence Mechanisms in Mesocopic Conductors.* PhD thesis, Université Pierre et Marie Curie - Paris VI, Sept. 2003. (pp. 23, 33, 129)

[5] Anthore, A., Pothier, H., and Esteve, D. Density of States in a Superconductor Carrying a Supercurrent. *Phys. Rev. Lett. 90*, 12 (Mar. 2003), 127001. (pp. 33, 34, 66)

[6] Ashcroft, N. W., and Mermin, N. D. *Solid State Physics.* Saunders college, Philadelphia, Pa., 1976. (pp. 37, 43, 44)

[7] Bardeen, J. Critical Fields and Currents in Superconductors. *Rev. Mod. Phys. 34*, 4 (Oct. 1962), 667–681. (pp. 32, 96)

[8] Bardeen, J., Cooper, L. N., and Schrieffer, J. R. Theory of Superconductivity. *Phys. Rev. 108*, 5 (Dec. 1957), 1175–1204. (pp. 1, 12, 34, 76, 120)

[9] Bardeen, J., Rickayzen, G., and Tewordt, L. Theory of the Thermal Conductivity of Superconductors. *Physical Review 113*, 4 (Feb. 1959), 982–994. (p. 76)

[10] Belzig, W., Wilhelm, F. K., Bruder, C., Schön, G., and Zaikin, A. D. Quasiclassical Green's function approach to mesoscopic superconductivity. *Superlattices and Microstructures 25*, 5 (May 1999), 1251–1288. (pp. 21, 22)

[11] Binnig, G., Rohrer, H., Gerber, C., and Weibel, E. Tunneling through a Controllable Vacuum Gap. *Appl. Phys. Lett. 40*, 2 (Jan. 1982), 178–180. (p. 5)

[12] Blamire, M. G., Kirk, E. C. G., Evetts, J. E., and Klapwijk, T. M. Extreme critical-temperature enhancement of Al by tunneling in Nb/AlOx/Al/AlOx/Nb tunnel junctions. *Physical Review Letters 66*, 2 (Jan. 1991), 220–223. (p. 34)

[13] Blumberg, R. H., and Seraphim, D. P. Effect of Elastic Strain on the Superconducting Critical Temperature of Evaporated Tin Films. *Journal of Applied Physics 33*, 1 (Jan. 1962), 163–168. (p. 48)

[14] Bourgeois, O. *Heat Transfer in Low Temperature Micro- and Nanosystems.* Springer-Verlag, 2009. (pp. 75, 79)

[15] Bourgeois, O., Frydman, A., and Dynes, R. C. Inverse Proximity Effect in a Strongly Correlated Electron System. *Physical Review Letters 88*, 18 (Apr. 2002), 186403. (p. 54)

[16] Bueno, J., Coumou, P. C. J. J., Zheng, G., de Visser, P. J., Klapwijk, T. M., Driessen, E. F. C., Doyle, S., and Baselmans, J. J. A. Anomalous response of superconducting titanium nitride resonators to terahertz radiation. *Applied Physics Letters 105*, 19 (Nov. 2014), 192601. (pp. 1, 127)

[17] Caroli, C., and Cyrot, M. Thermal conductivity in dirty superconducting alloys in high field. *Physik der kondensierten Materie 4*, 4 (Dec. 1965), 285–296. (p. 109)

[18] Chandrasekhar, V. An introduction to the quasiclassical theory of superconductivity for diffusive proximity-coupled systems. In *The Physics of Superconductors*, bennemann and ketterson, springer-verlag ed., vol. II. Nov. 2004. (pp. 21, 133)

[19] Clarke, J., Eckern, U., Schmid, A., Schön, G., and Tinkham, M. Branch-imbalance relaxation times in superconductors. *Physical Review B 20*, 9 (Nov. 1979), 3933–3937. (p. 119)

[20] Clem, J. R., and Berggren, K. K. Geometry-dependent critical currents in superconducting nanocircuits. *Physical Review B 84*, 17 (Nov. 2011), 174510. (p. 128)

[21] Couedo, F., Crauste, O., Bergé, L., Dolgorouky, Y., Marrache-Kikuchi, C., and Dumoulin, L. Superconductor—Insulator Transitions in Pure Polycrystalline Nb Thin Films. *Journal of Physics: Conference Series 400*, 2 (Dec. 2012), 022011. (p. 53)

[22] Crauste, O., Couëdo, F., Bergé, L., Marrache-Kikuchi, C. A., and Dumoulin, L. Destruction of superconductivity in disordered materials: A dimensional crossover. *Physical Review B 90*, 6 (Aug. 2014), 060203. (p. 56)

[23] Crauste, O., Gentils, A., Couëdo, F., Dolgorouky, Y., Bergé, L., Collin, S., Marrache-Kikuchi, C. A., and Dumoulin, L. Effect of annealing on the superconducting properties of a Nb x Si 1 - x thin films. *Physical Review B 87*, 14 (Apr. 2013), 144514. (p. 55)

[24] Cuevas, J. C., and Belzig, W. Dc Transport in Superconducting Point Contacts: A Full-Counting-Statistics View. *Phys. Rev. B 70*, 21 (Dec. 2004), 214512. (pp. 24, 25)

[25] De Gennes, P. G. Boundary Effects in Superconductors. *Reviews of Modern Physics 36*, 1 (Jan. 1964), 225–237. (p. 27)

[26] De Simoni, G., Paolucci, F., Puglia, C., and Giazotto, F. Josephson Field-Effect Transistors Based on All-Metallic Al/Cu/Al Proximity Nanojunctions. *ACS Nano 13*, 7 (July 2019), 7871–7876. (pp. 37, 93, 94, 95)

[27] De Simoni, G., Paolucci, F., Solinas, P., Strambini, E., and Giazotto, F. Metallic supercurrent field-effect transistor. *Nature Nanotechnology 13*, 9 (Sept. 2018), 802–805. (pp. 2, 37, 38, 93, 94, 95)

[28] de Visser, P. J., Baselmans, J. J. A., Diener, P., Yates, S. J. C., Endo, A., and Klapwijk, T. M. Number Fluctuations of Sparse Quasiparticles in a Superconductor. *Physical Review Letters 106*, 16 (Apr. 2011), 167004. (p. 1)

[29] de Visser, P. J., Goldie, D. J., Diener, P., Withington, S., Baselmans, J. J. A., and Klapwijk, T. M. Evidence of a Nonequilibrium Distribution of Quasiparticles in the Microwave Response of a Superconducting Aluminum Resonator. *Physical Review Letters 112*, 4 (Jan. 2014), 047004. (p. 99)

[30] Delacour, C., Ortega, L., Faucher, M., Crozes, T., Fournier, T., Pannetier, B., and Bouchiat, V. Persistence of superconductivity in niobium ultrathin films grown on R-plane sapphire. *Physical Review B 83*, 14 (Apr. 2011), 144504. (p. 53)

[31] DeSorbo, W. Effect of Dissolved Gases on Some Superconducting Properties of Niobium. *Physical Review 132*, 1 (Oct. 1963), 107–121. (p. 42)

[32] Dynes, R. C., Narayanamurti, V., and Garno, J. P. Direct Measurement of Quasiparticle-Lifetime Broadening in a Strong-Coupled Superconductor. *Phys. Rev. Lett. 41*, 21 (Nov. 1978), 1509–1512. (p. 12)

[33] Eliashberg, G. M. Film superconductivity stimulated by a high-frequency field. *Zh. Eksp. Teor. Fiz. Pisma 11* (1970), 186. [JETP Letters 11, 114 (1970)]. (p. 34)

[34] Erez, A., and Meir, Y. Proposed Measurement of Spatial Correlations at the Berezinski-Kosterlitz-Thouless Transition of Superconducting Thin Films. *Physical Review Letters 111*, 18 (Nov. 2013), 187002. (p. 127)

[35] Feigel'man, M. V., Ioffe, L. B., Kravtsov, V. E., and Yuzbashyan, E. A. Eigenfunction Fractality and Pseudogap State near the Superconductor-Insulator Transition. *Physical Review Letters 98*, 2 (Jan. 2007), 027001. (p. 54)

[36] Finkel'stein, A. M. Superconductivity-transition temperature in amorphous films. *Zh. Eksp. Teor. Fiz. Pisma 45* (Jan. 1987), 37–40. [JETP Letters 45, 46 (1987)]. (pp. 52, 53)

[37] Fischer, Ø., Kugler, M., Maggio-Aprile, I., Berthod, C., and Renner, C. Scanning Tunneling Spectroscopy of High-Temperature Superconductors. *Rev. Mod. Phys. 79*, 1 (Mar. 2007), 353–419. (pp. 6, 14)

[38] Fominov, Y. V., and Feigel'man, M. V. Superconductive properties of thin dirty superconductor–normal-metal bilayers. *Physical Review B 63*, 9 (Feb. 2001), 094518. (pp. 21, 28, 29, 58, 131)

[39] Frydman, A. The superconductor insulator transition in systems of ultrasmall grains. *Physica C: Superconductivity 391*, 2 (Aug. 2003), 189–195. (p. 51)

[40] Fulde, P. Gapless Superconducting Tunneling-Theory. In *Tunneling Phenomena in Solids: Lectures Presented at the 1967/NATO Advanced Study Institute at Risö, Denmark*, E. Burstein and S. Lundqvist, Eds. Springer US, Boston, MA, 1969, pp. 427–442. (pp. 108, 109)

[41] Gao, J., Vissers, M. R., Sandberg, M. O., da Silva, F. C. S., Nam, S. W., Pappas, D. P., Wisbey, D. S., Langman, E. C., Meeker, S. R., Mazin, B. A., Leduc, H. G., Zmuidzinas, J., and Irwin, K. D. A titanium-nitride near-infrared kinetic inductance photon-counting detector and its anomalous electrodynamics. *Applied Physics Letters 101*, 14 (Oct. 2012), 142602. (pp. 1, 127)

[42] Giazotto, F., Heikkilä, T. T., Luukanen, A., Savin, A. M., and Pekola, J. P. Opportunities for Mesoscopics in Thermometry and Refrigeration: Physics and Applications. *Rev. Mod. Phys. 78*, 1 (Mar. 2006), 217–274. (pp. 1, 75, 116)

[43] Gladstone, G., Jensen, M. A., and Schrieffer, J. R. Superconductivity in transition metals. In *Superconductivity*, R. D. Parks. Dekker, New York, 1969, p. 734. (pp. 43, 58)

[44] Graybeal, J. M., and Beasley, M. R. Localization and interaction effects in ultrathin amorphous superconducting films. *Physical Review B 29*, 7 (Apr. 1984), 4167–4169. (p. 53)

[45] Gubin, A. I., Il'in, K. S., Vitusevich, S. A., Siegel, M., and Klein, N. Dependence of Magnetic Penetration Depth on the Thickness of Superconducting Nb Thin Films. *Phys. Rev. B 72*, 6 (Aug. 2005), 064503. (pp. 44, 53, 55)

[46] Hadacek, N., Sanquer, M., and Villégier, J.-C. Double reentrant superconductor-insulator transition in thin TiN films. *Physical Review B 69*, 2 (Jan. 2004), 024505. (p. 53)

[47] Halloran, M. H., Condon, J. H., Graebner, J. E., Kunzier, J. E., and Hsu, F. S. L. Experimental Study of the Fermi Surfaces of Niobium and Tantalum. *Physical Review B 1*, 2 (Jan. 1970), 366–372. (p. 44)

[48] Haviland, D. B., Liu, Y., and Goldman, A. M. Onset of superconductivity in the two-dimensional limit. *Physical Review Letters 62*, 18 (May 1989), 2180–2183. (p. 52)

[49] Helfand, E., and Werthamer, N. R. Temperature and Purity Dependence of the Superconducting Critical Field, H c 2 . II. *Physical Review 147*, 1 (July 1966), 288–294. (p. 45)

[50] Heslinga, D. R., and Klapwijk, T. M. Enhancement of superconductivity far above the critical temperature in double-barrier tunnel junctions. *Physical Review B 47*, 9 (Mar. 1993), 5157–5164. (pp. 34, 35)

[51] Hortensius, H. L., Driessen, E. F. C., Klapwijk, T. M., Berggren, K. K., and Clem, J. R. Critical-current reduction in thin superconducting wires due to current crowding. *Applied Physics Letters 100*, 18 (Apr. 2012), 182602. (p. 128)

[52] Hübler, F., Lemyre, J. C., Beckmann, D., and v. Löhneysen, H. Charge imbalance in superconductors in the low-temperature limit. *Physical Review B 81*, 18 (May 2010), 184524. (p. 119)

[53] Ivry, Y., Kim, C.-S., Dane, A. E., De Fazio, D., McCaughan, A. N., Sunter, K. A., Zhao, Q., and Berggren, K. K. Universal scaling of the critical temperature for thin films near the superconducting-to-insulating transition. *Physical Review B 90*, 21 (Dec. 2014), 214515. (p. 55)

[54] Jaeger, H. M., Haviland, D. B., Goldman, A. M., and Orr, B. G. Threshold for superconductivity in ultrathin amorphous gallium films. *Physical Review B 34*, 7 (Oct. 1986), 4920–4923. (p. 52)

[55] Jani, A. R., Brener, N. E., and Callaway, J. Band Structure and Related Properties of Bcc Niobium. *Phys. Rev. B 38*, 14 (Nov. 1988), 9425–9433. (p. 43)

[56] Jennings, L. D., and Swenson, C. A. Effects of Pressure on the Superconducting Transition Temperatures of Sn, In, Ta, Tl, and Hg. *Physical Review 112*, 1 (Oct. 1958), 31–43. (p. 48)

[57] Kabanov, V. V., and Alexandrov, A. S. Electron relaxation in metals: Theory and exact analytical solutions. *Physical Review B 78*, 17 (Nov. 2008), 174514. (p. 80)

[58] Kaplan, S. B. Acoustic Matching of Superconducting Films to Substrates. *J Low Temp Phys 37*, 3-4 (Nov. 1979), 343–365. (pp. 75, 76)

[59] Kaplan, S. B., Chi, C. C., Langenberg, D. N., Chang, J. J., Jafarey, S., and Scalapino, D. J. Quasiparticle and Phonon Lifetimes in Superconductors. *Phys. Rev. B 14*, 11 (Dec. 1976), 4854–4873. (pp. 79, 80, 118, 119, 124)

[60] Karasik, V. R., and Shebalin, I. Y. Superconducting Properties of Pure Niobium. *Sov. Phys. JETP 57*, 6 (1970), 1973. [JETP Letters 30(6), 1068 (1970)]. (p. 43)

[61] Karvonen, J. T., Taskinen, L. J., and Maasilta, I. J. Observation of Disorder-Induced Weakening of Electron-Phonon Interaction in Thin Noble-Metal Films. *Phys. Rev. B 72*, 1 (July 2005), 012302. (pp. 75, 83)

[62] Klapwijk, T. M., and de Visser, P. J. The discovery, disappearance and re-emergence of radiation-stimulated superconductivity. *Annals of Physics 417* (June 2020), 168104. (p. 34)

[63] Klein, N., Chaloupka, H., Müller, G., Orbach, S., Piel, H., Roas, B., Schultz, L., Klein, U., and Peiniger, M. The effective microwave surface impedance of high Tc thin films. *Journal of Applied Physics 67*, 11 (June 1990), 6940–6945. (p. 61)

[64] Kohen, A., Proslier, T., Cren, T., Noat, Y., Sacks, W., Berger, H., and Roditchev, D. Probing the Superfluid Velocity with a Superconducting Tip: The Doppler Shift Effect. *Physical Review Letters 97*, 2 (July 2006), 027001. (p. 109)

[65] Kuit, K. H., Kirtley, J. R., van der Veur, W., Molenaar, C. G., Roesthuis, F. J. G., Troeman, A. G. P., Clem, J. R., Hilgenkamp, H., Rogalla, H., and Flokstra, J. Vortex trapping and expulsion in thin-film YBa 2 Cu 3 O 7 - δ strips. *Physical Review B 77*, 13 (Apr. 2008), 134504. (p. 112)

[66] Kupryanov, M. Y., and Lukichev, V. F. Temperature dependence of pair-breaking current in superconductors. *Fiz. Nizk. Temp. 6:4* (Apr. 1980), 445. [Sov. J. Low Temp. Phys. 6, 210 (1980)]. (p. 25)

[67] Landau, I. L., and Parshin, I. A. Increase in the superconducting transition temperature of thin films as a result of a normal metal deposition on their surface. *Physica B: Condensed Matter 194-196* (Feb. 1994), 2339–2340. (p. 54)

[68] Larkin (late), A., and Varlamov, A. *Theory of Fluctuations in Superconductors*. Oxford University Press. (p. 52)

[69] le Sueur, H., and Joyez, P. Room-Temperature Tunnel Current Amplifier and Experimental Setup for High Resolution Electronic Spectroscopy in Millikelvin Scanning Tunneling Microscope Experiments. *Review of Scientific Instruments 77*, 12 (Dec. 2006), 123701. (p. 15)

[70] Lee, P. A., and Ramakrishnan, T. V. Disordered electronic systems. *Reviews of Modern Physics 57*, 2 (Apr. 1985), 287–337. (p. 53)

[71] Lemberger, T. R. One-to-one correspondence of charge-imbalance relaxing mechanisms with pair-breaking mechanisms in superconductors. *Physical Review B 29*, 9 (May 1984), 4946–4950. (p. 119)

[72] Levy-Bertrand, F., Klein, T., Grenet, T., Dupré, O., Benoît, A., Bideaud, A., Bourrion, O., Calvo, M., Catalano, A., Gomez, A., Goupy, J., Grünhaupt, L., v. Luepke, U., Maleeva, N., Valenti, F., Pop, I. M., and Monfardini, A. Electrodynamics of granular aluminum from superconductor to insulator: Observation of collective superconducting modes. *Physical Review B 99*, 9 (Mar. 2019), 094506. (p. 35)

[73] Likharev, K. K. Superconducting weak links. *Reviews of Modern Physics 51*, 1 (Jan. 1979), 101–159. (pp. 61, 111, 112)

[74] Little, W. A. The Transport of Heat Between Dissimilar Solids at Low Temperatures. *Can. J. Phys. 37*, 3 (Mar. 1959), 334–349. (p. 76)

[75] Lowell, J., and Sousa, J. B. Mixed-state thermal conductivity of type II superconductors. *Journal of Low Temperature Physics 3*, 1 (July 1970), 65–87. (p. 109)

[76] Martinis, J. M., Ansmann, M., and Aumentado, J. Energy Decay in Superconducting Josephson-Junction Qubits from Nonequilibrium Quasiparticle Excitations. *Physical Review Letters 103*, 9 (Aug. 2009), 097002. (pp. 1, 99)

[77] Mattheiss, L. F. Electronic Structure of Niobium and Tantalum. *Physical Review B 1*, 2 (Jan. 1970), 373–380. (p. 44)

[78] Maxwell, E. Isotope Effect in the Superconductivity of Mercury. *Phys. Rev. 78*, 4 (May 1950), 477–477. (p. 19)

[79] Mitra, S., Tewari, G. C., Mahalu, D., and Shahar, D. Finite-size effects in amorphous indium oxide. *Physical Review B 93*, 15 (Apr. 2016), 155408. (p. 50)

[80] Nahum, M., Eiles, T. M., and Martinis, J. M. Electronic microrefrigerator based on a normal-insulator-superconductor tunnel junction. *Applied Physics Letters 65*, 24 (Dec. 1994), 3123–3125. (p. 105)

[81] Novotny, V., and Meincke, P. P. M. Single superconducting energy gap in pure niobium. *Journal of Low Temperature Physics 18*, 1-2 (Jan. 1975), 147–157. (p. 58)

[82] Nsanzineza, I., and Plourde, B. L. T. Trapping a Single Vortex and Reducing Quasiparticles in a Superconducting Resonator. *Physical Review Letters 113*, 11 (Sept. 2014), 117002. (pp. 1, 99)

[83] Pan, S. H., Hudson, E. W., and Davis, J. C. 3He Refrigerator Based Very Low Temperature Scanning Tunneling Microscope. *Review of Scientific Instruments 70*, 2 (Feb. 1999), 1459–1463. (p. 7)

[84] Paolucci, F., De Simoni, G., Solinas, P., Strambini, E., Ligato, N., Virtanen, P., Braggio, A., and Giazotto, F. Magnetotransport Experiments on Fully Metallic Superconducting Dayem-Bridge Field-Effect Transistors. *Physical Review Applied 11*, 2 (Feb. 2019), 024061. (pp. 37, 93, 94)

[85] Paolucci, F., De Simoni, G., Strambini, E., Solinas, P., and Giazotto, F. Ultra-Efficient Superconducting Dayem Bridge Field-Effect Transistor. *Nano Letters 18*, 7 (July 2018), 4195–4199. (pp. 2, 37, 93, 94)

[86] Parmenter, R. H. Enhancement of Superconductivity by Extraction of Normal Carriers. *Physical Review Letters 7*, 7 (Oct. 1961), 274–277. (p. 34)

[87] Patel, U., Pechenezhskiy, I. V., Plourde, B. L. T., Vavilov, M. G., and McDermott, R. Phonon-mediated quasiparticle poisoning of superconducting microwave resonators. *Physical Review B 96*, 22 (Dec. 2017), 220501. (p. 99)

[88] Pekola, J. P., Maisi, V. F., Kafanov, S., Chekurov, N., Kemppinen, A., Pashkin, Y. A., Saira, O.-P., Möttönen, M., and Tsai, J. S. Environment-Assisted Tunneling as an Origin of the Dynes Density of States. *Phys. Rev. Lett. 105*, 2 (July 2010), 026803. (pp. 11, 12, 34, 63, 117)

[89] Puglia, C., De Simoni, G., and Giazotto, F. Electrostatic Control of Phase Slips in Ti Josephson Nanotransistors. *Physical Review Applied 13*, 5 (May 2020), 054026. (pp. 37, 38, 93, 94, 95, 96)

[90] Renema, J. J., Gaudio, R., Wang, Q., Zhou, Z., Gaggero, A., Mattioli, F., Leoni, R., Sahin, D., de Dood, M. J. A., Fiore, A., and van Exter, M. P. Experimental Test of Theories of the Detection Mechanism in a Nanowire Superconducting Single Photon Detector. *Physical Review Letters 112*, 11 (Mar. 2014), 117604. (pp. 1, 2, 127)

[91] Ristè, D., Bultink, C. C., Tiggelman, M. J., Schouten, R. N., Lehnert, K. W., and DiCarlo, L. Millisecond charge-parity fluctuations and induced decoherence in a superconducting transmon qubit. *Nature Communications 4*, 1 (May 2013), 1913. (pp. 1, 99)

[92] Riwar, R.-P., Hosseinkhani, A., Burkhart, L. D., Gao, Y. Y., Schoelkopf, R. J., Glazman, L. I., and Catelani, G. Normal-metal quasiparticle traps for superconducting qubits. *Physical Review B 94*, 10 (Sept. 2016), 104516. (p. 1)

[93] Romijn, J., Klapwijk, T. M., Renne, M. J., and Mooij, J. E. Critical Pair-Breaking Current in Superconducting Aluminum Strips Far below T c. *Phys. Rev. B 26*, 7 (Oct. 1982), 3648–3655. (pp. 31, 32, 62)

[94] Sacépé, B., Chapelier, C., Baturina, T. I., Vinokur, V. M., Baklanov, M. R., and Sanquer, M. Disorder-Induced Inhomogeneities of the Superconducting State Close to the Superconductor-Insulator Transition. *Physical Review Letters 101*, 15 (Oct. 2008), 157006. (p. 54)

[95] Sacépé, B., Chapelier, C., Baturina, T. I., Vinokur, V. M., Baklanov, M. R., and Sanquer, M. Pseudogap in a thin film of a conventional superconductor. *Nature Communications 1*, 1 (Dec. 2010), 140. (p. 54)

[96] Sacépé, B., Chapelier, C., Marcenat, C., Kačmarčik, J., Klein, T., Bernard, M., and Bustarret, E. Tunneling Spectroscopy and Vortex Imaging in Boron-Doped Diamond. *Phys. Rev. Lett. 96*, 9 (Mar. 2006), 097006. (p. 14)

[97] Sacépé, B., Dubouchet, T., Chapelier, C., Sanquer, M., Ovadia, M., Shahar, D., Feigel'man, M., and Ioffe, L. Localization of preformed Cooper pairs in disordered superconductors. *Nature Physics 7*, 3 (Mar. 2011), 239–244. (p. 54)

[98] Sacépé, B., Seidemann, J., Gay, F., Davenport, K., Rogachev, A., Ovadia, M., Michaeli, K., and Feigel'man, M. V. Low-temperature anomaly in disordered superconductors near Bc2 as a vortex-glass property. *Nature Physics 15*, 1 (Jan. 2019), 48–53. (pp. 46, 54, 104)

[99] Savich, Y., Glazman, L., and Kamenev, A. Quasiparticle relaxation in superconducting nanostructures. *Physical Review B 96*, 10 (Sept. 2017), 104510. (pp. 1, 107, 128)

[100] Schmidt, D. R., Schoelkopf, R. J., and Cleland, A. N. Photon-Mediated Thermal Relaxation of Electrons in Nanostructures. *Phys. Rev. Lett. 93*, 4 (July 2004), 045901. (p. 16)

[101] Sergeev, A., and Mitin, V. Electron-Phonon Interaction in Disordered Conductors: Static and Vibrating Scattering Potentials. *Phys. Rev. B 61*, 9 (Mar. 2000), 6041–6047. (pp. 75, 80)

[102] Simonin, J. Surface term in the superconductive Ginzburg-Landau free energy: Application to thin films. *Physical Review B 33*, 11 (June 1986), 7830–7832. (p. 56)

[103] Skalski, S., Betbeder-Matibet, O., and Weiss, P. R. Properties of Superconducting Alloys Containing Paramagnetic Impurities. *Phys. Rev. 136*, 6A (Dec. 1964), A1500–A1518. (p. 25)

[104] Sohn, L. L., Kouwenhoven, L. P., and Schön, G. *Mesoscopic Electron Transport*. Springer Science & Business Media, June 2013. (pp. 21, 22, 133)

[105] Stan, G., Field, S. B., and Martinis, J. M. Critical Field for Complete Vortex Expulsion from Narrow Superconducting Strips. *Physical Review Letters 92*, 9 (Mar. 2004), 097003. (p. 112)

[106] Szczyrbowski, J. A new simple method of determining the effective mass of an electron or the thickness of thin metal films. *Journal of Physics D: Applied Physics 19*, 7 (July 1986), 1257–1263. (p. 43)

[107] Takane, Y. Charge Imbalance Relaxation in Superconductors at Low Temperatures. *Journal of the Physical Society of Japan 75*, 2 (Feb. 2006), 023706. (p. 119)

[108] Takane, Y., and Nagato, Y. Magnetic Field Effect on Charge Imbalance Conversion in Superconducting Wires. *Journal of the Physical Society of Japan 77*, 9 (Sept. 2008), 093713. (p. 119)

[109] Taupin, M., Khaymovich, I. M., Meschke, M., Mel'nikov, A. S., and Pekola, J. P. Tunable quasiparticle trapping in Meissner and vortex states of mesoscopic superconductors. *Nature Communications 7*, 1 (Mar. 2016), 10977. (p. 99)

[110] Tikhonov, K. S., Skvortsov, M. A., and Klapwijk, T. M. Superconductivity in the presence of microwaves: Full phase diagram. *Physical Review B 97*, 18 (May 2018), 184516. (p. 34)

[111] Tinkham, M. *Introduction to Superconductivity: Second Edition*. Dover Publications, June 2004. (pp. 1, 29)

[112] Tonnoir, C., Kimouche, A., Coraux, J., Magaud, L., Delsol, B., Gilles, B., and Chapelier, C. Induced Superconductivity in Graphene Grown on Rhenium. *Phys. Rev. Lett. 111*, 24 (Dec. 2013), 246805. (pp. 14, 20)

[113] Toxen, A. M. Size Effects in Thin Superconducting Indium Films. *Physical Review 123*, 2 (July 1961), 442–446. (p. 48)

[114] Usadel, K. D. Generalized Diffusion Equation for Superconducting Alloys. *Physical Review Letters 25*, 8 (Aug. 1970), 507–509. (p. 51)

[115] van den Hamer, P., Montie, E. A., Meijer, P. B. L., Mooij, J. E., and Klapwijk, T. M. Enhancement of Superconductivity by Quasiparticle Injection. II. Critical Current Experiments. *J Low Temp Phys 69*, 3 (Nov. 1987), 287–311. (pp. 1, 36, 37)

[116] van den Hamer, P., Montie, E. A., Mooij, J. E., and Klapwijk, T. M. Enhancement of superconductivity by quasiparticle injection. I. Model analysis. *Journal of Low Temperature Physics 69*, 3 (Nov. 1987), 265–286. (pp. 36, 37)

[117] Wellstood, F. C., Urbina, C., and Clarke, J. Hot-Electron Effects in Metals. *Phys. Rev. B 49*, 9 (Mar. 1994), 5942–5955. (pp. 75, 80)

[118] Werthamer, N. R., Helfand, E., and Hohenberg, P. C. Temperature and Purity Dependence of the Superconducting Critical Field, H c 2 . III. Electron Spin and Spin-Orbit Effects. *Physical Review 147*, 1 (July 1966), 295–302. (p. 45)

[119] Zaytseva, I., Abaloszew, A., Syryanyy, Y., and Cieplak, M. Z. Double critical regimes at the superconductor-metal transition in ultrathin niobium films. *arXiv:1912.03080 [cond-mat]* (Dec. 2019). (p. 55)